Dissertation
submitted to the
Combined Faculties for the Natural Sciences and for Mathematics
of the Ruperto-Carola University of Heidelberg, Germany
for the degree of
Doctor of Natural Sciences

presented by

M.Sc. Physik Joran Deschamps
born in Céret
Oral examination: October 13th 2017

Towards quantitative high-throughput 3D localization microscopy

Referees: Dr. Robert Prevedel
Prof. Dr. med. Hans-Georg Kräusslich

Parts of the work described in this thesis have been published:

Deschamps, J., Mund, M., & Ries, J. (2014). 3D superresolution microscopy by supercritical angle detection. Optics Express, 22, 29081-29091.

Deschamps, J., Rowald, A., & Ries, J. (2016). Efficient homogeneous illumination and optical sectioning for quantitative single-molecule localization. Optics Express, 24, 28080-28090.

Balazs, B., **Deschamps, J.**, Albert, M., Ries, J. & Hufnagel, L. (2017). A real-time compression library for microscopy images. bioRxiv.

Abstract

Advances in light microscopy have allowed circumventing the diffraction barrier, once thought to be the ultimate resolution limit in optical microscopy, and given rise to various superresolution microscopy techniques. Among them, localization microscopy exploits the blinking of fluorescent molecules to precisely pinpoint the positions of many emitters individually, and subsequently reconstruct a superresolved image from these positions. While localization microscopy enables the study of cellular structures and protein complexes with unprecedented details, severe technical bottlenecks still reduce the scope of possible applications. In my PhD work, I developed several technical improvements at the level of the microscope to overcome limitations related to the photophysical behaviour of fluorescent molecules, slow acquisition rates and three-dimensional imaging.

I built an illumination system that achieves uniform intensity across the field-of-view using a multi-mode fiber and a commercial speckle-reducer. I showed that it provides uniform photophysics within the illuminated area and is far superior to the common illumination system. It is easy to build and to add to any microscope, and thus greatly facilitates quantitative approaches in localization microscopy.

Furthermore, I developed a fully automated superresolution microscope using an open-source software framework. I developed advanced electronics and user-friendly software solutions to enable the design and unsupervised acquisition of complex experimental series. Optimized for long-term stability, the automated microscope is able to image hundreds to thousands of regions over the course of days to weeks. First applied in a system-wide study of clathrin-mediated endocytosis in yeast, the automated microscope allowed the collection of a data set of a size and scope unprecedented in localization microscopy.

Finally, I established a fundamentally new approach to obtain three-dimensional superresolution images. Supercritical angle localization microscopy (SALM) exploits the phenomenon of surface-generated fluorescence arising from fluorophores close to the coverslip. SALM has the theoretical prospect of an isotropic spatial resolution with simple instrumentation. Following a first proof-of-concept implementation, I re-engineered the microscope to include adaptive optics in order to reach the full potential of the method.

Taken together, I established simple, yet powerful, solutions for three fundamental technical limitations in localization microscopy regarding illumination, throughput and resolution. All of them can be combined within the same instrument, and can dramatically improve every cutting-edge microscope. This will help to push the limit of the most challenging applications of localization microscopy, including system-wide imaging experiments and structural studies.

Zusammenfassung

Durch die Entwicklung neuer Techniken in der Lichtmikroskopie konnte das Brechungslimit überwunden werden, welches einst als ultimative Auflösungsgrenze der optischen Mikroskopie angesehen wurde. Als eine von diesen nutzt Einzelmolekül-Lokalisationsmikroskopie das Blinken von Fluorophoren aus, um die Positionen vieler Emitter nacheinander zu bestimmen, und aus diesen ein hochauflösendes Bild zu rekonstruieren. Obwohl mittels Lokalisationsmikroskopie möglich ist, zelluläre Strukturen und Proteinkomplexe mit hoher Auflösung zu untersuchen, gibt es einige technische Hindernisse, die das derzeitige Anwendungsspektrum einschränken. In meiner PhD-Arbeit entwickelte ich mehrere technische Verbesserungen auf dem Level des Mikroskops, um Limitierungen bezüglich der Einzelmolekül-Photophysik, langsamer Aufnahmegeschwindigkeiten und drei-dimensionaler Bildgebung aufzulösen.

Ich habe ein Beleuchtungssystem konstruiert, welches mittels einer Multimode-Faser und einem kommerziellen Speckle-Reduzierer eine gleichmäßige Beleuchtung im gesamten Sichtfeld erzeugt. Dadurch wird gleiches photophysikalisches Verhalten aller Fluorophore erreicht, was mit dem derzeit meistverbreiteten Beleuchtungssystem nicht realisierbar ist. Es lässt sich problemlos zu jedem Mikroskop hinzufügen, und erleichtert daher quantitative Experimente mittels Lokalisationsmikroskopie.

Des Weiteren habe ich ein vollständig automatisiertes Lokalisations-Mikroskop entwickelt, welches auf einer Open-Source-Softwareumgebung basiert. Ich entwickelte hochspezialisierte Elektronik- und nutzerfreundliche Software-Lösungen, mittels derer komplexe Experimente geplant und durchgeführt werden können. Ich optimierte die Langzeitstabilität, wodurch die Aufnahme hunderter bis tausender Bilder über Tage und Wochen möglich wurde. In einer ersten Anwendung wurde Clathrin-vermittelte Endozytose in Hefe untersucht, und ein Datensatz aufgenommen, welcher in Größe und Umfang in der Lokalisationsmikroskopie beispiellos ist.

Schließlich etablierte ich einen völlig neuen Ansatz für drei-dimensionale Lokalisationsmikrosopie. Superkritische-Winkel-Lokalisationsmikroskopie (SALM) basiert auf Oberflächen-generierter Fluoreszenz, welche von Fluorophoren nah am Deckglas emittiert wird. SALM kann mit einem einfachen Mikroskop theoretisch isotrope Auflösung erreichen. Nachdem ich das Konzept technisch demonstrierte, entwickelte ich das Mikroskop mittels Adaptiver Optiken weiter, um das volle Potential der Methode auszuschöpfen.

Zusammengenommen habe ich einfache, aber wirkungsvolle, Lösungen für drei grundlegende technische Hindernisse in Lokalisationsmikroskopie etabliert, welche

Beleuchtung, Durchsatz und Auflösung betreffen. All diese können kombiniert werden, und dadurch jedes moderne Mikroskop deutlich verbessern. Dadurch wird es immer besser möglich, auch höchst anspruchsvolle Anwendungen der Lokalisationsmikroskopie durchzuführen, wie beispielsweise systemweite Mikroskopie-Experimente, und strukturelle Studien.

Acknowledgements

As any time in life, these last four years have been made of ups and downs. Looking back, there is nothing I regret about my time as a PhD student. Living in Germany and working at EMBL have been the best experiences of my life, and many people contributed to making it so.

Above all, I am profoundly grateful to Jonas for giving me the opportunity to join the lab. You were a great mentor and I can't event measure of much I learned here. Thank you for building such an amazing environment and for your availability on any occasion.

I am thankful to the people in the lab for coping with my accent, my impersonations of other accents, my badly timed jokes, French curses and my mood swings (especially during microscope break downs): Markus, Ulf, Kostrich, Li-ling, Jan, Jervis, Andreas, Raja, Manuel, Jooske, Yiming, Phil'O and Daniel. Thanks for all the fun day by day and during our amazing retreats. In particular, I am happy we did not suffer any casualty during our adventures.

I would like to thank my TAC members, Rainer Pepperkok, Hans-Georg Kräusslich and Edward Lemke, for their advice and constant reminders to keep away from a thousands projects. Many thanks to Michael Knop and Robert Prevedel for joining my thesis committee. Thank you very much Robert for saving the day, quite literally. An additional thanks goes to Robert and Hans-Georg for reviewing this thesis. A special mention should be given to the mechanical and electrical workshops of EMBL for their precious help, and to Jonas, Philipp, Markus, Laura, Gustavo and Nika for reading the manuscript.

The hundred fifty pages and more of this manuscript are pale in comparison of what I would like to write to thank the people that made my life so enjoyable this past few years. Among them, thank you Paul, Hannah, Martina, Balint, Emo, Deni and Stephen, it has been an amazing time and I hope that more is to come.

Years of training card games never made me good at it, neither did our bi-weekly Dopplekopf meetings. But I was surely looking forward to them. Thank you so much, Markus, Nik and Simon, for sharing this German experience, cards in one hand and a suspicious Kölsch in the other.

Thank you Gustavo, Stefan and Manuela for letting me climb on board of "Life in Perspective". It was a truly wonderful experience, of which I can't wait to see the next steps.

Thank you also Kostek, for your weird movie tastes and your incomparable mastering of gin-tonic. I am sorry we stapled you labbook. Twice. I am also very grateful to you Sofya, for appearing at the moment where I needed it! I can't wait to resume our nocturnal expeditions in the wild Heidelberger night life. Serge, you hold a very special place in my Heidelberg years. I can admit it publicly now, I only joined EMBL because of the lecture you gave my young self in 2012, in your beautiful French rugby jersey. You have been an amazing friend, and I hope you

will remain the crazy high-voltage Judo-biking person you are. Don't hurt my ankle ever again. Jan, you were my best male flatmate. I can't thank you enough for coming back so often to us, for our netflix nights and all the cheese. Finally, thank you so much Nika for all your care during the writing and your determination in elaborating complex plans to take over the world at 3 am. I still can't believe you are real.

There are three people in particular that have been overwhelmingly important throughout those four years and that deserve a longer note. First of all, Markus, thank you so much for making these years an uninterrupted laughter attack, in the lab as well as during the long nights in crowded Londonian or deserted Göttinger bars. I am sorry I filled the complaint forms. Your friendship alone would have made these years worth living. You, Hanna and the kids, have made me feel at home from day one and I can't be grateful enough for that.

Thomas, la vie à Heidelberg n'a peut-être pas été parfaite, mais les nombreux moments que l'on a passés ensemble le furent assurément. Des pizzas surgelées à l'arrière-goût d'aérosol aux silences de la ville rompus par des parties de basket-bouteille, sans toi une grande partie de mes meilleurs souvenirs n'auraient pas existé. Merci de m'avoir accompagné dans l'écriture à des heures indues et au long d'interminables parties de scotch shooting (et pour avoir importé le 10000).

Laura, it is difficult to express how important you are to me. Thank you so much for taking care of me all year round. Living with you has been the best decision I could have made. I am sorry for my morning grumpiness, as well as for the evening one. I surely was not the best flatmate one could have had, especially since you hold this title. Thank you for organising the best costume parties in town, for your humour and for pushing me whenever I needed it. Thanks also for the strange man that is always sitting at our table and for the fluffy, noisy and demoniac raccoons you call cats. I am sad that our time as flatmates is coming to an end, but I find comfort in the fact that you probably will have a garden in your next place. I own a tent.

Finally, I am deeply grateful to my family and my friends from France. Papa, Maman et Julia, j'aurais aimé avoir été plus présent. Je ne peux vous exprimer combien je suis heureux de vous avoir dans ma vie, et tout ce que vous m'avez apporté pendant 28 ans. Je suis l'emmerdeur que je suis grâce à vous. Merci aussi à tous les amis qui m'ont rendu visite en ces contrées sauvages, Rémi, Thibault, Kevin, Benjamin, Seb, Thibaut, Matthieu, Petit Matthieu, Quentin, Bonjamin, Zaza, Maylis, Perrine et Manue.

As a conclusion, I would like to express my discontent with the organizers of the Tour de France for scheduling it in July and to electrical plugs in general. No cats were harmed in the writing of this thesis.

Contents

Abstract **vii**

Zusammenfassung **ix**

Acknowledgements **xi**

Contents **xiii**

1 Introduction **1**
- 1.1 The diffraction limit 1
- 1.2 Spatial frequencies in microscopy 4
- 1.3 Shifting and breaking the diffraction barrier 9
- 1.4 Stimulated-emission depletion microscopy 11
- 1.5 Structured illumination microscopy 14
- 1.6 Localization microscopy 17
  - 1.6.1 Principle of localization microscopy 19
  - 1.6.2 The choice of fluorescent labels and labelling strategies 23
  - 1.6.3 Conducting SMLM experiments: microscope and analysis . . 26
  - 1.6.4 Multicolour imaging 31
  - 1.6.5 Extension to the third dimension 35
  - 1.6.6 Live imaging 40
  - 1.6.7 Application to biological questions 40

2 Aim of the study **43**

3 Homogeneous illumination **45**
- 3.1 Introduction 45
  - 3.1.1 Quantitative studies in SMLM 46
- 3.2 Results 47
  - 3.2.1 Multi-mode and single-mode fibers 47
  - 3.2.2 Optical path 49
  - 3.2.3 Illumination profile 50
  - 3.2.4 Application to localization microscopy 52
  - 3.2.5 Optical sectioning with homogeneous excitation 54

3.3 Discussion 56

4 High-throughput superresolution microscopy 61
4.1 Introduction 61
4.2 Results 63
4.2.1 Hardware control 64
4.2.2 User interface 68
4.2.3 Automatic SMLM acquisitions 71
4.2.4 Data storage 74
4.2.5 High-throughput localization microscopy 77
4.3 Discussion 79

5 Supercritical angle localization microscopy 83
5.1 Introduction 83
5.2 Principle of surface-generated fluorescence 85
5.3 Results 88
5.3.1 Supercritical angle localization microscopy 88
5.3.2 Theoretical precision 90
5.3.3 Calibration 91
5.3.4 Validation 93
5.3.5 Imaging of biological samples 94
5.3.6 Improving SALM 96
5.3.6.1 Adaptive optics SALM 97
5.3.6.2 Adaptive optics correction 98
5.4 Discussion 101

6 Conclusion 103

7 Materials and methods 105
7.1 Microscopes 105
7.1.1 Homogeneous illumination system 105
7.1.2 High-throughput microscope 106
7.1.3 SALM microscope 108
7.1.4 SALM masks 109
7.1.5 AO-SALM microscope 110
7.2 Microscope control 110
7.2.1 Micro-manager device adapters 112
7.2.2 Micro-Mojo 112
7.2.3 Interface plug-in 112
7.3 Sample preparation 113
7.4 Imaging 115
7.5 Localization analysis and rendering 116
7.6 Adaptive optics correction 118

7.7 Theoretical and experimental calculations 119

A Supercritical angle localization precision **121**

Bibliography **125**

List of Figures

1.1 Diffraction and point-spread function 2
1.2 Fourier transformation 5
1.3 Angular spectrum representation 6
1.4 Optical transfer function 8
1.5 Stimulated-emission depletion 13
1.6 Structured-illumination microscopy 15
1.7 Principle of localization microscopy 20
1.8 Blinking mechanisms 24
1.9 Localization microscope 27
1.10 Multicolour imaging 33
1.11 3D imaging 37

3.1 Single-mode vs multi-mode fibers 48
3.2 A new system for homogeneous illumination 50
3.3 Effect of the illumination on the molecules' photophysics 53
3.4 Recovering TIR capabilities with homogeneous excitation 55

4.1 Layers of modern microscopy 64
4.2 Computer controlled elements of a microscope 65
4.3 Laser triggering with Micro-Mojo 68
4.4 Micro-Mojo inputs/outputs 69
4.5 Micro-Interface 70
4.6 Focus stability across the coverslip 71
4.7 Automated activation 73
4.8 Unsupervised acquisitions pipeline 75
4.9 Data transfer and compression 76
4.10 High-throughput localization microscopy 78
4.11 Study of the radial organization of CME 79

5.1 Supercritical angle fluorescence 87
5.2 SALM microscope 89
5.3 SALM resolution 91
5.4 SALM calibration 92
5.5 Validation of SALM 94

5.6 Resolving biological structures with SALM 95
5.7 Improving SALM with high NA 96
5.8 AO-SALM microscope 98
5.9 Wavefront sensing and correction 99
5.10 Zernike polynomials 100
5.11 Sensorless PSF optimization 100

7.1 Homogeneous illumination system 106
7.2 High-throughput microscope 107
7.3 SALM microscope 108
7.4 SALM masks 110
7.5 AO-SALM microscope 111
7.6 Micro-Interface 113

List of Tables

7.1 Illumination components 106
7.2 High-throughput microscope components 107
7.3 SALM microscope components 109
7.4 AO-SALM microscope components 111
7.5 Custom device adapters 112

List of Abbreviations

2D	Two-dimensional
2PE	Two-photons excitation
3D	Three-dimensional
AO	Adaptive optics
AO-SALM	Adaptive optics supercritical angle localization microscopy
BFP	Back-focal plane
CCD	Charge-coupled device
CSLM	Confocal scanning light microscope
DH-PSF	Double-helix point-spread function
EMCCD	Electron-multiplying CCD
FFP	Front focal plane
FRC	Fourier ring correlation
FT	Fourier transform
µM	Micro-Manager
MM	Multimode
NSOM	Near-field scanning optical microscope
PSF	Point-spread function
SALM	Supercritical angles localization microscopy
SH-WFS	Shack-Hartmann wavefront sensor
SIM	Structured-illumination microscopy
SM	Single-mode
SMLM	Single-molecule localization microscopy
STED	Stimulated-emission depletion
TIR	Total-internal reflection
UI	User interface

1 Introduction

The history of Microscopy closely intertwined with the early developments of biology. During the late 17th century, the improvement in quality of optical lenses and compound microscopes (composed of several such lenses) led to striking discoveries and a flourishing literature. In 1665, Robert Hooke published his famous work entitled Micrographia (Hooke, 1665). Describing his observations with carefully executed drawings, he reported for the first time details of various forms of life, such as insects or sponges. He additionally coined the term “cell” when observing boxlike structures in cork tissue. One of his contemporaries, Antony van Leeuwenhoek, became famous by describing bacteria and red blood cells using precisely crafted lenses, whose magnification were superior to compound microscopes of these times. The direct observation of the microscopic world enabled the possibility to study life at small scales and established microscopy as an essential tool of life sciences. Later developments in both manufacturing quality and understanding of light phenomenon, allowed the production of better microscopes. A striking example is the partnership between Ernst Abbé, one of the founders of modern optics, and Otto Schott, a glass chemist, within the Zeiss workshop in the 19th century. More than a century later, microscopes are still designed according to the principles laid out at the time of Abbé. In spite of later important technological developments, such as laser sources or charge-coupled device cameras (CCD), for a long time microscopes were thought to be limited in resolution to a fundamental and unsurpassable limit called the diffraction barrier.

1.1 The diffraction limit

Diffraction The diffraction limit is better understood when considering a point-like source emitter, such as a single-molecule, in focus in the microscope. The light emitted by the source travels through the specimen and is collected by the microscope objective. Each time the incident light encounters an element of smaller size, such as a lens or an aperture, only a portion of the wavefront will propagate through the element (see figure 1.1-a). Owing to diffraction, the light will bend at the edges of the encountered object. Since objectives have a limited collection angle and a finite aperture, diffraction will occur and degrade the wavefront. Using a lens to form an image of the source, the impact of diffraction can readily be observed in the fact that the image of the source is no longer a point (figure 1.1-b). In effect, diffraction causes an enlargement of the surface where the rays intersect each other and interfere constructively (thus forming an image). The pattern formed in the image of the point source presents a bright central spot, called the Airy disk, surrounded by circular side-lobes of lesser intensity (figure 1.1-c). In a more general setting, the image of a point source in 3D formed by an optical system is called the point-spread function (PSF). This Airy pattern is the consequence of the diffraction of light at a circular aperture (Airy, 1835), in our case the stop-aperture of the objective. Such broadening of the signal has direct consequences on the resolving power of microscopes. Indeed if we now consider not only a unique point source but a multitude of emitters decorating a biological object (such as fluorescently labelled antibodies), the broadened images of each point will overlap and cause a blurring of the object image itself.

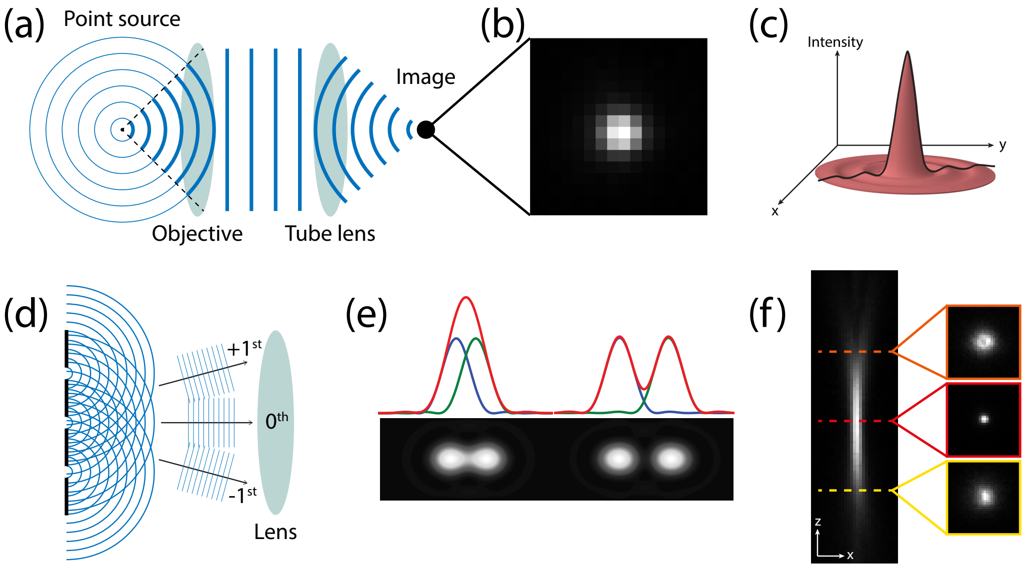

Figure 1.1: **Diffraction and point-spread function**. **a)** Only a portion of the total wavefront emitted by a source will propagate through the microscope due to the finite extent of the components. The image of a point formed by the microscope will then be broader than the source. **b)** The image of a point source is described by the Point-Spread function (PSF). Imaged onto the camera, it appears as a pixelated Gaussian. **c)** A perfect PSF in focus is mathematically described by an Airy function. It displays a bright central peak surrounded by circular side lobes. **d)** Following Huygens' principle, constructive interferences occur only in specific directions after a grating, giving rise to several diffraction orders. **e)** The separation of two point source emitters is the basis for the Rayleigh criterion. When two point sources are close to each other, their signal overlap and can become indistinguishable from one another. When the two sources are far away, then their signal peak are clearly separated. **f)** The 3D PSF is larger along the axial direction than laterally.

Abbé's limit The effects of diffraction within an optical system have been extensively studied long before an explicit link between a resolution limitation of microscopes and diffraction was stated. Although Émile Verdet was possibly the first one to enounce it, the most famous work related to the diffraction barrier originates from Ernst Abbé (Abbe, 1873). Based on the diffraction of (coherent) light through a grating and its subsequent imaging through a microscope, Abbé derived a formula linking the smallest observable features of the sample with the maximum collection angle of the optical system. A diffraction grating can for example be regularly spaced etched lines on a glass surface, extending the famous double-slit experiment (Young, 1802) to a large number of "holes" with equal distances. Interestingly, the transmitted light is composed of a certain number of beams propagating at different angles, called diffraction orders (figure 1.1-d). The angle difference depends on the wavelength of light as well as on the distance between the etched lines. The reason behind this phenomenon is that the diffraction of light at each groove creates a spherical wave propagating beyond the grating (Huygens-Fresnel principle). However, the different waves are only in phase in certain directions, thus interfering constructively. In the other directions, the phase differences cancel each other and interfere destructively. In order to form an image of the grating with a microscope, the 0^{th} and 1^{st} diffraction order must be collected by the objective lens and brought to focus in the image plane. If the 1^{st} diffraction order propagation angle is larger than the maximum collection angle of the microscope objective, then the grating will not be resolved. Therefore, Abbé concluded that the limit of the resolution of the microscope, that is to say how small of a grating can be resolved, depends only on the wavelength of the light and the maximum collection angle, leading to the famous relation:

$$d_{Abb\acute{e}} = \frac{\lambda}{2n\sin(\alpha)} \tag{1.1}$$

where d is the smallest feature a microscope can resolve, λ is the wavelength of the light, n is the refractive index in between the sample and the objective lens and α is half the aperture angle of the objective. The product of the refractive index and the sine of α is more commonly called the numerical aperture (NA): NA $= n\sin(\alpha)$. For instance, using an $NA = 1$ and 600 nm light, the diffraction limit of the microscope is placed at 300 nm according to Abbé's formula. It provided guidelines to improve the resolution of images. For instance, it prompted researchers to use light of small wavelengths or to increase the NA of the objectives (immersion lenses were already in use at the time of Abbé).

Rayleigh's criterion A few years after Abbé's work, Lord Rayleigh published another formula (Rayleigh, 1896), still widely used nowadays when estimating the diffraction limit. As opposed to Abbé, he included self-luminous objects in his theoretical study and adopted a different point of view. Indeed, Rayleigh considered two point sources close to each other and defined a criterion for the minimal distance between them at which they can still be discriminated (see figure 1.1-e). Since the image of a point source is the aforementioned PSF, the Rayleigh criterion is based on the mathematical expression of the Airy pattern. According to the criterion, the two sources are only discernible if the distance in between them is greater than the distance between the maximum intensity of the Airy pattern and the first minimum, leading to:

$$d_{Rayleigh} = \frac{0.61\lambda}{NA} \tag{1.2}$$

The Rayleigh criterion is very similar to Abbé's formula and presents the same λ/NA dependency. Other criteria have been introduced throughout the years (e.g. the Sparrow criterion) to overcome bottlenecks, such as the fact that the Rayleigh criterion might holds for the eyes but not for detectors sensitive to small intensity variation, for instance modern cameras. In most cases, resolution criteria are arbitrary and their value remain close to each other.

Diffraction barrier in z So far, the diffraction limit was expressed only laterally. However, biological samples are fundamentally three-dimensional (3D). Once again, the size of the PSF in 3D hints at the expected resolution limit. Along the optical axis, the PSF is substantially more elongated than it is laterally, as shown in figure 1.1-f. Therefore, one expects a very limited z-resolution. The Abbé limit in z reads as following:

$$d_{Abbé,z} = \frac{2\lambda}{\mathrm{NA}^2} \tag{1.3}$$

where in this case the dependency on the NA is squared. Using the same values than before, one finds a limit along the optical axis of $d_{Abbé,z} = 1200$ nm, as opposed to $d_{Abbé,x,y} = 300$ nm.

Those limits, although published more than hundred years ago, are still dictating the manufacturing of optical components and the assembling of microscopes. In addition, the work of Airy, Abbé, Helmholtz or Rayleigh is at the foundation of important theoretical developments that allowed a better understanding of optical phenomena.

1.2 Spatial frequencies in microscopy

In Abbé's work, the grating's grooves are equally spaced with a certain characteristic period d and an orientation. In the same way the oscillations of a pendulum are described by a (time) frequency that is the inverse of the period, the diffraction grating is characterized by a specific spatial frequency: $k \sim 1/d$. The diffraction limit of the microscope then defines a maximum spatial frequency that can be imaged by the microscope. The assumption behind Abbé's derivation is that any sample can be described by a superposition of gratings with different spatial frequencies and orientations. Similar decomposition is the fundamental idea behind the Fourier transform (FT).

Fourier transform Published by Joseph Fourier (Fourier, 1822), the FT was originally introduced in order to decompose any function as an infinite sum of sinusoids of various frequencies ($\sum sin(k_x x)$ or $\sum e^{-ik_x x}$ in complex representation). The simplest example is the FT of a sine function, which yields two peaks corresponding to its frequency (figure 1.2-a). A more complex time signal gives a FT with a larger set of frequency peaks (figure 1.2-b). However, the FT is not limited to time signals and can be used to decompose a spatial signal (such as the function describing the density of fluorophores in a 3D biological sample) as a sum of sine functions (or of complex exponentials) with different spatial frequencies. The FT of a 2D sinusoid has also two peaks at a single frequency pair, as illustrated in figure 1.2-c. In effect, the FT takes a function in the real space (our object of interest) where the coordinates are (x,y,z) and represents it in the frequency space (also called Fourier space or reciprocal space) where the coordinates are (k_x, k_y, k_z), with $k_i \sim 1/i$, i=x,y,z. The FT is reversible and applying the inverse transform returns the initial function without loss of information. Because the FT has interesting mathematical properties, such representation in the Fourier space can be advantageous. Probably the best example of motivation to use a FT is the fact that in real space convolution is a demanding process while in frequency space it becomes a simple multiplication: $FT[f \otimes g] = FT[f] * FT[g]$ (where $\otimes$ denotes a convolution and $*$ multiplication).

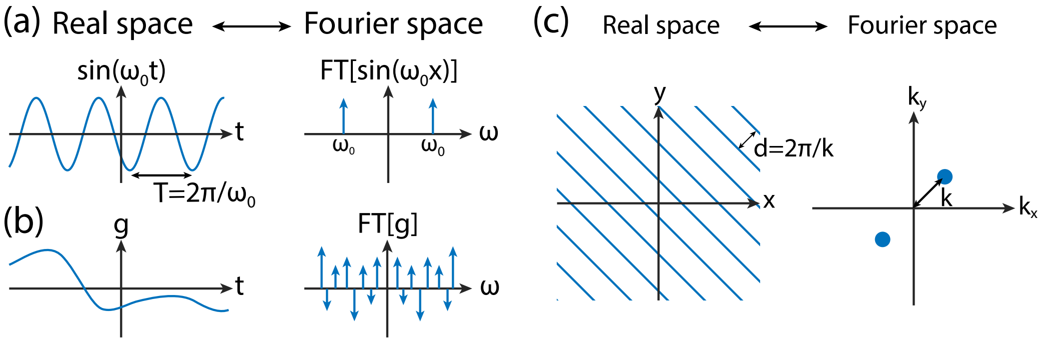

FIGURE 1.2: **Fourier transformation**. **a)** In Fourier space, a sine function is represented as two peaks corresponding to w_0 and $-w_0$, where w_0 is the sine frequency. **b)** More complicated functions will be represented as a sum of a large number of sine functions, and will be represented in Fourier space by the corresponding number of frequencies and their negative counterpart. **c)** In 2D, the FT of a sinusoidal grating will be represented in a 2D Fourier space as two peaks. These two peaks correspond once again to the grating's frequency.

Plane waves representation In wave optics, plane waves are usually described as a complex function of the form $U(\vec{r}) = e^{-i\vec{k}.\vec{r}}$ (ignoring time dependence and a constant phase offset). In this expression, the vector $\vec{k}$ is called the wave vector and is linked to the wavelength of the wave by $|\vec{k}| = 2\pi/\lambda$. It is important to note that in this case the wave propagates in the direction of the wave vector as illustrated in figure 1.3.a (in a homogeneous medium). Plane waves are the simplest solution of Maxwell's equations. Since the amplitude of the wave vector is fixed by the wavelength of the light, the direction of propagation depends on the relative amplitude of k_x and k_y, while $k_z^2 = k^2 - k_x^2 - k_y^2$ (by convention the optical axis is chosen to be the z-axis). Any optical field $E(\vec{r})$ can be described by an infinite sum of plane waves, in what is called the *angular spectrum representation* (Goodman, 1968). A simple illustration is found in figure 1.3-b. Under certain assumptions (such as the paraxial limit) this representation becomes identical to the Fourier transform of the optical field, enforcing the analogy between plane waves and Fourier components. It holds a fundamental place in wave optics as it recapitulates both geometrical (tracing of rays) and Fourier optics (treatment of optics with the FT). Additionally, it keeps intuitive objects such as plane waves in the mathematical calculations. One striking consequence of this representation is that it allows for the existence of non-propagating contributions to the total optical field. Indeed, the angular spectrum is comprised of the propagating plane waves with $k_x^2 + k_y^2 \leq k^2$ and *evanescent waves* with $k_x^2 + k_y^2 > k^2$. Because of this inequality, evanescent waves have a k_z that is purely imaginary. In consequence, evanescent waves are non-propagating and their amplitude decays exponentially. Such stationary fields have important impact in *near-field* optics (Novotny and Hecht, 2010) or for dipole emission close to interfaces (Novotny, 1996). Evanescent waves appear as well when light is directed to an aperture of sub-wavelength dimension and can only be measured half a wavelength away from the aperture (Novotny and Hecht, 2010). Last but not least, they limit the illumination depth in total-internal reflection microscopy (TIRF, Axelrod, 2013), allowing optical sectioning.

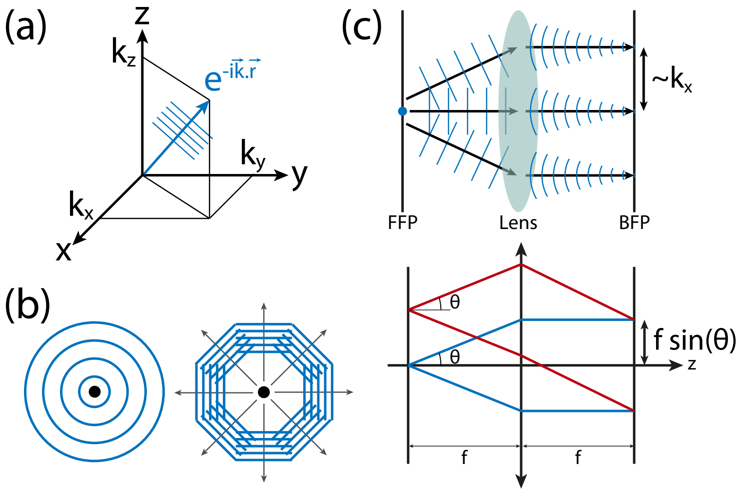

FIGURE 1.3: **Angular spectrum representation**. **a)** The simplest solution of Maxwell's equations is a plane wave. Plane waves travel in homogeneous medium along their wavevector k. **b)** Any electrical field can be represented by a superposition of plane waves. **c)** A source placed at the front focal plane (FFP) of a lens. The plane waves describing the emitted field will each converge in the back focal plane (BFP) to a point. The coordinates of the point are proportional to the components of the wavevector (upper panel). Geometrical optics predicts that the BFP is the distribution by angle of the light emanating from the FFP (lower panel). These two representations relate the wavevector components to the propagation angle of the plane waves.

Remarkably, the Fourier transform is not only found during the treatment of wave propagation in free space but also when calculating the effect of a lens on an incident radiation. Indeed, lenses perform a FT of the optical field in between their front and back focal plane (Goodman, 1968). From geometrical optics, we know that the back focal plane (BFP) of a lens is the distribution by angle θ of the rays emanating from the front focal plane (FFP, see figure 1.3-c lower panel). The interpretation of the FT property of lenses is that the BFP is now the frequency space mapping (k_x, k_y) of the field distribution at the FFP of the lens (figure 1.3-c lower panel). From the plane waves expansion, one can now relate the angle θ with corresponding spatial frequencies (coordinates of a wave vector) of the angular spectrum representation: $\theta = arctan(k_y/k_x)$. The consequence of the finite physical extent of the lens is that not all portions of the angular spectrum will be transmitted. The plane waves propagating at angles larger than the lens' collection angle will be blocked. Therefore, the corresponding high frequencies will be absent of the FT spectrum of the field (the lens acting as a low-pass filter), causing a broadening of the image. We found again the diffraction limit. The two descriptions of the system, in real space and in frequency space, are equivalent. While the real space response of the optical system is the PSF, the response in the frequency domain (for incoherent light) is called the *optical transfer function* (OTF, Williams and Becklund, 1989).

Optical transfer function As expected, the OTF is defined as the FT of the PSF. It describes with which strength the spatial frequencies are transferred through the system. Given that the diffraction limit corresponds to a cut-off in frequency space, the OTF falls to zero at this very spatial frequency (see figure 1.4-d). Another consequence from the Fourier equivalence between OTF and PSF is that the sharper the PSF, the broader the OTF and inversely. Systems with higher resolving power will have a narrower PSF. In frequency space, this translates into higher frequencies being transmitted through the optical system. That is to say a wider range of frequencies on which the OTF is non-null.

As we have seen before, the resolution of microscopes is often quantitatively expressed with one number, whether it is the Abbé limit or the Rayleigh criterion. In frequency space, this corresponds to a certain cut-off frequency, the maximum frequency transmitted through the optical system. This maximum frequency is found where the OTF falls to zero. Frequencies k_i which are attenuated through-out propagation corresponds to a small OTF value, $OTF(k_i) << 1$. Therefore it becomes obvious in spectral representation that if the OTF has a long tail close to zero, the cut-off frequency will be large while the contributions of high-frequencies to the final image will be negligible. This observation illustrates the shortcomings of the historical description of microscope resolution. Indeed complete description of the OTF of an optical system is a more reliable indication of the resolving power.

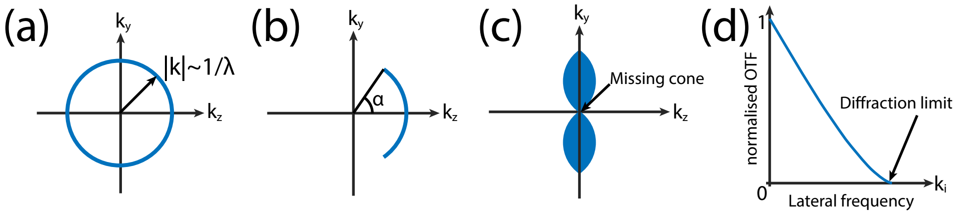

FIGURE 1.4: **Optical transfer function. a)** A quasi-monochromatic source emits light in all directions. The waves have similar wavelengths, therefore similar wavevector k. In the Fourier space, the field is then described by a ring of radius $k \sim 1/\lambda$. **b)** Only a portion of the wavefront propagates through the microscope, limited by the $NA = nsin(\alpha)$. **c)** The image recorded by the microscope is the intensity of the field, which is the square of the field. In Fourier space, this corresponds to the autocorrelation of the field in b), called the optical transfer function (OTF). The OTF is non-null only on toroidal shape, leaving a missing cone in the axial direction. **d)** The OTF describe how well spatial frequencies are transmitted through the microscope. It falls to 0 at the diffraction limit.

OTF in 3D Wide-field microscopes have a limited z-resolution, illustrated by the extended shape of the PSF in 3D. Given the FT properties, one then expects the OTF to have a very narrow extent along k_z. It is a useful to look at the *support* of the 3D OTF, that is to say the 3D volume in which the OTF is non-null. This facilitates representations, as the intensity of the OTF is not displayed, while keeping in mind that the total support is not the sole indication of resolution. If we consider monochromatic light, we have seen that in the plane waves representation the emitted waves have the same $|\vec{k}|$ and differ only by their propagation direction (figure 1. 4-a). In the 3D frequency space,(k_x, k_y, k_z), the waves propagating through the objective are all contained in a spherical cap delimited by the NA of the system (figure 1.4-b). The other waves are not collected by the objective. It is important to note that this spherical cap corresponds in real space to the amplitude of the optical field that composes the image. However, the detectors are sensitive to intensities and not amplitudes. Intensity and amplitude are related by: $I(\vec{r}) = |E(\vec{r})|^2$. As mentioned earlier, multiplication and convolution are conjugated operations by the FT. The Fourier equivalent of the square operation is then the autocorrelation. Therefore, the previous relation implies that the 3D spatial frequencies composing the final image are contained within the autocorrelation of a spherical cap. This volume is the support of the OTF in 3D and displays a torus-like shape (Streibl, 1985), as exemplified in figure 1.4-c. A particular feature of the OTF support is the so-called *missing cone* which illustrates the loss of z information in a wide-field microscope and the very poor optical sectioning capacity.

Since the OTF describes how well frequencies are transmitted by the optical system, it is an important characterization of a microscope. Obtaining diffraction-limited imaging requires a microscope with an OTF as close as possible to theoretical OTF. In practice this can be severely impeded by the presence of aberrations. In order to increase the resolving power of a microscope further than the conventional diffraction limit, it is necessary to extend the support of the OTF and its amplitude.

1.3 Shifting and breaking the diffraction barrier

For a long time the diffraction barrier remained unchallenged and microscopes were designed in order to tweak Abbé's formula, lowering the limit value as much as possible. An obvious parameter to play on is the wavelength of the light, directly proportional to the diffraction limit. Unfortunately, short wavelengths are damaging biological specimens and do not allow deep imaging because of scattering. In practice, the benefits are small since the attainable diffraction limit with visible light remains much larger than important cellular processes. Another possibility is to increase the NA of the microscope. The success of commonly used immersion-oil objectives with $NA \sim 1.4$ have validated this approach. However, the NA cannot be increased infinitely with a single-objective. Besides the physical angle limitation ($NA \sim 1.4$ have already a collection angle of $\sim 70^o$), spherical aberrations due to index mismatch between the sample medium and the glass/oil scale with the NA. High NA objectives have also a limited depth of imaging.

Confocal microscopy The emergence of confocal microscopy (Minsky, 1961; Davidovits and Egger, 1969, dubbed confocal scanning light microscope, CSLM) opened the way to a substantial improvement of resolution in light microscopy. Instead of illuminating the sample on a large area (as in wide-field microscopy), a CSLM focuses the laser light in a tiny spot in the sample. In addition, the image of the focus is formed on a pinhole, allowing further reduction of the effective area. The pinhole efficiently blocks out-of-focus light, at the expense of the collected intensity. In order to create an image, the sample is scanned, keeping the pinhole and the illumination focus at conjugated positions. While a wide-field image is recorded at once, the scanning procedure of a CSLM slows down image acquisition. The sample must be scanned appropriately to maximize speed and maintain a high enough sampling. The confocal PSF is reduced compared to the conventional one (Wilson, 2011). In particular, small pinholes help getting rid of the side lobes of the Airy pattern. In the Fourier space, theoretical calculations show that the OTF support is almost twice as large as the conventional wide-field OTF in the lateral directions (Sheppard and Gu, 1992). This prompted CSLM to be called a superresolution method (Wilson and Sheppard, 1984), denomination that was later abandoned. The confocal OTF indeed conveys higher frequencies than the conventional OTF, but most of those will contribute only imperceptibly to the final image. Indeed, the OTF value at high frequencies is close to zero. It was shown that the improvement in lateral resolution is on the order of $\sqrt{2}$ (Wilson, 2011). In practice, the low light level and the finite size of the pinhole prevent confocal microscopy to reach this limit (Cox and Sheppard, 2003). The main advantage of confocal microscopy is to be found in its sectioning capacity (Wilson, 1989). By rejecting out-of-focus light, the effective optical section gets greatly reduced compared to conventional microscopy. With an adequate choice of objective and pinhole size, the optical section can reach a thickness of $\sim \lambda$ (Wilson, 2011). In the case of the 3D OTF this means that the missing cone has been filled and that the OTF is extended in the k_z-direction.

Multi-photon microscopy One promising approach considered was multi-photon microscopy (Denk et al., 1990; Zipfel et al., 2003). By exploiting the non-linear absorption of longer wavelengths, one can decrease the effective PSF without the need of a pinhole. Indeed, the absorption of multiple photons at once requires high intensity and occurs mainly at the centre of the illumination spot. However, since the wavelength of the illumination used is m-times larger than the emission light (m being the degree of non-linearity, e.g. m=2 for two-photons), the focus size also correspondingly increases. The resolution of a multi-photon microscope has been calculated theoretically and does not surpass the resolution of a confocal microscope (Gu and Sheppard, 1995). Here again, the main advantage of multi-photon microscopy is in its depth of imaging (less scattering occurring at larger wavelengths) and optical sectioning (Zipfel et al., 2003).

Microscopy with two objectives Confocal microscopy and multi-photon imaging are close in spirit as they aim at reducing the effective size of the PSF, either by a physical stop or by a smaller absorption cross-section. In both cases the lateral resolution exceeds the axial resolution due to the limited NA of the microscopes. While the NA of objectives cannot be increased indefinitely, a second objective can be added, focusing on the same plane. In order to achieve a higher resolution, the light collected by the two objectives must interfere constructively on the same detector, recombining all the spatial frequencies together. Should the image collected by each objective be formed on individual detectors, the microscope would just be equivalent to its single-objective counterpart. This idea has originally been applied to confocal microscopy in the so-called 4Pi configuration (Hell and Stelzer, 1992). An additional improvement of the resolution can be obtained when making use of interferences in the illumination as well. In the case of 4Pi microscopy, focusing the illumination spot of the confocal microscope from both sides at the same time produces a more spherical illumination spot. This effectively reduces the total PSF to an even smaller volume. A similar approach has later been implemented in wide-field microscopy, and dubbed I^5M (Bailey et al., 1993; Gustafsson et al., 1995; Gustafsson et al., 1996). In this case, the interference of two illumination beams creates a pattern of intensity along the axial direction. We will see later how a patterned illumination has the potential to extend the bandwidth of the microscope. In both cases, the axial resolution is well below the diffraction barrier, in spite of the presence of intense side lobes that create artefacts (Bewersdorf et al., 2006).

Breaking the diffraction barrier Altogether, these methods have proved that imaging below the diffraction barrier was possible, in particular along the axial direction. However, the limit in resolution of these microscopes is still governed by diffraction and the improvements in the lateral directions were limited. Instead of breaking the diffraction limit, confocal, 2-photon, 4Pi and I^5M microscopy rather shifted it. It has been argued that in order to fundamentally overcome the Abbé limit and achieve superresolution, a microscopy method must have the prospect of an infinite resolution (Hell, 2003). The first method to have reached resolution well below the diffraction barrier laterally exploits near-field interactions. Based on a scanning microscope, near-field scanning optical microscopy (NSOM or SNOM, Novotny, 2007) makes use of a sub-diffraction aperture (small effective PSF) to either excite the surface of the sample with evanescent waves or to collect them. Since evanescent waves carry high-order frequency information, NSOM leads to an improved resolution only limited by technological development: how small is the aperture and how much power can be delivered to the specimen. The previous microscopy methods exposed here were all making use of focusing to define the illuminated volume or the image of the sample. NSOM on the other hand, exploits the fact that the aperture or probe defines a volume of observation that does not rely on the focusing of light but only on the dimension of the probe itself. Based on a visionary idea from Synge (Synge, 1928), it was first shown at visible wavelength by Ash and Nicholls (Ash and Nicholls, 1972) and later refined by Betzig (Betzig et al., 1991). Because NSOM is a near-field method (as opposed to far-field imaging such as wide-field or confocal), the sub-wavelength aperture must be positioned ~ 100 nm away from the surface of the sample and does not allow probing of the specimen in 3D.

Several far-field methods have in effect managed to overcome the diffraction barrier and are now called superresolution imaging: stimulated-emission depletion (STED, Hell and Wichmann, 1994b), structured-illumination microscopy (SIM, Heintzmann and Cremer, 1999; Gustafsson, 2000), single-molecule localization microscopy (SMLM, Betzig et al., 2006; Rust et al., 2006; Hess et al., 2006) and super-resolution optical fluctuation imaging (SOFI, Dertinger et al., 2009). We will focus on the first three methods in the next sections.

1.4 Stimulated-emission depletion microscopy

Principle The fundamental phenomenon at the root of STED, and which gives it its name, is the stimulated emission of photons by incoming radiations. In his attempt to formulate a quantum theory of radiation (Einstein, 1917), Einstein examined molecules oscillating between two energy levels while being irradiated by light. He hypothesized that if the molecules were able to absorb energy (a photon) from the field to reach a higher energy level, the inverse phenomenon should exist. An incoming radiation on excited molecules could also lead to the emission of the same quanta of energy, later called stimulated emission. As opposed to spontaneous emission (stimulated emission by a vacuum field), which happens regardless of the environment of the molecule, stimulated emission is the result of the incident light action on the molecules. Stimulated emission was first experimentally observed in 1928 (Kopfermann and Ladenburg, 1928), before becoming the working principle of lasers (Schawlow and Townes, 1958; Maiman et al., 1961). In terms of energy level, fluorescence happens when molecules in their ground state (S_0) absorb a photon of the right frequency and release the energy with a small delay by spontaneous emission (see figure 1.5-a inset). Because some of the absorbed energy will be dissipated in electronic vibrational states, the spontaneously emitted photon will have a red-shifted wavelength (lower energy). This effect is known as the Stokes shift (Stokes, 1852). The idea behind STED microscopy is to spatially quench fluorescence using stimulated emission, thereby restricting fluorescence to a sub-diffraction volume (Hell and Wichmann, 1994a). The STED beam should be carefully chosen so that it does not excite molecules to a fluorescent state itself, It should also be delayed from the excitation beam in order to let time for the vibrational states to relax. In the first experimental realization of STED microscopy, the STED beam was slightly offset spatially from the excitation beam in order to suppress fluorescence in a portion of the excitation beam (Klar and Hell, 1999). Later on, a phase mask was introduced in the STED beam path, thus creating a 3D volume with zero intensity in the centre (Klar et al., 2000, see figure 1.5-b). The two beams were then superimposed, and fluorescence was suppressed in the centre of the volume, leading to a five-fold decrease in the size of the effective PSF. 2D STED is now commonly used with a donut shape as well (figure 1.5-a). STED microscopy is the first far-field method to have durably overcome the diffraction barrier. Indeed the resolution in STED does not depend anymore on diffraction, but on the size of the central minimum of the donut shape:

$$\delta \approx \frac{\lambda}{2\mathrm{NA}\sqrt{1 + I/I_s}}$$

Where λ is the wavelength of the excitation light, NA is the numerical aperture of the objective, I is the depletion laser intensity and I_s is the saturation intensity of the fluorophores, which depends on the absorption cross-section and the lifetime of the fluorescent state.

Phototoxicity In theory, STED is capable of achieving infinite resolution as the latter depends solely on the depletion beam power. However, the high energy beam necessary to obtain a $\delta < 50$ nm also entails strong bleaching of the fluorophores. Therefore, the requirements on the fluorophores in terms of photostability are very high, stimulating the development of specialized dyes. The possibility to tune the power of the depletion beam allows balancing between the need for resolution and the total time of imaging (limited by bleaching). Although STED is a live-cell imaging method, another consequence of the high power is the important phototoxicity induced in the sample. The need for limited phototoxicity was an original concern, which prompted Hell and his collaborators to devise similar

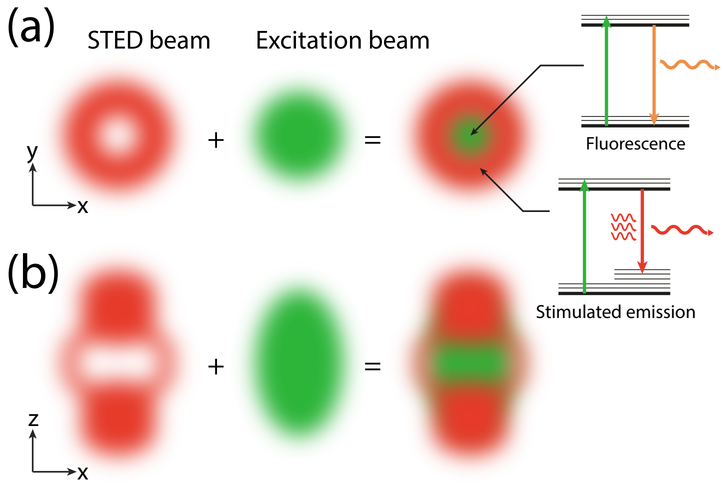

FIGURE 1.5: **Stimulated-emission depletion**. **a)** In 2D, two beams of different wavelength are aligned. The excitation beam allows the molecules to absorb energy and emit fluorescence photons. The STED beam triggers stimulated emission, which quenches the fluorescence by leading to the emission of a photon of the same wavelength as the STED beam. The fluorescence is then limited to the central region of the STED beam. **b)** The same principle also applies in 3D.

concepts to STED, albeit using lower intensities. Ground-state depletion (GSD, Hell and Kroug, 1995), and the more general concept of reversible saturable optical transitions (RESOLFT, Hell et al., 2004), makes use of a dark state to which the fluorophores can be driven through illumination at a particular wavelength. GSD was experimentally demonstrated in 2007 (Bretschneider et al., 2007). The smaller I_s lowers the requirement for strong laser power without lifting durably the concerns relative to phototoxicity.

Technical developments STED and RESOLFT microscopy have benefitted from many developments, among which the extension to multicolour (Donnert et al., 2007; Meyer et al., 2008; Wildanger et al., 2011; Göttfert et al., 2013; Sidenstein et al., 2016), 4Pi configuration (Dyba and Hell, 2002; Dyba et al., 2003; Curdt et al., 2015; Böhm et al., 2016), 2PE (Ding et al., 2009; Moneron and Hell, 2009; Coto Hernández et al., 2016), fluorescence correlation spectroscopy (Eggeling et al., 2012), TIRF (Bewersdorf et al., 2011), parallelization (Chmyrov et al., 2013) or adaptive optics (Gould et al., 2012; Burke et al., 2013; Patton et al., 2016). Beyond the many technical developments, STED microscopy has been successfully applied to various biological questions, demonstrating the usefulness of superresolution method in deciphering small-scale processes. In particular, STED imaging has been preferentially applied to neuroscience owing to the scale of synaptic processes. Examples include the clustering of proteins on the membrane of synaptic vesicles (Willig et al., 2006), the organization of a protein involved in the presynaptic active zone in *Drosophilia* (Kittel et al., 2006) or the live tracking of sub-diffraction vesicles in cultured neurons (Westphal et al., 2008). Other areas of successful application are membrane studies (Mueller et al., 2011; Garcia-Parajo et al., 2014; Gallego et al., 2016), pathology

(Siskova et al., 2014; Benda et al., 2016) and virology (Hanne et al., 2016). An extensive review has recently been published, covering most of the major technical developments and applications (Blom and Widengren, 2017).

Because it is capable of resolving structures down to 100 nm routinely in live cells without post-processing, STED has proven a useful tool to study nanoscale biology. Since it is based on a confocal microscope, STED shares some features with it, such as a moderate speed. The primary source of resolution increase is the size of the effective excitation spot, which is intensity dependent. Higher resolution requirements necessitate a smaller excitation volume and therefore a longer imaging time due to the scanning. As in a confocal microscope, the speed can however be maximized by limiting imaging to the region of interest. A particular concern in STED microscopy concerns phototoxicity induced by the use of very high laser power in the order of 100 $\mathrm{kW/cm^2}$ to 1 $\mathrm{GW/cm^2}$ (Minoshima and Kikuchi, 2017). The other consequence of STED high laser intensity is the rapid bleaching of the fluorophores, shortening imaging times. Research on novel dyes with suitable properties is on-going (Blom and Widengren, 2017), while other photophysical perspectives that allow longer imaging are emerging (Danzl et al., 2016). Finally, it is note-worthy that STED microscopes are complex instruments, in particular due to the careful alignment of the two beams. This complexity limits method development to specialized groups, and the routine use in biology to commercial instruments.

1.5 Structured illumination microscopy

Principle We have seen that an object with simple periodic symmetry will appear in the Fourier space as a discrete number of points. Such assertion holds true for structured light, for instance a 1D sinusoid pattern illumination, as in figure 1.6-a, will display in the Fourier space a succession of equally spaced peaks. Through a microscope, a cut-off applies in the frequency space and only few peaks (the *orders*), including the central peak, will remain (figure 1.6-b). In a microscope, the intensity of the image can be described by:

$$I(\vec{r}) = (\rho(\vec{r}) * L(\vec{r})) \otimes PSF$$

Where ρ is the intensity response of the sample and L is the intensity of the illumination. The product of $\rho(\vec{r})$ and $L(\vec{r})$ is the intensity emitted at the point $\vec{r}$, but only ρ holds information about the sample. The convolution ($\otimes$) with the PSF expresses the effect of the microscope on the light coming from each source. By virtue of the convolution theorem, the previous expression becomes in the Fourier space (where $\hat{F}$ denotes the FT of F): $\hat{I} = (\hat{\rho} \otimes \hat{L}) * OTF$, where we recall that $OTF = P\hat{S}F$. The Fourier transform of the illumination and of the intensity response are shown in figure 1.6-b and c, respectively. Because in Fourier space, $\rho * L$ has become $\hat{\rho} \otimes \hat{L}$, the spatial frequencies describing the system hare shifted and superimposed (see figure

1.6-d). This remapping of frequencies implies that some spatial frequencies, which would otherwise be outside the cut-off of the OTF, are now propagated through the microscope at different positions. This phenomenon manifest itself as Moiré fringes: additional high-frequency information appearing as low-frequency information. By acquiring several images and applying image analysis in Fourier space, the high-frequency information can be extracted and placed at its correct position, leading to an image with improved information content in real space (Bailey et al., 1994).

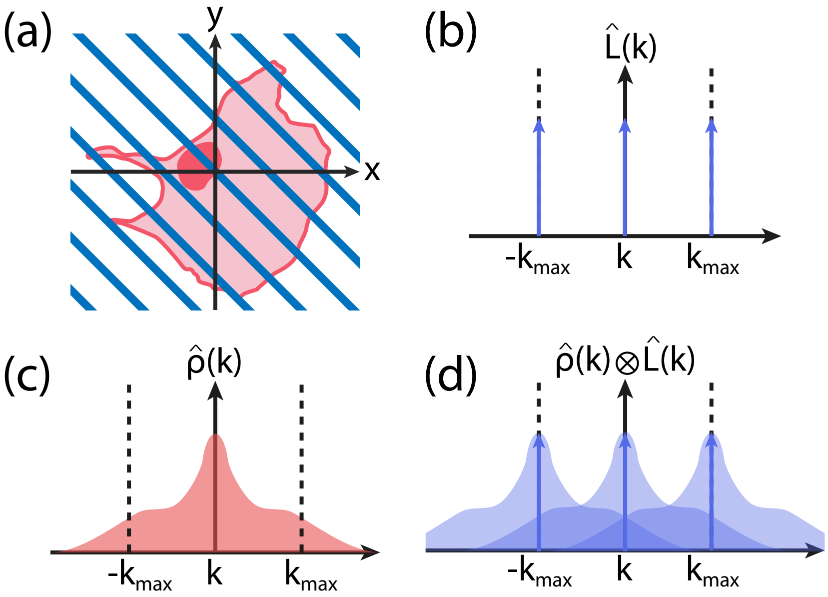

FIGURE 1.6: **Structured-illumination microscopy. a)** The sample, here a cell (red), is illuminated by a sinusoidal intensity pattern. **b)** The Fourier transform of the illumination pattern L displays three peaks. **c)** Fourier transform of the sample signal ρ, only the frequencies within the cut-off frequency will be detected. **d)** In Fourier space, the product $\rho \times L$ is a convolution of the two corresponding FT. Frequencies that were originally not transmitted because of the frequency cut-off are now present in the image.

The principle of using structured illumination to propagate higher frequencies has first been used to increase the axial resolution of microscopes with two objectives in the so-called standing wave microscopy (Bailey et al., 1993; Bailey et al., 1994). Structured illumination was also used to obtain optical sections (Neil et al., 1997; Neil et al., 1998) using a 2D grid pattern. Extension of the lateral resolution following the principle of figure 1.6 was later achieved with beads (Heintzmann and Cremer, 1999; Frohn et al., 2000) and cells (Gustafsson, 2000), giving birth to SIM.

Structured illumination microscopy is mainly a live wide-field method. In order to reconstruct a 2D superresolved image, several images must be taken, with different 2D grid orientations, in order to cover the full extent of the OTF in frequency space, and several phases. Since the grid pattern is projected from the objective lens, the maximum frequency of the structured illumination is limited by the cut-off frequency of the OTF. For that reason, the maximum lateral resolution enhancement is limited to a two-fold improvement, that is to say a resolution around ∼150 nm. The computational treatment to recover the additional frequencies is complex and subject to artefacts (Schaefer et al., 2004). Those artefacts arise from progressive bleaching of the fluorophores, sample motion, optics misalignment or out-of-focus light. They mostly appear as small-scale patterns. Although a SIM image requires typically nine wide-field images, the time resolution remains better than other superresolution methods presented here. Additionally, SIM does not rely on the fluorophore properties and can be performed with routinely used dyes. Phototoxicity during SIM acquisitions is low compared to other superresolution methods, as the only requirement is a good signal to noise ratio of the illumination.

Nonlinear SIM It has been argued that because the resolution enhancement in SIM is limited to a factor two, it fails to provide the potential for an *infinite* resolution (Hell, 2003). By introducing non-linearities in the intensity response of the fluorophores (for instance by saturating their absorption), the 2D pattern is no longer a perfect sinusoid but contains some higher frequencies. Those higher harmonics will cause corresponding shifts of high-resolution information in the Fourier space, albeit at a larger scale than the original sinusoid. Performing SIM with saturation was theoretically studied under the name of saturated patterned excitation microscopy (SPEM, Heintzmann et al., 2002) and experimentally carried out under the name of non-linear structured illumination microscopy (NL-SIM, Gustafsson, 2005). In theory, NL-SIM provides unlimited resolution. However, the need for strong saturation of the fluorophores imposes constraints on the photostability of the dyes and increases the phototoxicity (Gur et al., 2010). Additionally, NL-SIM requires more images for reconstruction. It is therefore slower and more subject to sample motion artefacts. Recent developments have lowered the requirements of power intensity by exploiting photoswitchable (Rego et al., 2012) and photoactivatable (photoactivable-SIM, PA-SIM, Li et al., 2015) proteins. By allowing a faster imaging and an even lower light intensity, PA-SIM has made NL-SIM live-cell compatible. It should be noted that NL-SIM falls under the description of RESOLFT microscopy (Hell et al., 2003), in an attempt to describe superresolution methods within the same theoretical framework.

Technical developments Artefacts due to out-of-focus light have originally constrained SIM to the imaging of thin samples. An early solution was to couple SIM with TIRF (Chung et al., 2007; Gliko et al., 2006; Gliko et al., 2008; Stemmer et al., 2008; Beck et al., 2008; Kner et al., 2009) and recently with high NA-TIRF (Li et al., 2015). An additional well-known limitation was imaging speed, in particular due to the mechanical rotation of the grating used to create the illumination pattern. This was later overcome by using a spatial-light modulator (SLM, Stemmer et al., 2008; Kner et al., 2009). SIM has also been extended to 3D using one objective (Gustafsson et al., 2008; Schermelleh et al., 2008; Shao et al., 2011) or coupled with I^5S in the so-called I^5M (double-objective, Shao et al., 2008). It should be noted that 3D-SIM is still limited in the thickness of the samples, but can easily image single cells live, given that the imaging speed is faster than sample motion (Shao et al., 2011; Fiolka et al., 2012). Additionally, since SIM does not require specialized dyes, multicolour SIM has been tackled early on (Schermelleh et al., 2008).

Light-sheet SIM The biggest step towards a fast non-invasive use of SIM in living cells and organisms is probably to be attributed to light-sheet microscopy SIM (Keller et al., 2010; Planchon et al., 2011; Gao et al., 2012; Chen et al., 2014; Gao et al., 2014). Indeed, the reduced background resulting from light-sheet illumination decreases the risk of artefacts in SIM reconstructions. Light-sheet illumination additionally entails reduced bleaching and phototoxicity, allowing for longer imaging. This opened the way to the imaging at higher lateral resolution of developing embryos, such as zebrafish or *Drosophilia melanogaster* (Keller et al., 2010). The use of a lattice-light sheet further improved the speed of imaging, albeit at lower SIM resolution (Chen et al., 2014). PA-SIM coupled with lattice-light sheet allowed observation of sub-cellular processes in 3D with higher resolution than wide-field microscopy (Li et al., 2015). Finally, lattice-light sheet in its SIM mode was also successfully applied to the imaging of the peripheral ER in mammalian cells (Nixon-Abell et al., 2016), allowing the observation of rapid morphology changes in the ER membrane tubular network.

Coupling it with other microscopy modalities has made structured-illumination a technique of choice for live-cell superresolution. Although SIM is not widely accepted as a superresolution method, as opposed to nonlinear-SIM, commercial instruments offer undeniable improvements in resolution. As in the case of STED, SIM microscopes require expert hands, in the handling of the microscope as well as in the analysis. However, sample preparation is largely simplified compared to other superresolution methods since there are no strong requirements on the fluorophores, labelling and buffer. The limitations in speed and reconstruction artefacts are slowly lifted and should in the future allow SIM to become a routinely used method for resolution enhancement at subcellular levels. More specialized need such as structural biology and protein assembly studies, however, are for the moment still out of reach and benefit from the use of other superresolution methods.

1.6 Localization microscopy

Molecules often exhibit complex interactions with their surroundings and can act as nanometer-sized reporters of their environment. The first observation of single-molecules in a solid (Moerner and Kador, 1989) established the possibility to optically detect single absorbers. The advent of single-molecule studies (Moerner, 2002) thereon brought to light unforeseen behaviours, such as spontaneous change in absorption wavelength due to local interactions (Orrit and Bernard, 1990) or light-driven spectral shifts (Basché and Moerner, 1991). An important step in the development of single-molecule imaging was the transition to microscopy, with the observation of carbocyanine dye molecules in NSOM (Betzig and Chichester, 1993). In this study, the authors directly observed the electric dipole orientation of the individual molecules, probing fundamental aspects of fluorescence processes. Later developments led to nanometer measurements of distances using single-molecule FRET (Ha et al., 1996). Single-molecule imaging was also extended to confocal microscopy (Macklin et al., 1996) or wide-field microscopy (Funatsu et al., 1995).

Localization below the diffraction barrier While biological structures imaged in a wide-field microscope appear blurred, a single molecule can be located much more precisely than the diffraction barrier. Under the hypothesis that the region of interest contains a single emitter, its position can be measured with nanometer range precision by fitting a Gaussian to the molecule's PSF (Thompson et al., 2002). Such approach was termed *super-localization*. The precision in determining the position of the particle depends primarily on the number of detected photons. In first approximation, the localization precision scales as (with least-square fitting, Thompson et al., 2002):

$$\sigma \simeq \frac{s}{\sqrt{N}}$$

where σ is the localization precision in determining the position, s is the spread of the model PSF (in the case of a Gaussian PSF, s is then the standard deviation) and N is the number of photons emitted by the molecule and measured by the camera. According to this formula, while the diffraction limit is about 250 nm, a fluorescent molecule position can be determined down to a precision of 10 nm with only 600 photons. In addition, tracking the position over time gives precious information on diffusion, directed movements or interaction between particles. This concept, called single-particle tracking, was early on applied to large objects, such as fluorescently-labelled complexes (Barak and Webb, 1982), gold particles (Geerts et al., 1987) or plastic beads (Gelles et al., 1988). The possibility to image single fluorescent molecules extended the scope of single-particle tracking. It was then possible to precisely track specifically proteins or lipids with fluorescence (Schmidt et al., 1996; Schütz et al., 2000; Sako et al., 2000). Contributions from single-particle and single-molecule tracking to biology are of great value and a review can be found in Manzo and Garcia-Parajo, 2015.

Separating overlapping PSF As soon as the density of fluorescent molecules increases, however, their signals (described by the PSF of the microscope) start to overlap and information concerning their position cannot be individually extracted anymore. It was already proposed in 1995 (Betzig, 1995) that molecules within a small focal volume could be separated by identifying them along an additional optical dimension (e.g. fluorescence wavelength) and then spatially localize them. This idea was effectively implemented at low temperatures in a crystal to resolve seven molecules within a diffraction spot by tuning very precisely the laser into resonance with a single one of them at a time (Van Oijen et al., 1999). Emission wavelengths were subsequently used to identify co-localizing molecules and measure their distance (Lacoste et al., 2000; Churchman et al., 2005). Other optical parameters were also used in order to distinguish overlapping molecules, such as fluorescence lifetime (Heilemann et al., 2002), photobleaching (Gordon et al., 2004; Qu et al., 2004) and blinking (Lidke et al., 2005). However, these methods were limited to few molecules within each focal volume or were not applicable to biological structures.

In the mean time, single-molecule studies focused as well on fundamental aspects of fluorescence in proteins and organic dyes. A striking example is the observation of spontaneous blinking of the green fluorescent protein (GFP, Dickson et al., 1997). Developments of GFP mutants led to the description of a photoactivatable GFP (Patterson and Lippincott-Schwartz, 2002), a fluorescent protein that can be converted to a fluorescent state by light of a specific wavelength. Later on, switching between a dark state and a fluorescent state was reported in cyanide dyes (Heilemann et al., 2005; Bates et al., 2005). Together, the idea of separating neighbouring molecules in order to localize them independently and the switching mechanisms observed in certain fluorescent molecules paved the way to single-molecule localization microscopy (SMLM). In 2006, three research groups independently achieved a ten-fold improvement over the diffraction limit by stochastically switching fluorescent molecules between a fluorescent and a dark state: (fluorescence) photoactivation localization microscopy ((f)PALM, Betzig et al., 2006; Hess et al., 2006) and stochastic optical reconstruction microscopy (STORM, Rust et al., 2006).

1.6.1 Principle of localization microscopy

The contrast between a fluorescent state and a non-fluorescent state is also at the heart of STED microscopy. The reduction of the excitation volume (where molecules are in the fluorescent state) is achieved by “switching” off the fluorescence at the periphery of the laser focus. Because the quenching of the fluorescence is controlled by the STED laser and occurs at a defined position, STED has been described as a coordinate-targeted method (Hell, 2009), as opposed to SMLM then labelled coordinate-stochastic. This distinction arises from the fundamentally different approach to the switching of fluorescence between bright and dark state.

Principle SMLM relies on a wide-field microscope and image the whole area of interest at once. When imaging a biological structure labelled with fluorescent molecules, the fluorescence collected by the microscope will form a blurred image of the structure (see figure 1.7-a). The central idea of localization microscopy is to temporally decouple the emission of the molecules by keeping a vast majority of them in a dark state and allowing only a small portion to emit light, as in figure

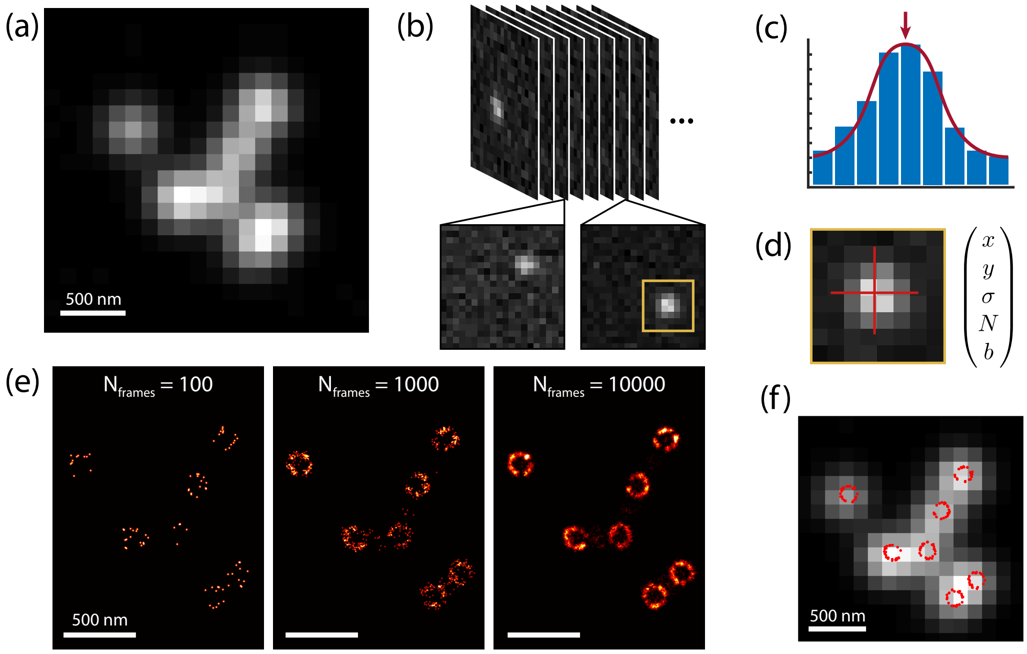

FIGURE 1.7: **Principle of localization microscopy**. **a)** In diffraction-limited imaging, many details are hindered by the overlapping of the fluorescent molecules signal. Sub-diffraction structures are therefore not visible. **b)** A SMLM experiment decouples in time the fluorescent emission of single-molecules. **c)** For each single-molecule, a model is fitted to the histogram of pixel intensity. **d)** The results of the fitting algorithm usually include several quantity such as positions, localization precision, number of emitted and background photons. **e)** Superresolved structures at the origin of the diffraction-limited image in a). The images are obtained by imaging N number of frames and illustrate the need for high sampling of the structure. With sufficient sampling, several rings clearly appear. **f)** Comparison between the diffraction-limited and the ground-truth image. The images were obtained by simulation of the structures, diffraction-limited imaging and stochastic blinking. The blinking images were then analysed in the same way than real experiments.

1.7-b. If the density of fluorescing molecules is low enough, then each diffraction-limited volume contains only one emitter. Similarly to what is done in single-molecule tracking, the fluorescent molecules can be individually detected and their exact position calculated (figure 1.7-c). Other parameters can as well as be extracted such as the emitted number of photons N (figure 1.7-d). Since the switching mechanisms exploited in SMLM are not spatially controlled but rather rely on a stochastic blinking across the field-of-view, each frame contains a different subset of the molecules. Recording a high number of images allows sampling the labels along the biological structure and collecting their positions. Finally, an image is reconstructed from the list of measured positions that approximates the biological structure (figure 1.7-e). Because each fluorescent molecule can be located down to few nanometers, the rendered image contains features previously hidden in the diffraction-limited image (figure 1.7-f). It is important to note that the result of a SMLM experiment is a list of numbers and not an actual image. The output of the fitting routine is a list of localizations, which usually includes the estimation of the position (x, y and possibly z), the number of emitted photons, the number of background photons and the precision at which the position was inferred (the so-called localization precision). Subsequent filtering, rendering and further analysis vary with the need of the experiment.

Resolution Localization microscopy is often cited to yield a lateral resolution of 20 nm, that is to say a ten-fold improvement below the diffraction limit. Resolution is a difficult quantity to assess, but two important contributions need to be highlighted: the number of photons collected per localization event and the labelling density. As we have seen in the case of super-localization, the localization precision scales roughly with $1/\sqrt{N}$. In order to obtain a precise picture of the sample, the fluorescent labels must emit as many photons per localization event as possible. A very high average localization precision alone does not yield a high-resolution image. In the case of poor labelling, the biological structure cannot be sampled enough to form a representative image. In the same vein, stopping a SMLM experiment before enough localizations have been accumulated will lead to an under-sampled image. Figure 1.7-e shows an example of the same sample with different effective sampling. In this case the number of frames acquired vary between the reconstructed images. The structures are clearly visible if enough frames are acquired, but do not give a reliable impression when only a hundred frames are analysed. A similar observation prevails when considering the labelling efficiency of the same structure. To illustrate the impact of labelling on the ultimate resolution of the image, the Nyquist-Shannon theorem (Shannon, 1949) is often cited. According to this sampling theorem, the image resolution cannot be higher than two times the average spacing of the localizations (Shroff et al., 2008; Shim et al., 2012):

$$r = \frac{2}{(\frac{N}{a})^{\frac{1}{d}}}$$

where r is the Nyquist resolution, N is the number of localizations, a is the area of the structures of interest and $d = 1, 2, 3$ is the dimension. In this case $\frac{N}{a}$ is the density of localizations. If the localization precision is not significantly smaller than the mean localization spacing, this formula underestimates the resolution. In this case, it has been additionally proposed to approximate the image resolution by the following formula (Legant et al., 2016):

$$R = \sqrt{\sigma^2 + r^2}$$

where R is the overall resolution and σ is the localization precision.

These formulas do not account for additional errors, such as the linker size, the non-uniform density or the stochasticity of the blinking. Therefore, obtaining such resolution might require a higher sampling of the structure, and it constitutes mainly a lower bond. The resolution is often approximated by a line cut through a known structure, for instance nuclear pore complex or more commonly microtubules. This approach, however, does not work with unknown structure. The best show case in the field of view is usually chosen, thus constituting a local measure and in no means an overall constant. Such measures are also prone to artefact from low labelling density. Finally, an approach originating from electron microscopy has been applied to localization microscopy called Fourier ring correlation (FRC, Banterle et al., 2013; Nieuwenhuizen et al., 2013). In FRC, two independent datasets are extracted from the localization table are used to reconstruct two images. These images are subsequently compared in Fourier space and a criterion determines a spatial frequency cut-off beyond which the images lack similarity. The resolution of the image is then the inverse of the threshold frequency. A useful discussion on the definition of resolution in SMLM can be found in the supplementary of Legant et al., 2016, and in the following review: Demmerle et al., 2015.

Different approaches to SMLM A great number of "blinking" mechanisms, compatible with the concept of localization microscopy, have been exploited. Two of the original papers, termed (f)PALM (Betzig et al., 2006; Hess et al., 2006), used a photoactivatable fluorescent protein (PA-FP). Upon low irradiation at a specific wavelength, few of the PA-FPs become fluorescently active. By increasing the laser intensity, a higher number of activated molecules is present in the image. The laser intensity therefore controls the density of fluorescing proteins. The imaging process then cycles between exciting the activated proteins, bleaching them and photoactivating the next subset of molecules. The same principle was exploited in STORM (Rust et al., 2006), albeit with a pair of organic dyes, Cy5 and Cy3. Previous work from the authors demonstrated that Cy5 can be converted from a dark state to a fluorescent state by proximity to another cyanine dye, Cy3, and irradiation with a wavelength different from its excitation wavelength (Bates et al., 2005). Thereon, the initial STORM experiments alternated between imaging of fluorescent Cy5 molecules until they stabilized in their dark state and reactivation of sparse molecules with low light. Shortly after the publication of (f)PALM and STORM, a blinking mechanism based on diffusing molecules termed points accumulation for imaging in nanoscale topography (PAINT) was presented (Sharonov and Hochstrasser, 2006). In PAINT, the fluorescence state is triggered by interaction of the probe with its environment, here the structure of interest. While Nile red (as used in the PAINT paper) is not fluorescent in solutions, it starts emitting light as soon as it finds itself in a hydrophobic environment such as a vesicle membrane. The kinetics of collision between the probe and the vesicle then dictates the on and off switching of the signal and the density of emitters. Other processes include the fast blinking at a single wavelength of a fluorescent protein in PALM with independently running acquisition (PALMIRA, Geisler et al., 2007), the switching of organic dyes without an activator fluorophore in direct STORM (dSTORM, Heilemann et al., 2008), dyes transition to a metastable dark states in ground-state depletion and single-molecule return (GSDIM, Fölling et al., 2008), the fluorescence upon binding of DNA-binding probes in binding-activated localization microscopy (BALM, Schoen et al., 2011). Interestingly enough, the principle of localization microscopy can be extended to other area than optical imaging, such as acoustic microscopy (Errico et al., 2015).

Localization microscopy owes its rapid success to several aspects of the method. The first and foremost is its capacity to resolve very small features, much smaller than the diffraction limit. Additionally, the vast choice of fluorescent labels and techniques has made the application of localization microscopy to various fields of biology possible. Besides the lower requirements for a complex microscope, the growing number of users has prompted the publication of a large number of open-source analysis solutions, making SMLM particularly accessible to the imaging community. In the next sections, I will describe different facets of localization microscopy and their shortcomings.

1.6.2 The choice of fluorescent labels and labelling strategies

A large number of such blinking mechanisms have been identified that allow switching between an on (fluorescent) and an off (dark) state (see figure 1.8-a). Among this vast palette, one can classify the fluorescent probes in three main groups: photoswitchable (reversible conversion between a dark state and a fluorescent state), photoactivatable (irreversible transition from an off state to an on state) and binding probes. While the latter category mainly relies on the binding kinetics and photophysical changes upon binding and unbinding, photoswitching and photoactivatable probes stay bound to the structure of interest.

Important photophysical parameters In the case of photoswitchable and photoactivatable molecules, the on/off behaviour is intrinsic to the probe. Care must then be taken to choose a suitable fluorescent molecule. In both cases, three important characteristics prevail: the *brightness* of the on state, the *on/off contrast ratio* and the *duty cycle* (Dempsey et al., 2011; Chozinski et al., 2014). Since the precision at which the fluorescent molecules can be located depends mostly on the number of photons emitted (photon budget), bright molecules are preferred. The contrast ratio of the dark and fluorescent state is the ratio of the intensity measured in both states. Therefore, fluorescent molecules with a poor contrast ratio will exhibit strong background during the experiment, which in turn will degrade the resulting localization precision. A good localization precision is not sufficient to obtain high resolution in the final image. In the case of a high labelling ratio and high localization precision, an experiment can be unsuccessful if the fluorescent molecules have a large duty cycle value, defined as the amount of time the probe remains in its on state. Fluorescent molecules with low duty cycle will allow a higher number of molecules to be detected over time in a diffraction-limited spot. At higher duty cycle, if the density of molecules is too high, the fluorescent signals will often overlap and the structures will not be sufficiently sampled in order to reconstruct a superresolution image. Other important characteristics to consider are the resistance to photobleaching (recovering rate after switching off), spontaneous activation rate or the light intensity dependence of the blinking rate. The most successful fluorescent labels are organic dyes and fluorescent proteins, due to their advantageous labelling scheme and controlled on/off switching.

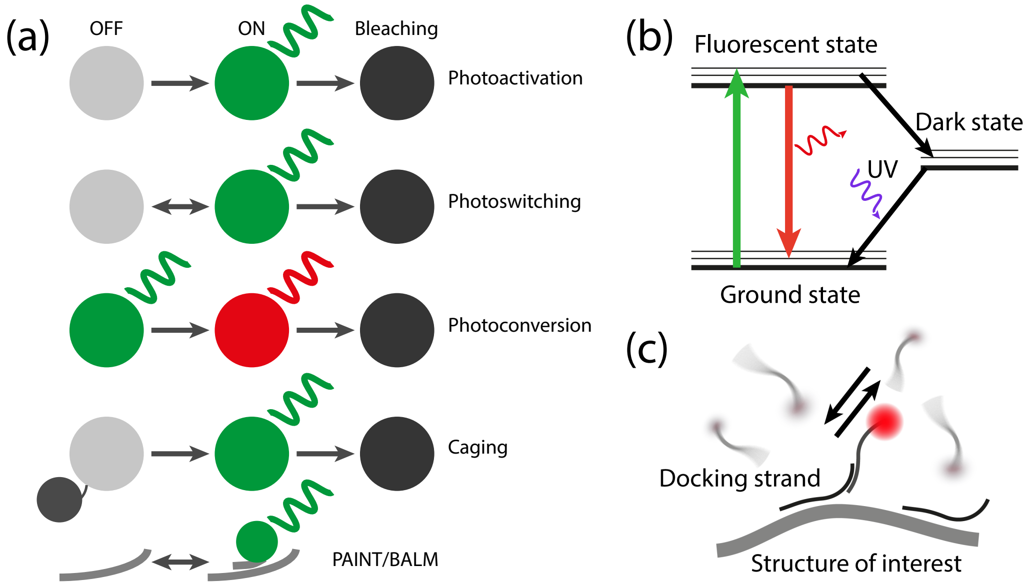

FIGURE 1.8: **Blinking mechanisms**. **a)** Several mechanisms are exploited in order to produce "blinking" in SMLM. The molecule can be activated and then bleached (photoactivation), or switch back and forth between a dark state and a bright state (photoswitching). The off state is sometimes also a fluorescent state, albeit at a difference wavelength than the on state (photoconversion). The fluorescence can also be quenched by caging in the off state, the on state is reached by a mechanism that removes the caging agent. Finally, fluorescent probes can mimic blinking simply by binding and unbinding a target (PAINT/BALM). This figure was inspired from http://aicblog.janelia.org/. **b)** Jablonski diagram illustrating the blinking of organic fluorophores. Upon absorption of light at a certain wavelength, the molecules will cycle between the fluorescent state and the ground state by emitting a photon and absorbing another one. Some molecules will stochastically reach and remain in a dark state. Illumination with UV light can activate the molecule by pushing them back into the ground state. **c)** DNA-PAINT principle. The imaging strand in the buffer constitutes a diffuse background. When a probe attaches to a docking strand, a localization event is captured. The dynamics of binding and unbinding produces a blinking at the target structure.

Organic dyes Organic dyes have been very successful in localization microscopy as they are able to emit thousands of photons per switching cycle, orders of magnitude higher than fluorescent proteins. They additionally usually exhibit superior resistance to photobleaching. Popular organic dye families include cyanine (Rust et al., 2006; Bates et al., 2007; Heilemann et al., 2008), oxazyne (Vogelsang et al., 2009; Heilemann et al., 2009) and rhodamine dyes (Fölling et al., 2007; Fölling et al., 2008). The photoswitching of organic dyes relies on a variety of phenomena (Chozinski et al., 2014), including conversion to non-fluorescent radical species upon illumination at a particular wavelength (Linde et al., 2011) and more commonly by reaction with thiols (Dempsey et al., 2009). Switching can be triggered by the excitation light (as in the case of Alexa Fluor 647 Zhuang, 2009) or by light of another wavelength (in particular UV light, as shown in figure 1.8-b). An interesting observation is that the switching dynamics is often dependent on the local light intensity. Organic dyes can also be used in a photoconvertible fashion, by quenching their fluorescence with a photolabile group and breaking the bond with the group using UV light (Vaughan et al., 2012; Minoshima and Kikuchi, 2017), as illustrated in figure 1.8-a. In order to prevent photobleaching, the use of an oxygen scavenger system is often necessary to stabilize the triplet state (Rust et al., 2006). Additionally, other buffer conditions can be introduced to maximize the dye performances (Vogelsang et al., 2009; Dempsey et al., 2011; Olivier et al., 2013a; Olivier et al., 2013b; Nahidiazar et al., 2016). The use of a specific imaging buffer complicates live-cell and multicolour imaging, as the buffer can be toxic to the cells and not compatible with other types of fluorescent molecules. Comparative studies are helpful to identify the most advantageous dyes (Dempsey et al., 2011; Zheng et al., 2014), especially in the case of multicolour imaging (Lehmann et al., 2015). Organic dyes are often conjugated to secondary antibodies in order to decorate the structure of interest. In particular, anti-GFP antibodies allow the imaging of many existing strain libraries. Immunodetection has the advantage that antibodies bind the target with high specificity and affinity. Because antibodies are large molecules, cumulating primary and secondary antibodies lead in localization microscopy to linkage errors arising from the displacement of the fluorescent molecule with respect to the target protein. The linkage error can be superior to 10 nm (Mund et al., 2014). In order to avoid linkage error, single-domain antibodies, called nanobodies, have been used to place the probe as close as possible to the target (Ries et al., 2012). Another alternative is the use of direct protein tagging by bio-orthogonal reactions such as SNAP-tag (Keppler et al., 2004), CLIP-tag (Gautier et al., 2008) or HALO-tag (Los et al., 2008).

Fluorescent proteins Because fluorescent proteins are rather small compared to antibodies and can be genetically fused with a protein of interest, they display lower linkage error and better labelling efficiency than organic dyes. However, fluorescent proteins are less bright than the latter, with a photon budget one order of magnitude smaller. While their labelling efficiency is much higher than organic dyes, low maturation rate might lead to non-fluorescent misfolded proteins. Fluorescent proteins can also exhibit photoswitchable and photoactivatable behaviours. In particular, some proteins can be reversibly switched between a fluorescent *cis* and a dark *trans* forms (Chozinski et al., 2014). Photoconversion, a shift of emission wavelength upon irradiation with UV (see figure 1.8-a), is often exploited to switch the proteins from a dark state (filtered out fluorescence) to a bright state (fluorescence selected for). A certain degree of switching can also be present in photoconvertible proteins such as mEos2 (Annibale et al., 2010) or be induced by caging with a chemical (as for mCherry Cloin et al., 2017). Several reviews and comparative studies are also available to help selecting fluorescent proteins for localization microscopy (Lippincott-Schwartz and Patterson, 2009; Chozinski et al., 2014; Wang et al., 2014).

Other types of labels Another class of fluorescent labels is related to PAINT (Sharonov and Hochstrasser, 2006) and BALM (Schoen et al., 2011) approaches. In these methods, the buffer contains the probes and the blinking originates from the binding/unbinding or bleaching of the probes onto the structure of interest. The fluorescence can be increased or triggered by the binding. Alternatively, fluorescent probes in the buffer create a diffuse background while short bindings are seen as a blinking event. This is the basis for DNA-PAINT (Jungmann et al., 2014). There, DNA strands (called docking strands) are bound to the target (for instance via immunolabeling) and complementary strands are coupled with a fluorophore (imaging strands). The imaging strands are added to the imaging buffer and binding/unbinding leads to a blinking event, as illustrated in figure 1.8-c. The length of the common sequence between imaging and docking strand dictates the kinetics of the binding/unbinding. DNA-PAINT can be used with any type of fluorophores and leads to extremely bright localization events. In addition, photobleaching is not a limiting factor as the buffer contains an excess of fluorescent probes. Furthermore, the sequence specificity allows for easy multicolour imaging by washing the probes and injecting new ones having a different target (Schnitzbauer et al., 2017).

Finally, because localization microscopy is mostly performed on fixed cells (Allen et al., 2013), attention should be paid during sample preparation to avoid fixation artefacts. In addition, as opposed to live imaging (see corresponding section), fixed cells allow for a much higher effective labelling density.

1.6.3 Conducting SMLM experiments: microscope and analysis

A peculiarity of localization microscopy among superresolution methods is the simple optical requirement of its microscope (figure 1.9-a). A SMLM microscope must obey mainly three criterion: high stability, sufficient laser power and efficient photon collection.

Stability Since the localization precision is in the order of few to tens of nanometers and the imaging time of minutes to hours, microscopes need to undergo minimal drift in all three dimensions. Any drift would smear the rendered image. However, thermal expansion and mechanical relaxation cannot be totally suppressed. Multiple drift correction methods have been published, including using the localization positions in post-processing (Dlasková et al., 2011) or live (Elmokadem and Yu, 2015), real-time correction with bright-field images (McGorty et al., 2013), fiducial markers (Grover et al., 2015; Seo et al., 2016; Ma et al., 2017b) or an electrically tunable lens (Seo et al., 2016). A particularly popular method for live axial correction uses an infra-red laser reflected in TIR (total internal reflection) at the coverslip and measured with a photo-detector in closed-loop with the objective stage (Jones et al., 2011). An open-source implementation of the latter system is available online under the name "PgFocus" (Bellve et al., 2014).

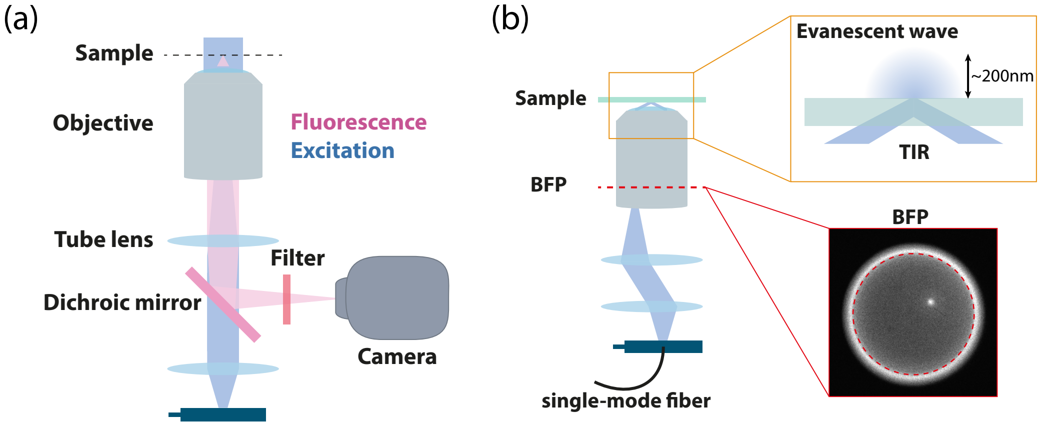

FIGURE 1.9: **Localization microscope.** **a)** The simplest form of a microscope for localization microscopy includes an objective, a tube lens, a dichroic mirror, an emission filter and a camera. **b)** In order to achieve TIR illumination, the laser light must be focused on the edge of the BFP (above the critical angle delimited by the red circle). As a consequence, the beam emerges with an angle larger than the critical angle and is totally reflected at the interface. In the sample, only an evanescent wave is generated, that exponentially decays with the distance to the interface.

Illumination The laser power used for a SMLM experiment depends mainly on the type of fluorescent label used. Optimization must be performed beforehand in order to maximize the number of photons measured per localization event and to match the speed of the switching cycles with the camera exposure time. Both of those quantities are intensity dependent. Typically, a flexible microscope should be able to deliver tens of kW/cm^2 at several wavelengths (488, 560 and 640 nm, the UV activation necessitating much lower intensity), which corresponds to high laser power in microscopy. A recent way around the high laser cost is to use cheap laser diodes capable of emitting hundreds of mW (Kwakwa et al., 2016). Additionally, a useful illumination system includes the possibility to image in total internal reflection (TIR, Axelrod et al., 1984). A common illumination scheme transmits the laser light through a single-mode optical fiber, such as built-on fibers in commercial laser boxes. The laser light is then focused at the edge of the objective BFP, allowing the beam to emerge from the lens in parallel fashion and with an angle larger than the critical angle. All of the energy will be reflected at the interface between the coverslip and the specimen, leaving only an evanescent wave illuminating the specimen close to the interface (figure 1.9-b). TIR illumination restricts the laser intensity to $\sim$200 nm above the coverslip, thus reducing dramatically the background from out-of-focus fluorescence. In order to implement TIR, the objective must have a large collection angle (NA>1.33 for a water solution). Since the analysis procedure in SMLM is very sensitive to background, TIR has been used extensively (Betzig et al., 2006; Hess et al., 2006; Sharonov and Hochstrasser, 2006). However, the low laser intensity at the periphery of the evanescent wave introduces a background haze. Indeed, there the intensity is not sufficient to switch off or bleach the emitters. TIR is therefore used only when structures are well separated axially and that efficient background reduction can be achieved. As an alternative, the focus of the laser can be shifted in the BFP to image in epi-fluorescence. In both cases, the illumination resulting from focusing in the BFP has a Gaussian profile. Such illumination leads to position-dependent photophysics of the molecules. I discuss this limitation and present an optics-based solution in chapter 3.

Objective High NA objectives are also beneficial to localization microscopy in that their large collection angle yields a higher number of collected photons, improving the localization precision. Attention should be paid to choose objectives with low auto-fluorescence, as it is a source of strong background and is scarcely removed by the imaging filters. Additionally, the objective used in a SMLM microscope should be able to sustain the high laser power focused in the BFP. It is often observed that a tight focus of high intensity laser light can burn holes in the lenses coating within the objective.

Camera The microscope must be sensitive enough to image single-molecules at low light. The images are commonly formed on an electron multiplying charge-coupled device (EMCCD), due to their high quantum efficiency (capacity to transform incident photons into electrons that can then be measured). Recent work has pushed forwards scientific complementary metal-oxide-semiconductor (sCMOS) as an alternative type of camera sensor (Long et al., 2011; Huang et al., 2013). Thanks to technological advances, sCMOS cameras now offer lower noise, large sensors and high quantum efficiency. In addition, the sCMOS architecture allows for a much faster frame rate than with an EMCCD. Since the readout noise is pixel-dependent, more complex noise modelling must be undertaken to properly estimates the number of photons during analyses of the localization microscopy images (Huang et al., 2013).

Aberrations correction The quality of a microscope can be ultimately judged by the shape of the PSF. Aberrations are unavoidable in microscopy due to imperfect optical components but can be minimized by careful alignment. Residual aberrations nonetheless degrade the PSF and consequently the localization precision (Coles et al., 2016). The sample itself is a source of aberrations since it often displays a non-homogeneous refractive index. In addition, index mismatch between the immersion medium and the sample are also a source of aberrations (Hell et al., 1993). Methods to correct for aberrations have been used in astronomy (Merckle et al., 1989; Rousset et al., 1990) and can be applied in microscopy as well (Booth, 2007). Aberration correction relies on two devices: a wavefront sensor and a correction element. The wavefront sensor (e.g. a Shack-Hartman sensor) measures the departure of the wavefront from a perfect one by imaging a single “bright star”, typically a fluorescent bead in the sample or the focus of a laser. The correction element manipulates the local phase of the wavefront and a closed-loop between the wavefront sensor and the correction element guides the correction towards a perfect wavefront. In the so-called indirect sensing scheme, an image-based metrics can be used instead of the wavefront sensor. The closed-loop with the correction device maximizes this metric iteratively. Correction elements are usually liquid-crystal spatial light modulators (SLM) or deformable mirrors (DM). A SLM is based on the electrical control of a pixel array. Each pixel can change in a controlled manner its different refractive index value, enabling manipulation of the light reflecting on its back surface. The most common type of DM consists of a highly reflective membrane sitting on top of an array of actuators. By changing the height of the actuators, the distance the light travels before reflection can be changed, imprinting a different phase to a specific portion of the wavefront. DMs are usually preferred over SLMs in applications where light intensity is critical. As opposed to SLMs, they are non-polarization dependent, high reflective and have a faster refreshment rate (kHz versus hundreds of Hz for SLM). Recently, adaptive optics has been successfully applied to localization microscopy to correct for both optics-induced (Izeddin et al., 2012b) and sample-induced aberrations (Burke et al., 2015).

Rotational freedom of the molecules Another source of localization errors is the rotational freedom of the fluorescent molecules. The emission pattern of an emitter depends on its rotational mobility and has been shown to lead to large localization error when its orientation is constrained (Engelhardt et al., 2011; Lew et al., 2013). While it has been shown that for typical sample, with flexible linkers, that non-freely rotating molecule constitute a negligible population (Backlund et al., 2013), care should be taken to image samples without orientation-induced bias. A promising all-optical solution to the orientation problem is to image only the azimuthally polarized light (Lew and Moerner, 2014; Backlund et al., 2016), as it does not carry any bias, as opposed to radially polarized light.

Acquisition The specific steps of a localization microscopy acquisition are label-dependent, especially in multicolour imaging. However, a rough experiment backbone can be defined. Samples are often tagged with a signal specific to some features of interest in order to get a diffraction-limited overview. This is particularly easy when the label for the SMLM experiment is conjugated with an antibody against GFP. There, a GFP image can be obtained to get a rough location of the structures of interest. The microscope is subsequently switched to the proper channel where the blinking of the label can be observed. The experiment consists of acquiring enough frames to sample the structure. Laser power and buffer need to be optimized to obtain maximum brightness of the fluorescent molecules and slow bleaching. In the case of high labelling it is sometimes necessary to pre-bleach the sample with high laser power to reach a density regime where only single-molecules are observed. As the experiment progresses, the number of available fluorescent molecules decreases due to irreversible bleaching. At constant activation rate (for instant constant intensity of the activating laser, generally in the UV), the density per frame is then declining. In order to speed up the experiment, the density of molecules visible per frame must be maintained constant while remaining in a non-overlapping regime. To do so, the pulse-length or the power of the activation laser must be slowly increased over time. Further increase in the imaging speed can be realized by resorting to a high density of molecules per frame. This necessitates the use of special multi-emitter fitting algorithms (Huang et al., 2011; Holden et al., 2011; Cox et al., 2012). However, such algorithms are usually slow and yield low localization precisions. Another approach makes use of a fast camera and intensity-dependent blinking rate (Huang et al., 2013). The latter however is not applicable to most fluorescent molecules. Aimed at performing live-cell imaging, this method leads to high phototoxicity.

Analysis While the quality of the labelling, of the probes and of the microscope are fundamental to a successful localization microscopy experiment, the analysis of the images should not be disregarded. Many reviews have been published to guide the users (Rees et al., 2013; Deschout et al., 2014; Small and Parthasarathy, 2014; Rieger et al., 2014). Many steps of the analysis can introduce artefacts or decrease the resolution of the final image. The complete process can be described in four stages: detection of candidate localization events, fitting of the localization positions, rendering of the localizations and analysis of the statistics/spatial distribution. The detection step is aimed at identifying local maxima in each image. This step must be fast and allow for the user to set a threshold to minimize the false-positive identification of noise or background. Then, small ROIs centred on the candidate localizations are cut out and run through a fitting algorithm. A variety of fitting routines have been implemented (Smith et al., 2010; Cox et al., 2012; Parthasarathy, 2012; Babcock and Zhuang, 2017). Preference should go to fast algorithms, such as those running on graphic cards (GPU) instead of processors (CPU). Care should be taken that the algorithm reaches the theoretical limit of the Cramér-Rao lower bound (Chao et al., 2016). Understanding the limitations of the algorithms is of great importance in order to avoid working outside of their application range. The output of the fitting routine is often a list of localizations, consisting of the (estimated) lateral positions, the number of emitted photons, of background photons and the localization precision. The localization precision is a first approximation for the quality of the experiment. It represents the uncertainty at which the positions are estimated. Since the molecule is usually only seen a few times, the localization precision is often theoretically calculated according to the number of estimated photons and background (Thompson et al., 2002; Mortensen et al., 2010). It is important to make sure that together, detection and fitting, minimize the number of false positive (adding spurious localization to the final image) and false negative (reducing the effective labelling density) localizations. Once the fitting is done, a table of localization has been compiled. Rendering of the final image is done by representing each localization by a point or a Gaussian at their measure position (Baddeley et al., 2010). In order to represent the data with fidelity, the intensity of the Gaussian and its spread can be weighted by the localization precision. To reconstruct an image with highest resolution, the localizations can be filtered to only draw the localizations fitted with high precision (low localization precision). Several softwares have been published, allowing non-expert users to perform these steps easily (Henriques et al., 2010; Wolter et al., 2010; Köthe et al., 2014; Ovesný et al., 2014). Several reviews have described the artefacts that can arise throughout localization microscopy analyses, examples can be found in the following references: Rees et al., 2013; Durisic et al., 2014; Rieger et al., 2014; Burgert et al., 2015; Erdélyi et al., 2015.

Quantitative experiments A particularly interesting aspect of localization microscopy is that the final data is not the rendered image but the localization table. A vast number of analyses can be performed to extract meaningful information from such list. Important examples includes implementing schemes to measures the stoichiometry of proteins (Gunzenhauser et al., 2012; Durisic et al., 2012; Lee et al., 2012; Puchner et al., 2013; Rollins et al., 2015; Finan et al., 2015; Zanacchi et al., 2017; Karathanasis et al., 2017), cluster analysis (Sengupta et al., 2011; Veatch et al., 2012; Sengupta et al., 2013; Rubin-Delanchy et al., 2015; Baumgart et al., 2016; Pageon et al., 2016; Jiang et al., 2017; Griffié et al., 2016) or spatial averaging to decipher the organization of protein complexes (Dani et al., 2010; Löschberger et al., 2012; Szymborska et al., 2013; Holden et al., 2014; Laine et al., 2015). A small discussion of the impact of the illumination scheme on quantitative studies is present in chapter 3.

1.6.4 Multicolour imaging

The performances of SMLM enable the localization of proteins within cells at the nanoscale. However, the distribution of a certain protein is often not sufficient to understand its function or the effect of a certain perturbation on its organization. Rather, it is sometimes of fundamental importance to image the change in distribution with respect to a protein or a structure of reference. By using a fluorophore of distinct colour and the proper optical filters, one can easily overlay a normal wide-field image of a particular structure with a localization microscopy experiment. In this case, the two images, diffraction-limited and superresolved, can be combined to obtain more information. Yet the diffraction-limited image has a much poorer resolution and precise nanometer-scale distances or clustering of the two proteins is out-of-reach. The straightforward manner for obtaining multiple colour images is simply to use fluorescent molecules of distinct emission wavelengths and the respective filters to separate them. Since localization microscopy relies on a photochemical trick, finding two different molecules with compatible blinking modalities is difficult. In addition, maximum brightness must be achieved in all colours to ensure high localization precision.

Alternating and sequential imaging The first two-colour localization microscopy image was obtained by combining a photo-switchable protein and an organic dye (Bock et al., 2007). Using sequential imaging, the images of microtubules were recorded in each colour and then manually aligned. The fluorescent protein led to a maximum of 200 photons per blinking event, while the dyes emitted as much as 700 photons. Shortly after, the original STORM pairing of cyanine dyes was extended to multicolour (Bates et al., 2007). Different activator dyes paired with the same reporter fluorophore can be activated independently using different wavelengths. By alternatively activating the different pairs, a two-colour composite image of microtubules and clathrin-coated pits was obtained with small cross-talk. Using the same reporter dye has the advantage that the exact same optical path is used for detection and therefore no error is introduced by chromatic aberration or channel registration. This approach was further extended to the chromatic discrimination of the reporter, achieving six-colour imaging on an artificial *in vitro* sample (Bates et al., 2012). This method suffers however from cross-talk, as organic dyes often undergo spontaneous activation. Photoactivatable and photoswitchable proteins were also used together to obtain two-colour images of adhesion proteins and the actin cytoskeleton with sequential acquisitions (Shroff et al., 2007). The recording of the photoactivatable protein signal first was a key element of the method as both proteins were activated at the same wavelength but the photoswitchable probe could be reversed to a dark state in between the two acquisitions. Image registration was realized by localization of fiducials emitting in both channels. Such registration can lead to errors on the order of ten nanometers (Churchman and Spudich, 2012). Multicolour SMLM has been achieved while imaging two photoswitchable proteins (Andresen et al., 2008), two photoactivatable proteins (Subach et al., 2009) or two organic dyes without pairing (dSTORM, Linde et al., 2009).

Ratiometric multicolour imaging Instead of alternating or sequential imaging (figure 1.10-a), chromatically separated fluorescence can be acquired simultaneously and split by a dichroic mirror for separate imaging. As in the case of sequential imaging and subsequent registration, inherent registration errors are present. An interesting alternative is to image fluorescent molecules with close but slightly shifted emission spectra (Bossi et al., 2008), as in figure 1.10-b. In this case, the

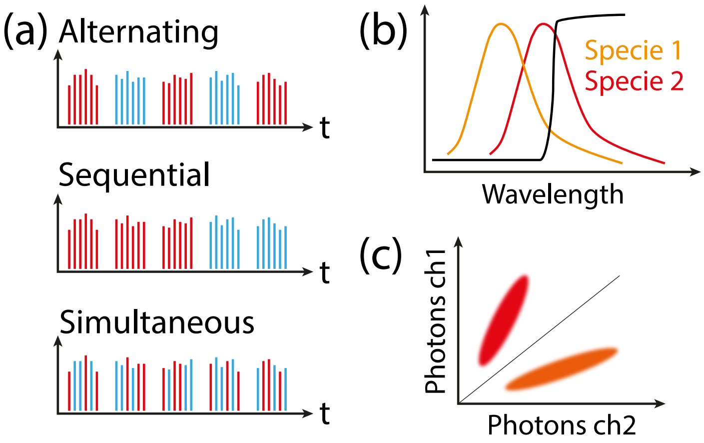

FIGURE 1.10: **Multicolour imaging.** **a)** Two chromatically separated fluorescent molecules can be imaged by alternating the activation/excitation, by sequentially or simultaneously imaging them. **b)** An alternative scheme, called ratiometric multicolour imaging, makes use of two very close species and images them both in two channels simultaneously. **c)** In ratiometric multicolour imaging, each localization event is identified in both channels and the ratio of the number of photons measured in each channel allows identifying the species.

fluorescence is also split by a dichroic mirror and imaged on several channels, typically two. Because the spectra are very similar, the localizations appear in both channels. By plotting the number of photons measured in the first channel versus the number of photons in the second channel, one can identify the fluorescent species by clustering (figure 1.10-c). Indeed, each fluorescent molecule has a different ratio of transmitted to reflected number of photons with respect to the splitting dichroic. Therefore, each population will appear in the 2D photon histogram as a cloud following a linear trend defined by the photon ratio. After identification, rendering of the final image can be done by using only one channel, circumventing the need for channel registration and therefore avoiding the subsequent registration error. Additionally, as the wavelength of the different emitters are close to each other, chromatic aberrations are minimal. Such a method has been applied to organic dyes (Bossi et al., 2008; Testa et al., 2010; Baddeley et al., 2011a; Winterflood et al., 2015) and fluorescent proteins (Gunewardene et al., 2011).

Bottlenecks of multicolour imaging In spite of the high number of publications presenting pairs or triplets of fluorescent molecules to be used, the multicolour images remain in most cases of lower quality than single-colour ones. The difficulty lies in finding a pair of molecules that exhibit similar photoswitching dynamics, duty cycle and maximum brightness in the same conditions. For instance, imaging of two fluorescent proteins with distinct emission wavelengths can be prevented by the fact that, for one protein, the non-activated state is fluorescent at a similar wavelength than the activate state of the other protein. Furthermore, the excitation wavelength of one protein can entail activation and subsequent bleaching of the second one, effectively decreasing the density of probes and the resolution of the final image. The buffer used in dSTORM can also induce blinking of fluorescent proteins, in addition to their laser-controlled switching or activation. The proteins will then present a different on-off duty cycle period, which can lead to a lower number of photons per blinking event. Using organic dyes only has some shortcomings. For instance, chromatically separated dyes can still absorb a non-negligible amount of light at each other's excitation wavelength, due to the very high laser power used in SMLM experiments, increasing photobleaching. In some cases, using alternating or sequential acquisition circumvents such problems at the cost of substantially longer imaging times and limited choice of fluorescent molecules. Multicolour is also scarcely applicable to live imaging in localization microscopy, due to multiple lasers excitation and blinking buffers. Finally, few fluorophores exhibit exceptional brightness and fast blinking. They are often in the same chromatic range or require different buffer for optimal performances (Nahidiazar et al., 2016). Reviews and articles compiling available probes for multicolour imaging can be found in the following references: Lehmann et al., 2015; Nahidiazar et al., 2016; Shcherbakova et al., 2014; Dempsey et al., 2011.

Other approaches Similar methods have been developed that do not suffer from these shortcomings. A first approach is to image the same fluorescent species conjugated with different antibodies. After each round of labelling, a SMLM experiment is performed until all the fluorophores are bleached, then the next fluorescently labelled antibody can be introduced. This method has been demonstrated with primary and secondary antibodies and a pair of organic dyes (Tam et al., 2014) and the use of a single dye with direct primary antibody labelling (Valley et al., 2015). While this avoids chromatic aberrations, registration errors and the downsides of using different fluorescent molecules, the imaging time is very long. The success of the experiment then relies on the labelling performances of the antibodies and low drift. The idea of sequential labelling was first demonstrated using fluorescently labelled oligonucleotides in DNA-PAINT (Jungmann et al., 2010) and exchange-PAINT (Jungmann et al., 2014). The synthesis and labelling of the imaging and docking strands is expensive, but DNA-PAINT can lead to high quality images thanks to its almost infinite probe reservoir. A similar approach, using barcoding and single-molecule FISH has led to the localization of thousands of RNA species (Chen et al., 2015; Moffitt et al., 2016b; Moffitt et al., 2016a). Finally, some methods directly encoded the wavelength in the shape of the molecule's PSF by using a spatial light modulator (Broeken et al., 2014; Shechtman et al., 2016) or by imaging the emission spectrum directly with a prism (Zhang et al., 2015; Dong et al., 2016). Such optical modalities are fast, since they do not require sequential labelling or acquisition, but require complex microscopes.

Although cumbersome to achieve, multicolour localization microscopy has proven precious in studying the organization of mammalian podosomes (Dries et al., 2013), the clustering of genomic regions (Boettiger et al., 2016; Wang et al., 2011) or sub-100 nanometers organization of cell features (Legant et al., 2016).

1.6.5 Extension to the third dimension

Imaging samples in 2D limits the understanding of the structures organization in space. In localization microscopy, the fluorescent labels are seen as single-molecule and their image is therefore described by the PSF of the microscope. The increasing spread of the PSF along z can be used to infer the position, but, to a large extent, the enlargement is symmetrical with respect to the focus plane. In addition, the PSF shape changes only slowly with z. If used for 3D imaging, the PSF would thus yield a very low axial resolution. Therefore, other solutions need to be pursued. The need to infer the axial position of single-molecules was an early concern in single-molecule tracking and localization microscopy benefited directly from the solutions explored, such as the use of an astigmatic lens (Kao and Verkman, 1994) or bi-plane imaging (Watanabe et al., 2007). The first methods to extract 3D information in localization microscopy were rapidly published and a vast choice of techniques is now available. We shall classify them in several categories: PSF engineering, multifocus imaging and interferometric approaches.

PSF engineering Astigmatism (Huang et al., 2008a) is a simple method as it only requires the insertion of a cylindrical lens in the detection path. Such a lens focuses the light in the x and y directions in different planes. As a consequence, while the PSF remains symmetrical when in focus, it extends in two different directions above and below the focus plane (see figure 1.11-a, blue). The use of such an astigmatic lens thereby breaks the symmetry of the PSF with respect to the focus plane. Molecules at various heights then display different lateral elongations. Fitting of an elliptical Gaussian gives PSF x and y size estimations. These quantities are then compared with a calibration curve to infer the axial position well below the diffraction-limit.

Because the axial information is encoded in the shape of the PSF (see figure 1.11-a), such methods are often referred to as PSF-engineering. While the use of an astigmatic lens is simple and cost-effective, more complex approaches have been developed. In order to modify the PSF in a controlled manner, a spatial light modulator (SLM) or a deformable mirror (DM) can be placed in a plane conjugated with the BFP of the objective in the detection path (see figure 1.11-b). The local wavefront phase in the BFP plane can be altered by changing the distance the light is travelling (in the case of DMs) or changing the refractive index along the path (phase masks and SLMs). The pattern displayed on the modulator will change the wavefront phase and lead to a new interference pattern, that is to say a different PSF. Phase changes in the BFP are translation invariant. In other words, each point in the field of view will appear with the same PSF. Modifying the wavefront requires precise alignment of the modulator, adding complexity to the microscope. Furthermore, the use of a modulation element increases the costs.

While phase-masks are non-adaptive, SLMs and DMs are able to additionally correct for aberrations and allow for different patterns to be implemented.

A great number of engineered PSFs have been published using such devices. Because DMs have a low number of pixels, they can only produce simple phase patterns. DMs were used to implements astigmatic (Izeddin et al., 2012b) and the so-called tetrapod (Gustavsson et al., 2017) PSFs. Various PSF models were obtained using SLMs, such as the double-helix (figure 1.11-a, Pavani et al., 2009), the corkscrew (Lew et al., 2011a), the phase-ramp (Baddeley et al., 2011b), the self-bending (Jia et al., 2014) or the tetrapod (figure 1.11-a, Shechtman et al., 2014; Shechtman et al., 2015). In addition, PSF engineering can be used to extract information other than the axial position, such as wavelength (Broeken et al., 2014; Shechtman et al., 2016) or dipole orientation (Backlund et al., 2012; Backer et al., 2013; Backer et al., 2014). Since SLMs are polarization dependent, half of the light must be discarded, decreasing the localization precision. This polarization dependency can be overcome by complex optical arrangements (Backlund et al., 2012; Jesacher et al., 2014).

The different published PSFs vary in localization precision, depth and complexity. For instance the astigmatic lens can be chosen to maximize the localization precision over a short range or to extend this range to a micrometer while decreasing the overall precision. Analysis of the astigmatic PSF is a simple extension of the commonly used algorithm, as the PSF remains Gaussian. The tetrapod PSF, however, is a complex looking PSF (see figure 1.11-a, green), designed to maximize the information content over large depths, and must therefore be analysed by fitting a theoretical model or an experimental measure of the PSF. Point spread functions that are designed to work over a large range tend to have a larger spatial extent. The main consequence of this is that the density of emitters in each frame must be accordingly decreased in order to avoid overlapping. This in turns increases the imaging time. Complex patterns also tend to decrease the lateral localization precision. The precision with which the molecules can be axially localized using PSF shaping depends mainly on the information content of the PSF (Badieirostami et al., 2010). In order to compare the different PSF, one then needs to calculate the so-called Cramér-Rao lower bound (CRLB). The CRLB corresponds to the lowest value the localization precision can reach. Comparison of the CRLB for the astigmatic, doulbe-helix and 6µm tetrapod is shown in figure 1.11-c. Astigmatism (blue) achieves a good resolution ($\sim$ 20 nm), but has a limited depth as illustrated by the rapid increase of the precision value. While around the focus the DH-PSF localization precision (purple) is more homogeneous, it decreases rapidly beyond 1 µm away from the focus plane. Finally, the 6µm tetrapod PSF performs slightly worse around the focal plane than the DH-PSF, but displays a constant localization precision over a large range. Several experimental and theoretical studies have been published in that respect (Middendorff et al., 2008; Mlodzianoski et al., 2009; Badieirostami et al., 2010). While the CRLB is a good comparison readout, other parameters should also be considered such as the optical, experimental and analytical complexities. Since

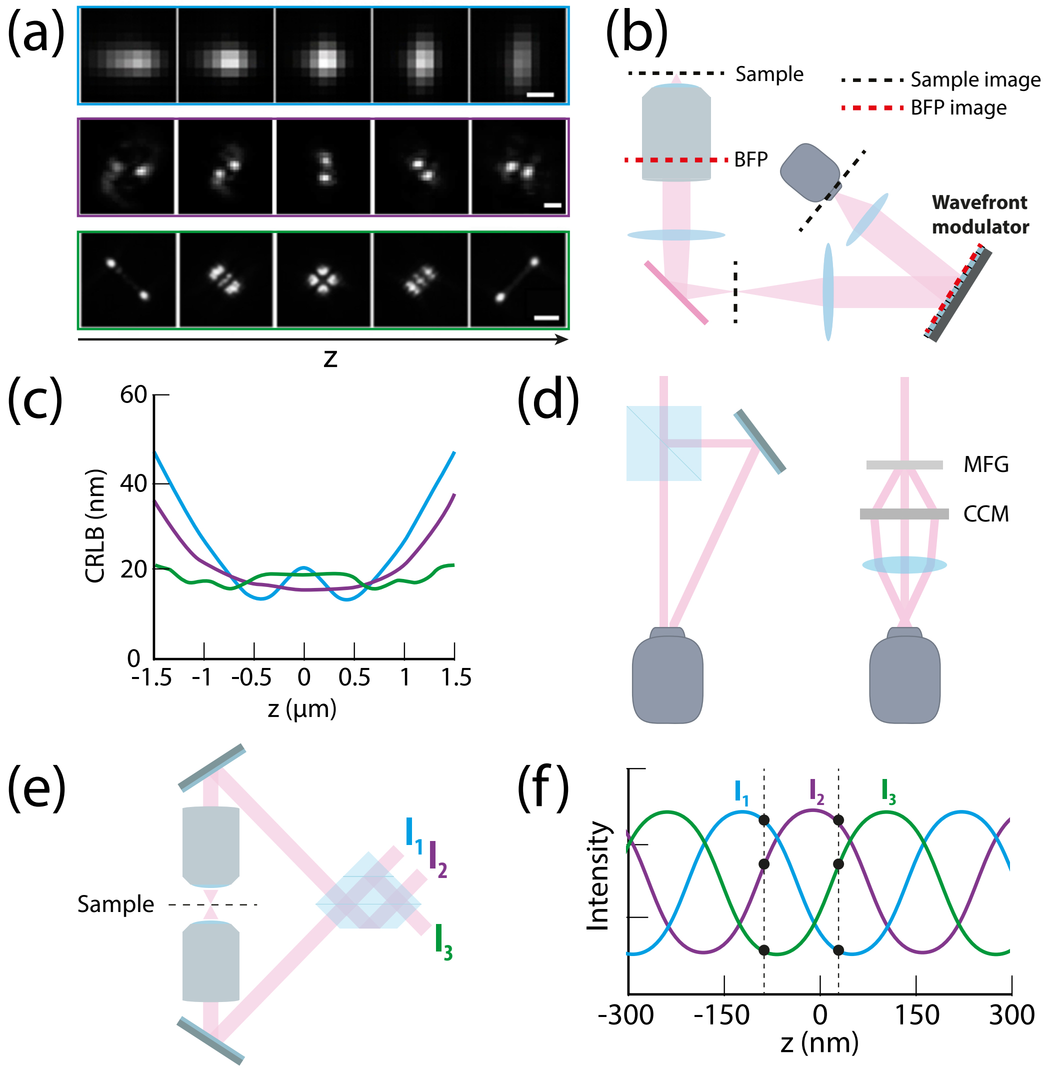

FIGURE 1.11: **3D imaging**. **a)** PSF engineering with astigmatism (blue, 0.5 μm scale bar, 0.8 μm range), double-helix (purple, 2 μm scale bar, 3 μm range) and 6 μm tetrapod (green, 2 μm scale bar, 6 μm range). **b)** PSF engineering in the BFP. A pair of relay lenses are used to create an image of the objective BFP directly onto a wavefront modulator. A lens then re-images the sample onto the camera. Modifications in the BFP can introduce controlled deformation of the PSF. **c)** CRLB comparison between astigmatism (blue), DH-PSF (purple) and 3 μm tetrapod (green). **d)** Multiplane imaging is achieved by forming images of the sample at different height on the detector. This can be achieved with a beam splitter and different path lengths (Juette et al., 2008, left) or using a multifocal grating (MFG) and a chromatic correction grating (CCM, Hajj et al., 2014, right). **e)** Simple schematic showing the principle of interferometric localization microscopy. Two objectives focus on the same plane of the sample. The light is collected on both sides and combined in a three-way beam splitter (Shtengel et al., 2009). The beams exit the beam-splitter in three directions whose respective intensities, I_1, I_2 and I_3, are axially dependent. **f)** Intensities I_1, I_2 and I_3 dependence on the axial position of the emitter. Each channel intensity is periodical with z. Within an axial slice of one wavelength, the axial position is uniquely determined by the value of the three intensities, as illustrated by the horizontal dashed lines. Figure a and c were adapted with permission from von Diezmann et al., copyright 2017 American Chemical Society. The original data from figure a was adapted with permission from Huang et al., copyright 2008 AAS (astigmatism), from Pavani et al., copyright 2009 National Academy of Science (double-helix) and Shechtman et al., copyright 2015 American Chemical Society (tetrapod).

PSF engineering methods must rely on calibration curves, careful attention should be paid to depth-induced (McGorty et al., 2014; Carlini et al., 2015) or field-dependent (Diezmann et al., 2015) aberrations.

Astigmatic imaging encountered a vast success in biological applications owing to its simplicity. Given good imaging conditions, bright localizations and low background, the achievable resolution can be sufficient to resolve many biological systems. Striking examples includes imaging of synapses in brain tissue (Dani et al., 2010), periodic actin and spectrin structures along axons (Xu et al., 2013; Zhong et al., 2015) or subdiffraction clustering of genomic regions (Boettiger et al., 2016). Other PSF have been less used for biological applications, to the exception of the double-helix PSF in localization microscopy (Lew et al., 2011b) and single-molecule tracking (Thompson et al., 2010) for instance.

Multiplane imaging Another approach to 3D localization microscopy is to sample the PSF at different planes in the sample, called multifocus or multiplane imaging. Instead of focusing through the sample, one can design a microscope capable of observing the sample at several heights at the same time. The simplest realization of such scheme is simply a two-channel microscope, where one arm is slightly longer that the other one, thus introducing defocus (figure 1.11-d, left, Juette et al., 2008; Ram et al., 2008). In this configuration, the light is split equally between the two channels. Since the two channels are observing the sample in different planes, the uncertainty on the molecule position with respect to the reference plane is lifted. Fitting procedures are identical to 2D imaging to the exception that they must include two images at the same time. Biplane imaging has been shown to yield an analogous theoretical resolution as astigmatism by comparison of CRLB (Middendorff et al., 2008). Multifocus has also been implemented using four planes in a similar arrangement as biplane using beam splitters (Prabhat et al., 2006) and a single camera per arm. A different biplane arrangement was realized using two objectives (Ram et al., 2009), further increasing the complexity of the microscope. However, focusing by increasing the optical length with high NA objective introduces spherical aberrations (Botcherby et al., 2007). An alternative scheme was proposed using diffraction gratings to create nine images on a single camera (figure 1.11-d, right, Abrahamsson et al., 2013; Hajj et al., 2014), free of aberrations and chromatically corrected. Diffraction gratings are responsible for a substantial loss of light ($\sim$25%) and require precise alignment. Increased depth was realized by coupling the latter method with astigmatism (Hajj et al., 2016). While biplane with a single objective is a simple method, extension to a higher number of planes leads to complex microscope and analysis. Furthermore, the redistribution of light to a certain number of planes decreases the number of photons per localization events by the same quantity. Since the axial localization derives from the presence of the molecule signal in two of the planes, the axial precision is not improved by the addition of new planes. The depth of imaging is on the other hand extended.

Interferometric imaging An impressive development in 3D SMLM is the axial localization of molecules using interferences. By exploiting a 4Pi optical arrangement, light from both objectives can be combined and subsequently separated in paths by a three-way beam splitter (figure 1.11-eShtengel et al., 2009) or by polarization (Aquino et al., 2011; Huang et al., 2016). In all cases, the light from a single molecule interferes with itself to give rise to images with different intensities in each arm (figure 1.11-e). If the molecule is moved axially, the path lengths in each arm change and so does the ratio of intensities on the different images. Measuring the intensity on each detector yields the axial position of the emitter, but within axial slice only (figure 1.11-f). Indeed, because the interferences are periodical, phase unwrapping must be performed to determine to which axial slice does the molecule belong to. Then only, is the molecule unambiguously located. In the most recent example, a DM was placed in each arm of a 4Pi microscope and introduced a certain level of astigmatism (Huang et al., 2016). The change in lateral size of the PSF then indicates in which slice of the periodical intensity pattern the emitter is to be found. Measurements lead to the localization in 3D of the molecule within a depth of nearly 10 μm. Interferometric approaches require extremely complex microscopes and are difficult to operate and maintain. Because the interferences are very sensitive to distances, the axial localization precision achieved is better than the lateral one and can be lower than 10 nm. A simpler, single objective, solution has been explored (Schnitzbauer et al., 2013), albeit with poorer resolution. The exceptional resolution reached by 4Pi interferometric microscopes has been used to decipher the axial nanoscale organization of focal adhesions (Kanchanawong et al., 2010; Case et al., 2015), the mitochondrial nucleoids membrane interactions (Brown et al., 2011; Kopek et al., 2012) or the distribution of proteins around clathrin invaginations in mammalian cells (Sochacki et al., 2017).

Three-dimensional imaging has been extensively explored and has proved to be one of the major axis of development in localization microscopy. Readers will find an excellent review in Diezmann et al., 2017. Interferometric approaches have yielded an unprecedented resolution in light microscopy and are a precious tool in structural studies. However, the complex instruments and analysis required are a serious drawback to its application, limiting the number of accessible microscopes. Multiplane and PSF engineering modalities are usually implemented using simpler microscopes. In particular, biplane and astigmatism are easy to introduce. In theory, they achieve an axial resolution about three times worse than laterally. Multifocus imaging with more than two planes is a useful implementation for extended depth but deteriorates the lateral resolution without gain in axial resolution. PSF engineering with SLM suffer from a similar drawback due to the polarization dependence of the phase patterns on the liquid crystal screen. Additionally, while most engineered PSF have a better range and localization precision than the astigmatic PSF, their axial precision remains poorer than the lateral one (when the latter is not deteriorated). In chapter 5, I introduce a new and simple approach to 3D localization.

1.6.6 Live imaging

Ignoring phototoxicity, SIM and STED microscopy are inherently live-cell compatible. In SIM, imaging occurs at the sub-second time scale, while it can take few seconds in STED (Minoshima and Kikuchi, 2017). Therefore, many cellular processes can be resolved by both methods, imaging length being mostly limited by the bleaching of the fluorescent molecules. Localization microscopy, on the other hand, requires the acquisition of thousands to hundreds of thousands of frames. Sample movement during acquisition will blur the final rendered image and it will thus lose its resolving power. Each time-slice must be acquired with sufficient density to resolve nanometer-scale features while imaging at fast enough scales to maintain a sufficient time resolution. As in the case of STED, SMLM experiments require high laser power and are therefore subject to phototoxicity (Wäldchen et al., 2015). Fixed-cell localization microscopy makes extensive use of organic dyes due to their brightness. The buffer used with organic dyes is often not live-cell compatible. Additionally, the proteins are often rapidly exchanged, limiting the use of immunodetection. A more straightforward approach is to image fusion proteins. Leaving recovering time in between SMLM frames allows for lower photodamages and recycling of the fluorescent proteins, increasing the total imaging time. Live-cell localization microscopy thus requires slowly varying features of interest, high labelling densities and photon-tolerant cells. This was first realized to image domains of the cell membrane (Hess et al., 2007) and adhesion complexes (Shroff et al., 2008), reaching a reported 60 nm resolution with a frame rate of 25 s. Live-cell PALM has been applied to single-molecule tracking (Manley et al., 2008), membrane probes (Shim et al., 2012) and a various number of biological systems such as bacteria (Biteen et al., 2008; Fu et al., 2010; Wang et al., 2011; Biteen et al., 2012) and yeast (Laplante et al., 2016).

1.6.7 Application to biological questions

Localization microscopy relies on the combination of carefully optimized factors, for example a high labelling efficiency and small linker size to image the structure of interest with fidelity, the use of bright fluorescent molecules in low background to maximize the localization precision, a microscope with minimal drift, free of aberrations, and an artefact-free analysis. This does not come together easily and necessitates good expertise, on the bench side as well as during analysis. Not every biological question would benefit from imaging in SMLM. An increase in resolution obtained using SIM or STED might be sufficient and avoids months of selecting for the right labelling scheme or fluorescent probe. In the case where the observation of nanoscale features is the missing piece of the puzzle, then localization microscopy has proven to be extremely valuable, providing access to details beyond the reach of any other existing method. It is particularly true for protein complexes. The interaction between a large number of proteins in time and space allows the execution of complicated tasks in cells, such as assembling contacts between the extracellular matrix and the cell cytoskeleton, the mediation of transport between the cytoplasm and the nucleus, or the internalization of receptors through remodelling of the membrane. Such macromolecular assemblies can contain hundreds of proteins while remaining as small as a hundred nanometers. Often, the signal of the entire complex is contained within few pixels. The ability to resolve the details of the architecture of such complexes provides invaluable information on the underlying mechanisms.

Application examples Focal adhesion complexes, for instance, can cover μm^2 surfaces but have an axial extent that is smaller than 200 nm. Kanchanawong and colleagues exploited the extraordinary resolution of 3D interferometry localization microscopy (iPALM) to image nine of the most prominent proteins of focal adhesions (Kanchanawong et al., 2010). Surprisingly, the core of focal adhesions seems to be composed of partially overlapping strata. Actin regulatory functions were hypothesized following the organization of certain proteins.

Using astigmatism and multicolour localization microscopy, Dani et al. have determined the axial position of ten proteins throughout the synaptic region.

Studying the nuclear pore, Szymborska et al. (Szymborska et al., 2013) realized a tour-de-force by single-particle averaging of the ring-shape distribution of several proteins within a nuclear pore sub-complex. While the orientation of this subcomplex was debated, their nanometer measurement of the radial distances of the imaged proteins helped discriminate between the different models.

Observing what was previously hidden within the diffraction limit has led to other striking images, such as the periodic structure formed by actin, spectrin and other interacting proteins along axons (Xu et al., 2013). Such scaffold could provide axons with a mechanism for large elastic extension capable of sustaining mechanical strain.

Localization microscopy is also not limited to proteins, but has also been successfully applied to the localizations of thousands of RNA species (Chen et al., 2015) or the organization of chromatin domains (Wang et al., 2016).

The previous examples were cherry-picked among the most impactful applications of localization microscopy. Many other studies have used this method to unravel unknown functional and structural details in cell biology and the scope of application remains wide. SMLM has achieved unprecedented resolution in light microscopy and benefit from an abundant literature. However, limitations are still faced. Labelling efficiency is the first and foremost, as immunodetection leads to partial labelling and unspecific binding, while endogenous overexpression does not exclude the presence of untagged proteins. While multicolour imaging has been achieved with different modalities, it is not yet straightforward to perform with high resolution. Besides labelling, the main obstacles in the way to routine structural studies are the limited throughput and axial resolution.

2 Aim of the study

Localization microscopy is now widely applied in biology, allowing the observation of the nanoscale organization of sub-cellular structures and protein complexes. While continuous efforts are being made to develop better fluorescent probes and labelling schemes, some limitations of localization microscopy can still be overcome by improving the microscopes themselves. During my PhD studies, I extended the typical localization microscope toolbox to overcome three of these limitations: inhomogeneous illumination, low throughput and the lack of a simple and isotropic 3D approach.

In section 3, I describe a new illumination scheme for localization microscopy that achieves a highly homogeneous intensity across the field of view. Quantification studies in localization microscopy rely on the hypothesis that all the fluorescent molecules have similar brightness, blinking and bleaching rates. These quantities, however, are intensity dependent. The common illumination system that is found in localization microscopes displays a Gaussian profile and therefore does not provide a constant power density in the illuminated region. This can lead to serious artefacts in quantitative studies such as clustering or molecular counting. In order to avoid such a bias, the field of view is often restricted to the central area. I developed an illumination system based on a multi-mode fiber and a speckle reducer, achieving a highly uniform illumination across the field of view. Comparisons of blinking rates and brightness are shown highlighting the advantages of this new illumination modality. Finally, I demonstrate the possibility to use total internal reflection activation together with homogeneous excitation to obtain optical sectioning. This work has been published in Deschamps et al., 2016.

To increase the throughput of localization microscopy experiments, one can image faster using sCMOS cameras and high laser power. Unfortunately, this is not applicable to all fluorescent labels. Another possibility is to increase the density of single-molecules per frame and to make use of multiemitter fitting routines. However, the complexity of these algorithms leads to very slow analysis time and low resolution. Together with Markus Mund, another PhD student in the lab, we increased the throughput of the microscope by enabling automated acquisition. By abolishing the need for human intervention, the rate of data acquisition was vastly improved. This microscope was used to decipher the radial organization of the endocytic machinery in yeast, in a study to be published on which I am a co-author.

In section 4, I present my work on the automation of the microscope using advanced electronic control and a tailored interface within Micro-manager (Edelstein et al., 2010). A brief summary of the result of our study on endocytosis is provided, in order to demonstrate the impact of automated localization microscopy.

A vast choice of 3D methods is available in SMLM. Most of the users turn to astigmatism for its simplicity (a single additional lens in the beam path). Such a method achieves in practice a much poorer localization precision along the axial direction than laterally. Other methods require a higher level of optical complexity, but achieve a better precision or a larger depth. In particular, interferometric approaches reach a better localization precision axially than laterally. Such improvement in resolution comes at the cost of expensive, complex to build and maintain microscopes. During my PhD, I explored a fundamentally new method to perform 3D localization microscopy based on the principle of surface-generated fluorescence. Termed supercritical angle localization microscopy (SALM), this approach has the potential to achieve isotropic localization precision in a range of few hundreds of nanometers above the coverslip. In section 4, I describe the theory of surface-generated fluorescence and the simple optical system necessary to implement SALM. I present the proof-of-principle experiments using DNA-origamis and biological samples. This work was published in Deschamps et al., 2014. Due to strong diffraction at one of the optical components, SALM has not achieved its full potential yet. I detail a new microscope aimed at optimizing SALM using a very high NA objective (NA 1.7) and adaptive optics.

3 | Homogeneous illumination

3.1 Introduction

Quantitative fluorescence microscopy is a prime tool to measure the spatial distribution and molecular abundance of proteins. Biases induced by background, noise or aberrations are important aspects to consider when evaluating the accuracy and the precision of the measurement (Waters, 2009). Since fluorescence is linear with the illumination intensity (before reaching saturation), non-uniform illumination should be avoided or corrected (Zwier et al., 2004). Non-uniform illumination can indeed cause conflicting measurement outcomes at similar protein concentration across the field of view, introducing large errors in quantitative studies. In order to maximize the uniformity of the illumination field, wide-field microscopes are aligned according to Köhler's principles (Köhler, 1893). As opposed to critical illumination where the image of the source is formed in the sample, Köhler illumination focuses the light in the back-focal plane (BFP) of the objective. This scheme prevents the inner structure of the light source from appearing in the sample.

In localization microscopy, the laser light is often conveyed through a single-mode optical fiber. Such fibers have a core size of a few micrometers (<10 µm) and their output can produce small foci. The light is then focused into the BFP of the objective, to image either in epi-fluorescence (focus in the undercritical region of the BFP) or TIR (focus in the supercritical region of the BFP). Because of the small core size, only one laser mode propagates through the fiber. This mode is called the fundamental mode and has a Gaussian profile. This property ensures that whatever the profile of the laser light at the entrance of the fiber and the torsion of the fiber, the output has a stable Gaussian profile. When the sample is imaged in epi-fluorescence, the intensity across the field of view is then Gaussian as well. In TIR, the illumination presents a Gaussian lateral profile (Axelrod et al., 1984) in addition to its exponential decay along the axial direction. Consequently, both TIR and epi-fluorescence illumination exhibit a non-uniform intensity profile.

Illumination schemes in localization microscopy are almost always inhomogeneous. The effect of non-uniform illumination must be taken into account when performing quantitative experiments.

3.1.1 Quantitative studies in SMLM

Because localization microscopy deals with single molecules, the data gathered is a list of estimated parameters for each localization event. In particular, the data can be exploited beyond the sole reconstruction of an image for quantitative purposes.

Clustering Localization microscopy can probe the nanoscale organization of proteins, facilitating clustering studies. Several methods have been developed in order to quantify the degree of clustering, using for instance Ripley's functions (Williamson et al., 2011; Rossy et al., 2012; Muranyi et al., 2013; Scarselli et al., 2012), pair-correlation (Sengupta et al., 2011; Veatch et al., 2012), Bayesian analysis (Rubin-Delanchy et al., 2015; Griffié et al., 2017), density-based approaches (Nan et al., 2013; Endesfelder and Heilemann, 2014), Voronoï segmentation (Levet et al., 2015; Andronov et al., 2016) and nearest-neighbour algorithms (Jiang et al., 2017). Such analyses are not free from artefacts. In particular, it was shown that the reactivation of proteins fluorescence mimic nanoscale clusters (Annibale et al., 2011b). Indeed, blinking molecules can appear several times throughout the experiment and be identified as different molecules arranged in a small cluster. This leads to severe overestimation artefacts. To a certain extent, these clusters can be discriminated from real clusters by analysing the localizations proximity in time (Annibale et al., 2011a; Spahn et al., 2016) or the spatial distribution profile (Sengupta et al., 2011). These methods have limitations when the molecules have long-lived dark states (and therefore reappear after many frames) or when the clusters size is on the order of the localization precision.

Counting Inferring the number of molecules from the number of localizations is also made difficult by reactivation. *In vitro* measurements of distribution of on-times (number of consecutive frames where the molecule appears) have been proposed to identify localizations (Annibale et al., 2011b; Gunzenhauser et al., 2012; Puchner et al., 2013). Other approaches to molecular counting include kinetic models of the fluorescent molecule (Lee et al., 2012) or of probe attachment dynamics (Jungmann et al., 2016), stochastic analysis of *in vivo* traces (Rollins et al., 2015) or model-independent fitting of the blinking statistics (Hummer et al., 2016; Karathanasis et al., 2017; Fricke et al., 2015). However, the kinetics of many fluorescent proteins are unknown and *in vivo* measurements can strongly differ from those *in vitro*. Kinetic models, on the other hand, might be incomplete or not applicable to proteins with unknown photophysical behaviours. An additional type of method makes use of constructs with known stoichiometry (Finan et al., 2015) or DNA origami platforms (Zanacchi et al., 2017) to calibrate the number of localizations per molecule.

Effect of photophysics In all cases, the photophysics of the fluorescent molecules, in particular the brightness and the blinking rate, has a deep impact on the final quantitative measurement. Molecules emitting a low amount of photons will have a lower probability of being detected, an increased uncertainty on their position and larger cluster size. Long-lived dark states will cause molecules to reappear later during the experiment and escape the grouping of localizations in time, leading to overestimation of molecular counts and cluster size. Slower blinking will cause the molecules to appear in several consecutive frames, effectively decreasing the number of measured photons per frame. This will also increase the density of emitters per frame, leading to overlapping signals. Obtaining uniform photophysics across the field of view should therefore be a primary concern in quantitative localization microscopy.

Impact of the illumination intensity The photodynamics of fluorescent molecules is largely dependent on the local intensity of the excitation light. Since illumination in localization microscopy usually exhibits a Gaussian intensity profile, uneven photophysical behaviour across the field of view is encountered. The solution commonly applied to overcome this problem is to restrict the field of view to the centre of the illuminated area, obtaining moderate homogeneity. A substantial portion of the light is then rejected out of the considered area. For instance, the area defined by an intensity equal to 80% of the peak power contains only 20% of the total light intensity. Unless the microscope is equipped with lasers of very high power, which come at a high cost, the field-of-view is restricted to a very small area.

In summary, uneven illumination poses a serious limitation to quantitative studies in localization microscopy. In this section, I detail a new illumination system for localization microscopy that achieves a highly uniform illumination, while preserving all the light at low cost and complexity. Two master students, Andreas Rowald and Daniel Gerz, assisted me in this project. Andreas made preliminary tests with the optical path while Daniel joined me in the optimization of the system. The localization and reconstruction of the data were performed in a custom Matlab software written by Jonas Ries. Finally, the biological samples have been prepared by Ulf Matti and Mai Baalbaki. This project has been published in Deschamps et al., 2016.

3.2 Results

3.2.1 Multi-mode and single-mode fibers

Single-mode optical fibers are not compatible with highly uniform illumination due to their Gaussian output profile. A straightforward alternative to obtain better homogeneity is to use a multi-mode fiber (MM). Multi-mode fibers have a much larger core (>50 µm) than single-mode fibers (SM, <10 µm), as illustrated in figure 3.1-a and 1-b. Regardless of the physical arrangement of a SM fiber, looped or straight, the output will have a Gaussian profile (see LP01, the fundamental mode, in figure 3.1-c). In the case of MM fibers, their large core allows the excitation of many modes (few examples can be found in figure 3.1-c). Consequently, the intensity profile along the fiber is the superposition of the profiles of all different excited modes. However, each mode is propagating at a different velocity (*modal dispersion*) and the output profile is not stable. In particular, it varies depending on the torsions, bending or stretching that the MM fiber undergoes. Changing the bending of the fiber causes the light to excite the modes with different amplitudes, resulting in a new output profile. However, the superposition of a high number of modes results in a profile that is more homogeneous than in the case of a SM fiber. Furthermore, an important advantage of MM fibers over SM ones is the higher coupling efficiency. The small core size of SM fibers makes the coupling difficult and commonly results in a maximum laser coupling efficiency of ∼65%. MM fibers, on the other hand, reach coupling efficiency values above 90%. In addition, the easy coupling with MM fibers leads to a higher stability.

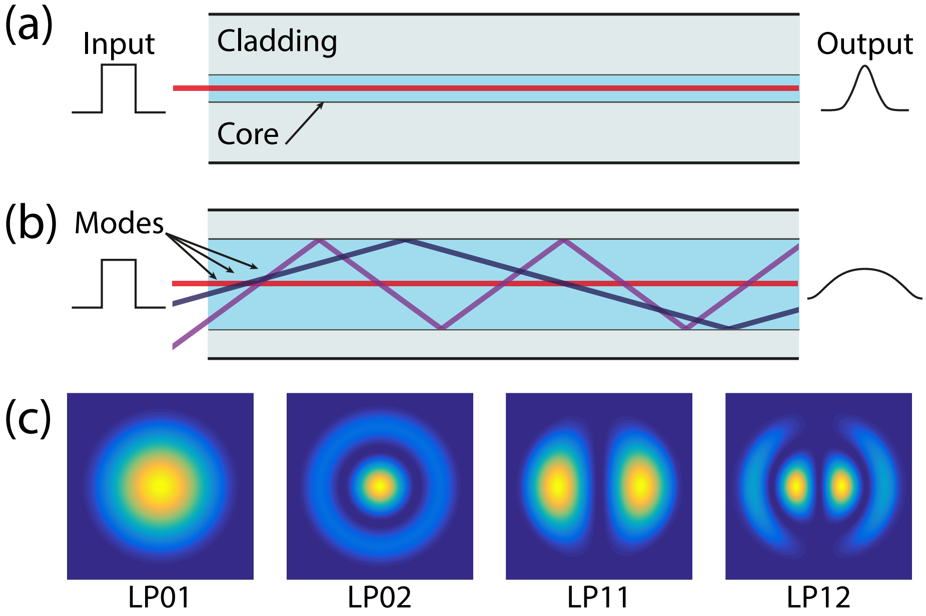

FIGURE 3.1: **Single-mode vs multi-mode fibers**. **a)** A single-mode optical fiber has a core size <10 µm. The main property of such a fiber is that only the fundamental mode can be excited and always results in a Gaussian output. **b)** A multi-mode fiber has a much larger core, resulting in the excitation of several modes. The output is then a superposition of many different modes. **c)** Examples of several modes present in round waveguides. The LP01 mode is the fundamental Gaussian mode observed in circular single-mode fibers, while the others are higher order examples that can be encountered in multi-mode fibers. The modes were computed using a code written by Lucian Bojor.

The high laser spatial coherence causes inter-modal interferences, which gives rise to a pattern of constructive and destructive interferences in the beam profile. This pattern is commonly referred to as a *speckle pattern*. Speckles create rapid and small-scale changes of intensity and would therefore be detrimental to single-molecule studies. Since MM fibers are used in many different fields, from communication to microscopy, a large spectrum of reduction strategies have been explored. Examples include agitation and vibration of a fiber (Inoué et al., 2001; Ha et al., 2009; Fujimaki and Taniguchi, 2014; Almada et al., 2015; Kwakwa et al., 2016) or a fiber bundle (Metha et al., 2012), introducing moving diffusers (Kubota and Goodman, 2010; Kuratomi et al., 2010; Graetzel et al., 2015) or digital micromirror devices (Akram et al., 2010). In localization microscopy, agitation has been able to produce a better homogeneity with the common illumination system (Kwakwa et al., 2016), while remaining nonetheless far from a uniform illumination.

3.2.2 Optical path

In order to achieve a highly homogeneous illumination, I built an optical system based on the use of a multi-mode fiber and of a commercial diffusive speckle reducer. A schematic of the optical arrangement is shown in figure 3.2-a. The illumination system is composed of two arms; the first arm (figure 3.2-a1) is the multi-mode homogeneous illumination path, while the second arm (see figure 3.2-a2) is the commonly used epi-fluorescence/TIR illumination (referred to in this manuscript as the single-mode path). The MM path makes use of a free-space emitting laser combiner focused onto the speckle reducer. A lens relay system (two lenses in 4f configuration, i.e. separated by the sum of their focal length) is used to image the previous focus onto the entrance of a MM fiber (105 µm core and 0.22 NA). The fiber is coiled around a post in order to homogenize the output profile. Finding a bending arrangement that results in a profile as flat as possible, regardless of the speckles, is an important aspect of this illumination system. A lens at the fiber exit forms an image of the output at the object plane of another pair of relay lenses. The position of the fiber exit and the first lens are adjusted to ultimately change the illuminated area in the sample. The pair of relay lenses after the fiber is used to remove spurious rays with the help of an iris. The position of the relay lenses is fixed so that the image of the fiber output is formed once again at the object plane of the last lens. Since the back focal plane of the last lens is a plane conjugated to the sample, the image of the fiber output is projected directly in the focus plane of the objective. The choice of the multi-mode fiber, as well as of the lenses focal length, was done by calculating the size and divergence of the laser focus on the entrance of the fiber. The calculation was carried out in WinLens (Qioptik) and took into account the increase in divergence due to the speckle reducer. The size of the illuminated area was chosen as to allow for two channels simultaneous illumination on the camera chip. Because the pixel size is 125 nm, and the chip 512 pixels large, we chose to illuminate a circular region of 30 µm diameter. The SM path (figure 3.2-a2) consists simply of a single-mode fiber connected either to the same laser box, or to a single UV laser, and of a lens placed in order to image the fiber exit to infinity. The last lens is shared by the two paths, and in the case of the SM illumination, it focuses the single-mode fiber output onto the BFP of the objective. The fiber exit is placed on a linear stage, allowing to either illuminate in TIR or in epi-fluorescence. The illumination arm can be selected by placing or removing a mirror at the intersection.

Additionally, a dichroic mirror can be placed to use both arms at the same time using different colours. Details of the components are available in the Methods 7.1.1.

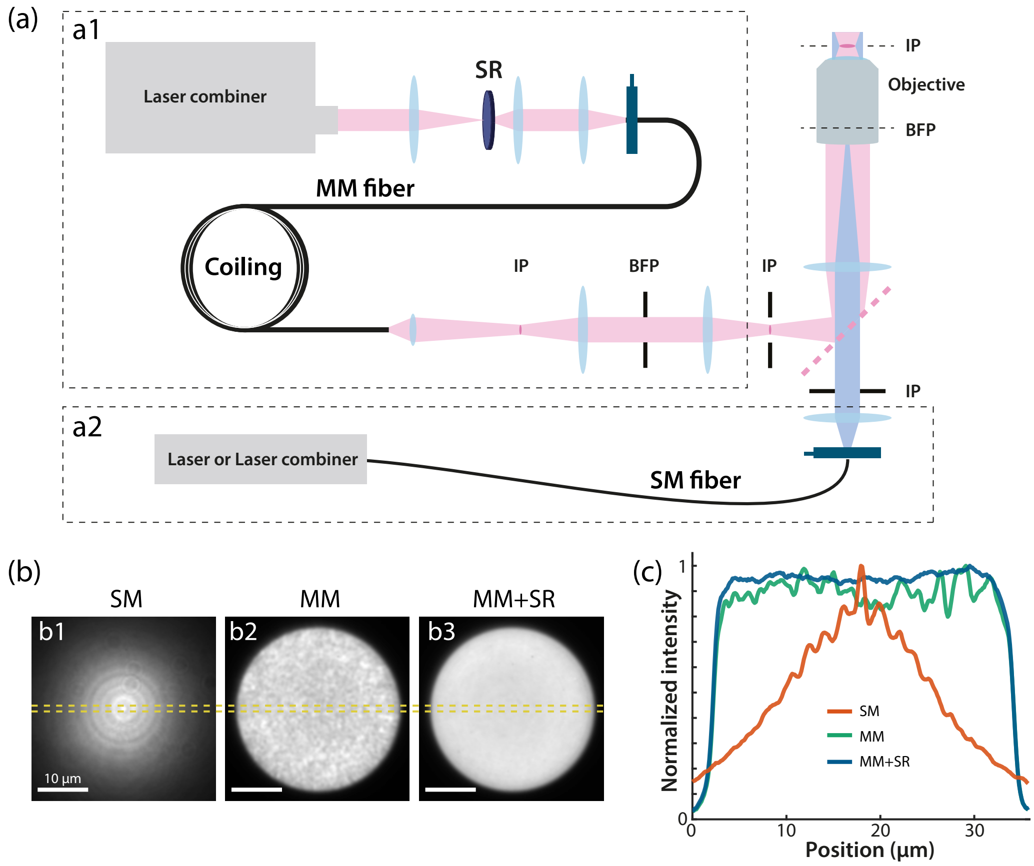

FIGURE 3.2: **A new system for homogeneous illumination. a)** This new system for homogeneous illumination is composed of two arms. The first path (a1), uses free-emitting lasers focused on a speckle reducer (SR) and coupled into a multi-mode (MM) fiber to create a uniform intensity profile in the sample. The fiber is coiled around a post to increase mode-mixing. A 4f relay lenses system is used to form the image of the fiber output in a plane conjugated to the image plane (IP). An iris is placed in a plane conjugated to the objective back-focal plane (BFP) to remove spurious rays. The second arm (a2) is the widely used epi-fluorescence/TIR illumination system. A single-mode (SM) fiber conveys the laser light that is then focused on the BFP. The SM fiber can be attached to either a single laser source or a laser combiner. A dichroic or a fully reflective mirror can be placed at the intersection of the two paths. **b)** Intensity profiles obtained with the typical SM illumination (b1), the multi-mode illumination without speckle reduction (b2) or the multi-mode illumination with speckle reduction (b3). **c)** Line profiles averaged over a thickness of 4 pixels (yellow box in (b)) of the three previous illuminations. The intensity is normalized for comparison purposes. Reprinted with permission from Deschamps et al., 2016, Optics Express, manuscript of which I am first author.

3.2.3 Illumination profile

To compare the two illumination modes, I imaged a layer of fluorescent molecules compressed between two coverslips (<2 µm thickness). As expected, the profile in the sample of the SM path in epi-fluorescence mode displays a Gaussian shape (see figure 3.2-b1). The rings present in the image are Newton rings, and arise from the interference of the multiple reflections on the coverslips. The profile of the MM illumination is shown in figure 3.2-b2. Imaging the fiber output directly into the sample results in a sharp boundary of the illumination, the fiber coiling ensuring a somewhat homogeneous intensity in the illuminated area. However, laser speckles appear in the image as small-scale heterogeneous structures. In figure 3.2-b2, the speckle reducer has been placed in the beam path but has not been activated. This device holds diffusers in a polymer membrane that is contracting or expanding following the current applied between electrodes (Graetzel et al., 2015). The resulting movement is a rapid oscillation (300 Hz) of the diffusers. Placed before the MM fiber, this speckle-reducer causes fast random changes in the speckle pattern. If the speckle pattern fluctuates much faster than the imaging speed of the camera (>5 ms), then the pattern averages out. The effective intensity across the field of view, integrated over one exposure, is then uniform (see figure 3.2-b3). Comparing the line profile (averaged over four pixels delimited by the dashed box in figure 3.2-b) of the three illuminations reveals the difference in uniformity between the single-mode and the multi-mode illumination (see figure 3.2-c). Even without speckle reduction, imaging the output of a multi-mode fiber in the sample leads to a top-hat intensity distribution that achieves a much better homogeneity than the Gaussian profile of the SM illumination. It should be noted that the SM illumination presented here is the very same that was used previously on this microscope. Finally, the line profiles of figure 3.2-c clearly demonstrate the effectiveness of the speckle reduction. A measure of the illumination profiles inhomogeneity can be computed by calculating the coefficient of variation:

$$cv = \frac{\sigma}{\mu} \tag{3.1}$$

where σ is the standard deviation of the pixel values and μ is the mean. A low cv value means that the profile is highly uniform, and inversely. The calculation yields a value of 34% for the SM illumination, indicating a low homogeneity. Speckle-reduced MM illumination on the other hand displays a cv value of 2.5%. Achieve a similar homogeneity with a Gaussian illumination would necessitate to dramatically increase the size of the illumination, reducing the mean power intensity. Disregarding the eventual use of strong lasers to compensate for the decreased peak power, restricting the field-of-view to an area of identical cv value would lead to a loss of 92% of the total intensity.

This analysis incontestably demonstrates the superiority of the MM illumination system in terms of homogeneity. However, the speckle reducer induces an increase of the beam divergence of about 17° in total. Such small increase is sufficient to complicate light coupling with the multi-mode fiber. The coupling efficiency of the single-mode fiber for each wavelength is about 60 to 65%. Multi-mode fibers are generally able to transmit >90% of the light at an optimized wavelength. In this case, the coupling efficiency ranged from 50% (405 nm) to 65% (638 nm, wavelength for which the coupling was optimized). The maximal power output obtained with two 638 nm lasers together was 165 mW, which corresponds to a power density (area of $\pi \times 15^2$ µm^2) of 23 kW/cm^2. Such power density is sufficient to perform fast imaging with an EMCCD and organic dyes such as Alexa Fluor 647.

3.2.4 Application to localization microscopy

The importance of illumination uniformity depends on the response of several photophysical parameters of the fluorescent molecules to the local light intensity. In order to compare the two illumination modalities, I imaged in localization microscopy the same cell region sequentially with both illumination profiles. The laser power was matched at the exit of both MM and SM fibers to allow for fair comparisons. The cells were fixed and their microtubule cytoskeleton was immunodetected with antibodies conjugated to Alexa Fluor 647, and imaged in a dSTORM buffer. Microtubules can be densely labelled while Alexa Fluor 647 is bright and blinks multiple times, allowing for long experiments. I imaged first the microtubules with the MM illumination, as the uniform intensity profile ensures an equal depletion throughout the field of view, then with the SM epi-fluorescence mode. Another MM illumination was finally performed to confirm the results of the first multi-mode experiment. Each experiment ran for 40000 frames, yielding enough localization events ($\sim 10^6$ ungrouped localizations) to draw statistically significant results. The analysis was carried out on a custom made Matlab software, including: detection of the blinking events, fitting of the localizations, filtering of spurious localizations and rendering of the image. Several parameters can be investigated to compare the two illumination schemes. The first one I examined is an estimation of the blinking rate: the frame on-time, which is the number of consecutive frames a molecule appears. To identify the molecules across frames, the localizations are grouped according to a spatial (50 nm) and temporal (consecutive frames) cluster. A molecule that spends a substantial amount of time in its bright state will appear in multiple frames, while the exposure time of the camera is usually set in order to have the molecules appearing in average in 1.5 frames only. In figure 3.3-a, the superresolved image of the region of interest is shown for SM illumination. The localizations are colour-coded according to the median of the on-time in their neighbourhood (defined by a 50 nm square). The intensity profile in figure 3.2-b1 nicely translates into the spatial distribution of the on-time (figure 3.3-a). The periphery of the field-of-view, where the intensity is low, contains slow blinking localizations (more than 6 consecutive frames), while the peak intensity region in the centre is composed of fast blinking molecules (<2 consecutive frames). The region of homogeneous on-time in this image is about half the size of the field-of-view, with a 6-fold increase in on-time throughout the illuminated area. In the case of the MM illumination, the same analysis leads to the image displayed in figure 3.3-b. Because the intensity profile has a very sharp boundary, the illuminated area is well defined. Here, the on-time is uniform across the field-of-view, spanning an effective area twice the size of the one obtained with SM illumination.

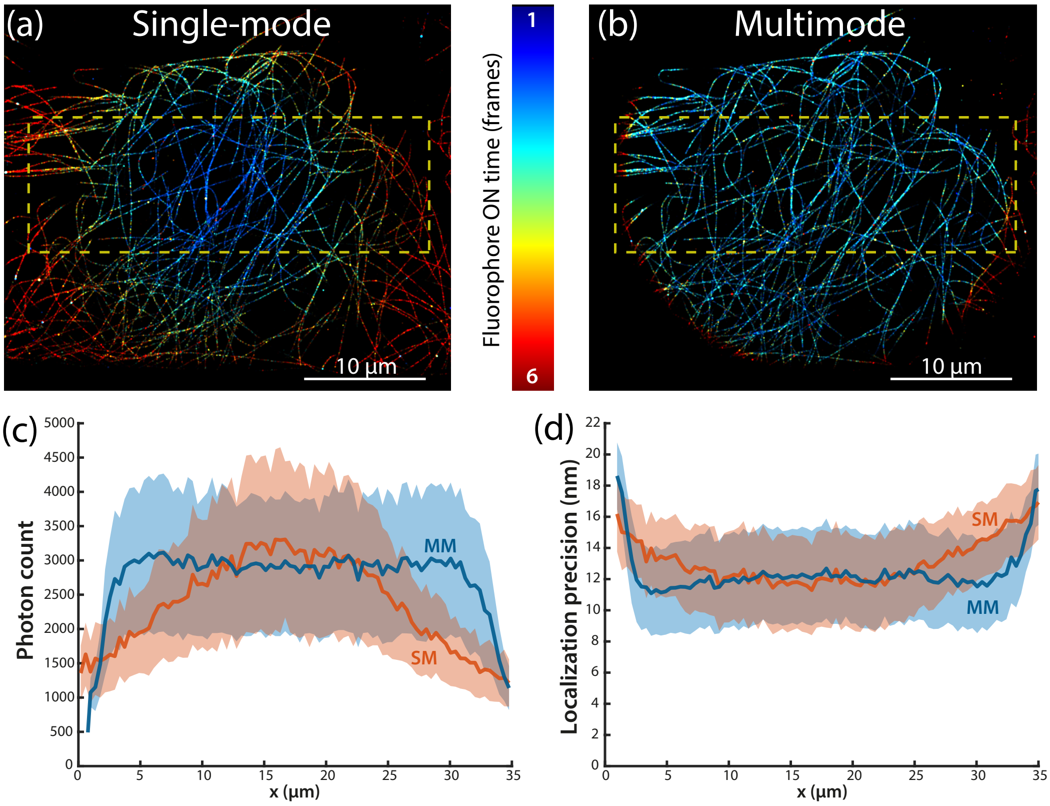

FIGURE 3.3: **Effect of the illumination on the molecules photophysics**. **a)** Super-resolved image of the microtubule cytoskeleton in a U2OS cell, immunodetected with Alexa Fluor 647 conjugated anti-tubulin antibodies, and imaged with the SM illumination. The localizations are colour-coded according to the median of the localization on-times in their 50 nm neighbourhood. The colour-coding ranges from a on-time of 1 to 6. **b)** Same as a), albeit using the MM illumination. **c)** The mean photon count along the x-direction in the yellow box drawn in a) and b), averaged over the y-direction, for both illumination systems. The standard deviation is illustrated as a transparent surface. **d)** Same as c) for the localization precision. Reprinted with permission from Deschamps et al., 2016, Optics Express, manuscript of which I am first author.

Another quantity to consider is obtained directly from the fitting algorithm: the brightness of the localization events. A slow blinking distributes the total number of photons over several frames, and a lower number of photons reduces the probability to be detected as well as the localization precision. The mean photon counts across the field of view of the previous images, averaged over the thickness of the boxes drawn on figure 3.3-a and 3-b, are compared in figure 3.3-c. The spatial dependency of the brightness follows once again the intensity profiles of figure 3.2-b. Localizations in the periphery of the SM illuminated area have half the photon count of the localizations located in the centre. This drop in brightness is not observed with the MM illumination. Since brightness is one of the major contributions to the localization precision, the same tendency is observed in this case (figure 3.3-d).

The localization precision value increases from the centre to the outermost region by about 20% with SM illumination. It remains roughly constant with uniform illumination.

Such analyses clearly highlight the effect of the local light intensity on photophysical parameters. In particular, the blinking rate and the photon count are heavily impacted by uneven illumination. Quantitative approaches in localization microscopy rely on the measurement of such parameters and can be biased by the discrepancy between sub-regions. For instance, counting analyses are very sensitive to the number of frames molecules appear in. In such measurement, the SM illumination would lead to different results in the outermost region than in the centre of the field of view. Clustering measurements also depend on the localization precision and larger clusters might be measured in the periphery of the SM illumination. The highly homogeneous illumination presented here is not subjected to such bias. This system is therefore a necessary addition to any microscope dedicated to quantitative localization microscopy. One major drawback, however, is that TIR illumination is not possible with the current MM illumination path only.

3.2.5 Optical sectioning with homogeneous excitation

The optical system I built consists of two different arms: a homogeneous illumination using a multi-mode fiber and an epi-fluorescence/TIR illumination path. Since the two systems coexist, they can be used simultaneously by inserting a dichroic mirror at the intersection and using light of different wavelengths. I reasoned that activating in TIR could be sufficient to obtain axial sectioning of fluorescent molecules with low self-activation rates. This is the case for photoactivatable proteins such as EosFP variants, e.g. the dimeric tdEOS (Wiedenmann et al., 2004) or the monomeric mEos3.2 (Zhang et al., 2012), as opposed to most organic dyes. The low self-activation rate ensures that the molecules fluorescence will be observed as a result of the activation light only. Therefore, exciting the molecules with the MM path (561 nm) should give the benefits of homogeneous illumination (uniform photophysics across the field of view) while activating (UV) with the SM illumination in TIR should lead to optical sectioning. The feasibility of confined activation was previously exploited with a light-sheet illumination in York et al., 2011.

To test this scheme, I imaged two different mammalian cell samples: clathrin light-chain fused with mEos3.2 (Huang et al., 2013) and an actin-binding peptide (LifeAct, Riedl et al., 2008) fused to tdEOS. Both samples were imaged in D_20 buffer (Ong et al., 2015). The experiments compared [MM activation; MM excitation] with [TIR activation; MM excitation] on the same region of interest. Once again, the MM activation was carried out before the TIR activation, as to not introduce bias due to the uneven activation of TIR. I switched from MM activation to SM-TIR activation halfway through depletion to obtain a comparable density of fluorescent molecules. Figure 3.4-a is a superresolved image obtained by overlaying the result of the MM and the SM activation experiments. Several clathrin-coated pits are present with the characteristic ring-like projection of the invaginations. The two experiments, MM excitation with either MM or SM-TIR activation, are colour-coded in red and cyan respectively. A magnified image of the boxed region of figure 3.4-a is shown in figure 3.4-b1. The signal from each pit colocalizes well between the two colours, sometimes completing each other. Figure 3.4-b2 and 3.4-b3 are the single colour images from the same sub-region. It becomes clear by comparing the two single-colour images that the clathrin-coated pits of the lower side of the plasma membrane are present in both images (stars), while the sites belonging to the upper membrane are only seen in the MM activated image (arrows). This observation confirms the prediction that SM-TIR activation alone can lead to optical sectioning. Some localizations are present in sites of the upper membrane with TIR activation. These residual events are the consequence of self-activation and are unavoidable. However, these localizations do not hamper any analysis of the region of interest due to their negligible weight in the image.

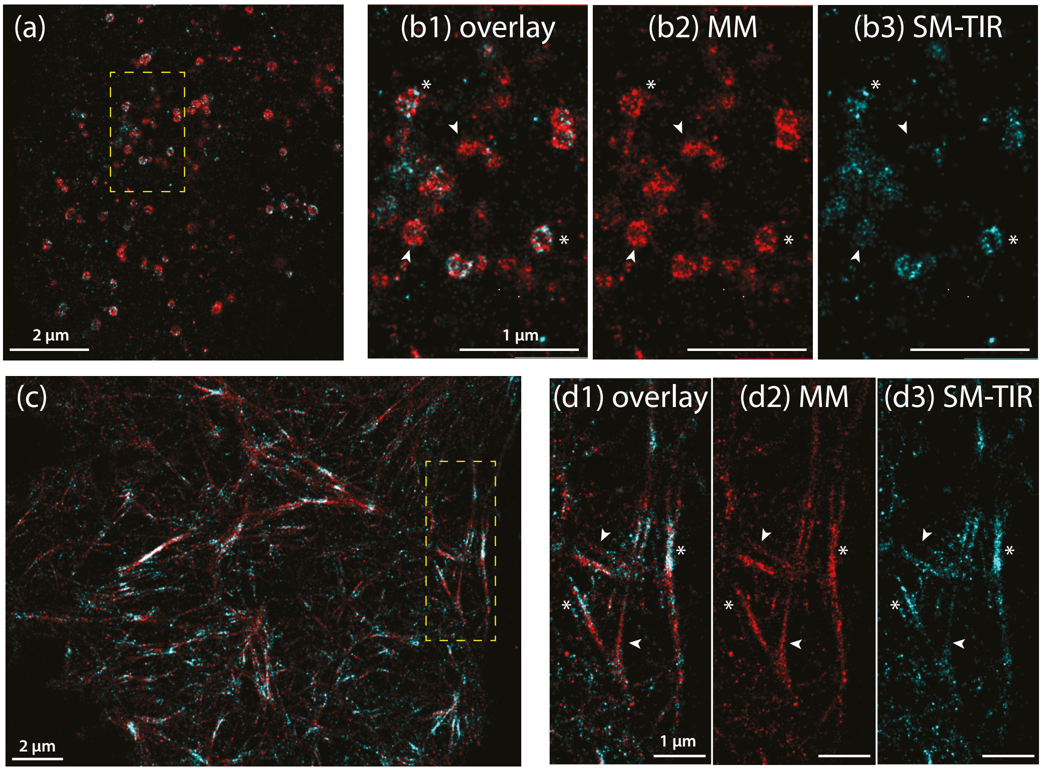

FIGURE 3.4: **Recovering TIR capabilities with homogeneous excitation**. **a)** Super-resolved image of a U2OS cell expressing clathrin light chain fused with mEos3.2. The image is the superposition of the localization collected with the SM-TIR activation (cyan) and the MM activation (red). In both cases, the excitation was carried out with MM illumination. **b)** Magnified image of the sub-region highlighted by the yellow box in a), for the overlay of the two activation modalities (b1), the MM activation alone (b2) or the SM-TIR activation (b3). Arrows indicate features that are observed only with the MM activation, while the stars denote features appearing with both activation. **c)** Same as in a), albeit with U2OS cells expressing LifeAct fused to tdEOS. d) Same as in b). Reprinted with permission from Deschamps et al., 2016, Optics Express, manuscript of which I am first author.

I repeated this experimental result by carrying out a similar study with the actin cytoskeleton. Figure 3.4-c shows an overview of an actin region in two-colour, once again with the MM activation in red and the SM-TIR in cyan. The two colours colocalize strongly in patches of actin close to the coverslip. Signal collected with MM activation appears in between the patches, indicating fibers away from the TIR range. The MM activated image gives a more complete picture of the cytoskeleton, while the SM-TIR is limited to the vicinity of the coverslip. Magnified images (figure 3.4-d) confirm the analysis by examining a small sub-region. The patchy zones of the SM-TIR activated image can also be seen in the MM activated one (stars), which is not the case for the signal located further away from the coverslip and therefore only seen using MM activation (arrows).

The comparisons of biological structures imaged with either MM or SM-TIR activation showed strong evidence that TIR activation is sufficient to realize optical sectioning. This was achieved with two different samples, clathrin-coated pits and actin. Exciting the molecules with the MM illumination scheme has the advantage that a uniform intensity is delivered across the field of view, and consequently leads to a homogeneous photophysical behaviour over the entire illuminated area. In addition, all the light intensity is used for excitation, as opposed to the need for a restricted area in the case of SM excitation.

Furthermore, TIR excitation exhibits an exponential decay in the axial direction. Such intensity decrease implies that the low light levels at the periphery of the evanescent field will prevent the bleaching of fluorophores, resulting in a strong background haze. Using MM excitation, bleaching occurs at the same rate, regardless of the axial and lateral position of the molecules. While the MM path presented in the previous section cannot yield optical sectioning, coupling it with activation in TIR using the SM path recovers the sectioning capabilities of TIR. It should be noted, however, that such a scheme is only applicable to fluorescent molecules that have a low self-activation rate.

3.3 Discussion

Since localization microscopy provides direct access to the single molecules composing the sample, quantitative studies can in principle extract precious information about the stoichiometry and nanoscale organization of protein complexes. A large number of tools has been developed to count molecules, decipher the organization of structures smaller than hundred nanometers or analyse cluster sizes. All these methods ultimately rely on the photophysical behaviour of the molecules during the experiments. As was shown here, the illumination scheme widely used in localization microscopy leads to position-dependent photophysical behaviours across the field of view, which needs to be taken into account in any quantitative analysis.

New homogeneous illumination system In this section, I detailed a new illumination scheme that achieves a highly homogeneous illumination across the field of view. The main components are a multi-mode fiber and a commercial mode-scrambler. The output profile of multi-mode fibers is largely dependent on the spatial arrangement of the fiber itself, and bending the fiber can help maximize its homogeneity. However, the interference between the different modes causes the apparition of granular pattern called speckles. The speckle pattern is very sensitive to movements of the fiber or changes in the light input profile. Therefore, it can be averaged out over the time of an exposure by inducing fast fluctuations. I used a speckle-reducer composed of diffusers, bound to a polymer membrane and oscillating at 300 Hz, to scramble the light before the fiber input. As a result, the speckle pattern fluctuates much faster than the time it takes the camera to record an image (>5 ms). Effectively, the averaged intensity is then uniform across the illuminated area. An additional novelty of this system is that the MM fiber output is imaged directly into the sample. This has several advantages: sharp boundaries of the illuminated area, use of all the available light in the field of view and no risk of damage to the objective. I have shown that this system is superior to the common illumination scheme by analysing the profile of the intensity in the sample. I analysed as well as the distribution of several important photophysical parameters: on-times, photon counts and localization precision. In each cases, my illumination system displays a far better homogeneity than the other one. However, this new illumination scheme does not allow for optical sectioning. To overcome this limitation, I implemented the MM illumination system in parallel to the common TIR optical path. The two systems are not optically exclusive and a dichroic mirror can be placed at the intersection of the two paths. I exploited this possibility and carried-out, to the best of my knowledge, the first experiments achieving homogeneous photophysics and optical sectioning. This was achieved by using in parallel MM excitation and SM-TIR activation. The homogeneous illumination system is composed of inexpensive optical components and can easily be implemented on commercial and custom-built microscopes. Nonetheless, it suffers from a moderate coupling efficiency caused by the divergence increase at the speckle reducer. This limits the output intensity to about 65% of the input (a value similar to a single-mode fiber). One way around this is to use higher laser power sources, such as cheap high power laser diodes ($\sim$ 1 W for 100 euros). I am currently investigating the possibility to add them to the current scheme. In addition, the speckle reducer has a limited lifetime if used too frequently. Here, the illumination system has been used in high-throughput studies (see Chapter 4), which led to a change of the speckle-reducing component every six months. Yet, it should be noted that in such study the microscope ran continuously for extended periods of time (days, nights and weekends). Finally, the imaging speed is limited to 5-10 ms by the speckle reducer.

Other approaches During the writing process and after publication of our article (Deschamps et al., 2016), several related studies have been published. Georgiades and colleagues (Georgiades et al., 2016) used the same speckle-reducer, albeit without a multi-mode fiber. Their illumination displays an improved homogeneity of the common Gaussian profile, reducing small-scale intensity variations. Nonetheless, it suffers from the drawbacks related to Gaussian illumination, in terms of overall uniformity and its consequences for quantitative analyses. A similar work, aimed at describing a simple and cheap microscope, made use of a rotating diffuser for the same effect (Ma et al., 2017a). Kwakwa and co-workers (Kwakwa et al., 2016) presented a low-cost TIR illumination scheme comprising cheap, yet powerful, laser diodes and multi-mode fibers. The use of cost-efficient laser sources is facilitated by the multi-mode fiber. The speckle pattern was reduced by vibrating the fiber, and since the image of the multi-mode fiber output was formed in the BFP, it achieved relative homogeneity (see supplementary figure 2, Kwakwa et al., 2016). The laser light cannot be focused as tightly with a multi-mode fiber as with a single-mode fiber. Consequently obtaining TIR illumination requires shifting the multi-mode output image to the very boundary of the BFP. A substantial portion of the light is then sacrificed, as it is not transmitted to the sample. Zhao and co-workers (Zhao et al., 2017) used a custom-made multi-mode fiber combiner coiled around a vibration motor to deliver a highly homogeneous illumination over the entire chip of a sCMOS camera. Since sCMOS are capable of much faster frame rate than EMCCD, they used Alexa Fluor 647 dye combined with high laser power to reach 0.5 ms exposure time. In their study, the output of the fiber was also focused in the sample. An earlier study achieved homogeneous illumination with sCMOS using a different approach (Douglass et al., 2016). Douglass and colleagues exploited a rotating diffuser and two consecutive microlens arrays. While this system requires more expert alignment, a software was provided to guide the user. Such a system has already been used for biological studies (Vancevska et al., 2017). Expanding the illuminated area mapped on the camera chip can increase the throughput of localization microscopy, at the cost of the mean laser intensity. The laser power can be increased to compensate for this loss. However, cheap laser diode sources are not widely used, while commercial lasers designed for microscopy and able to deliver 1 to 2 W laser power come at a high cost. In this respect, Douglass and colleagues imaged a $100 \times 100\ \mu\text{m}^2$ region using 1 W laser power ($10\ \text{kW/cm}^2$), while Zhao and co-workers delivered 1.5 W on an area of $200 \times 200\ \mu\text{m}^2$ ($3.75\ \text{kW/cm}^2$). The power density in both cases is much lower than what I obtained with a small field of view and maximum power ($23\ \text{kW/cm}^2$). Obtaining comparable power density would require more than 2 W laser intensity in the case of a rectangular illumination area of $100 \times 100\ \mu\text{m}^2$. Such density is not required for every experiment, but should be available in order to not be limiting. A drawback of using very high laser power, is the strong objective autofluorescence that can arise. In turns, this autofluorescence increases background and degrades the final image. In addition, Zhao and colleagues used a water-dipping objective with low NA (1.2) in order to image a large field of view. The use of low NA objective leads to a lower localization precision than the one obtained with high NA. In all cases, a compromise must be found between illuminated area and total delivered power. Finally, another interesting approach employed a waveguide to create a half-millimetre wide TIR-illuminated area (Diekmann et al., 2016). For the moment, this method is limited in its localization precision by the use of a water objective, an illumination degraded by speckles and detection from the non-illuminated side of the cells.

In conclusion, quantitative approaches in localization microscopy are limited by the uneven intensity profile resulting from the widely used Gaussian illumination. Here, I presented a new illumination scheme capable of achieving high uniformity of the laser intensity across the field-of-view. This system is easy to build and based on inexpensive optical components. In particular, its homogeneous profile overcomes the limitation pertaining to illumination-induced bias in quantitative studies. Current efforts in the lab are focused on improving the coupling efficiency by substituting the speckle reducer by a vibrating motor and using cheap, yet powerful, laser diodes. Nevertheless, homogeneous illumination systems are an important step in the development of the next generation of localization microscopes, and should in the near future be a standard feature of any custom-built or commercial instrument.

4 | High-throughput superresolution microscopy

4.1 Introduction

Technological developments have deeply impacted the field of light microscopy. Computer control, fast cameras, ever-increasing computational power and storage capacity have led scientists to produce an unprecedented amount of data. Automated microscopy is a promising direction of further developments, as it avoids the tedious and repetitive tasks of setting-up similar experiments in a row. Advances in automation are not limited to the experimental procedure alone, but also encompass sorting, analysing and storing the accumulated data (Pepperkok and Ellenberg, 2006; Wollman and Stuurman, 2007). Carrying-out experiments automatically generates large volumes of data and bottlenecks in image analysis and data transfer are rapidly reached. By recording a large number of experiments, high-throughput microscopy presents numerous advantages. For instance, by sampling the biological variability, better models can be built. The statistical power of large-scale imaging can determine if an observation is significant or analyse a vast number of experimental conditions at once. Likewise, capturing rare events is facilitated by the shear number of recorded experiments. Particularly, feedback between the microscope and an image-based algorithm helps speeding-up imaging by limiting acquisitions to regions displaying the features of interest. Finally, removing manual intervention dramatically improves the amount of data acquired and analysed per user hour. Hindrances to successful high-throughput applications are found at every step of the process: samples need to be stable over long times, flexible experimental design must be available, precise analyses and sorting of the data must be applied to prevent the accumulation of worthless statistics, and so forth.

The need for automation in localization microscopy As opposed to wide-field, localization microscopy requires thousands of images to create one final reconstruction. Consequently, experiments can range from fifteen minutes to several hours. Efforts to increase the acquisition speed have prompted the use of faster cameras (sCMOS) and high laser power, obtaining rapid imaging (Huang et al., 2013). However, such experimental conditions are not applicable to most fluorescent labels.

Automation of localization microscopy experiments is therefore an attractive way to increase the effective throughput. Beyond the improved data acquisition speed, the accumulation of a larger number of experiments is particularly relevant to SMLM. Since stochasticity plays a central role in the method, a single image often does not contain enough information to infer structural organizations. At the scale of tens of nanometers, labelling efficiency, misfolding of the fluorescent molecules, biological variability and photophysical processes give rise to random samplings of the real structure. As a consequence, structural studies cannot be performed on the basis of a few images, especially when combined with particle averaging.

Studying clathrin-mediated endocytosis in yeast One of the main systems studied in our group is clathrin-mediated endocytosis (CME) in yeast. CME is an essential cellular mechanism for the uptake of molecules at the membrane and subsequent signalling. It involves more than 50 proteins in yeast and occurs at a scale smaller than the diffraction limit. Since the structural organization of CME is not known and macromolecular machines are inherently stochastic, a large number of proteins must be imaged in order to infer its spatial arrangement. High resolution imaging of a CME site requires to maximize the labelling efficiency, prompting the use of fused fluorescent proteins. Since the endocytic process occurs at a time-scale too fast for live-cell localization microscopy, fixation is required. A typical field of view ($30 \times 30\ \mu m^2$) can contain up to 30 cells. However, the large curvature of yeast cells means that only very few sites are visible per cell. Depending on the specific protein abundance, the result of one experiment can consist of a single CME site in focus. Additionally, CME is a highly dynamic process. A consequence of its rapid execution is that the various sites are imaged at different stages of endocytosis and are thus in distinct spatial arrangements. In order to sample al the time points equally and to draw an accurate picture of the CME organization by radial averaging, thousands of sites need to be collected for each protein. Gathering such a large amount of data would require hundreds of experiments per protein, performed in the same conditions, far beyond the capacity of a single experimenter. To nevertheless gather such large sample, we decided to develop high-throughput imaging for localization microscopy. Unsupervised imaging and automated analyses reduce the user time per experiment, enable collection of an abundant number of experiments, ensure equal imaging conditions if properly controlled and allow studies at a much larger scale.

Automating localization microscopy While many aspects of automation can be directly transferred from wide-field microscopy or confocal imaging, some peculiarities of localization microscopy require specific attention. The success of a SMLM experiment relies particularly on the choice of labels, the fixation protocol and the buffer. The blinking conditions of the fluorescent molecules must be stable enough to perform equally throughout the many experiments. This is for instance difficult to achieve for more than two hours with dSTORM buffers. Additionally, localization microscopy is very sensitive to drift at the tens of nanometers scale. The microscope must then be optimized for minimal drift and incorporate focus stabilization. Flexible imaging is achieved with microscopes that grant access to all their devices and a computer program allowing the user to design different types of experiments. One specificity of localization microscopy is the use of an activation laser (often in the UV range). The activation laser power must be gradually increased throughout the experiment in order to maintain a sufficient emitters density per frame. Its power must then be reset in between every experiments, imposing a particular requirement on the control software. In addition to the localization microscopy experiments, other types of images can bring precious information, such as GFP channel images or z-stacks. Finally, the amount of data expected from high-throughput localization microscopy is such that data analysis must be automated as well, preferentially using GPU-accelerated algorithms to localize the emitters (Smith et al., 2010), and care must be taken to establish compression and storing pipelines.

In this chapter, I describe my work as part of a collaborative effort with Markus Mund, another PhD student, to establish a high-throughput localization microscopy pipeline. The unsupervised acquisitions and semi-automated analysis have permitted the quantitative study of the radial organization of 23 CME-involved proteins in yeast. This work is the subject of Markus Mund's PhD thesis. He established the strains and optimized the sample preparation and imaging conditions. Together, we defined and tested the instrumentation requirements for the project. The microscope was designed by Jonas Ries, and built by Jonas, Markus and me. In particular, the microscope includes the homogeneous illumination I implemented and presented in the previous chapter. I wrote the control interface and the algorithms as a Micro-manager plug-in (Edelstein et al., 2010), in addition to the adapters required to communicate with the various devices. I designed and wrote the electronic system and its firmwares. The sample preparation and imaging was performed by Markus, helped by Jan van der Beek and Jooske Monster, two interns in the lab. The analysis pipeline was established by Jonas and Markus. Finally, I developed a scheme for data compression, sorting and storing. The script for data storage was tested by Markus, and later refined together. Bálint Balázs, another PhD student at EMBL, developed the B^{3}D compression algorithm which I helped optimizing by analysing the effect of the compression on localization microscopy data (Balázs, Deschamps et al., submitted, 2017).

4.2 Results

The acquisition, analysis and storage of microscopy images results in a complex interaction between several distinct units: the microscope, the electronics, the computer, the server and of course the user (see figure 4.1). The user oversees the various processes through interfaces hosted by the computer. The latter communicates with the microscope devices directly, or through the electronics. The electronic layer can fulfil different functions, such as monitoring parameters or triggering devices, independently of the computer. Analyses are carried out within the computer, in most cases the same one used for microscope control, before being stored on a server.

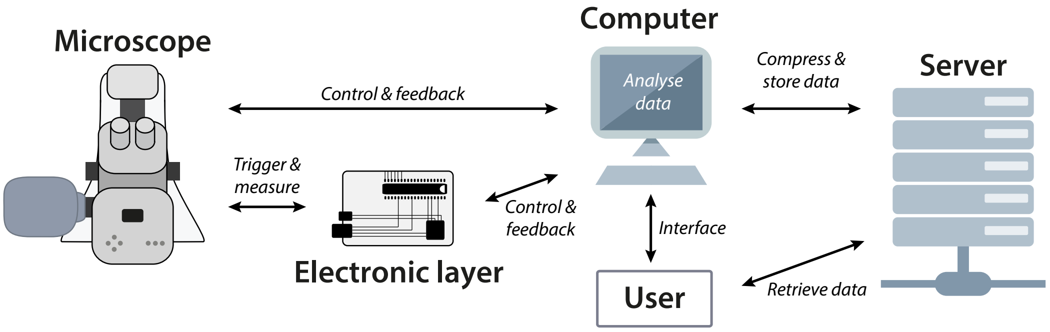

FIGURE 4.1: The different layers of communication and data exchange involved in modern microscopy.

Establishing a high-throughput pipeline in microscopy requires to automate most of the communication and tasks of the different units. The computer must control the microscope without the user involvement beyond the initial configuration. Continuous feedback and synchronization between the microscope, the electronics and the computer help carrying-out the experiments according to a certain design automatically. Because of the humongous amount of generated data, automated compression and storing must often be set-up. Therefore, several complementary layers must be engineered: computer control of the microscope devices and electronics, user interface allowing design and oversight of the measurements, an application capable of carrying-out flexible experimentations and an effective storage pipeline. In the next sections, I will describe my work in building efficient and robust systems for each of these categories. An additional layer required is automated analyses, which are usually tailored to the investigated system. I will only briefly mention what was established in the lab in the case of the study of yeast CME.

4.2.1 Hardware control

Computer control of the microscope devices is the first step towards automation. Motorizing certain aspects, such as filter insertion, increases its flexibility and possibilities to adapt its state to the experimental need. A typical microscope in localization microscopy is rather simple and only few devices need to be computer controlled (see figure 4.2). The most obvious device interfaced with the computer is the camera, which gets triggered, records frames and subsequently streams the images directly to the computer hard drive. The power of the lasers is in most cases regulated through a computer interface as well. While the position of the stages can be adjusted manually through a controller, they can also be set via communication with the computer. Electronic filter wheels are a useful addition to any microscope, allowing for automatic imaging of different channels. Several elements can be coupled to servomotors in order to change their position or trigger their insertion. This is the case for instance for the cylindrical lens for 3D imaging in localization microscopy, the Bertrand lens to image the objective BFP or beam blockers to stop residual laser light. Another example is the TIR lens: lateral movements of the lens permit to switch from epi-fluorescence to TIR illumination and inversely. Communication with electronic devices can also help monitoring certain parameters, as in the case of the widely used focus stabilization in localization microscopy: the signal of the quadrant photo-diode (QPD) is directly translated into focus position. Computer control of device properties and motorized elements enables precise tailoring of the microscope state to the need of the experiments, and thus more flexible experimental design.

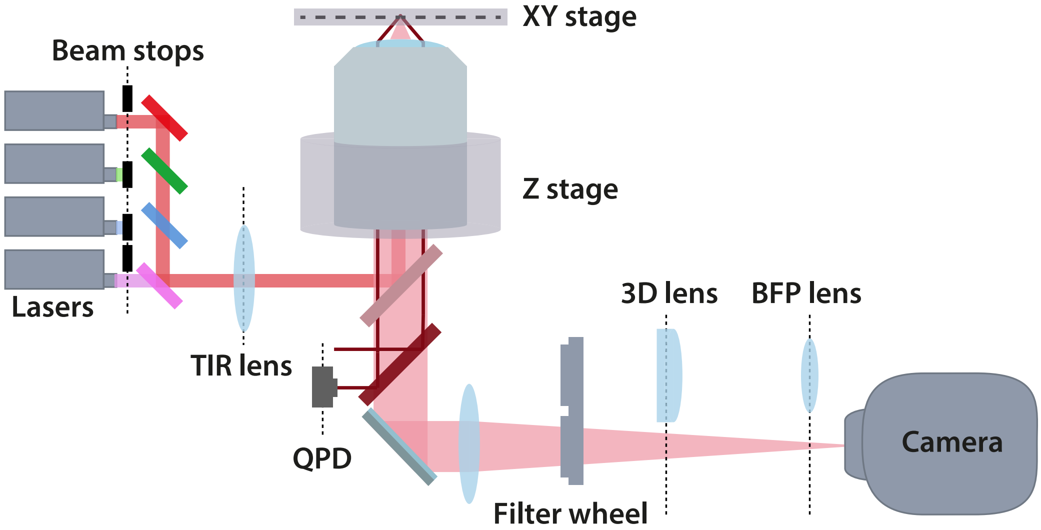

FIGURE 4.2: **Computer controlled elements of a microscope**. Dash lines indicate lateral movements. The device control can take the shape of a simple feedback (QPD signal, stages positions), data streaming (camera) or positioning (lenses, filter wheel, beam stops).

Micro-manager Devices are often shipped with their own user interface, allowing the adjustment of a wide range of properties. This is the case for instance with lasers. However, automation of the microscope requires the devices to be controlled by the same program. Fortunately, communication protocols are usually also delivered by the manufacturers, allowing experienced users to build their own program for device control. Communication usually takes the shape of an exchange of serial commands (RS232 or USB). Several existing software includes ready-made adapters for a large range of devices. Commercial solutions, which are usually expensive, include LabVIEW (National Instruments) or MetaMorph (Molecular Devices). Micro-Manager (µM, Open Imaging) has emerged as a successful open-source alternative (Edelstein et al., 2010). Device adapters for µM are mostly contributed by the community, giving rise to an increasing device support. For the compatible devices, µM is usable right away and does not require any coding skill.

It includes in particular an acquisition engine for multiplexed acquisitions in time, z-stacks, channels and different positions. The images can be streamed directly to the hard-drive or a server. Several plug-ins are present, allowing for stage control or tiling. Furthermore, experienced users can write their own plug-ins or design their own experiments thanks to a scripting panel. In order to have access to the devices on the microscope, I programmed several device adapters for µM, and modified others to exploit the full potential of the corresponding instruments. In particular, I wrote an adapter for the SmarAct HCU-3D stage, that has been included in the µM source-code and is used by several other groups. I also extended existing adapters such as PI GCS (objective stage) to include an option for focus stabilization, the Omicron laser to add safety check preventing crashes and I largely extended the Aladdin syringe pump adapter to make use of a wider range of possibilities (e.g. more than one pump, custom pumping programs, synchronization between pumps). The Omicron and Aladdin device adapters will be submitted for inclusion in µM in the near future, due to their potential usefulness to the community. The Aladdin adapter has already been intensively used by Thomas Chartier, another PhD student, to investigate sensory responses of annelid worms in a microfluidic system.

Electronic layer Another important aspects of microscope control is the electronic layer. Preferentially constituted of a single electronic board, the microscope electronics has several functions. An important task is to update the computer on the evolution of sensors feedback. In localization microscopy, the focus stabilization often makes use of a quadrant photo-diode (QPD). The electronics can monitor the value of the QPD signals and inform the user about the live axial drift correction. Electronic boards can also be used as a bridge between motorized devices, that are not equipped with their own controller, and the computer. This is exploited for example to move optical elements with cost-efficient actuators such as servomotors. Finally, the electronics can carry-out rapid tasks without the intervention of the computer, as in the case of laser triggering. In localization microscopy, care must be taken to not expose unnecessarily the sample to laser light. For that reason, the lasers are often directly triggered by the camera. In this case, the camera sends a digital trigger that is high when the camera records the frame and low when it reads out the pixel values. Additionally, it might be required to pulse the lasers in order to deliver a low and controlled intensity to the sample, in particular in the case of activation laser light. This task cannot be carried out by the computer without the help of an additional electronic device. Data acquisition devices, such as the National Instruments DAQ, are of wide use but come at a high price. Microcontrollers are an affordable and powerful alternative, as they are easy to program and exhibit a sufficiently high number of input and outputs. A prime example is the open-source Arduino board, that benefits from a large community and can be programmed using a simplified high level language. However, microcontrollers are usually based on a single processor unit and are therefore not capable of carrying-out several tasks at once. This becomes a bottleneck when the application requires fast processing of the camera signal to pulse lasers. To a certain extent, an Arduino can perform this task but the temporal resolution will be low (compared to the clock frequency) and will not be able to handle many lasers at the same time.

Micro-Mojo In order to integrate the entire microscope electronic control into a single board, while achieving a high temporal resolution and the capacity to perform complex tasks in parallel, I turned to field-programmable gate arrays (FPGA). FPGA are reprogrammable integrated circuits that can be found in the control unit of many modern devices, such as cameras. Based on an array of logic blocks that can be bridged together, they can implement complex processes without the help of a processor (as opposed to microcontrollers). This allows FPGAs to be extremely fast and able to perform a large amount of tasks independently. They are becoming very popular in microscopy, in particular due to the LabVIEW FPGA module (National Instruments). In spite of its cost of several thousands euros, the LabVIEW module has the advantage that the FPGA can be configured using its LabVIEW visual language. Natively, FPGA are programmed using hardware description language (HDL), which requires solid electronic knowledge and strong programming skills. I turned to an affordable FPGA called the Mojo (Embedded Micro). The Mojo is based on a freely available software (as opposed to LabVIEW) and is programmed using a friendlier HDL language. I developed a program for the Mojo, called Micro-Mojo, aimed at offering the typical inputs and outputs necessary to control movable elements of the microscope, read-out signals and trigger the lasers in a flexible manner. Additionally, the programmed Mojo is made compatible with µM via a device adapter. Micro-Mojo allows complex triggering of several lasers thanks to three parameters: behaviour (follow the camera signal, pulse on rising or falling edge, on or off), pulse length (if pulsing) and a sequence pattern (16 bits, 0 or 1, describing if the laser should be triggered or not during the frame). Although FPGA programming is more challenging than microcontroller programming, Micro-Mojo presents a clear superiority over Arduino in terms of speed and multi-threading. Figure 4.3-a shows a reproducible response time of the laser trigger of about 60 ns to a rising edge of the camera signal. The pulse length resolution was set to 1 µs, artificially increasing the minimum pulse time by a factor 50, as illustrated in figure 4.3-b. In addition, the triggering of the laser is made highly flexible by the possibility to introduce a pattern enabling sequential illumination. Figure 4.3-c is an example of two lasers triggered by Micro-Mojo. The first laser is pulsed (pulse length 100 µs) once every four images (on the falling edge of the signal). The second laser repeats the camera signal, albeit with the following pattern: 0111011101110111 (0 the laser will not be triggered). These figures illustrate the tight and precise control of the FPGA over the laser triggering. In addition to the laser triggering, Micro-Mojo offers various inputs/outputs (see figure 4.4): eight analog input read-outs (e.g. signals from the QPD or various sensors), several TTL outputs (e.g. for flip mirrors or any device that can be turned on and off with a digital signal), PWM signals (coupled with a low pass filter electronic circuit, this can be used to produced an analog signal, e.g. for an acousto-optic modulator) and servo controllers (to move elements on the microscope). Care should be taken to not input voltage larger than 3.3 V. For this purpose, a 5 V to 3 V converter was used for the camera and the sensor signals. The number of each type of output can be set upon compilation or chosen within the arbitrary maximum in µM. The source-code and compiled versions are freely available on github (https://github.com/jdeschamps), together with the µM device adapter. A flexible interface will soon be available as well. Micro-Mojo offers an out-of-the box solution for electronic control of lasers and various devices, at extremely fast speed and parallel processing. The computational capacity of the Mojo FPGA being not fully exploited by Micro-Mojo, the number of inputs/outputs will be increased.

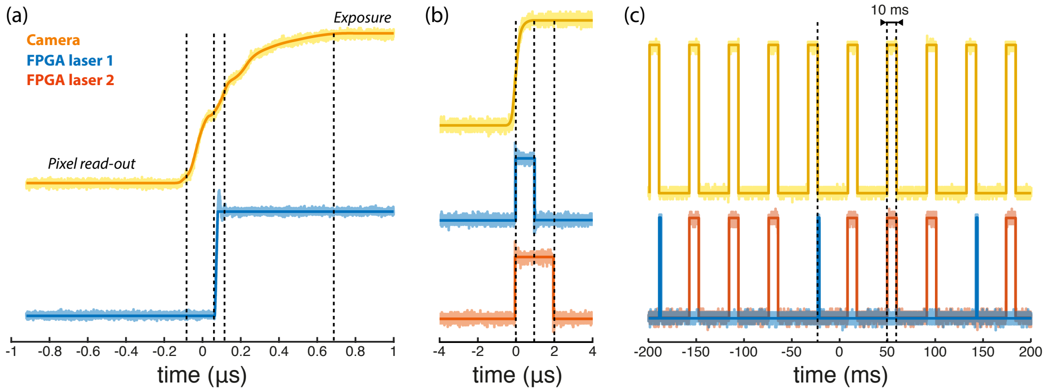

FIGURE 4.3: **Laser triggering with a FPGA**. **a)** Response of the Micro-Mojo laser trigger to the camera signal rising edge. The FPGA signals rises and stabilizes in 60 ns. **b)** The temporal resolution of the Micro-Mojo laser triggering is set on purpose to µs resolution. Example of two lasers triggered at the same time on a rising edge with pulse lengths of 1 and 2 µs. **c)** Sequential triggering of two lasers, one following the camera signal with the pattern 0111011101110111, the second one pulsing with a pulse length of 100 µs on the falling edge following the sequence 1000100010001000.

In conclusion, in order to allow maximum flexibility in the design of experiments, I interfaced many aspects of the microscope with µM. The code is freely available online. I also developed a FPGA program to integrate the entire electronic layer into a single board, called Micro-Mojo. Currently, Micro-Mojo controls essentially the lasers on two microscopes. On the AO-SALM microscope (see chapter 5 and Methods) in particular, Micro-Mojo not only handles the lasers, but also one flip mirror, a filter-wheel, a BFP lens on a servomotor and reads out three analog inputs from the QPD.

4.2.2 User interface

In Micro-manager, the user can interact with the devices through the property browser. The latter lists all the properties that were implemented by the programmer

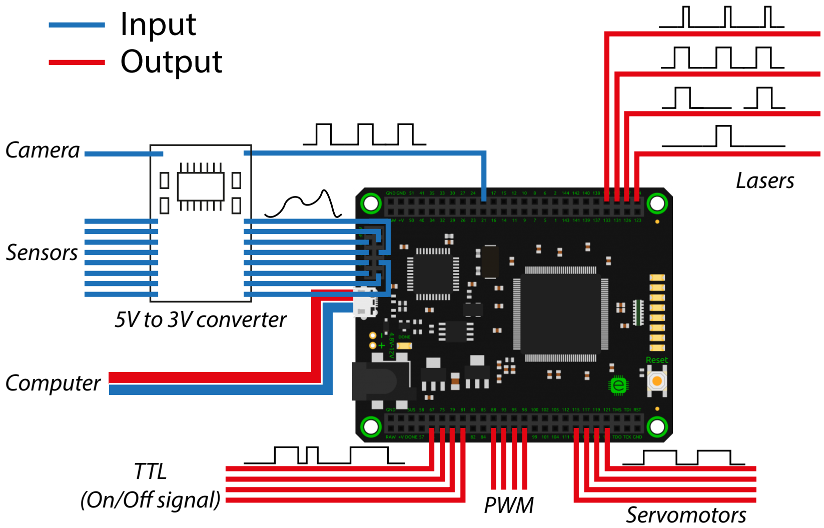

FIGURE 4.4: **Current inputs/outputs present in the Micro-Mojo**. Since the Mojo FPGA runs with 3.3 V, the inputs must be scaled down to the correct voltage using a 5 V to 3 V converter. Communication with the computer allows the user to change parameters regarding the outputs and to retrieve information on the input values. Micro-Mojo currently offers 4-laser triggering, 4 servomotors control, 4 PWM (0% to 100% signal) and 4 TTL signals (On/Off). The Mojo FPGA design was adapted with permission from Embedded Micro, embeddedmicro.com.

of the device adapters used. For instance, lasers often have an on/off and a power percentage property. The property browser is useful to set directly the state of a device, but becomes slow and tedious during repetitive use, in particular with a large number of devices. One way to rapidly change properties, regardless of the number of devices involved, is to define groups of properties with preset values. Switching between the different preset allows for fast switching of the microscope state. The property groups appear in a small list in the µM interface. Using presets is very advantageous for devices used in a limited number of states. One such example is an EMCCD camera, where the user can define presets related to imaging with or without electron-multiplying gain. Because each experiment will be carried-out in either one of these presets, the camera can be configured by the click of one button. Each preset contains several camera properties at specific values that the user need not to set one by one every time. However, in the case of a custom-built microscope with many devices and tunable elements, one cannot define a small number of presets encompassing all the possible microscope states. Ultimately, the user will be required to modify some properties directly in the property browser.

User interface To operate our custom-built microscopes, I implemented a user-friendly interface (UI) as a µM plug-in, which I refer to here as Micro-Interface. Written in Java, the interface is shown in figure 4.5. It is tailored to the type of elements that user must interact with when using the microscope. The UI grants straightforward access to the most commonly modified features of the microscope, such as the UV pulse length (figure 4.5-a), the laser intensities (figure 4.5-b), the filter

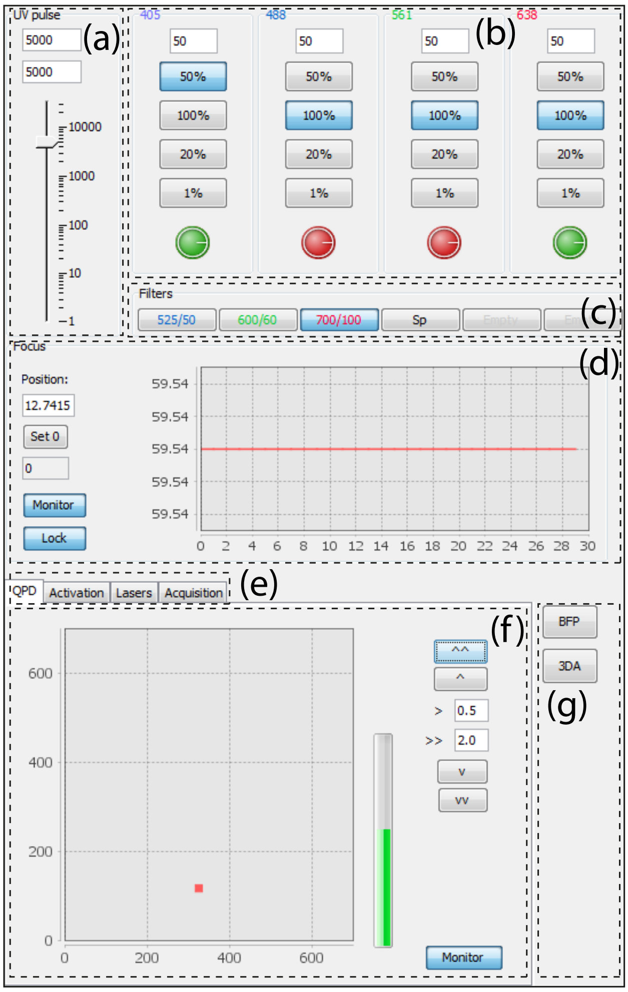

FIGURE 4.5: **Micro-Interface: a UI developed to control the microscope. a)** UV pulse length in µs, the text fields allow to set the value of the pulse and a maximum that automatic UV adjustment cannot cross. **b)** Laser panel. Each laser power percentage and on/off can be set. **c)** Filter wheel panel. **d)** Focus monitoring. The user can track the evolution of the objective stage position and set its value. Locking triggers live focus stabilization thanks to a direct electronic feedback from a QPD (perfect focus system). **e)** Different tabs are available. The activation and acquisition tabs are shown in the next figures. The lasers tab allows the user to change the behaviour, pulse length and sequence pattern of the lasers (see Micro-Mojo). **f)** Focus stabilization monitoring with the X-Y and Sum signals from the QPD. Buttons allow moving the objective stage or the QPD stage depending whether the focus stabilization is on or not. **g)** Lens panel. The BFP and 3D lenses can be inserted into the beam path thanks to servomotors.

wheel (figure 4.5-c), the focus position (figure 4.5-d) and motorized lenses (figure 4.5-g). A tab menu (figure 4.5-e) includes more specialised aspects of the microscope to be monitored or changed. In particular, the focus stabilization and positioning can be tuned in the QPD tab (figure 4.5-f). The lasers tab is not shown here but allows the user to set the laser triggering as desired within the framework of Micro-Mojo. The other tabs are described in the next section.

While interacting with the device properties through the property browser is slow and cumbersome, the UI makes modifications of the microscope state convenient, intuitive and swift. Operating the microscope is thus greatly simplified, whether the user is performing experiments or just exploring the sample. For the moment the devices used by Micro-Interface are set in a configuration file, which requires manual input of the property names. A configuration menu is currently being tested to allow rapid exchange of the device properties name directly within the interface, improving the ease to transfer the interface to another microscope or to exchange devices without programming.

4.2.3 Automatic SMLM acquisitions

Stable focus Several specificities of localization microscopy require a particular attention when automating the imaging. A necessary condition is the stability of the focus over time and space. A SMLM experiment can last hours and any drift on the nanometre scale, especially along the axial direction, will cause a blurring of the reconstructed structure. The focus must also be maintained when moving to different regions of the coverslip. Perfect focus systems (such as PGfocus, Bellve et al., 2014) are therefore a necessity in localization microscopy (details about the focus stabilization in our microscopes can be found in the methods). Figure 4.6 shows two regions of the same coverslips containing fluorescent beads. The two images were taken with focus stabilization and are separated from each other by 2 mm, which represents about 60 regions of interest. The in-focus PSF displayed by the beads in each image attests of the spatial stability of the focus.

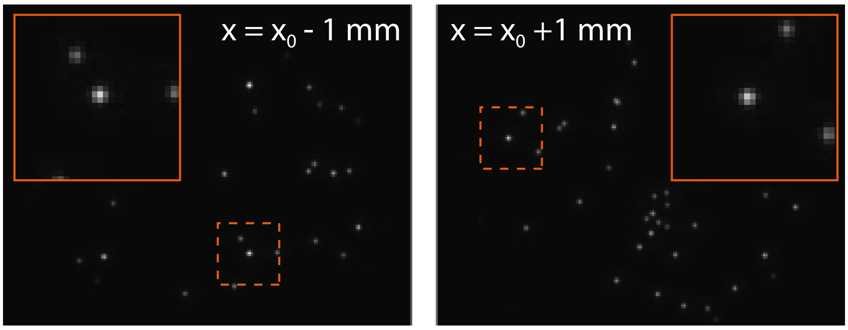

FIGURE 4.6: **Focus stability over a 2 mm distance on the coverslip**. The beads stay in focus without manual intervention. The insets are magnified view of the dashed rectangles. The distance between the two images is larger than 60 field of views.

Automatic adjustment of emitter density An additional requirement for automated localization microscopy is the possibility to adaptively control the density of emitters over the course of each experiment. In most cases, molecular blinking is achieved by illuminating the sample with very low doses of UV laser. Because of the sensitivity of the molecules to the activation, the laser is preferentially pulsed to reduce the total intensity. Pulsing the laser has the advantage of a long dynamic range, as opposed to modulating the laser intensity only. Throughout the experiment, the pool of molecules that can be activated decreases and maintaining a constant density per frames implies increasing the UV pulse length. I implemented an algorithm for automatic and live adjustment of the UV pulse length (see figure 4.7-a). The algorithm extracts two frames from the µM circular buffer. The last frame is used and one imaged 15 frames before. This ensures that the two frames were imaged with the same lasers, as Micro-Mojo is capable of 16 frames long patterned triggering of the lasers. The past frame is subtracted from the most recent one and the resulting image is Gaussian blurred. Then, an efficient and fast non-maximum suppression algorithm (NMS, Neubeck and Van Gool, 2006) is run on the blurred image to estimate the number of local maxima (see figure 4.7-b). A cut-off is applied to discriminate between signal and background local maxima. The cut-off can be fixed by the user, calculated once or computed each time. The calculation of the cut-off is a cumulative moving average of the mean of the Gaussian blurred image, $\Delta\mathrm{Im}_{\mathrm{g}}$, to which the standard deviation, $\sigma_{\Delta\mathrm{Im}_{\mathrm{g}}}$ is added, weighted by a user defined parameter Sd. The output of the NMS algorithm is then the number N of peaks. The new UV pulse, p_{i+1}, is computed according to $p_{i+1} = p_i + a_{\mathrm{UV}} \times (1 - \frac{N}{N_0})$, where p_i is the previous pulse value, N_0 is the number of peaks per frame the user wishes to obtain and a_{UV} is a parameter dictating how fast should the pulse values change. Every user input can be set in the activation tab of Micro-interface (see figure 4.7-c). The 2D graph displays the evolution of the estimated number of emitters per frame. The user can retrieve the last number and set it as the aimed N_0 by pressing the get N button. Since over-activation can render the experiment unusable, the algorithm can be run without updating the UV pulse length (by unchecking the checkbox highlighted in figure 4.7-c). This allows the user to tune the parameters such as the cut-off, the averaging window size dT and the a_{Sd} coefficient. In particular, the result of the NMS (see figure 4.7-b) can be displayed by checking the NMS checkbox. Once the user is satisfied with the result of the NMS, the activation algorithm can be set to modify the UV pulse length. This algorithm is in daily use on the microscope, with various sample such as dim fluorescent proteins and bright organic dyes. The robustness of the algorithm is exemplified by the fact that in most cases the parameters do not need to be changed between experiments with similar sample as well as in between different experiments. In the case where tailored parameters must be used, the assessment of the parameter values is effortless.

µM acquisitions With stable focus and automatic adjustment of the emitter density, the only requirement left is to be able to design and perform the various experiments in a flexible manner. The user interface of µM includes a tool for designing experiments to be carried out, the so-called multi-dimensional acquisition (MDA). This powerful interface allows the user to select different experiments to be performed in a multiplexed manner. However, the fixed framework of the MDA does not allow for different types of experiments to be carried-out one after the

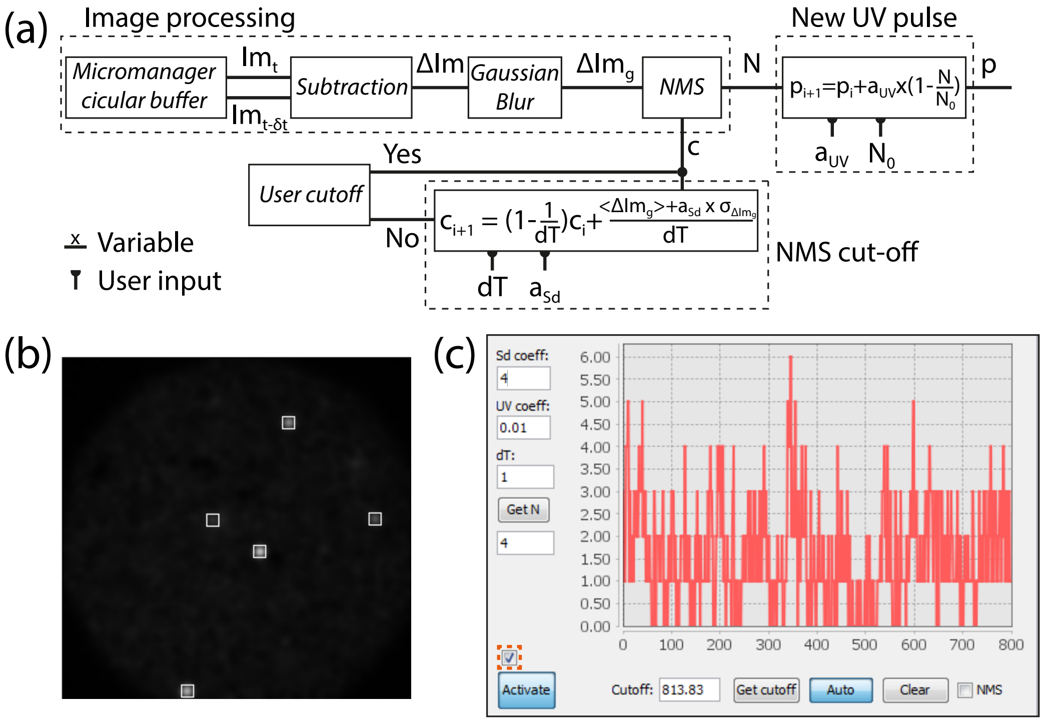

Sd coeff: 4

UV coeff: 0.01

dT: 1

4

☑

Cutoff: 813.83

☐ NMS

FIGURE 4.7: **Activation automation. a)** Algorithm for automatic activation of the emitters in order to maintain a constant number of localizations per frame. The process tunes the pulse length of the UV laser depending on the density of emitters per frame. Two images are extracted from µM circular buffer, then subtracted and Gaussian blurred. A non-maximum suppression (NMS) algorithm runs for fast detection of the number of emitters on the frame. NMS requires a threshold that can either be fixed by the user or calculated according to a cumulative moving average. The threshold calculation has two inputs: the averaging length in frames and a parameter for the weight of the Gaussian blurred image standard deviation. The NMS algorithm returns a number of emitters found in the Gaussian blurred image. The new pulse is calculated according to two parameters, the expected number of emitters N_0 and a coefficient UV dictating how fast should the pulse increase or decrease. **b)** Example of a NMS detection on the Gaussian blurred image. **c)** Activation tab from figure 4.5-5. The parameters can be set on the left (Sd, UV, dT and N_0). The get N button replaces N_0 by the last measured N. The NMS cut-off can also be set by the user at the bottom of the tab, calculated once (with the get cut-off button) or automatically updated. The NMS checkbox allows the user to visualize the results of the NMS runs, allowing for tuning of the different parameters. The algorithm runs when the activate button is toggled, but the UV pulse is only changed when the checkbox above the button is selected (highlighted checkbox). This allows the user to monitor the algorithm without any effect on the sample. Finally, the 2D plots shows the evolution of the measured number of emitters.

other. Additionally, resetting the automatic UV adjustment algorithm is a complex task when both the algorithm and the acquisition are run by different processes. To allow more flexibility, µM gives access to its acquisition engine either via the scripting interface or the implementation of a plug-in. Many groups resolve to built complex scripts to abide their experimental need. This permits tailored acquisitions, easily controlled and reproducible. However, modifying the experiment requires profound knowledge of the script and of the scripting language.

Unsupervised acquisition tool I integrated in Micro-Interface a tab that exploits the µM acquisition engine to perform localization microscopy experiments in an unsupervised manner. The user must use the µM position list to define a set of positions. Then, a set of experiments can be designed from within the acquisition tab of Micro-Interface. Figure 4.8-a shows the unsupervised acquisitions pipeline. Experiments in the list are performed sequentially at every position. Once the stage has moved to one position, the various devices are set according to the experiment parameters. This includes the lasers, the filter wheel, the motorized lenses and the camera. Three types of experiments are currently used: time, BFP and z experiments. Time experiments can be used to take a snapshot or to perform localization microscopy acquisitions. In particular, the activation algorithm can be set to run during the time experiment and is reset when it ends, which avoids compromising the next experiment. A useful feature available is the interruption of the experiment when the UV pulse length reaches a maximum set by the user. When one experiment ends, the microscope devices are prepared for the next one. Once all the experiments have been carried out at a certain position, the stage is moved again. Figure 4.8-b shows the acquisition tab of figure 4.5-e. The user can either perform the same experiment on all positions without change in the microscope states or define a more complex set of experiments by checking the advanced acquisition checkbox and clicking on configure (highlighted box, figure 4.8-b). A new window appears (figure 4.8-c), where the user can add experiments, define their type (time, BFP image or z-stack) and choose the microscope state (filters, laser triggering with Micro-Mojo, exposure time, number of frames, 3D lens on and automatic activation).

Altogether, the stable focus, the automatic adjustment of the UV pulse length and the advanced acquisition feature are capable of performing localization microscopy experiments and complementary acquisitions over the course of days in a totally unsupervised manner, accumulating several hundreds regions of interest. Besides SMLM, the z-stack experiments can be used to segment the cells outline, and the BFP experiments serve as quality control (e.g. presence of bubbles in the oil). Having a user interface simplifies the setting up of experiments, as opposed to scripts. In addition, the user has the possibility to save and load the experimental design, saving time when running an established pipeline. Finally, the object-oriented paradigm applied by Java allows for easy extension of the advanced acquisition features.

4.2.4 Data storage

Localization microscopy generates a large amount of raw data, which can be greater than 180 GB/h, due to the many frames required to reconstruct one image. Unsupervised acquisitions of many regions of interest is bound to rapidly fill the physical memory of any computer. Therefore, the data is often streamed or transferred to a server with much larger capacity than a single computer. In addition to the accessibility of the server beyond one computer, this can allow backing-up of the

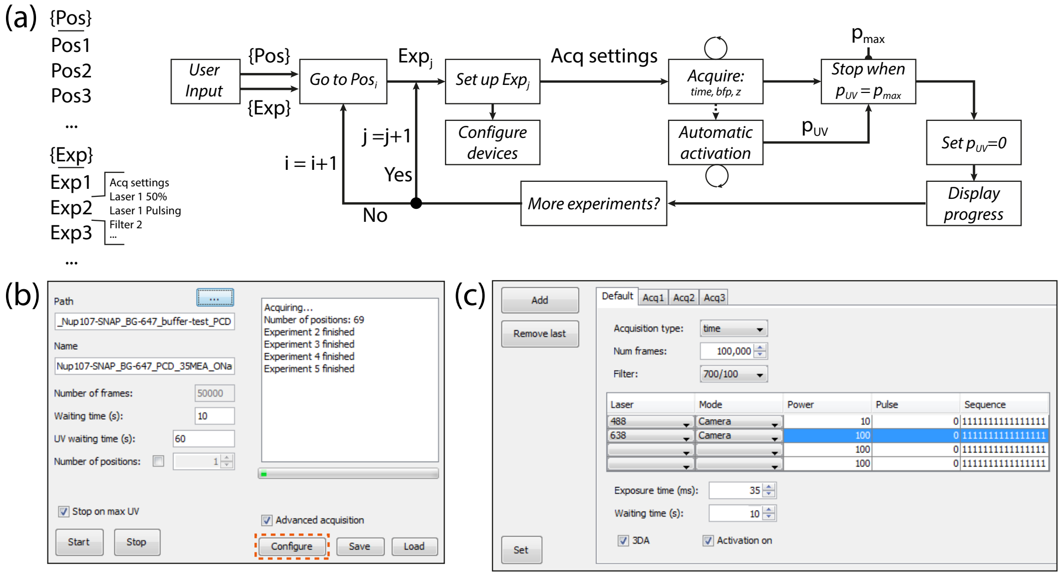

Path: _Nup107-SNAP_BG-647_buffer-test_PCD

Name: Nup107-SNAP_BG-647_PCD_35MEA_ONa

Number of frames: 50000

Waiting time (s): 10

UV waiting time (s): 60

Number of positions: ☐ 1

☑ Stop on max UV

Acquiring...
Number of positions: 69
Experiment 2 finished
Experiment 3 finished
Experiment 4 finished
Experiment 5 finished

☑ Advanced acquisition

Acquisition type: time

Num frames: 100,000

Filter: 700/100

Laser	Mode	Power	Pulse	Sequence
488	Camera	10	0	1111111111111111
638	Camera	100	0	1111111111111111
		100	0	1111111111111111
		100	0	1111111111111111

Exposure time (ms): 35

Waiting time (s): 10

☑ 3DA ☑ Activation on

FIGURE 4.8: **Unsupervised acquisitions pipeline**. **a)** Pipeline for unsupervised acquisitions. The users design a set of experiments to be carried-out (via the interface) and a set of positions (through µM position lists). One experiment is defined as a list of properties including the value of the devices parameters and the acquisition settings. At each position, the experiments are performed one after the other. Before every experiment, the state of the microscope is configured according to the list of properties. In the case of time experiments requiring automatic UV pulse adjustment, the user can set a maximum for the UV pulse length. When the maximum is reached, the experiment is stopped. The automatic UV adjustment is reset and the next experiment is carried out. **b)** Acquisition tab. The user can set the path to the experiment on the hard drive and its name. A waiting time is possible to give time to the sample to equilibrate after a movement of the stage. "Stop on max" UV enables the interruption of the experiments when the UV pulse length reaches a maximum. UV waiting time indicates the time the experiment spends at the maximum UV pulse (when applicable). While time experiments at many positions without changes in the microscope device can be carried-out, the user can also design more complex experimental procedures by ticking the "advanced acquisition" checkbox and click on configure. **c)** Advanced acquisition window that opens when the user presses the "configure" button in b). The user can add or remove experiments to the tab list. Each experiment will be performed in the order of the tabs. In each experiment tab, the user can configure 4.the type of experiment (time, BFP or z-stack), some parameters related to the experiment (e.g. the number of frames in a time experiment), the states of the lasers, the exposure time, the filter wheel position, whether the 3D lens should be inserted and if the activation should be adjusted automatically.

data as part of the service. However, server space is expensive and often limited. Compression can decrease sizes without loss of information up to a certain point. While the gain of lossless compression is marginal for the localization tables, it can be significant for the raw images. Figure 4.9-a illustrates a typical, although rather small, experimental folder. It contains three experiments of various sizes, constituted exclusively of images. The localization data is obtained by analysis of the images (here with Matlab) and is often stored in the same folder. Other files are present, such as single images or text files. In order to transfer the experiments to the server, it is necessary to compress the heavy folder containing images (highlighted folders in figure 4.9-a). Once the experiments have been fitted, the rest of the analysis is performed on the localization tables and not on the images itself.

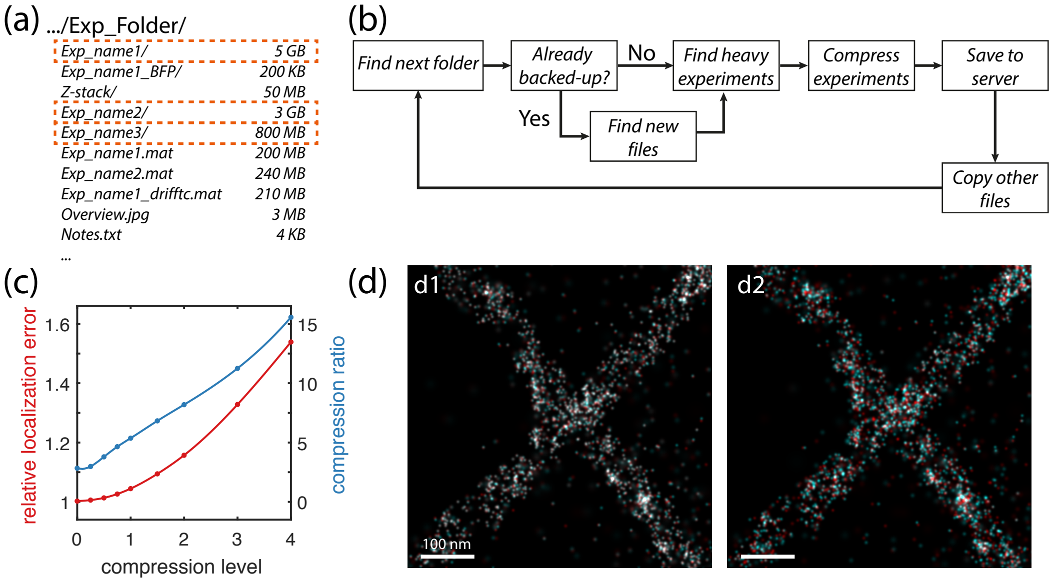

FIGURE 4.9: **Data transfer and compression. a)** Example of an experimental folder with the size of each element. **b)** Data back-up pipeline. **c)** B^3D algorithm effect on localization microscopy simulated data (1000 signal photons, 20 background photons). **d)** Comparison of uncompressed localized images of microtubules (red localizations) and the same images compressed then localized with a B^3D compression level of 1 (cyan, d1) or 3 (cyan, d2). The overlapping localizations are shown in white.

Compression and streaming to the server To automate the saving of the data to the server, I wrote a powershell script that scans the experimental folders on the microscope computers, compresses the folders containing large experiments (>500 MB) and copies the files to a server (see figure 4.9-b). The script is able to discriminate between experiments that have already been backed-up and new ones. It also identifies the new files, experiments or localization tables in the backed-up folders in order to avoid losing them. This script is responsible for the reliable transfer of more than 30 TB of experimental data per year in the group.

A new algorithm for image compression Lossless compression only achieves a limited compression ratio (compressed size divided by original size). Although compression algorithms with information loss are widely used (for instance in compressed TIFF or JPEG2000), they are usually avoided for critical scientific data. A partial reason is that the loss of information is not controlled at the pixel level, as the lossy steps are not performed in the pixel space but for instance in Fourier space. Bálint Balázs, a PhD student at EMBL, developed B^3D, a GPU-accelerated compression algorithm for microscopy (Balazs et al., 2017). B^3D can apply both lossless and lossy compression. A major difference to the common lossy algorithm is that the compression is realised directly on a single pixel basis. Images contain a certain level of noise due to the photons themselves (shot noise) and to the camera (e.g. read-out noise). B^3D quantifies the information loss by comparison to the inherent image noise. The user can specify the amount of error tolerated as an input to the algorithm. Another advantage of B^3D is its remarkable compression and decompression speed, thanks to an implementation on graphic processing unit (GPU). The algorithm is perfectly suitable for integration in high-throughput imaging pipeline as it is able to compress images faster than they are acquired. Together with Bálint, we investigated the effect of the compression on the localization precision in SMLM. Using simulated data, an array of single-emitters with variable spacing and realistic signal to noise ratio, we measured the localization error with respect to the compression level (see figure 4.9-c). In particular, a compression level of 1 induces errors not bigger than the noise present in the image. Compression within the noise level (compression level 1) accounts for a localization precision loss of only 5% while leading to a compression ratio twice as big as the lossless compression. With real data, the effect of the precision loss can be visualised by comparing the localizations obtained with the uncompressed and the compressed images (figure 4.9-d). In the case of compression within the noise level (figure 4.9-d1), the errors are negligible and the structure remains very similar as illustrated by the overlay colour (white). When the compression is increased (level 3), on the other hand, the colocalizations are rarer and the microtubules become wider.

Localization microscopy raw images are in general kept for safety once they have been fitted. The major part of the analysis is done on the localization table itself. Well established analysis pipelines rarely require to fit again the raw data. Additionally, losses of localization precision inferior to 10% are acceptable for most analyses. Lossy compression can play an important role in high-throughput by reducing the weight of the experiments and therefore the cost of data storage, while maintaining the integrity of the data. In this respect, B^3D, as opposed to most algorithms, offers the possibility to tune the error introduced to the experimental need. Furthermore, its extremely fast execution time, regardless of the compression level, makes it a perfect tool for the handling of high-throughput data.

4.2.5 High-throughput localization microscopy

The various aspects of the work presented in this chapter are different steps of the same pipeline aimed at establishing high-throughput imaging in the lab. The original motivation stemmed from the problem faced in structural studies with localization microscopy. Studying the spatial organization of a dynamic processes such as clathrin-mediated endocytosis in yeast requires a resolution that, for the moment, only localization microscopy is able to approach. However, since cells must be fixed to obtain a high enough resolution, the various CME sites are stopped at different stages of endocytosis. The difference of spatial arrangements between sites thus comes on top of the already present biological variability and stochasticity of the labelling efficiency. In order to perform meaningful averaging, the microscope focus can be placed at the bottom of the yeast cells, where the endocytic sites are not tilted. The reconstructed images are then two-dimensional projections of the endocytic structures, and radial information can be extracted. Due to the low number of CME sites per field of view, obtaining valuable information by radial averaging necessitates thousands of sites. The only approach able to collect such a colossal amount of data in a reasonable time is high-throughput imaging.

In addition to my contributions in automated imaging and data transfer, Markus Mund and Jonas Ries implemented a semi-automated pipeline of data sorting and analysis (see figure 4.10-a). The experiments are fitted automatically in parallel to the image acquisition by the Matlab software used in the lab. The algorithm processes the frames as soon as they are saved to the hard-drive. Consequently, the first steps of the analyses have already been performed when the last experiment in the unsupervised acquisition is done. Quality control is carried out by looking at the BFP acquired at every position (figure 4.10-b) or at the localization table statistics for each field of view (figure 4.10-c). The localization tables are then processed for semi-automated cells and CME sites segmentation. The various endocytic sites are geometrically analysed and averaged to yield the mean radial distribution.

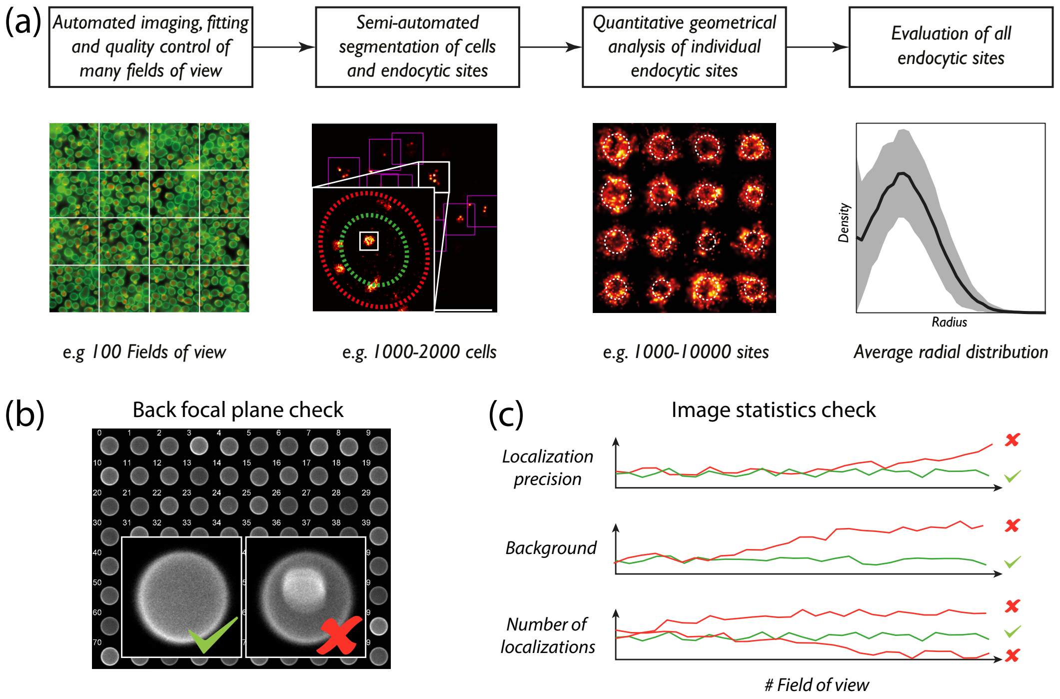

FIGURE 4.10: **High-throughput localization microscopy**. **a)** High-throughput pipeline established to study clathrin-mediated endocytosis. **b)** Quality control can be performed by discarding experiments with non-uniform back-focal planes. **c)** An additional control post-fitting follows the evolution of statistics such as localization precision, background or number of localizations, in order to identify experiments where contamination or buffer ageing occurred. This figure has been made by Markus Mund and is reprinted from his PhD thesis (Mund, 2016).

Within this study, the nanoscale radial organization of 23 endocytic proteins was determined (figure 4.11), amounting to more than 100000 CME sites from 20000 cells.

The data gathered is equivalent to more than 3 months of continuous imaging on the microscope. This superresolution dataset is of unprecedented size and scope. Beyond the attractive numbers, precious insights into the biology of endocytosis can be extracted from the radial profiles of the different proteins. In particular, we found that the assembly of the endocytic machinery initiates stochastically from irregular structures. The proteins subsequently recruited to the invagination are radially ordered according to their function within the complex, as figure 4.11 illustrates. Strikingly, actin nucleation promoters (WASP family) form a ring structure that constrains actin polymerization close to the membrane. Modelling showed that the actin nucleated at this nano-template can create the necessary force for invagination. This nano-patterning of actin nucleation could therefore be a general design-principle for actin-mediated membrane remodelling. This project is currently being prepared for publication (Mund, van der Beek, Deschamps et al., in preparation).

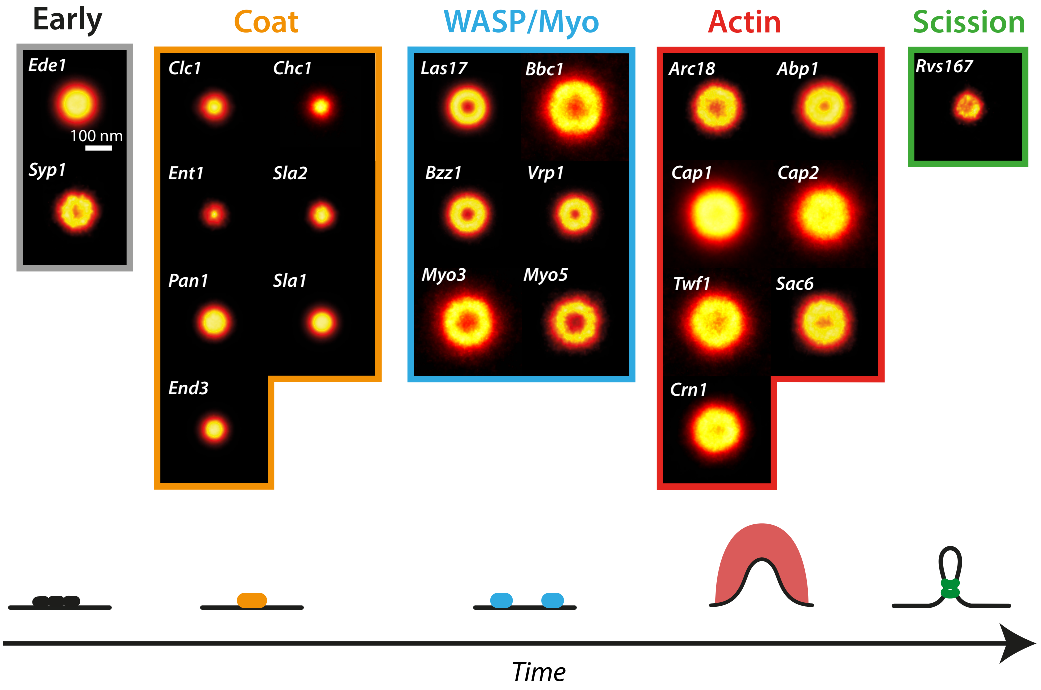

FIGURE 4.11: **Radial distribution profiles of endocytic proteins**. Proteins with related function are distributed similarly, which indicates that the nanoscale organization of proteins is predictive of their functional role during endocytosis. This figure has been made by Markus Mund and is reprinted from his PhD thesis (Mund, 2016).

4.3 Discussion

Conducting high-throughput microscopy requires computer control of the devices, an interface for complex experimental design and unsupervised imaging, automated analysis and storing of the large amount of data generated. Establishing high-throughput localization microscopy poses additional challenges and constraints on the imaging, such as control of emitter density, extreme drift stability and possibility to juggle between different modalities (e.g. 3D or two-colours). In this chapter, I presented my work on the automation of multiple steps of a high-throughput pipeline.

Open-source microscopy with µM The control of the microscope devices was integrated in Micro-manager (Edelstein et al., 2010). This software presents several advantages over commercial solutions: its freely available, it already encompasses the control of many devices, it is based on a large community of users and is integrated within ImageJ (Collins, 2007). Notably, the latter enables the application of the various ImageJ features to the analysis of images directly from the camera. Plug-ins and device adapters developed for specific projects can be shared with the community and grant easy transfer to other researchers. I developed several device adapters to communicate with instruments installed on the microscope (stages, lasers, syringe pumps, electronics). One of the device adapter I wrote is now part of µM. I also implemented a FPGA firmware and the corresponding device adapter for µM, called Micro-Mojo. While programming for a FPGA is much more complex than for devices such as an Arduino, they present crucial advantages in terms of speed and parallel computation. Micro-Mojo allows for fast and flexible triggering of several lasers given a camera exposure signal. It also encompasses multiple inputs and outputs that can be used to control motorized elements or trigger devices. Micro-Mojo provides the user with a simple and straightforward way to integrate the entire electronic layer of the microscope within a single board interfaced with µM. I am currently developing an interface plug-in for Micro-Mojo, within µM. The scope of application of such electronics is not limited to localization microscopy and could benefit any custom-built or modified commercial microscope.

Compressing microscopy images As microscopy evolves, data is generated at an ever-increasing rate. Faster cameras such as sCMOS are becoming the norm in light-sheet or localization microscopy. Research labs must then deal with larger amount of data than in the past. Considering the cost of storage that comes with the use of servers and high number of hard drives, compression of microscopy images is a necessity. I participated in the optimization of a new algorithm for rapid and controlled compression of microscopy images, called B^{3}D and written by Bálint Balázs (Balázs, Deschamps et al., 2017). Most of the analysis in localization microscopy is carried out on the localizations table and not on the raw data. Therefore, images are usually fitted only once before being stored in case of need. Well established localization procedures are unlikely to be performed twice on the same sample. The size of the raw data can be dramatically reduced using lossy compression. Besides its remarkable speed due to GPU-based implementation, B^{3}D provides a net benefit compared to established algorithms: because the compression is performed on a pixel basis, the information loss can be tuned by the user. In particular, the errors introduced can be set to be smaller than the inherent noise variability of the images. While this would not dramatically change the analysis of the images after decompression, it allows for higher compression ratios.

High-throughput localization microscopy for CME Localization microscopy is a powerful tool for structural studies as it reaches a precision of few nanometers. However, between the labelling efficiency and the biological variability, collecting few superresolved images is often not sufficient to draw conclusions the distribution of one protein within a complex. Averaging structures is in theory a straightforward way to get conclusive information. Several studies in localization microscopy have used averaging to infer meaningful spatial arrangements. For instance, Dani and colleagues imaged ten synapse scaffold proteins from few hundreds synapses to infer their position relative to the synaptic cleft (Dani et al., 2010). The nuclear pore is another example of a system in which localization microscopy can decipher crucial information (Löschberger et al., 2012; Szymborska et al., 2013; Löschberger et al., 2014). Notably, Szymborska and co-workers carried out a large-scale study of the radial position of seven proteins present in the y-shaped subcomplex of the nuclear pore. For each protein, they averaged between 1500 and 10000 pores to obtain the mean radius with great precision. This allowed them to discriminate between different models of the y-complex positioning within the mammalian nuclear pore. Other structural studies have been conducted with virus such as HIV (Van Engelenburg et al., 2014) or herpes HSV-1 (Laine et al., 2015).

However, these studies benefited from fields of view containing many sites of interest, allowing rapid collection of large statistical samples. Depending on the structure of interest, only very few sites might be present in each field of view. In the case where the imaged structure is highly dynamic, fixing the cells for maximum resolution leads to the addition of another source of variability: the fixation of the sites at different time points of the process. Therefore, an even higher number of statistical points is necessary. A solution is to turn towards high-throughput imaging. To automate the acquisition of localization microscopy images, I developed a µM plug-in that allows the user to design a set of experiments to be performed on a large number of positions. Each localization microscopy experiment is acquired in an unsupervised manner owing to a stable focus and an automatic adjustment of the UV intensity to control the density of emitters. Furthermore, the acquisition process is embedded in a user-friendly microscope control interface. Additionally, it takes advantage of the various features of the microscope, such as a cylindrical lens for 3D imaging or the Micro-Mojo laser triggering capacities.

This acquisition platform has permitted the study of the radial organization of clathrin-mediated endocytosis in yeast, as part of a collaboration with Markus Mund. Within the study, 23 proteins were imaged, and more than 100000 CME sites were averaged. The total acquisition time, performed without user intervention, accounts for more than 3 months of continuous imaging. The size of the data gathered, as well as the decisive information inferred, constitutes an unprecedented tour-de-force in localization microscopy. Such a study would not be possible without high-throughput capacity.

During our study, another high-throughput paper has been published (Holden et al., 2014). The authors carried out unsupervised imaging of 300 live cells to study the organization of a single protein throughout the cell cycle. A strong point of the study is the use of an image analysis algorithm to decide if each position should be imaged or not, based on features detection. Additionally, they developed their own µM plug-in and an automatic UV intensity adjustment that has been integrated in Micro-manager (Autolase). The automated UV algorithm lacked robustness, and was not used in our work. Live studies in localization microscopy are complex and often yield a low resolution. The FtsZ ring imaged by Holden and colleagues is about 500 nm wide, a scale at which poorer resolution is not an obstacle. In our study, the structures are five times narrower and maximum resolution is necessary. Following their example, our high-throughput imaging pipeline could be extended to feedback analysis. Another promising direction is the development of automated buffer exchange to use organic dyes for longer periods of time.

The establishment of high-throughput localization microscopy has the potential to fulfil an old dream of light microscopy: solving the nanoscale organization of protein complexes. Our study of yeast CME showed the path to data acquisition at a much larger scale. From the automation of imaging facilitated by an open-source software to new algorithm for data compression, the work presented here paves the way to many other applications of high-throughput imaging.

5 | Supercritical angle localization microscopy

5.1 Introduction

Direct access to single molecules one at a time allows probing certain quantities that are not accessible to diffraction-limited microscopy. One such quantity is the axial position of the emitters. In confocal-based methods the illumination volume encompasses a substantial number of molecules. In dealing with a unique emitter, single-molecule studies can exploit optical tricks and fluorescence properties to extract the axial information of each molecule. It is not surprising then, that localization microscopy benefits from a large choice of methods for 3D imaging.

PSF engineering PSF engineering methods encode the z-position of the molecules in the shape of their signal. The optical and analytical complexities required in order to extract axial information from the PSF range from simple methods like astigmatism (Huang et al., 2008a) to more involved processes such as the tetrapod PSF (Shechtman et al., 2015). Astigmatism necessitates the insertion of a single cylindrical lens in the optical path and a slight modification of the analysis algorithm, as compared to 2D localization microscopy. Other methods modify the PSF using a deformable mirror or a spatial light modulator (Pavani et al., 2009; Baddeley et al., 2011b; Jia et al., 2014; Shechtman et al., 2014), both implying a more complex optical path, sensitive alignment and expert hands to control the devices. An intermediate solution is to imprint the phase pattern, usually displayed on the DM or SLM, on a phase mask. The pattern can no longer be changed, but the optical path is simplified. In most cases, the fitting routine has to be modified to deal with more complicated PSF shapes, the imaging time is increased because of the PSF lateral extent and the lateral localization precision can be degraded (e.g. because of the use of a SLM or the difficulty to locate the centre of complex patterns).

Multiplane imaging Another approach to 3D localization microscopy is the simultaneous recording of multiple planes (Juette et al., 2008; Ram et al., 2012; Abrahamsson et al., 2013; Hajj et al., 2014; Hajj et al., 2016). The additional information given by the presence of the molecules in the different planes allows sub-diffraction localization of the molecules. However, the total amount of light per plane is divided by the number of planes. Therefore, the lateral localization precision suffers from the decrease of photons per localization. While bi-plane (Juette et al., 2008) remains optically simple, multiplane imaging with aberration-corrected gratings (Abrahamsson et al., 2013; Hajj et al., 2014; Hajj et al., 2016) or with more than two channels (Prabhat et al., 2006) are more challenging.

Interferometry The most complex and cumbersome methods to carry out are the interferometric approaches: the iPALM (Shtengel et al., 2009), 4Pi-SMS (Aquino et al., 2011) and W-4PiSMSN (Huang et al., 2016). Interferometric approaches make use of two opposable objectives to guide the light, collected from both sides, towards beam splitters. Multiple beams will be generated and form an image of the sample on several cameras or different areas of the same camera chip. Each beam is the result of the interference of the light from both objectives, albeit with different path lengths. Because interferences are a very sensitive read-out of the distance travelled by the light, the ratio of the intensity of the different images gives a precise measure of the axial position. Such a method requires a complex microscope, extremely precise alignment and involved analysis. In addition, the most recent implementation uses two deformable mirrors (Huang et al., 2016), adding another layer of technical complexity.

Resolution Interferometric approaches reach in general a better localization precision in z than laterally. PSF engineering and multiplane imaging, on the other hand, lead in practice to an axial precision about three to five times worse than laterally. Additionally, index mismatch and various aberrations induce deformations, preventing measurements to be an absolute measure of height. In spite of many developments, astigmatism remains the method of choice owing to its simplicity. However, its moderate axial resolution limits the imaged samples to rather large complexes and structures. Interferometric microscopes have had successful applications to biological problems, but expert knowledge in optics is required to build and operate the few microscopes currently existing. Designing a method with isotropic precision and simple optical requirements is therefore still needed to reach the full potential of localization microscopy in structural studies.

During my PhD, I explored a new approach to 3D localization microscopy called supercritical angle localization microscopy (SALM). It exploits the axial dependency of the angular emission pattern of fluorescent molecule close to the water-glass interface. The analyses presented here have been carried out in a custom Matlab software written by Jonas Ries, including the typical localization microscopy analysis, SALM calibration, DNA origami analysis and 3D rendering. I was assisted in the preparation of the calibration gels and the imaging of the biological samples by Markus Mund. The latter samples were made by Ulf Matti. Jonas Ries planned and built the microscope used in the proof of concept, while I designed and aligned the adaptive optics microscope.

5.2 Principle of surface-generated fluorescence

The environment of a molecule has strong effects on its photophysical behaviour, this is in particular the case when fluorescent molecules are located above a metal layer or a dielectric surface (e.g. glass). For instance, the lifetime of a fluorescent molecule can be decreased in the vicinity of a metal surface (Drexhage, 1970; Lukosz and Kunz, 1977b). Another interesting phenomenon pertains to the angular distribution of the light emitted by the molecules above a water-glass interface. According to the Snell-Descartes law of classical optics, the fluorescence emitted in the water and transmitted through the glass will be entirely contained in a cone defined by the critical angle θ_c:

$$\theta_c = arcsine(\frac{n_1}{n_2})$$

where n_1 and n_2 are the refractive indices of the upper medium and lower medium respectively. In the case of $n_1 = 1.33$ and $n_2 = 1.52$, the calculation yields $\theta_c = 61^o$. In figure 5.1-a, several coloured rays are shown, propagating at different angles, illustrating the change in direction occurring at the interface due to refraction. Fluorescence from single molecules is well described by the *oscillating dipole model*. When considering only light emitted in the water by a single emitter, the expected emission pattern in the glass is the profile displayed on figure 5.1-a as a polar plot. In this representation, the curve's distance to the origin is the intensity emitted by the fluorescent molecule at this specific angle. The profile presents a maximum at the critical angle and no light exists beyond this limit. In addition, this profile is independent of the molecule axial position.

However, considering only propagating light in water fails to describe the emission pattern of fluorescent molecules close to the interface. The angular spectrum representation of the field emitted by a fluorescent molecule is a continuous sum of plane waves $e^{-i\vec{k}.\vec{r}}$ with a wavevector obeying:

$$k_1^2 = k_{1,x}^2 + k_{1,y}^2 + k_{1,z}^2 = \frac{n_1^2\omega^2}{c^2} \tag{5.1}$$

where k_1 is the wavevector amplitude, $k_{1,x,y,z}$ are the wavevector coordinates, n_1 is the refractive index of the medium surrounding the molecule, ω is the frequency of the emitted light and c is the speed of light in the vacuum. In the specific case where $k_{1,x}^2 + k_{1,y}^2 \geq k_1^2$, the expression of the wave has an exponentially decaying amplitude stemming from the fact that $k_{1,z}^2 < 0$. Such a wave is therefore not propagating and is referred to as *inhomogeneous* or *evanescent*.

When plane waves cross the interface with the glass, the refractive index changes and the wavevector amplitude becomes k_2. A similar relationship to equation 1, between k_2 and n_2, applies in the medium 2. The boundary conditions impose that $k_{1,x} = k_{2,x}$, and similarly for k_y. For propagating waves, relating the angles of propagation in each medium to $k_{1,z}$ and $k_{2,z}$ leads to the Snell-Descartes law.

If the decay of an evanescent wave is long enough, then its tail crosses the interface and the same rule applies. Evanescent waves with small $k_{x,y}$ have less chances of crossing the interface because of the fast decay of their amplitude (large $k_{1,z}$). Furthermore, the same boundary conditions yield:

$$k_{2,z}^2 = \frac{(n_2^2 - n_1^2)\omega^2}{c^2} + k_{1,z}^2$$

Remembering that $k_{1,z}^2$ is negative, large values of the imaginary part of $k_{1,z}$ will lead to negative values of $k_{2,z}^2$. This means that some inhomogeneous waves will remain evanescent in the second medium. Other inhomogeneous fields, on the other hand, will be transformed into propagative waves in the glass, giving rise to a phenomenon called surface-generated fluorescence. This happens when $k_{2,z}^2$ becomes positive. The larger the difference between the refractive indices at the interface, the higher the number of evanescent waves coupling their emission directly into the glass. One can show that the minimum angle of propagation of surface-generated waves is none else than the critical angle θ_c. Such light is also referred to as *forbidden light* (Novotny, 1996) as it violates the Snell-Descartes law. It can also be seen as the inverse phenomenon of TIR illumination, albeit in emission.

Near-field conversion therefore yields to large propagation angles as shown in the emission profile of figure 5.1-b (calculated from Enderlein et al., 1999; Ries et al., 2008). There, as opposed to figure 5.1-a, the intensity profile is not null beyond the critical angle. Because the evanescent fields decay exponentially with z, the further the molecule is from the interface, the smaller the number of inhomogeneous waves capable of coupling their emission into the glass. Figure 5.1-b compares the emission profile of an emitter at two different heights, illustrating how strongly the amount of supercritical light decreases with the axial position. Furthermore, surface-generated fluorescence acts as an additional decay channel and can account for a substantial portion of the total emitted light. As shown on the curve of figure 5.1-c, the amount of light in the supercritical channel can constitute more than 40% of the total light collected in the glass when the emitter is directly located at the interface. The exponential decay of the coupling defines a small volume above the coverslip from where the surface-generated fluorescence originates. Yet, emission in the glass does not necessary result in collection of the light by the objective. In order to image supercritical light, the objective must have a sufficiently high NA. Therefore, TIRF objectives must be employed to image surface-generate fluorescence. As a result, the image of a high-NA objective's BFP is similar to the one displayed in figure 5.1-d1, given that the fluorescent molecules are close enough to the interface. Since the BFP is the distribution by angles of the light propagating through the objective, the critical angle appears as a circular ring, delimiting the boundary

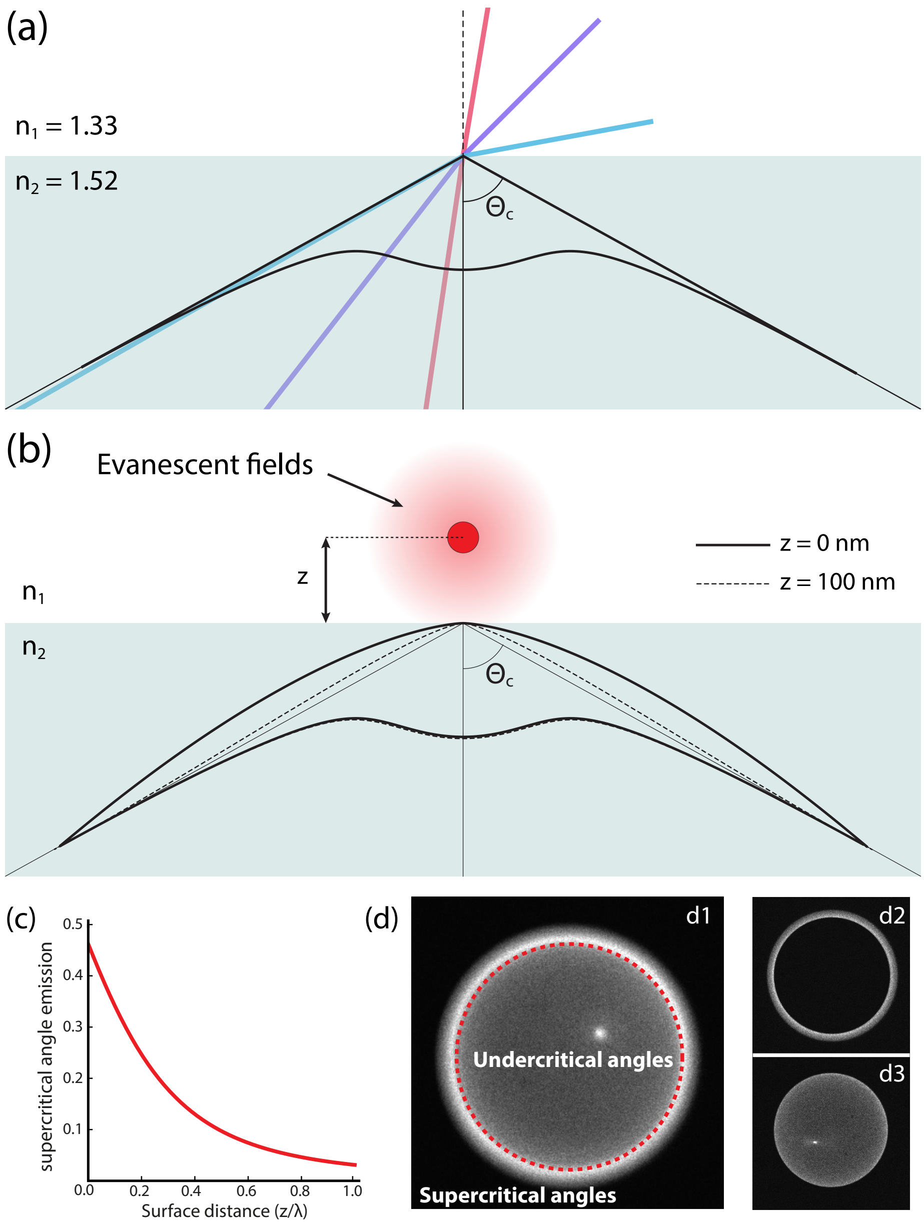

Figure 5.1: **Supercritical angle fluorescence.** **a)** Refraction at the interface between two media of different refractive indices (such as water and glass) causes incident rays (in blue, purple and red) to change direction. The refracted rays propagate further in the lower half-space within a cone delimited by the critical angle θ_c. The solid line is a polar plot of the expected intensity profile in the glass of the rays emitted in water by a fluorescent molecule and refracted at the interface. The intensity of radiation at a certain angle is the distance of the curve from the origin in the direction defined by this angle. **b)** Fluorescent molecules also possess a near-field composed of evanescent waves. Evanescent waves are non-propagating, but can be converted into propagating fields under certain conditions when the molecule is close to the interface. In particular, this surface-generated fluorescence propagates above the critical angle. The emission profile in the glass therefore covers also high angles. The solid line is the radiation pattern of a molecule located at the coverslip, while the dashed curve corresponds to the fluorescence emission of a molecule 100 nm away from the interface. **c)** Dependency of the relative amount of supercritical light on the distance of the emitter from the interface. This figure is reprinted with permission from Deschamps et al., 2014, Optics Express, manuscript of which I am first author. **d)** Back-focal plane images of a high-NA objective. The total fluorescence exhibits signal outside and inside the critical angle ring (d1). By placing an opaque disk (d2) or a ring aperture (d3), supercritical and undercritical light can be selected, respectively.

between undercritical and supercritical regions.

While surface-generated fluorescence has been known and studied for a long time, few applications emerged beyond theoretical calculations (Lukosz and Kunz, 1977b; Lukosz and Kunz, 1977a; Lukosz, 1979; Hellen and Axelrod, 1987; Novotny, 1996; Enderlein, 1999; Mertz, 2000; Axelrod, 2012). One example is the use of supercritical light to form images with enhanced contrast in NSOM (Hecht et al., 1995). In this work, the authors used an elliptical mirror to collect the light propagating at large angles. A similar system was also put in practice in sample-scanning microscopy with a glass paraboloid (Enderlein et al., 1999; Ruckstuhl et al., 2000), in a method dubbed supercritical angle fluorescence (SAF). Thanks to the high collection efficiency (>65%) of this custom-made optical component, single-molecules were imaged in a greatly reduced axial volume. Since SAF emission is highly sensitive to the distance of the emitter from the interface, the ratio of supercritical and undercritical angle fluorescence holds information about the emitter position. This was exploited to measure the height of biological structures (Winterflood et al., 2010) or single-molecules (Ruckstuhl et al., 2011) by computing the intensity ratio $I_{\mathrm{SA}}/I_{\mathrm{UA}}$ for each pixel. The optical sectioning capacities of surface-generated fluorescence detection was then exploited in fluorescence correlation spectroscopy (Ries et al., 2008) with the same optical collector. Axelrod proposed in 2001 (Axelrod, 2001) to block the undercritical fluorescence, in a plane conjugated to the BFP of a high NA objective, in order to select for the supercritical light only (resulting in the BFP of figure 5.1-d2). Such a method is able to achieve a high quality optical sectioning of the same order of magnitude than TIR, and can be used simultaneously with full-BFP imaging (Barroca et al., 2011). Placing such a mask in the BFP results in strong diffraction as the BFP is only slightly larger than the mask. Most of the PSF intensity is then transferred to the side-lobes, increasing its width. In order to improve the lateral resolution, another approach (called vSAF) imaged both total fluorescence (I_{Tot}) and undercritical (I_{UA}, with a circular mask similar to figure 5.1-d3), and obtained the supercritical image by subtraction: $I_{\mathrm{SA}} = I_{\mathrm{Tot}} - I_{\mathrm{UA}}$ (Barroca et al., 2012; Brunstein et al., 2014). This virtual supercritical image had a better lateral resolution while maintaining a high quality optical sectioning. Finally, another application took advantage of supercritical light to measure refractive indices of cellular organelles (Brunstein et al., 2017).

5.3 Results

5.3.1 Supercritical angle localization microscopy

The intensity emitted in the supercritical domain depends on the axial position of the emitter. However, the brightness per frame of blinking molecules depends additionally on how long was the molecule in its bright state throughout the frame. Indeed, molecules switch on and off at random times. In addition, the brightness of a fluorescent molecule depends on its direct environment. In order to extract axial information from a single-molecule, it is therefore necessary to renormalize the supercritical by the undercritical intensity: $I_{\mathrm{SA}}(z)/I_{\mathrm{UA}}$. To obtain 3D localization microscopy, I developed a method called supercritical angle localization microscopy (SALM) using a simple two-channel TIR microscope. This microscope was designed for localization microscopy and the optical path can be seen in figure 5.2-a. I used a 50/50 beam splitter to divide the light equally in both channels. The microscope includes a pair of relay lenses after the first image plane (IP), allowing the propagation of a plane conjugated to the objective BFP. As mentioned previously, the BFP is the distribution of light by angle. Placing a mask in a conjugated plane enables the selection of the supercritical (disk mask) or the undercritical light (ring aperture), as shown in figure 5.1-d2 and d3. The camera records an image of the sample in each channel, side by side, albeit with a different angular content (see figure 5.2-b). To achieve superresolution, the localizations are identified in each channel (figure 5.2-b), their intensity is fitted with a Gaussian and the ratio $I_{\text{channel 2}}/I_{\text{channel 1}}$ is calculated.

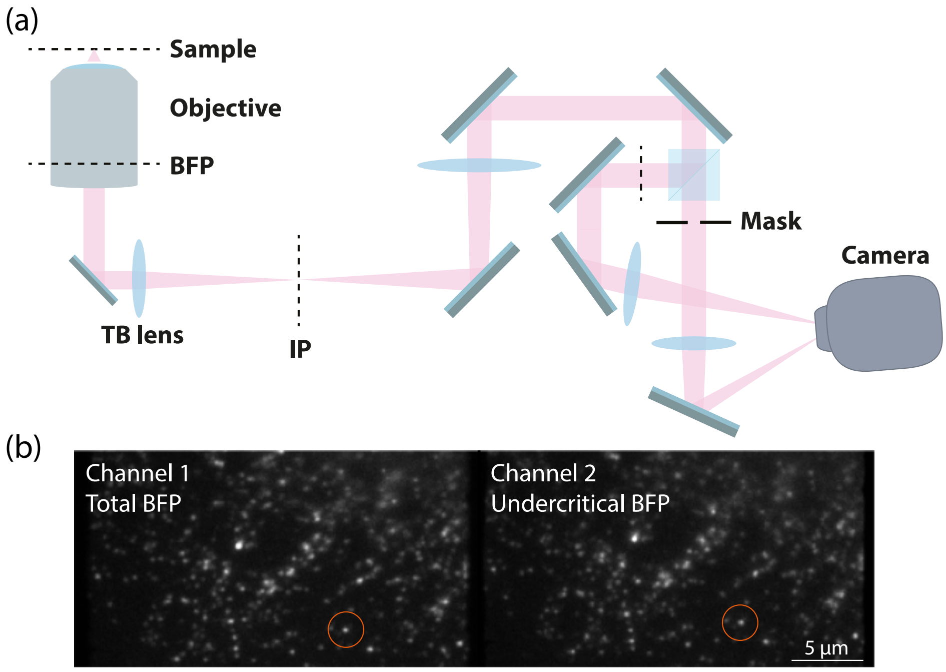

FIGURE 5.2: **Microscope**. **a)** Optical path of the microscope. The tube lens (TB) focuses the light in an intermediate image plane (IP). A lens is placed afterwards in order to form an image of the back-focal plane (BFP). A 50/50 beam splitter splits the light before the plane conjugated to the BFP. Each channel contains therefore a BFP image, in which a mask can be placed to select for an angular region of the total intensity. Finally, each channel creates an image of the sample onto one half of the camera chip. **b)** Image of a sample on the camera. Each channel contains the image of the same region of interest, albeit with different BFP. In order to extract the axial information, the molecules are identified in both channels (orange circle) and the ratio of their intensities calculated.

Three approaches to measure a z-dependent ratio are possible:

- Configuration 1, supercritical measure: total BFP in one channel, disk mask in the other: $f(z) = I_{\mathrm{SA}}(z)/(I_{\mathrm{Tot}}(z) - I_{\mathrm{SA}}(z))$
- Configuration 2, undercritical measure: total BFP in one channel, ring aperture in the other: $f(z) = I_{\mathrm{Tot}}(z)/I_{\mathrm{UA}} = I_{\mathrm{SA}}(z)/I_{\mathrm{UA}} + 1$
- Configuration 3, independent measures: disk mask in one channel, ring aperture in the other: $f(z) = I_{\mathrm{SA}}(z)/I_{\mathrm{UA}}$

In essence, the third configuration is equivalent to the supercritical measure (configuration 1) as the quantity holding axial information, I_{SA}, is estimated directly. Direct splitting with an elliptical mirror (instead of the beam splitter) can also implement the independent measures of I_{SA} and I_{UA}, albeit without loss of light and therefore a better precision in all three dimensions. The mask size must be manufactured with care to fit the size of the critical angle in the magnified image of the BFP. Configuration 1 and 2 require the use of a beam splitter, as done in the present microscope. A consequence is that the lateral localization precision in configuration 1 is degraded by a factor $\sqrt{2}$. For configuration 2, on the other hand, the x-y position can be averaged between the two channels, recovering the full lateral precision. Once $f(z)$ is calculated, its value can be compared to a theoretical model or a calibration curve to determine the axial position of each molecules.

5.3.2 Theoretical precision

What precision can we expect from such a method? A theoretical model has been derived to calculate the relative emission intensities in both supercritical and undercritical domains (Enderlein et al., 1999; Ries et al., 2008). Calculating the error associated with the measure of the intensities in each channels and relating it to the error in z by error propagation yields the theoretical localization precision (the details of the calculation can be found in Annexe A). Figure 5.3 shows a comparison of the axial localization precision obtained in the case where only the undercritical mask is used ($\sigma_{z,\mathrm{UA}}$), direct measurements ($\sigma_{z,\mathrm{SA}}$) or when using 3D astigmatism. In addition, the lateral localization precision is shown. Because the large angles hold the axial information, an indirect measure of the supercritical intensity (as when subtracting the intensity obtained with a ring aperture from the total intensity) is less precise than the direct measurement. Indeed, the higher intensity in the undercritical domain comes together with a higher shot noise, which degrades the precision in determining the supercritical intensity. The direct estimation of the supercritical intensity is better than isotropic in the first 150 nm, achieving a lower localization precision value than astigmatism. As expected, the precision degrades rapidly with z and this method is not beneficial above 200 nm. The expected localization precision also depends on the NA of the objective. For instance, using a high NA objective with NA $= 1.7$ greatly improves the localization precision (compare the dashed and solid lines in figure 5.3).

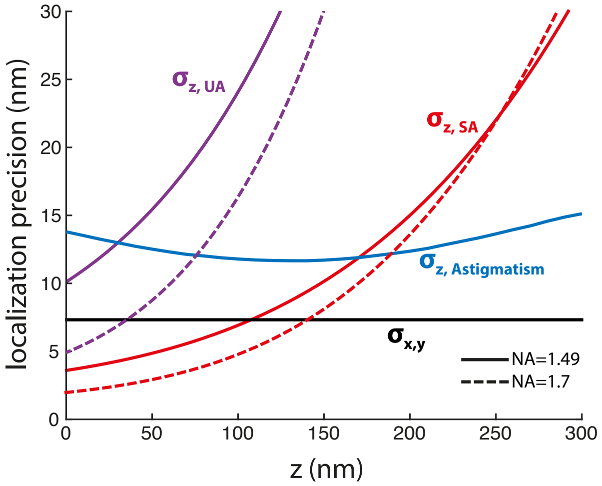

FIGURE 5.3: **Resolution**. Theoretical localization precision along the axial direction for the configuration with the direct measurements (configuration 3, red curve), the ring mask (configuration 2, purple), astigmatism (blue) and the lateral localization precision (black). The curves were calculated for a total number of photons $N = 2000$, 20 photons of background and NA $= 1.49$ (solid lines) or NA $= 1.7$ (dashed lines). The astigmatism localization precision was obtained by approaching the CRLB with a simulation.

These theoretical calculations do not take into account the effect of diffraction. Yet, it has been shown that employing a disk mask, as in configurations 1 and 3, leads to severe diffraction (Barroca et al., 2011). In practice, the loss of intensity and the enlargement of the PSF make this configuration ineffective with the described microscope. While the expected resolution obtained with the ring aperture is poor, it can be used to prove the feasibility of supercritical angle localization microscopy. Therefore, in the following sections, the second configuration will be employed: one channel propagates the total fluorescence, while the other images the sample solely with undercritical light (ring aperture).

5.3.3 Calibration

The direct calculation of the molecules' distance to the coverslip from the theoretical brightness ratio is compromised by aberrations in the microscope, imperfect splitting of the light at the beam splitter and alignment of the undercritical aperture. Altogether, these contributions lead to a systematic error in estimated intensity. Therefore I decided to experimentally calibrate the SALM ratio with fluorescent beads. In order to do so, I used agarose gels in which 40 nm fluorescent beads were immobilized at different heights. The beads were imaged simultaneously in the two channels (see figure 5.4-a), and their intensity was extracted. As expected, the ratio of the intensity in both channels is a read-out of the beads axial position, as shown in figure 5.4-b. In order to extract the beads absolute z-position precisely, a

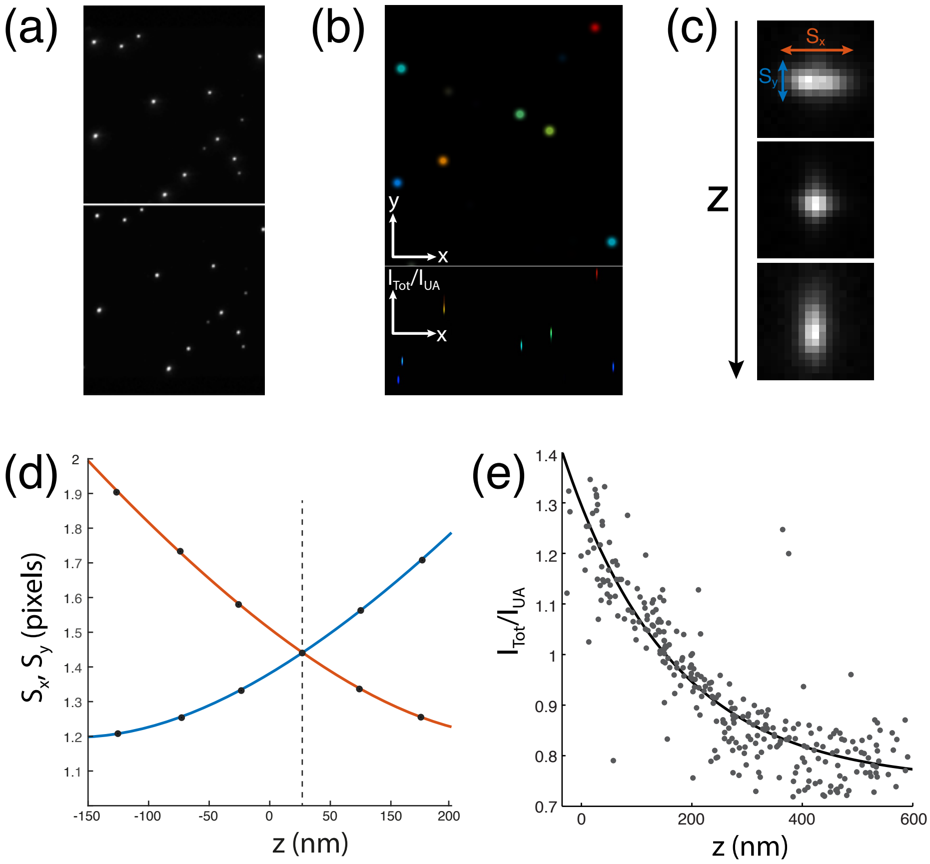

FIGURE 5.4: **Calibration**. **a)** In order to calibrate SALM, an image of beads embedded in an agarose gel at different height is recorded in both channels. **b)** For each bead in the field of view, the ratio of the intensities in both channels is calculated. **c)** Then a cylindrical lens is inserted in the beam path, producing an astigmatic PSF. A z-stack is recorded and for each bead in each frame, the size of the PSF in the x and y directions is measured. **d)** The precise position of the beads can be estimated by interpolating the size of their PSF in x and y along the axial direction and calculating the intersection. **e)** The calibration curve is obtained by fitting a decaying exponential function to the scatter plot of the SALM intensity ratio in function of the bead height. Figure e) is reprinted with permission from Deschamps et al., 2014, Optics Express, manuscript of which I am first author.

cylindrical lens was then inserted in the beam path, introducing astigmatism in the PSF. The widths in x (S_x) and y (S_y) of an astigmatic PSF change differently along the axial direction (figure 5.4-c). Z-stacks were recorded and, for each bead, the change in lateral width of their PSF was plotted. This allowed estimating precisely their axial position from $S_x = S_y$, as shown in figure 5.4-d. Finally, the ratio of the total fluorescence intensity by the undercritical intensity was plotted against the axial position (see figure 5.4-e). The beads' signal is well approximated by an exponentially decreasing curve in function of the height, as predicted by the theory. The calibration curve was obtained by fitting such an exponential decay to the scatter plot, as exemplified in figure 5.4-e. The bead measurements from different fields of view were aligned thanks to their exponential fit, and then fitted again all together. The SALM ratio of the beads decays below 1, which seems to be in contradiction with the intensity ratio formula: $f(z) = I_{\text{Tot}}/I_{\text{UA}} = I_{\text{SA}}/I_{\text{UA}} + 1$. However, the beam splitter used in the optical path was not splitting the light equally. Since the calibration curve is valid as long as the same optical path is used, no correction was applied.

5.3.4 Validation

A calibration does not imply that the method is capable of resolving meaningful features in biological samples. To validate the capabilities of SALM, I imaged commercial DNA origami tetrahedra (GATTAquant, Iinuma et al., 2014). Since DNA origamis are artificial nanostructures designed to adopt a precise conformation, they are the perfect calibration standard for 3D superresolution methods (Schmied et al., 2013). In particular, the tetrahedra used here are 82 nm in height and 100 nm in width (see figure 5.5-a), smaller than the diffraction limit. In addition, the tetrahedra allowed employing localization microscopy using the PAINT method (see figure 5.5-b), yielding bright localizations.

Figure 5.5-c shows the overview of a region obtained by SALM containing a dozen tetrahedra. For the following analyses, I selected manually only complete tetrahedra exhibiting four corners. The localization precision measured as the standard deviation of the localization precision for each tetrahedron's corner was found to be $\sigma_{x,y} = 11.2 \pm 4.7$ nm in the lateral direction. Imaging with SALM allowed to estimate the axial position of each localization event. Reconstructing superresolved images of each tetrahedron yield not only the typical four corners signal seen in the x-y views of figure 5.5-d, but it allows discriminating the corners axially as shown on the x-z projections (figure 5.5-d). Using the calibration curve of figure 5.4-e, the SALM ratio can be converted into a z position. The axial localization precision was calculated to be $\sigma_z = 26.4 \pm 8.4$ nm. For more than a hundred tetrahedra, I analysed the height by clustering the localizations, identifying them with one of the corner and measuring the axial distance between the uppermost cluster and the average of the base.

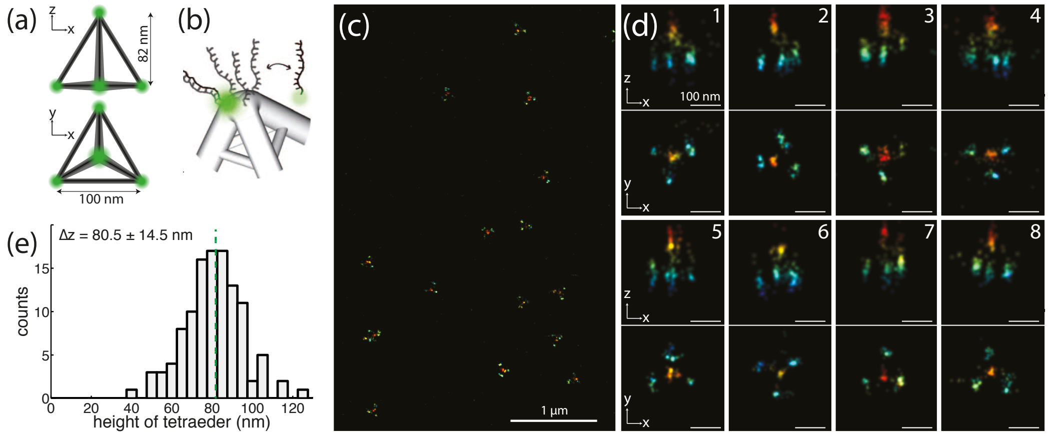

FIGURE 5.5: **Validation**. **a)** DNA origami tetrahedra are nanostructures displaying fluorescence at their corners only. **b)** Their fluorescence is based on PAINT imaging. Each corner exhibits several docking strands. The buffer contains imaging strands that are complementary to the docking strands, and are fused with a fluorescent molecule. Upon binding, the diffuse fluorescence is immobilized for a certain time, leading to a localization event. Figure a) and b) are reproduced with permission from Iinuma et al., 2014. **c)** 2D images of the tetrahedra colour-coded according to their height, obtained with SALM. **d)** Lateral (x-y) and axial (x-z) projections of the tetrahedron localizations, colour-coded according to their estimated axial position. **e)** Height distribution measured by SALM for 113 tetrahedra. The dotted line corresponds to the theoretical height of the structure. Reprinted with permission from Deschamps et al., 2014, Optics Express, manuscript of which I am first author.

Figure 5.5-e shows the distribution of heights measured with SALM. The average tetrahedra height was $\Delta z = 80.5 \pm 14.5$, in close agreement with the theoretical height. The distribution is however broad and several effects can contribute to this result. First, electron microscopy images reveal that the tetrahedra do not have an infinite rigidity (see figure 5.3 in Iinuma et al., 2014), consequently the distance between corners varies. Secondly, the SALM images indicate that the origamis are often tilted with respect to the coverslip, which was not taken into account in this analysis. Yet, the imaging of nanostructures and comparison of the 3D rendering with their theoretical architecture clearly demonstrates that SALM is applicable to 3D localization microscopy. Finally, the observed axial precision proved to be lower than the theoretical prediction of figure 5.3-a, effect than can be attributed to aberrations and improper alignment.

5.3.5 Imaging of biological samples

I then proceeded to image biological samples with SALM. Cellular structures such as clathrin-coated pits or microtubules are of great interest to evaluate 3D methods, as their shape is well defined. Both samples were immunodetected with antibodies conjugated to Alexa 647, allowing for dSTORM imaging.

Figure 5.6 demonstrates that SALM is capable to resolve smaller than diffraction-limited structures within cells. As the number of emitted photons is lower than in the case of the tetrahedra, the achieved precision is not as good as in figure 5.5.

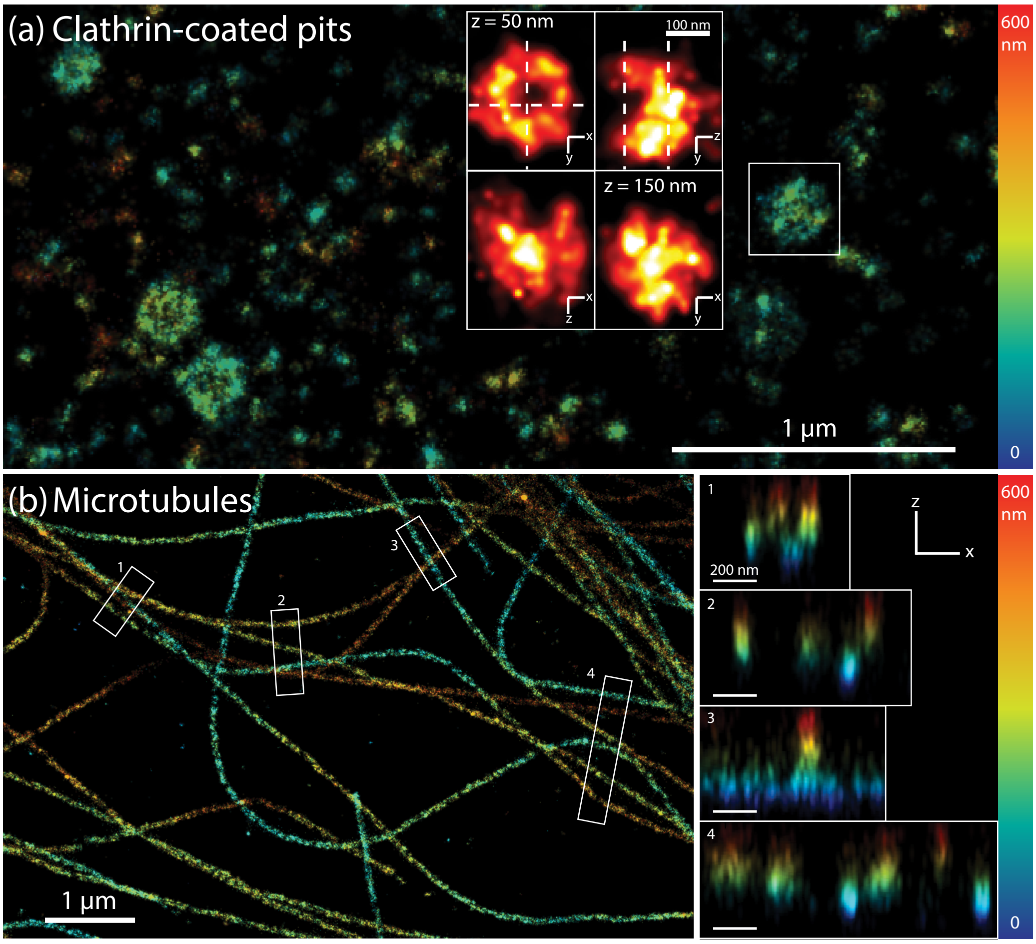

FIGURE 5.6: **Resolving biological structures with SALM**. **a)** Clathrin-coated pits imaged in a U2OS cell with Alexa Fluor 647 conjugated antibodies. The insets reveal the three-dimensional structure of the invagination in the white box. The dashed line indicates the two planes (z=50 nm and z=150 nm) at which the x-y profiles are taken. **b)** Microtubule network in a U2OS cell. The insets are the x-z profiles of the microtubules in the corresponding numbered region. Reprinted with permission from Deschamps et al., 2014, Optics Express, manuscript of which I am first author.

However, I was able to observe the half-sphere shape of clathrin-coated pits (see figure 5.6-a) and microtubules at different heights (figure 5.6-b). The resolution achieved close to the coverslip is comparable to PSF engineering methods, but degrades quickly with the height of the emitters, as expected from the theoretical calculation. Additionally, the apparent localization precision reached in the biological experiments was worse than predicted (see figure 5.3). One cause can be aberrations present in the microscope, which tend to be stronger at high angles. In the next section, I explore several possible improvements to reach the theoretical resolution of SALM.

5.3.6 Improving SALM

SALM has the prospect of an isotropic localization precision over 150 nm above the coverslip. However, experiments showed that in practice the theoretical prediction is not reached. In the previous section, I used a ring aperture to image the undercritical angles. The supercritical signal is recovered by dividing the total intensity I_{Tot} by the undercritical intensity I_{UA}. Since I_{SA} is not directly measured, the precision in estimating it is lowered. However, direct measurements with a disk (configuration 1) are not possible due to diffraction at the edge of the mask. Diffraction causes an enlargement of the PSF, which in turns increases the error in determining I_{SA}. Besides improving the brightness of the localizations, an increase of the objective NA also enhances the expected localization precision in both supercritical and undercritical measurements (configurations 1 and 2, as seen in figure 5.3). Another positive effect of the use of a 1.7 NA objective is a foreseeable reduction of the diffraction at the disk mask's edge. Figure 5.7-a shows a comparison of two objectives BFP: Olympus UAPON 100XOTIRF ($\mathrm{NA} = 1.49$) and APON100XHOTIRF ($\mathrm{NA} = 1.7$). Increasing the NA of the objective (and of the mounting medium) decreases the critical angle, in this case from 61^o ($\mathrm{NA} = 1.49$) to 52^o ($\mathrm{NA} = 1.7$). The higher collection angle for NA 1.7 objective then results in a much larger area occupied by the supercritical angles in the BFP (see figure 5.7-a). A diffraction calculation shows that the resulting intensity profile of the PSF is less affected with higher NA, resulting in a brighter central peak (see figure 5.7-b).

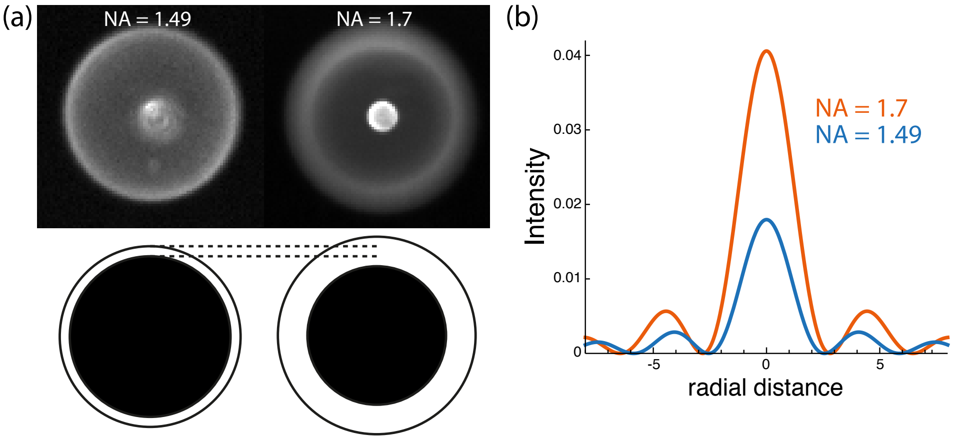

FIGURE 5.7: **Improving SALM with high NA**. **a)** BFP images of two objectives with different NA: 1.49 and 1.7 (upper panels). The lower panels show the profile of the BFP when obstructed with a disk mask of size equal to the corresponding critical angle. Dashed lines highlight the difference in surface occupied by the supercritical angles in both objectives' BFP. **b)** Intensity profile of the PSF obtained by calculating the diffraction at an annulus, that is to say a circular aperture obstructed in its centre by an opaque disk. The radius of the opaque disk was taken to match the obstruction illustrated in a), for NA=1.49 (blue) and NA=1.7 (red).

Unfortunately, the use of such a very high NA for SALM is compromised by the large angle aberrations present in the objective. Aberrations can be compensated by adaptive optics, to the detriment of the simplicity and cost of SALM. Several approaches to aberration correction exist. In all cases, a correcting element is necessary. Spatial light modulators (SLM) are often preferred in the illumination path, rather than for detection, since their polarization-dependent behaviour decreases the number of photons that can be collected. Deformable mirrors (DM) are perfectly suitable for detection purposes, as they are largely wavelength and polarization independent. Two main schemes are employed to drive the correction of aberrations: a wavefront sensor can be used in closed-loop with the DM or an image-based algorithm can optimize a certain metric by changing the shape of the mirror. In the next section, I detail the adaptive optics (AO) microscope I built in order to increase the precision of SALM, using a deformable mirror, a wavefront sensor and a commercial software suite.

5.3.6.1 Adaptive optics SALM

Adaptive optics requires precise alignment of the microscope and several parameters need to be taken into account. In particular, the deformable mirror must be placed in a plane conjugated to the objective BFP to allow for space-invariant corrections of the wavefront. The microscope optical path must then contain an intermediate BFP plane. The relay lenses must be chosen as to maximize the size of the BFP image on the mirror, without being cut by the mirror edge. Note that the effective aperture of some deformable mirrors is smaller than the apparent reflective surface due to edge effects induced by the peripheral actuators. A BFP image too small for the DM aperture reduces the precision of the correction, while too big of an image causes additional aberrations and loss of information. In addition, the angle at which the light hits the deformable mirror increases the size of the BFP image on the reflective membrane, and must therefore be minimized. The wavefront sensor (Shack-Hartmann wavefront sensor, SH-WFS, in this case) should be placed in a 4f configuration with the DM, an image of the mirror being formed onto the microlens array. This can be achieved by placing a beam-splitter on the way. Because such configuration causes a loss of light in the final image, I chose to use an electronic flip mirror to either conjugate the DM and the SH-WFS or to image the sample. Since I designed this microscope for SALM, another pair of relay lenses is used to form a BFP image in which the undercritical or supercritical mask can be placed.

Figure 5.8 shows the optical path of the microscope I built for adaptive optics SALM (AO-SALM). A feature of this microscope is the possibility to by-pass the adaptive optics, resulting in a normal SALM microscope. The adaptive optics path includes a DM and a SH-WFS. Manually placing or removing a mirror on a magnetic base switches between the shortcut and the AO paths. The image formed by the tube lens and the one formed at the exit of the AO path are of same magnification. Therefore, switching between shortcut and AO arms enables the possibility of direct comparison of the adaptive optics system performances.

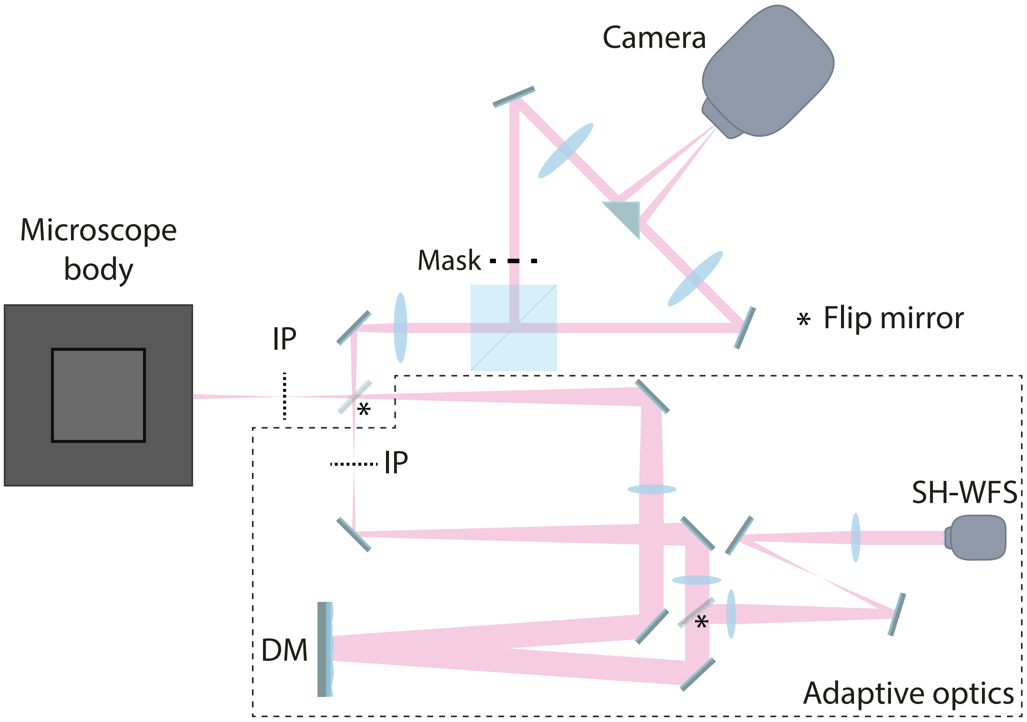

FIGURE 5.8: **Optical path of the AO-SALM microscope**. The tube lens forms an image (image plane, IP) of the sample after the microscope body. After the image plane, a magnetic base allows placing a mirror (flip mirror). When the mirror is present, the microscope is equivalent to a normal two-channels localization microscope and the adaptive optics path (dashed box) is by-passed. If the mirror is removed, then a lens forms an image of the objective BFP on the deformable mirror (DM). An electronic flip mirror permits, in its on state, to divert the light towards a path conjugating the deformable mirror with the wavefront sensor (SH-WFS) for direct aberration sensing and closed-loop correction. Once the correction has been carried-out, the mirror can be removed from the path and a lens recreates an image plane. The first flip mirror is located at equal distance from both image planes, allowing for sequential comparisons between the short-cut path and the AO path. A beam splitter gives rise to two channels. After the image plane, relay lenses recreate the image on two halves of the camera chip. A mask can be placed in one channel to select a specific angular region of the BFP (supercritical or undercritical). The whole microscope is in 4f configuration, allowing for the BFP, the DM, the WS microlens array and the mask to be conjugated.

5.3.6.2 Adaptive optics correction

The AO-SALM microscope includes both a wavefront sensor and a deformable mirror. The working principle of a SH-WFS is illustrated on figure 5.9-a. An array of identical microlenses is placed one focal length away from a CCD chip. To each microlens corresponds a sub-region of the CCD chip. When a purely unaberrated plane wavefront hits perpendicularly the microlenses array, each microlens will focus a portion of the wavefront to the centre of its corresponding CCD sub-region. In the case of an aberrated wavefront, local phase differences cause the wavefront to effectively propagate at a certain angle. The resulting focus after the microlens will be shifted compared to the unaberrated case. Since the aberrations are not constant

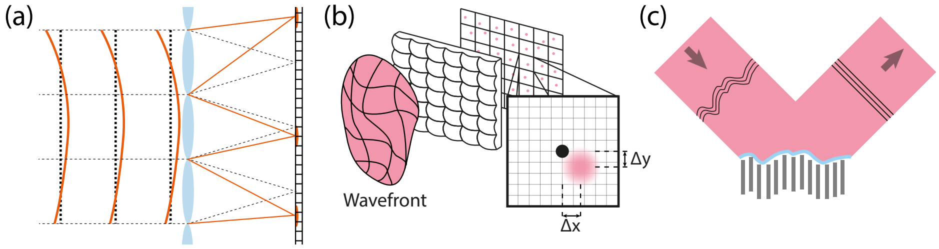

FIGURE 5.9: **Wavefront sensing and correction.** **a)** Working principle of a Shack-Hartmann wavefront sensor. It is composed of a microlenses array placed one focal length away from an array of CCD pixels. Local phase differences in the wavefront are translated into lateral shifts of the microlens foci on the CCD. **b)** Each microlens corresponds to a sub-region of the CCD chip. The displacement in x and y is measured and directly corresponds to a local wavefront phase difference. **c)** A deformable mirror consists of a reflective membrane placed on top of an array of actuators. Axial movements of the actuators change the shape of the mirror. An aberrated wavefront can be corrected by inverting the optical path differences, resulting in a flat wavefront.

across the field of view, each microlens will produce a different shift with respect to the reference position. The distance in x and y from the unaberrated focus is a read-out of the local phase difference and therefore of the local aberration (see figure 5.9-b). It is important to note that the SH-WFS returns meaningful information only when it measures a single wavefront, that is to say a wavefront originating from the same source, for instance a single fluorescent bead. In order to correct for the measured aberrations, the SH-WFS can be combined with a deformable mirror (figure 5.9-c) in a closed-loop setting. The DM simply inverts the local path differences to remove the phase disparities from the wavefront by modulating the shape of a highly reflective membrane sitting on an array of actuators.

For efficient correction, the commercial software suite (HASO and CasAO, Imagine Optic) I used decomposes the measured wavefront on the Zernike polynomials basis (examples of Zernike polynomials can be found in figure 5.10). Well defined mathematically, Zernike polynomials form an orthogonal basis, which ensures a unique decomposition of the wavefront in terms of Zernike modes. Defined on a unit circle, they provide a good analogy with the microscope pupil and some iconic aberrations encountered in microscopy (see figure 5.10). For instance, while tilt is an inoffensive aberration causing a lateral displacement of the image, astigmatism arises from imperfect lenses and induces a strong deformation of the PSF in 3D. Other well known aberrations are for instance comatic aberration from coverslip tilt or spherical aberrations due to refractive index mismatch. To correct for the aberrations, a calibration is performed between the DM and the SH-WFS. This allows to define DM membrane shapes that correspond to each Zernike mode. Then, the closed-loop operation is performed until the measured wavefront appears flat.

The bright-star used for wavefront correction, usually a single-bead of large size, is not a perfect approximation for a single emitter due to its large size (e.g. 1 µm). Correction with the SH-WFS is not enough to obtain a perfect PSF, in particular

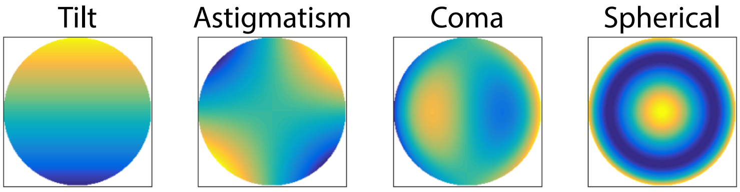

FIGURE 5.10: **Example of four Zernike polynomials corresponding to well-known aberrations in microscopy**. The polynomials were computed using a code by Paul Fricker.

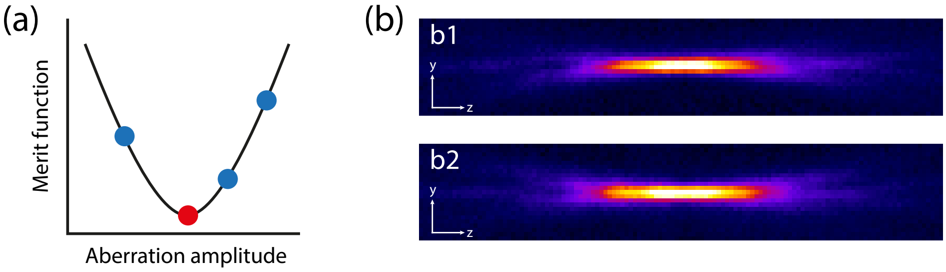

FIGURE 5.11: **Sensorless PSF optimization**. **a)** Image-based correction of aberrations makes use of a merit function related to a property of the image. An aberration is applied successively with three different amplitudes. In the mean time, the image metric is calculated. Fitting a quadratic function to the measurements allows the calculation of the optimum of the merit function. **b)** Aberration correction of the Olympus UAPON 100XOTIRF NA $= 1.49$ objective. The two orthogonal (y-z) views of the PSF are taken with the shortcut path of the AO-SALM microscope (b1) and after sensor and sensorless corrections in the AO arm of the same microscope (b2).

for a PSF-sensitive method like localization microscopy. Image-based correction algorithms have already been used to correct for aberrations in SMLM (Izeddin et al., 2012a; Tehrani et al., 2015; Burke et al., 2015). The core principle of these algorithms is to rapidly apply aberration modes at different amplitudes to find the extrema of a merit function, such as the maximum or the mean intensity within the image. The merit function, related to the image of a single emitter (a sub-diffraction bead for instance), is computed while a single aberration mode is applied by the DM. Three different amplitudes of the aberration are successively applied. The merit function value is approximatively quadratic with the mode amplitude. Three measurements are enough to fit a quadratic function and infer the optimum of the merit function for a single aberration (figure 5.11-a). This is repeated for several aberrations to optimize the PSF. I used MicAO (Imagine Optic), a software linking the acquired image and the DM, to perform sensorless correction. Preliminary results can be found in figure 5.11-b. In this figure, the y-z projection of the NA $= 1.49$ objective PSF with and without AO correction from a single sub-diffraction bead are compared. In figure 5.11-b1, the PSF corresponds to the one obtained when imaging the bead with the microscope in its shortcut configuration. The PSF appears comatic (banana-shape), which is detrimental to localization microscopy (Coles et al., 2016). The second

PSF (figure 5.11-b2) is the result of the wavefront correction followed by image-based optimization. The correction results in a brighter signal in focus and a less pronounced coma. While residual aberrations still appear, I will further optimize the correction pipeline in the near future. The present improvement of the PSF shape suggests that the AO system is well aligned and that optimization of the SALM PSF is possible. In the next steps, I will attempt to measure and correct aberrations using the $\mathrm{NA} = 1.7$ objective and then turn to the optimization of the PSF with a disk mask placed in the BFP.

5.4 Discussion

In this chapter, I introduced a new approach to 3D localization microscopy called supercritical angle localization microscopy. Relying on the axial dependency of the amount of light radiated at high angles, the z-position of the emitters is inferred by measuring the ratio of the intensity emitted above and below the critical angle. In order to do so, the light is split in half and a mask is placed in a plane conjugated to the objective BFP. Since the back-focal plane represents the light distribution by angles, the supercritical and undercritical regions can be selected by a disk mask or an aperture ring respectively. The ratio measured for each localization is then related to a calibration curve to estimate the axial position. Another group published a very similar method, albeit without calibration (Bourg et al., 2015). Because supercritical fluorescence stems from the proximity of the molecules to the water-glass interface, it can provide absolute axial localization. In other approaches, the z axis origin depends on the focus plane position and absolute measurements are not possible. I determined that SALM can reach an isotropic localization precision over a range of 150 nm above the coverslip in the case of the disk mask, according to a theoretical calculation; a resolution comparable to what is achieved in interferometric approaches with complex and expensive microscopes. However, diffraction at the mask strongly degrades the PSF and makes the intensity estimation difficult. I described a proof of principle of the method using the aperture ring, imaging DNA origami tetrahedra as well as biological samples. The method achieves a resolution good enough to observe the architecture of 100 nm tall origamis and the organization of the clathrin coat around endocytic invaginations. A particularity of SALM is its simplicity. It is based on a two-channel microscope equipped with a TIR objective. The only additional requirement is a pair of relay lenses in order to image the BFP.However, the localization precision was found to be lower than the theoretical prediction. The resolution obtained in the undercritical configuration did not surpass the localization precision reported with PSF engineering methods.

Improving SALM Using higher NA increases the amount of supercritical light, while also collecting more photons, thereon improving the localization precision in all dimensions. Such gain is in particular beneficial when selecting for the supercritical angles. There, the main cause for the low experimental resolution is diffraction at the disk mask. As the critical angle decreases with the NA of the objective, the fraction of the BFP occupied by the mask becomes smaller. Notably, moving from a NA 1.49 to 1.7 should double the peak intensity of the supercritical PSF. Yet, the increase in NA comes with stronger aberrations at high angles. In order to implement high NA SALM, an aberration correction scheme should be implemented. To this purpose, I designed and built a new microscope dedicated to the optimization of SALM. The microscope can accommodate an objective of NA $= 1.7$ and includes a deformable mirror and a wavefront sensor. In the near future, I will test the correction capabilities of the adaptive optics system with the 1.7 NA objective, in particular regarding the supercritical PSF. Since the latter configuration has a much higher theoretical localization precision over a larger axial range, AO-SALM is a promising approach. Furthermore, the localization precision can be increased by substituting the beam splitter for an elliptical mirror. By doing so, direct measurement of the supercritical and undercritical intensities is possible, while increasing the number of photons in both channels. An additional technical source of imprecision is the model used to extract the intensities. Throughout this work, I used a Gaussian fit to extract the intensity in both channels. While this is a good approximation for the total fluorescence, diffraction at the mask causes the PSF to deviate from it. Using finer approaches, such as circular aperture estimation (Franke et al., 2016) or experimental PSF fitting (Li et al., 2017), for intensity extraction should enhance the overall quality of the measurements.

Limitations The main limitation of SALM is its limited axial depth. The resolution rapidly deteriorates away from the coverslip. In practice, the range of advantageous axial resolution is confined to 150 nm above the coverslip. While the original SALM implementation is simple and inexpensive, the use of adaptive optics increases both cost and complexity. Finally, the rotational mobility of the fluorescent molecule is particularly impacting the emission angular profile (Novotny, 1996). Attention should be paid to ensure that the fluorescent labels are freely rotating to avoid dramatic localization biases. Measurements using a polarizing beam-splitter can help estimating the degree of rotational freedom.

SALM is perfectly suitable for biological processes localized at the cell membrane close to the coverslip, such as focal adhesions, endo- or exocytosis. It has, for instance, already been applied to decipher the axial organization of several proteins in mammalian podosomes (Bouissou et al., 2017). Developments in high NA objectives and adaptive optics might help SALM reach its theoretical localization precision. In such case, SALM will be a precious tool in structural approaches to localization microscopy.

6 | Conclusion

More than ten years after its emergence, localization microscopy is widely applied to biological systems. Its resolving power, down to tens of nanometers, has proven itself crucial to many studies. Obtaining high quality images requires the convergence of expertise in three domains: sample preparation, microscopy and image analysis. in particular, without a high-end microscope, much of the information can be lost during imaging. Years of development have expanded the microscopes toolbox but limitations remain. In this thesis, I detailed several technical advances aimed at overcoming illumination biases, slow throughput and limited 3D resolution.

In chapter 3, I developed a new illumination system achieving a highly homogeneous intensity profile in the sample using a multi-mode fiber and a speckle-reducer. As opposed to the common illumination approach, this system provides uniform photophysics of the molecules across the field of view. It is therefore a prerequisite to any quantitative study in localization microscopy. Owing to its simple optical path and cost-efficient components, it can easily be implemented on any commercial or custom-built microscope. However, it suffers from a limited laser coupling efficiency due to the speckle-reducer. In the future, substituting it by vibration motors should lead to similar homogeneity with higher coupling efficiency, while maintaining its simplicity.

In addition, I fully automated the microscope encompassing the homogeneous illumination. As described in chapter 4, automating localization microscopy required several developments such as electronic control of the devices, algorithmic solutions for unsupervised acquisitions, automated analyses, data compressing and storing routines. In particular, I developed a microscope control platform, using advanced electronics and an interface plug-in within an open-source software, to enable the automated acquisition of localization microscopy data over the course of weeks. The system has been successfully applied to the study of clathrin-mediated endocytosis in yeast. The dataset acquired in this particular study is of unprecedented size and scope in localization microscopy. To further increase the potential of the acquisition interface, extension to feedback microscopy should be developed, in particular feature dependent acquisitions.

I detailed in chapter 5 a new approach to 3D localization microscopy called supercritical angle localization microscopy (SALM), based on the principle of surface-generated fluorescence. As opposed to most 3D method, SALM does not require expensive optics and advanced analysis algorithms. So far, it has remained limited in resolution due to diffraction and has not reached its prospect of an isotropic localization precision over a 150 nm range above the coverslip. Advanced optics, such as very high NA objectives and adaptive optics, can in theory be used to fulfil its potential, albeit at the cost of an increased complexity. If such approach is validated, an elliptical mirror could be used instead of the current 50/50 beam splitter, improving the localization precision in all three directions. In the future, development of very high NA objective with low aberrations at high angles would eliminate the need for adaptive optics, simplifying greatly this new approach to SALM. Since many important biological processes occur close to the plasma membrane, SALM with isotropic resolution could turn out to be an invaluable tool in the 3D study of these phenomenon.

The diversity of approaches to localization microscopy and investigated systems call for flexible microscopes, able to accommodate different methods. Cutting-edge localization microscopes must then offer a wide range of features. The tools developed during my PhD stand out by their technical simplicity compared to other published systems and can easily be combined within the same microscope. As illustrated by a new localization approach called MINFLUX (Balzarotti et al., 2016), single-molecule based superresolution microscopy has not reached its limit yet. The most advanced developments often involve highly complex optics, as in the case of MINFLUX or interferometric approaches. However, simple concepts can dramatically improve certain aspects of the microscope and have a broader impact on the scientific community.

Undoubtedly, homogeneous illumination, automation and advanced 3D will soon be features of any high-end microscope. My work made substantial progress in that direction and provides a framework for the routine use of quantitative high-throughput 3D localization microscopy.

7 | Materials and methods

7.1 Microscopes

During my PhD, I used three custom-built microscopes. In this method section, I detail the different elements composing each microscope. In particular, I describe four beam paths:

- Homogeneous illumination (Chapter 3). This is the illumination beam path of the **high-throughput microscope**.
- **High-throughput microscope** (Chapter 4).
- **SALM microscope** (Chapter 5). The proof of principle of 3D localization microscopy with SALM was realised using this microscope.
- **AO-SALM microscope** (Chapter 5). I designed and built this microscope in order to optimize SALM with a high NA objective and adaptive optics.

A figure illustrating each beam path is included with the focal length of the lenses and the various elements, as well as a table listing the most crucial devices.

7.1.1 Homogeneous illumination system

As described in the chapter 3, I built an illumination system with two arms: an optical path for homogeneous illumination, referred to as path 1, and an epi-fluorescence/TIR path (path 2). Figure 7.1 shows the illumination beam path and the different components. The polarization beam splitter, irises and lenses have been purchased from Thorlabs. The main components of the first path are a speckle reducer (LSR-3005, Optotune) and a multi-mode fiber (105 µm, NA 0.22, Thorlabs). The output of the fiber is projected directly into the sample, resulting in a flat illumination with sharp boundaries. Multi-mode fibers often produce auto-fluorescence, which can be discarded by placing a clean-up filter after the fiber exit. In order to increase the power in the red, I added another 640 nm diode laser (iBeam Smart, Toptica) to the system and combined its output to the laser emission of the laser combiner (Omicron) using a polarization beam-splitter. The single-mode fiber can be exchanged to connect either to the laser combiner or to an additional UV laser (Oxxius). The XY stages are custom-built flexure stages. All the lenses and reflective mirrors were bought from Thorlabs. In particular, dielectric mirrors were chosen to avoid UV losses. A mirror and a dichroic mirror on magnetic bases allow selecting either one of the paths or both at the same time. Finally, the illuminated area can be chosen by moving the multi-mode fiber output and the lens at its exit. The important components are described in table 1.

TABLE 7.1: Illumination components

Component	Name	Manufacturer
Laser combiner	LightHUB	Omicron
	LuxX 405	Omicron
	LuxX 488	Omicron
	LuxX 638	Omicron
	Cobolt 561	Cobolt
Stand-alone lasers	iBeam Smart 640	Toptica
	LBX-HPE 405	Oxxius
Speckle reducer	LSR-3005-17S-VIS	Optotune
Multi-mode fiber	M105L02S-A	Thorlabs
Clean-up filter	390/482/563/640 HC Quad	AHF
Dichroic mirror	TechSpec 550 nm short pass	Edmund Optics
Objective	HCX PL APO 160x/1.43 Oil CORR GSD	Leica

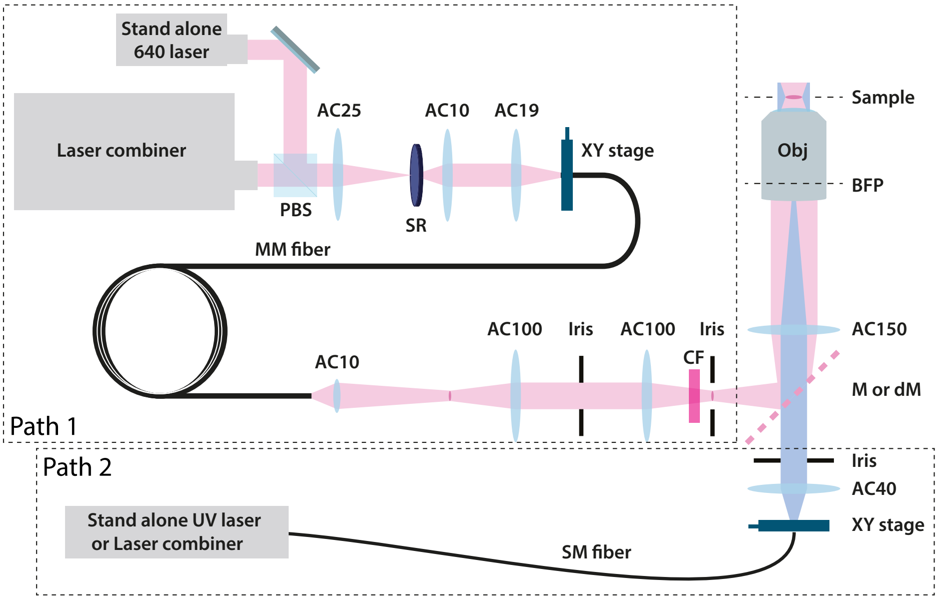

FIGURE 7.1: **Homogeneous illumination system**. PBS: polarization beam splitter, ACxxx: achromatic doublet of focal length xxx, SR: speckle reducer, MM: multi-mode, SM: single-mode, CF: laser clean-up filter, M: mirror, dM: dichroic mirror, BFP: back-focal plane and Obj: objective.

7.1.2 High-throughput microscope

The microscope used for homogeneous illumination and high-throughput localization microscopy is shown in figure 7.2, where the illumination path (described

TABLE 7.2: High-throughput microscope components

Component	Name	Manufacturer
Fluorescence dichroic mirror	TIRF Quad Line Beamsplitter zt405/488/561/640rpc	AHF, Chroma
Perfect focus dichroic mirror	SP beam splitter T750SPXRXT	AHF, Chroma
Filter wheel	525/50	AHF, Chroma
	600/60	AHF, Chroma
	676/37 BrightLine HC	AHF, Semrock
Laser clean-up	Quad-Notch Filter 400-410/488/561/631-640	AHF, Semrock
Two-colour dichroic	680 LP	AHF
Perfect-focus laser	iBeam Smart 785	Toptica
Quadrant photodiode	SD197-23-21-041	Laser components
XY stage controller	HCU-3D	SmarAct
Z stage	P-726	PI
Objective	HCX PL APO 160x/1.43 Oil CORR GSD	Leica
Camera	Evolve 512 Delta	Photometrix

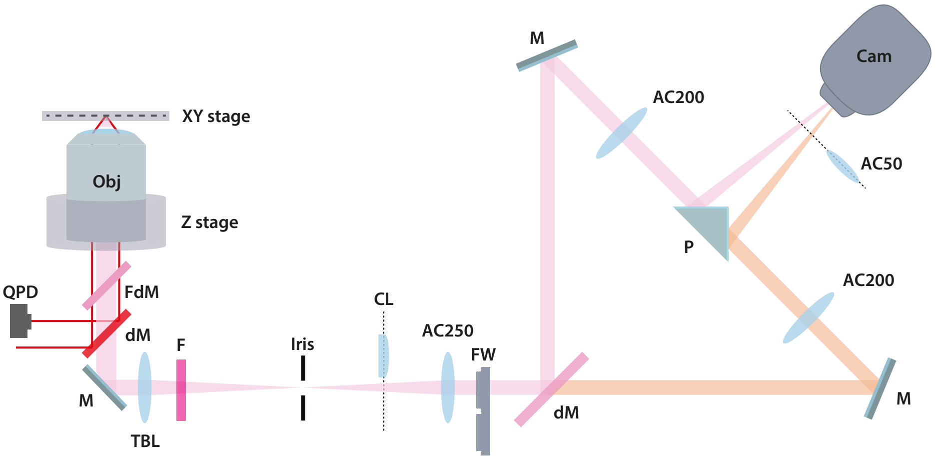

FIGURE 7.2: **High-throughput microscope**. Obj: objective, FdM: fluorescence dichroic mirror, QPD: quadrant photo-diode, M: mirror, TBL: tube lens, CL: cylindrical lens, ACxxx: achromatic doublet of focal length xxx, FW: filter-wheel, dM: dichroic mirror, F: filter, P: right-angle reflective prism and Cam: camera.

in figure 7.1) has been ignored. It has been designed by Jonas Ries, and built by Jonas Ries, Markus Mund and myself. This microscope has a simple two-channels optical path, with the lenses in 4f configuration. The laser light is coupled in the custom-build microscope body by reflection on the fluorescence dichroic mirror. A perfect-focus system for live axial drift correction has been implemented, based on the TIR reflection of 785 nm laser (Toptica), detection of the laser light by a quadrant photo-diode and direct feedback between the detector and the z stage. Two servos can move in the beam path a cylindrical lens for 3D localization microscopy and a Bertrand lens for BFP imaging. Another servo allows rotating the filter-wheel. Finally, a dichroic mirror splits the light by wavelength in two channels that are imaged each on a half of the camera chip. The dichroic is placed on a magnetic base and can be removed for single-channel imaging. Lenses and dielectric mirrors were bought from Thorlabs. Details of the main components are to be found in table 2. The control of the microscope was carried out through Micro-manager and a custom-written interface (see the relevant section).

7.1.3 SALM microscope

The SALM study made use of an already existing TIR two-channels custom-build microscope. It was designed and build by Jonas Ries. The illumination system is equivalent to the second path of figure 7.1. A focus-lock (perfect focus) system is also present in the microscope. A 50/50 beam splitter can be placed in the path to image two channels equally. A custom-built mask or aperture was placed in one of the channel in a plane conjugated to the objective BFP. The size of the disk mask or ring apertures were matched to the size of the undercritical domain in the BFP (~8.6 mm). The achromatic doublets, mirrors and the beam splitter were purchased from Thorlabs. A servo controls the movement of a Bertrand lens to image the BFP and of a cylindrical lens (1 m) to perform 3D stacks or imaging. The microscope was controlled with LabView and the camera by Micro-manager.

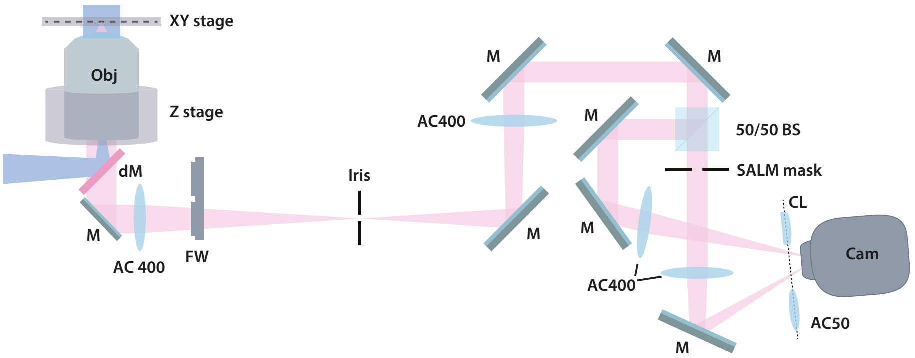

FIGURE 7.3: **SALM microscope**. Obj: objective, FdM: fluorescence dichroic mirror, dM: dichroic mirror, QPD: quadrant photo-diode, M: mirror, ACxxx: achromatic doublet of focal length xxx, FW: filter-wheel, BS: beam splitter, CL: cylindrical lens, Cam: camera.

TABLE 7.3: SALM microscope components

Component	Name	Manufacturer
Fluorescence dichroic mirror	TIRF Quad Line Beamsplitter zt405/488/561/640rpc	AHF, Chroma
Perfect focus dichroic mirror	SP beam splitter T750SPXRXT	AHF, Chroma
Filter wheel	525/50	AHF, Chroma
	600/60	AHF, Chroma
	700/100	AHF, Chroma
Laser clean-up	Quad-Notch Filter 400-410/488/561/631-640	AHF, Semrock
Perfect-focus laser	iBeam Smart 785	Toptica
Quadrant photodiode	SD197-23-21-041	Laser components
XY stage controller	HCU-3D	SmarAct
Z stage	P-726	PI
Objective	SR Apochromat TIRF 100x 1.49	Nikon
Camera	iXon EMCCD	Andor

7.1.4 SALM masks

In chapter 5, two types of masks were referred to: ring and disk masks. Both masks were mounted on a 1" lens tube (Thorlabs) screwed to a XY translation mount (Thorlabs) on a magnetic base. To precisely align the masks in the intermediate back-focal plane, a Bertrand lens was inserted, giving access to the BFP image. Then, light was shined on the mask and the whole system (mask and post holding the magnetic base) was translated until markings on the mask appeared in focus. Translation using the mount then helped placing the mask exactly at the supercritical region, either selecting or blocking it.

Ring mask To manufacture the ring mask (figure 7.4-a), holes of various diameter were drilled into 25 mm aluminium disks. To minimize diffraction, a linear thickness gradient was created starting from minimum at the edge of the central hole. The ring mask is then fixed within a 1" lens tube (Thorlabs) and screwed on the translation stage.

Disk mask The disk mask is more complex to build as it must block only the central part of the BFP. To do so, a magnetic rod was fitted in the centre of 38 mm high quality optical window (Edmund Optics). The magnet was then glued to ensure stability. It is important to use as less glue as possible, to avoid aberrations in transmission. Disks were custom-made with diameters approximately equal to the undercritical region of the BFP. A ring of inner diameter slightly bigger than the magnetic rod was glued to the bask of the disk mask. The ring was thick enough to allow the mask to rest on the magnetic rod. Additionally, the disk mask being magnetic, interaction with the magnetic rod allowed reproducible placement of the

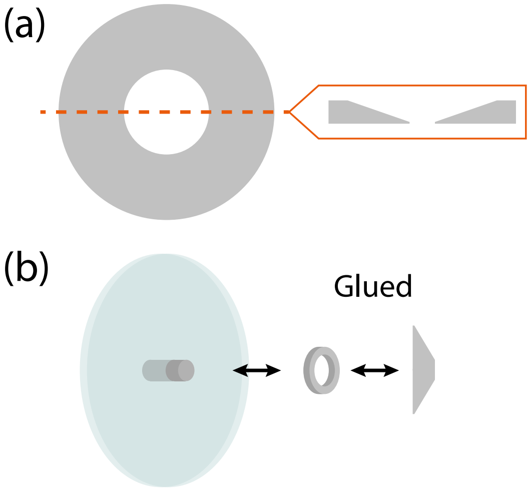

FIGURE 7.4: **SALM masks. a)** The ring mask consists of a disk with a central hole of size corresponding to the undercritical region of the BFP. A thickness gradient was applied from the centre to reduce diffraction. **b)** The disk mask was manufactured by placing a magnet within a high quality optical window and glueing a ring to a disk of size approximately equal to the undercritical region of the BFP. The ring size corresponds to the magnetic rod so that it can be easily fitted on it. The disk is magnetic, leading to a stable positioning of the mask upon the window.

mask. Finally, the window was glued to a 1" lens tube (Thorlabs) and screwed onto the translation stage.

7.1.5 AO-SALM microscope

Figure 7.4 shows the optical path of the AO-SALM microscope, which I designed and aligned. This microscope is similar to the high-throughput microscope presented above when a mirror on a magnetic base is placed right after the iris, by-passing the adaptive optics arm. When the mirror is removed, the light propagates towards deformable mirror (Mirao, Imagine Optic). An electronic flip mirror controls the choice between wavefront-correction with a Shack-Hartmann wavefront sensor (HASO, Imagine Optic) and imaging with the camera. The light can be split equally by a beam-splitter to give rise to two channels. In one channel, a SALM mask can be placed. For alignment purposes, I designed several lens holders, in particular a tailored tube lens holder. Lenses and dielectric mirrors were bought from Thorlabs.

7.2 Microscope control

The control scheme I designed for the high-throughput and the AO-SALM microscopes is based on Micro-manager. The source code of Micro-manager was cloned locally, either through svn (old versions) or git (https://github.com/micro-manager), and subsequent additions and modifications were made within this framework.

TABLE 7.4: AO-SALM microscope components

Component	Name	Manufacturer
Laser combiner	iChrome MLE	Toptica
Fluorescence dichroic mirror	TIRF Quad Line Beamsplitter zt405/488/561/640rpc	AHF, Chroma
Perfect focus dichroic mirror	SP beam splitter T750SPXRXT	AHF, Chroma
Filter wheel	525/50	AHF, Chroma
	600/60	AHF, Chroma
	676/37 BrightLine HC	AHF, Semrock
Laser clean-up	Quad-Notch Filter 400-410/488/561/631-640	AHF, Semrock
Objectives	APON 100XHOTIRF	Olympus
	UAPON 100XOTIRF	Olympus
Tube lens	U-TLU	Olympus
Deformable mirror	MIRAO 52E	Imagine Optic
Wavefront sensor	HASO3	Imagine Optic
XY stage controller	HCU-3D	SmarAct
Z stage	P-726	PI
Camera	Evolve 512	Photometrix

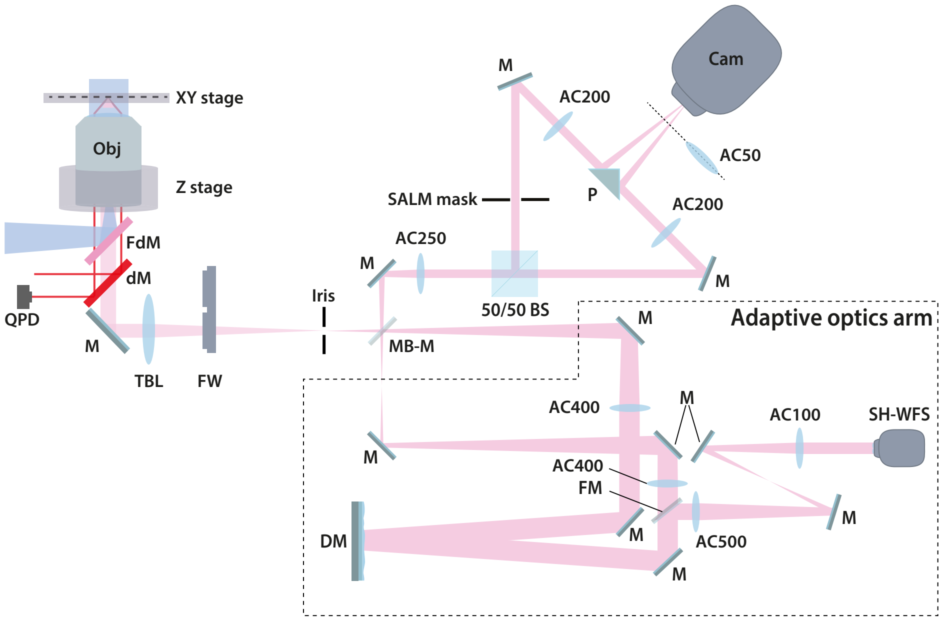

FIGURE 7.5: **AO-SALM microscope**. Obj: objective, FdM: fluorescence dichroic mirror, dM: dichroic mirror, QPD: quadrant photo-diode, M: mirror, TBL: tube lens, ACxxx: achromatic doublet of focal length xxx, FW: filter-wheel, MB-M: mirror on a magnetic base, BS: beam splitter, FM: flip mirror, DM: deformable mirror, SH-WFS: Shack-Hartman wavefront sensor, P: right-angle reflective prism and Cam: camera.

7.2.1 Micro-manager device adapters

All Micro-manager device adapters were written following the guidelines available on Micro-manager's wiki. Each one of them was either written from scratch or modified from existing versions within Visual Studio (Microsoft). One device adapter has been integrated in Micro-manager's distribution, while those that are of interest for the community are freely available on https://github.com/jdeschamps. Table 7.5 sums up the device adapters I have worked with.

TABLE 7.5: Custom device adapters

Device	Modifications	Availability
SmarAct HCU-3D	Wrote new	Integrated in μM
Micro-Mojo	Wrote new	Available on github
PI	Focus-lock system	Available on github
Omicron	Sanity checks	Available on github
Cobolt	Change of class	Available on github
Aladdin	Multiple pumps Functions properties	Available on github

7.2.2 Micro-Mojo

Micro-Mojo is based on the Mojo FPGA (Embedded Micro) and was developed within the Mojo IDE, freely available for download on the manufacturer website. The Mojo FPGA contains a Xilinx FPGA and therefore requires Xilinx' ISE to function. Mojo IDE allows two languages for the projects: Verilog and Lucid. Micro-Mojo was entirely written in Lucid, a friendlier version of Verilog. Reference guide and tutorials are available on Embedded Micro's website. The Micro-Mojo source code is available on github.com/jdeschamps.

7.2.3 Interface plug-in

Micro-Interface was written in Java within the Eclipse IDE. Conceived as a Micro-manager plug-in, it is subdivided in several packages:

- Micro-manager: classes used to load the interface as a plug-in and build the rest of the classes.
- Swing related classes: all the graphical elements, panels and windows.
- Threads: all the classes running independent processes, such as the automated UV activation, the monitoring of the focus position or the unsupervised acquisitions.
- Devices: the definition class of all the devices on the microscope, e.g. lasers, filters, camera, servos.

- Other packages with some utility class definitions and functions.

Figure 7.6 shows a simplified schematic of the plug-in organisation. In brief, upon calling within Micro-Manager, the Plug-in class reads the configuration file (.txt) and instantiates the System and UI classes. The System holds a list of all the devices defined in the configuration file and is able to modify their properties. The UI class creates the interface the user can interact with. In addition, the UI also contains a list of processes, the Threads. Through the panels and tabs, the user can modify the properties of the devices (via a callback to the Plug-in class) or of the threads. The Threads run on the background and perform calculations related to their function. They in turn can modify the user interface (feedback to the UI class) or the device properties (callback to the Plug-in class). In order to not freeze the interface, the threads (Monitor, Acquisition and Activation) are defined as SwingWorkers and are run independently from the event dispatch thread (EDT) according to the Java guidelines.

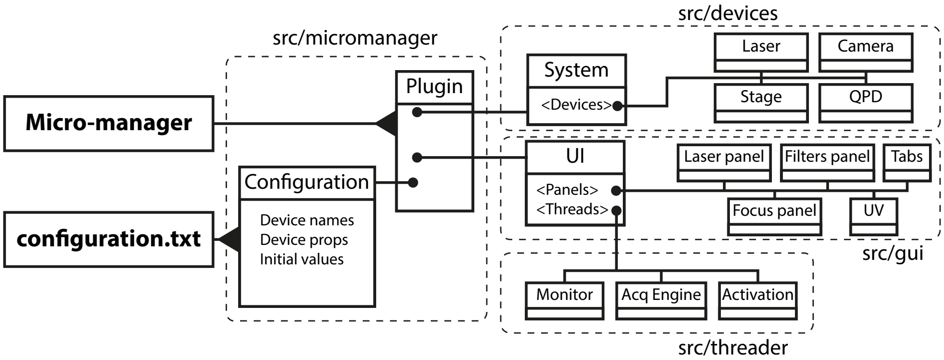

FIGURE 7.6: **Micro-interface simplified organization**.

7.3 Sample preparation

Fluorescent dyes layer (figure 3.2) The fluorescent layer imaged in chapter 3 was created by depositing 0.2 µL of diluted Alexa Fluor 647 (Thermo Fisher Scientific) onto a 24 mm coverslip. An 11 mm coverslip was then put on top of the Alexa Fluor 647 drop and then moved around while pressed against the other coverslip. Once the layer thin enough, the 11 mm coverslip was then glued to the 24 mm coverslip using nail polish.

Microtubules (figure 3.3 and 5.6) In both chapters 3 and 5, U2OS cells were used to image microtubules. In order to prefix and permeabilize the cells, they were incubated in 3% glutaraldehyde in cytoskeleton buffer (10 mM MES pH 6.1, 150 mM NaCl, 5 mM EGTA, 5 mM glucose, 5 mM $MgCl_2$) with 0.25% TX-100 for 1-2 minutes. Then, the cells were fixed with 2% glutaraldehyde in cytoskeleton buffer for 10 minutes. They were subsequently washed with PBS, reduced with

0.1% NaBH4/PBS for 7 minutes, and washed again three times. Labelling was accomplished by incubating the cells with 1:500 mouse anti-alpha tubulin primary antibody (Neomarker, MS581) in 3% BSA/PBS for 30 min, PBS washing and staining with 1:500 of a secondary goat anti-mouse antibody conjugated to Alexa Fluor 647 (A21236 Molecular Probes) in 3% BSA/PBS for 2-3 hours. The imaging buffer was composed of 50 mM Tris pH 8, 10 mM NaCl, 10% glucose, 35 mM cysteamine, 0.5 mg/mL glucose oxidase and 40 µg/mL catalase.

Actin (figure 3.4) To image actin filaments (chapter 3), U2OS cells were transfected with a lifeAct-tdEOS plasmid using Lipofectamin in optiMEM buffer (Thermo Fisher) for 12 h. After washing, the cells were fixed using 4% Formaldehyde in PBS for 10 min, then quenched with 50 mM NH_4Cl for 5 min. The sample were imaged in a D_2O buffer.

Clathrin (figure 3.4 and 5.6) The clathrin-coated pits of chapter 3 were prepared following the same protocol than the actin sample. The plasmid mEos3.2-Clathrin-15 was a gift from Michael Davidson (Addgene plasmid # 57452, Huang et al., 2013).

In the case of the clathrin sample of chapter 5, the cells were fixed with 3% Formaldehyde/PBS at room temperature for 10 minutes, washed in PBS and subsequently reduced by 0.1% NaBH4/PBS for 7 minutes. The permeabilization was realised using a 3% BSA/PBS solution containing 0.5% Triton X- 100 for 30 minutes. Then, the cells were stained with 1:300 mouse anti-clathrin heavy chain (cloneX22, ab2731, abcam), 1:300 rabbit anti-clathrin light chain (sc-28276, Santa Cruz Biotechnology) and 1:300 mouse anti-clathrin heavy chain (msCHC5.9, BM295, Acris) in 2% BSA/PBS overnight. After incubation, the cells were washed and stained with 1:200 anti- mouse (A21236, Molecular Probes) and anti-rabbit secondary antibodies conjugated to Alexa Fluor 647 (A31573, Molecular Probes) in 2% BSA/PBS for 2-3 hours. The sample was imaged in the same buffer than used for the microtubules.

Beads in agarose gel (figure 5.4) In order to obtain beads at different heights in a very thin gel (chapter 5), a 1% low melting point agarose (A9414, Sigma-Aldrich) solution was prepared in water by heating up the mix in a microwave. 1 µL of 1:400 diluted 0.1 µm fluorescent beads (TetraSpeck, T7279, Thermo Fisher Scientific) was added to 49 µL of warm agarose solution and deposited onto a coverslip. The coverslip was then centrifuged at room temperature and 2500 g, leading to a thickness of about 1 µm. The sample was then mounted in water in the microscope sample holder.

DNA origami tetrahedra (figure 5.5) The DNA origami tetrahedra (chapter 5) were graciously offered by GATTAquant. The tetrahedra were biotinylated and attached to BSA-biotin-neutravidin coated coverslips. Each corner contained 16 docking strands, each consisting of 10 nucleotides binding sequence and 1 nucleotide spacer (TTAAATGCCCG). The immobilized origamis were imaged in a buffer composed of 5 mM Tris pH 8, 10 mM MgCl2, 1 mM EDTA, 0.05% Tween20 to which 3 nM of imaging strands (CGGGCATTTA-Atto655) were added.

Clathrin-mediated endocytosis related proteins All the sample preparation, as well as the imaging and analysis are available in Markus Mund thesis, "Superresolution imaging of clathrin-mediated endocytosis in yeast", 2016.

7.4 Imaging

Fluorescent dyes layer (figure 3.2) To image the intensity profiles of both single-mode and multi-mode illumination schemes, I looked for residual dirt at the bottom coverslip interface with the fluorescent dyes layer, allowing for precise focusing. I then moved to regions free of any structure. Using ImageJ live profile plot, I tuned down the 638 laser power in order to minimize bleaching. Once in a regime where the intensity profile was stable, I moved to another region and acquired one image. I repeated the same procedure for the other modality. Given that the coupling efficiency is different for single-mode and multi-mode illumination scheme, the laser was set to different power. In the analysis, only the normalized profiles were compared.

Microtubules (figure 3.3) The microtubules network in figure 3.3 was imaged on the high-throughput microscope using both single-mode and multi-mode illumination schemes, combining each time excitation and activation within the same fiber. The sample was excited using the LuxX638 laser from the LightHUB laser combiner and an additional "booster" laser (Toptica iBeamSmart 640), resulting in 14 kW/cm^2 (diameter of the circular illumination of 35 µm). The activation was performed with a UV laser. The power at the exit of the multi-mode fiber was measured to be about 150 mW by a powermeter (Thorlabs). An experiment was first acquired using the multi-mode illumination with 10 ms exposure time for 40000 frames. Since the intensity profile is homogeneous by design, no spatial bias is induced by imaging with the multi-mode scheme first. Then, illumination was switched to the single-mode path, without changing the region of interest. The power at the exit of the single-mode fiber was matched with the power measured in the previous experiment and another 40000 frames experiment were recorded. An additional multi-mode experiment was acquired afterwards to confirm the first experiment results. The camera EM gain was set to 100.

Actin (figure 3.4) The actin experiments of figure 3.4 were aimed at comparing multi-mode and single-mode activation: first a multi-mode activation experiment (activation + excitation within the multi-mode fiber) was recorded, then a TIR single-mode one (activation using single-mode fiber in TIR + multi-mode excitation). To do so, a dichroic mirror was placed at the intersection of the beam paths (see figure 7.1). The TIR adjustment was realised thanks to a flexure stage holding the single-mode fiber exit. The UV power at the exit of the single-mode fiber was matched to the power measured after the multi-mode fiber. The acquisitions were conducted with 25 ms exposure time and a 561 nm laser power density of 12 kW/cm^2. In both cases, the UV power was only few mW and was pulsed automatically according to a desired emitter density (see chapter 4). The imaging was performed in high density regime in order to minimize self-activation. The multi-mode experiment was stopped when the automated UV activation reached a pulse length corresponding to half depletion of the molecules (given by previous experiments with the same conditions and parameters), resulting in about 60000 frames. The single-mode experiments was then performed until depletion (30000 frames), leading to a similar number of localizations. The camera EM gain was set to 200.

Clathrin (figure 3.4) The experiments with mEos3.2-clathrin were carried-out following the same procedure detailed in the previous paragraph. In this case, the exposure time was 30 ms and the power density with the 561 nm laser was 5 kW/cm^2.

Beads in agarose gel (figure 5.4) Multiple regions of the same gel were imaged using the two-channels SALM microscope (figure 7.3). First, 50 identical two-channel images were acquired with a mask placed in the BFP intermediate image of one channel. Then, a cylindrical lens (f=1 mm, Thorlabs) was inserted and a single-channel z-stack was acquired with a step size of 50 µm.

DNA origami tetrahedra (figure 5.5) Imaging of the DNA origamis was performed in TIR with an exposure time of 400 ms.

Microtubules and clathrin (figure 5.6) Both samples were imaged in the SALM microscope with an exposure time of 30 ms and an EM gain of 200. The power density was 2-5 kW/cm^2 using the combined laser light from the 640 nm laser from the iChrome-MLE laser combiner (Toptica) and a 640 iBeamSmart (Toptica). In total, about 100000 frames were recorded for both samples.

7.5 Localization analysis and rendering

Single-molecule localization and subsequent analysis of the localizations have been performed in a Matlab software custom-written by Jonas Ries. This comprehensive package allows for live fitting of ongoing experiments, rendering, filtering and various analysis of the results.

Localization pipeline All localization microscopy experiments have been fitted and rendered according to similar pipelines. First, the background of the images was estimated using either wavelet (chapter 3, Izeddin et al., 2012a) or median filtering (chapter 5). The background subtracted image was used for peak detection using a fast non-maximum suppression algorithm (Neubeck and Van Gool, 2006). A probabilistic cut-off was then applied ($p<0.01$, Köthe et al., 2014) to select specifically the signal corresponding to molecules. Region of interests centred on the detected peaks were cut-out from the raw images (non background subtracted) and a GPU-based maximum-likelihood estimator fitting routine (Smith et al., 2010) was used to estimate the molecules' position, number of signal and background photons, as well as the theoretical localization precision. A filtering on the likelihood and the localization precision was applied to remove spurious localization, e.g. non-converging localizations. Rendering of the localizations was carried-out representing them as symmetrical Gaussian with a standard deviation equal to the localization precision and an amplitude equal to the number of estimated photons. Drift correction was performed in the case of long experiments by adding all localizations from a time windows and cross-correlating the time windows (Dlasková et al., 2011). Localizations were usually filtered out when their localization precision was larger than 30 nm and their PSF size larger than 150 nm.

On-times distribution Figure 3.3 was obtained by calculating the median on-time in a neighbourhood of 50 nm around the localization for each one of them. The localizations were then colour-coded according to this median value, with the look-up table stretching from 1 to 6.

Intensity and precision profiles The photon count and localization precision plots of figure 3.3 were calculated by setting a spatial window centred on the localizations centroid. The window size was spanning the entire region of interest's length in x (s_x) and was half the region's size in y (s_y). The mean parameter (photon count or localization precision) was averaged over entire tranches of $\frac{s_x}{100} \times s_y$. The plots shows the average and the standard deviation for each window.

Astigmatic axial position determination To infer the axial position of beads, a z-stack acquired with a cylindrical lens was localized using an elliptical Gaussian (Smith et al., 2010). The PSF widths in x and y were fitted with a quadratic function and the axial position was extracted by calculating the intersection points of the two curves, after correction for the refractive index mismatch (Huang et al., 2008b).

SALM intensity ratio To estimate the relative intensity in the two channels, an approximate shift between the channels was estimated by cross-correlation of the raw images. The brightest molecules in each frame were identified using the cross-correlation result and were used to compute an affine transformation between the two channels. After identification of the localizations, a region of interest centred on each of them was cut-out from the raw data and fitted again with a Gaussian function of constant width to estimate the total number of photons per localization. The intensity ratio was then determined by dividing the number of photons measured in one channel by the number obtained in the other one.

SALM calibration Immobilized beads in an agarose gel were imaged with the SALM microscope in two-channels mode, with one channel containing a mask in the BFP for supercritical or undercritical angles selection. After fitting of a symmetrical Gaussian, the localizations were identified between the two channels and intensity ratios calculated. The same region of interests was imaged with cylindrical lens and the beads axial position extracted. The intensity ratio was plotted against the axial position. An decaying exponential function was then fitted to the data set. Multiple region of interests were imaged and their exponential fit aligned along z to correct for the axial offset. Then the cloud of points containing each dataset was fitted again with a decaying exponential function using non-linear least square.

SALM analysis For each localization, the axial position was determined by calculating the SALM intensity ration and inferring the z-position using a calibration curve. The experiment was performed with the microscope in the same optical state than the calibration.

Tetrahedra The tetrahedra of figure 5.5 were manually selected in the rendered image according to their completeness (4 corners). For each tetrahedron, the localizations were identified to one of the corners automatically by k-means clustering in 3D. The centroid of each corner was then calculated, as well as the lateral and axial standard deviations. The height of the tetrahedron was obtained by subtracting the average z-position of the bottom three corners from the z-position of the top one. This analysis did not include tilt correction.

7.6 Adaptive optics correction

Bead sample In order to perform both wavefront and sensorless corrections, differently sized beads are necessary. Large beads are used for wavefront correction as they provide the contrast ratio necessary to obtain reliable wavefront measurements with the SH-WFS. Beads smaller than the diffraction limit provide a good approximation of the PSF, a prerequisite for image-based correction. Such beads are not suitable for wavefront correction as they bleach too fast to allow calibration and subsequent closed-loop correction. Therefore, 0.5 and 0.1 µm fluorescent beads were mixed together and deposited on a coverslip. The sample is left at room temperature for few minutes to allow time for the large beads to stick to the glass. Several washing are necessary to remove any unbound bead. The density of beads was arbitrarily chosen and based on previous results using the available, already diluted, stocks in the lab. The beads density should be sparse enough that one can easily single out a bead. Every time a bead is chosen, a field iris is closed to prevent light from other beads to perturb the measurement. Out of focus beads can in particular degrade the wavefront measures.

Wavefront correction To perform wavefront correction, a single 0.5 µm bead was placed in the centre of the field of view. The shortcut mirror was removed and the flip mirror was inserted on the path as to send light to the wavefront sensor. Alignment of the light beam with the HASO was carried out thanks to two mirrors. Once the tip and tilt measured by the HASO low enough, the CASAO software (Imagine Optic) was used. Within CASAO, the HASO exposure time was set to about 50 ms and the laser adjusted to a non-bleaching regime while maintaining sufficient brightness. CASAO allows for the measurement of an interaction matrix (16 averaged measurements) calibrating the effect of the DM on the wavefront. The matrix is then inverted and a closed-loop operation between the HASO and the mirror is run to correct for aberrations. The tip and tilt aberrations were excluded from the correction and only the first 32 Zernike modes were targeted. The closed-loop correction was stopped when the wavefront remained stable.

Sensorless correction For sensorless correction, a 0.1 µm bead was single-out in the field of view. Continuous acquisition of images was performed within µM, using 500 ms intervals between images. Image-based correction was realised with MICAO (Imagine Optic) and a 3N algorithm (Facomprez et al., 2012). The algorithm reads the continuously-acquired images and modifies the DM shape to minimize the merit function (here maximum intensity). First, the lower modes were targeted (astigmatism 0^o to trefoil 90^o) a couple of times, then higher modes were corrected. The merit function was chosen to be the maximum intensity. Subsequent correction, in particular spherical aberrations, was realised manually.

7.7 Theoretical and experimental calculations

Optical fiber resonant modes The fiber modes shown in figure 3.1 were computed using the analytical expressions of the Laguerre-Gaussian polynomials in a Matlab code written by Lucian Bojor (Matlab file exchange, Fiber modes, version 1.0).

Illumination intensity profile The illumination intensity profiles displayed in figure 3.2 were obtained by averaging a 4 pixels large window along the central line of the illumination pattern (see figure 3.2-b) using ImageJ line profile tool.

Micro-Mojo laser triggering The FPGA response time, µs triggering and sequential patterns (figure 4.3) were recorded using an oscilloscope (TDS 3034B, Tektronix) with one channel receiving the actual trigger from the camera (10 ms exposure time) and the others the laser trigger signals. The cables were selected to be as short as the ones used for triggering on the microscope.

B^{3}B The B^{3}B algorithm has been written by Bálint Balázs. Details can be found in Balazs et al., 2017. The curves in figure 4.9 were obtained by simulating an array of molecules (1000 photons of signal) on a grid with 0.1 pixel cumulating offset in both x and y directions. The pixel size was set to 100 nm. A constant illumination background was added (20 photons) before application of Poisson noise (shot noise). The simulation was repeated 1000 times. Then the images were compressed at different compression level, then uncompressed. Each image was fitted according to the localization pipeline described in the previous section. Next, the average localization error was calculated for the different compression level.

Radiation profile at an interface The radiation profiles of figure 5.1 were calculated according to previous publications (Enderlein et al., 1999; Ries et al., 2008).

Astigmatism localization precision The Cramér-Rao lower bound (CRLB) of Astigmatism with z (figure 5.3) was obtained by first fitting an experimental astigmatic calibration curve with a quadratic function (Huang et al., 2008a; Smith et al., 2010), then using the resulting curve to simulate a thousand PSF (2000 photons of signal and 20 photons of background) at different axial positions and subsequently localize them. The average CRLB calculated according to Smith et al., 2010 was then plotted.

SALM localization precision The theoretical SALM localization precision (figure 5.3) can be found in Annexe A.

Obscured Airy pattern The PSF profile obtained by diffraction of the light at a ring aperture (figure 5.7), also called obscured Airy pattern, was calculated according to Rivolta, 1986.

Zernike modes The Zernike modes displayed in figure 5.10 were computed directly from their mathematical expression using a Matlab code written by Paul Fricker (Matlab file exchange: Zernike polynomials, version 1.3.0.1).

A | Supercritical angle localization precision

In SALM, the axial position of the fluorescent molecules is inferred from an intensity ratio. The theoretical axial localization precision can therefore be derived from the Cramer-Rao Lower Bound (CRLB) corresponding to the precision in determining the number of photon (Rieger and Stallinga, 2013). The following calculation is reproduced with permission from Deschamps et al., 2014, Optics Express.

Let us define $f(z)$, the intensity ratio from which z can be inferred for a single-molecule. The uncertainty in determining z relates to the error in measuring f:

$$\delta z = \frac{\partial z}{\partial f}\delta f = \left(\frac{\partial f}{\partial z}\right)^{-1}\delta f \tag{A.1}$$

Depending on the masks placed in the channels, f can have different forms. Configuration 2 (see Chapter 5), for instance, yields:

$$f(z) = \frac{I_{\mathrm{Tot}(z)}}{I_{\mathrm{UA}}} = \frac{I_{\mathrm{SA}(z)}}{I_{\mathrm{UA}}} + 1 \tag{A.2}$$

Where one channel measures the total intensity, $I_{\mathrm{Tot}(z)}$, and in the other channel the undercritical intensity, I_{UA}. If the disk mask and the ring mask are each placed in one channel, then f becomes:

$$f(z) = \frac{I_{\mathrm{SA}(z)}}{I_{\mathrm{UA}}} \tag{A.3}$$

For freely rotating molecules, the intensity emitted in the supercritical and undercritical domains can be calculated numerically from expressions derived in previous work (Enderlein et al., 1999; Ries et al., 2008):

$$I_{\mathrm{SA}}^{r}(z) = \int_{0}^{\nu_{\mathrm{NA}}} \frac{2(n_1^2+n_2^2)\nu\bar{\lambda}\sqrt{n_2^2-n_1^2-\nu^2\bar{\lambda}^2}(n_1^2+\nu^2\bar{\lambda}^2)}{3(n_2^2-n_1^2)(n_1^4+(n_1^2+n_2^2)\nu^2\bar{\lambda}^2)} e^{-2\nu z} d\nu \tag{A.4}$$

Where λ is the wavelength of the emitted light, considered monochromatic, and $\bar{\lambda} = \lambda/2\pi$, n_1 and n_2 are the refractive indices of the buffer and of the glass coverslip respectively, $\nu_{\mathrm{NA}} = \bar{\lambda}^{-1}(\mathrm{NA}^2 - n_1^2)^{1/2}$, with the numerical aperture defined as $\mathrm{NA} = n_2 \sin\theta_c$.

$$I^r_{\mathrm{UA}} = \int_0^{w_0} \frac{2Q\bar{\lambda}w}{3} \left(\frac{1}{(w\bar{\lambda} + Q)^2} + \frac{n_1^2 n_2^2}{(n_1^2 Q + n_2^2 w\bar{\lambda})^2} \right) dw \tag{A.5}$$

with $Q = (n_2^2 - n_1^2 + w^2\bar{\lambda}^2)^{1/2}$ and $w_0 = n_1/\bar{\lambda}$.

From equation (A.4) and (A.5), $\partial f/\partial z$ can be numerically computed:

$$\frac{\partial f}{\partial z} = \frac{1}{I^r_{\mathrm{UA}}} \frac{\partial I^r_{\mathrm{SA}}(z)}{\partial z} \tag{A.6}$$

One still need to calculate δf to obtain δz from equation (A.1). Error propagation can be applied to equation (A.2), using the errors in intensity determination δI_{Tot} and δI_{UA}:

$$\delta f^2 = \left(\frac{\partial f}{\partial I_{\mathrm{Tot}}} \delta I_{\mathrm{Tot}} \right)^2 + \left(\frac{\partial f}{\partial I_{\mathrm{UA}}} \delta I_{\mathrm{UA}} \right)^2 = \left(\frac{\delta I_{\mathrm{Tot}}}{I_{\mathrm{UA}}} \right)^2 + \left(\frac{I_{\mathrm{Tot}}}{I_{\mathrm{UA}^2}} \delta I_{\mathrm{UA}} \right)^2 \tag{A.7}$$

If measured in photons, the uncertainties δI_{Tot} and δI_{UA} can be approximated by (Thompson et al., 2002):

$$\delta I^2_{\mathrm{Tot}} = I_{\mathrm{Tot}} + 4\pi I_{\mathrm{BG}} \frac{s^2}{a^2}, \quad \delta I^2_{\mathrm{UA}} = I_{\mathrm{UA}} + 4\pi I_{\mathrm{BG}} \frac{s^2}{a^2} \tag{A.8}$$

Where s is the standard deviation of the PSF, a the pixel size and δI_{BG} is the number of background photons.

In the case of a fluorescent molecule with low quantum yield, supercritical and undercritical angle emissions do not compete. Having N the number of photons detected when the molecule is far from the interface and accounting for the 50/50 beam splitter, we obtain:

$$I_{\mathrm{UA}} = \frac{N}{2}, \quad I_{\mathrm{Tot}} = \frac{N}{2} \left(1 + \frac{I^r_{\mathrm{SA}}}{I^r_{\mathrm{UA}}} \right) \tag{A.9}$$

In the limit of high quantum yield, the total number of observed photons does not change, and the undercritical intensity is decreased by the amount of supercritical light.

$$I_{\mathrm{UA}} = \frac{N}{2} \left(1 - \frac{I^r_{\mathrm{SA}}}{I^r_{\mathrm{SA}} + I^r_{\mathrm{UA}}} \right), \quad I_{\mathrm{Tot}} = \frac{N}{2} \tag{A.10}$$

Together (A.9) or (A.10) and (A.8) allows calculating δf from (A.7). Then, using (A.6), one can obtain the value of δz from (A.1). Equation (A.7) was derived following configuration 2. A similar expression can be obtained for configuration 3. In particular, taking $N = 2000$ and $I_{\mathrm{BG}} = 20$ photons, as well as $\mathrm{NA} = 1.49$ and 1.7, the curves of figure 5.3 can be computed for configurations 2 and 3.

LaTeX

I composed this thesis with TeXstudio, and used a custom document structure based on the 'Masters/Doctoral Thesis' LaTeXtemplate (www.latextemplates.com, authors Steve Gunn, Sunil Patel, vel@latextemplates), modified by Markus Mund, which is available under CC BY-NC-SA 3.0 (http://creativecommons.org/licenses/by-nc-sa/3.0/).

Bibliography

Abbe, E (1873). "Beiträge zur Theorie des Mikroskops und der mikroskopischen Wahrnehmung". In: *Archiv für mikroskopische Anatomie* 9.1, pp. 413–418.

Abrahamsson, Sara et al. (2013). "Fast multicolor 3D imaging using aberration-corrected multifocus microscopy". In: *Nature Methods* 10.1, pp. 60–63.

Airy, G B (1835). "On the Diffraction of an Object-glass with Circular Aperture". In: *Transactions of the Cambridge Philosophical Society* 5, p. 283.

Akram, M Nadeem, Zhaomin Tong, Guangmin Ouyang, Xuyuan Chen, and Vladimir Kartashov (2010). "Laser speckle reduction due to spatial and angular diversity introduced by fast scanning micromirror." In: *Applied Optics* 49.17, pp. 3297–3304.

Allen, John R, Stephen T Ross, and Michael W Davidson (2013). "Sample preparation for single molecule localization microscopy". In: *Physical Chemistry Chemical Physics* 15.43, pp. 18771–18783.

Almada, Pedro, Siân Culley, and Ricardo Henriques (2015). "PALM and STORM: Into large fields and high-throughput microscopy with sCMOS detectors." In: *Methods (San Diego, Calif.)* 88, pp. 109–121.

Andresen, Martin, Andre C Stiel, Jonas Fölling, Dirk Wenzel, Andreas Schönle, Alexander Egner, Christian Eggeling, Stefan W Hell, and Stefan Jakobs (2008). "Photoswitchable fluorescent proteins enable monochromatic multilabel imaging and dual color fluorescence nanoscopy". In: *Nature Biotechnology* 26.9, pp. 1035–1040.

Andronov, Leonid, Igor Orlov, Yves Lutz, Jean-Luc Vonesch, and Bruno P Klaholz (2016). "ClusterViSu, a method for clustering of protein complexes by Voronoi tessellation in super-resolution microscopy". In: *Scientific reports* 6, srep24084.

Annibale, P, M Scarselli, A Kodiyan, and A Radenovic (2010). "Photoactivatable Fluorescent Protein mEos2 Displays Repeated Photoactivation after a Long-Lived Dark State in the Red Photoconverted Form". In: *The Journal of Physical Chemistry Letters* 1.9, pp. 1506–1510.

Annibale, Paolo, Stefano Vanni, Marco Scarselli, Ursula Rothlisberger, and Aleksandra Radenovic (2011a). "Identification of clustering artifacts in photoactivated localization microscopy." In: *Nature Methods* 8.7, pp. 527–528.

— (2011b). "Quantitative photo activated localization microscopy: unraveling the effects of photoblinking." In: *PLOS ONE* 6.7, e22678.

Aquino, Daniel, Andreas Schönle, Claudia Geisler, Claas V Middendorff, Christian A Wurm, Yosuke Okamura, Thorsten Lang, Stefan W Hell, and Alexander Egner (2011). "Two-color nanoscopy of three-dimensional volumes by 4Pi detection of stochastically switched fluorophores." In: *Nature Methods* 8.4, pp. 353–359.

Ash, E A and G Nicholls (1972). "Super-resolution Aperture Scanning Microscope". In: *Nature* 237.5357, pp. 510–512.

Axelrod, D, T P Burghardt, and N L Thompson (1984). "Total internal reflection fluorescence." In: *Annual review of biophysics and bioengineering* 13, pp. 247–268.

Axelrod, Daniel (2001). "Selective imaging of surface fluorescence with very high aperture microscope objectives". In: *Journal of Biomedical Optics* 6.1, pp. 6–13.

Axelrod, Daniel (2012). “Fluorescence excitation and imaging of single molecules near dielectric-coated and bare surfaces: a theoretical study”. In: *Journal of Microscopy* 247.2, pp. 147–160.

— (2013). “Evanescent Excitation and Emission in Fluorescence Microscopy”. In: *Biophysical journal* 104.7, pp. 1401–1409.

Babcock, Hazen P and Xiaowei Zhuang (2017). “Analyzing Single Molecule Localization Microscopy Data Using Cubic Splines.” In: *Scientific reports* 7.1, p. 552.

Backer, Adam S, Mikael P Backlund, Matthew D Lew, and W E Moerner (2013). “Single-molecule orientation measurements with a quadrated pupil”. In: *Optics Letters* 38.9, pp. 1521–3.

Backer, Adam S, Mikael P Backlund, Alexander R von Diezmann, Steffen J Sahl, and W E Moerner (2014). “A bisected pupil for studying single-molecule orientational dynamics and its application to three-dimensional super-resolution microscopy”. In: *Applied Physics Letters* 104.19, p. 193701.

Backlund, Mikael P, Matthew D Lew, Adam S Backer, Steffen J Sahl, Ginni Grover, Anurag Agrawal, Rafael Piestun, and WE Moerner (2012). “Simultaneous, accurate measurement of the 3D position and orientation of single molecules”. In: *Proceedings of the National Academy of Sciences* 109.47, pp. 19087–19092.

Backlund, Mikael P, Matthew D Lew, Adam S Backer, Steffen J Sahl, and W E Moerner (2013). “The Role of Molecular Dipole Orientation in Single-Molecule Fluorescence Microscopy and Implications for Super-Resolution Imaging”. In: *ChemPhysChem* 15.4, pp. 587–599.

Backlund, Mikael P, Amir Arbabi, Petar N Petrov, Ehsan Arbabi, Saumya Saurabh, Andrei Faraon, and W E Moerner (2016). “Removing orientation-induced localization biases in single-molecule microscopy using a broadband metasurface mask”. In: *Nature Photonics*, pp. 1–5.

Baddeley, David, Mark B Cannell, and Christian Soeller (2010). “Visualization of Localization Microscopy Data”. In: *Microscopy and Microanalysis* 16.01, pp. 64–72.

Baddeley, David, David Crossman, Sabrina Rossberger, Juliette E Cheyne, Johanna M Montgomery, Isuru D Jayasinghe, Christoph Cremer, Mark B Cannell, and Christian Soeller (2011a). “4D Super-Resolution Microscopy with Conventional Fluorophores and Single Wavelength Excitation in Optically Thick Cells and Tissues”. In: *PLOS ONE* 6.5, e20645–18.

Baddeley, David, Mark B Cannell, and Christian Soeller (2011b). “Three-dimensional sub-100 nm super-resolution imaging of biological samples using a phase ramp in the objective pupil”. In: *Nano Research* 4.6, pp. 589–598.

Badieirostami, Majid, Matthew D Lew, Michael A Thompson, and W E Moerner (2010). “Three-dimensional localization precision of the double-helix point spread function versus astigmatism and biplane”. In: *Applied Physics Letters* 97.16, p. 161103.

Bailey, Brent, Daniel L Farkas, D Lansing Taylor, and Frederick Lanni (1993). “Enhancement of axial resolution in fluorescence microscopy by standing-wave excitation”. In: *Nature* 366.6450, pp. 44–48.

Bailey, Brent, Vijay Krishnamurthi, Daniel L Farkas, D Lansing Taylor, and Frederick Lanni (1994). “Three-dimensional imaging of biological specimens with standing wave fluorescence microscopy”. In: *IS&T/SPIE 1994 International Symposium on Electronic Imaging: Science and Technology* 2184, pp. 208–213.

Balazs, Balint, Joran Deschamps, Marvin Albert, Jonas Ries, and Lars Hufnagel (2017). “A real-time compression library for microscopy images”. In: *bioRxiv*. DOI: `10.1101/164624`. eprint: `http://www.biorxiv.org/content/early/2017/07/21/164624.full.pdf`. URL: `http://www.biorxiv.org/content/early/2017/07/21/164624`.

Balzarotti, Francisco, Yvan Eilers, Klaus C Gwosch, Arvid H Gynnå, Volker Westphal, Fernando D Stefani, Johan Elf, and Stefan W Hell (2016). “Nanometer resolution imaging and tracking of fluorescent molecules with minimal photon fluxes”. In: *Science*, aak9913.

Banterle, Niccol, Khanh Huy Bui, Edward A Lemke, and Martin Beck (2013). “Fourier ring correlation as a resolution criterion for super-resolution microscopy”. In: *Journal of Structural Biology* 183.3, pp. 363–367.

Barak, L S and W W Webb (1982). “Diffusion of low density lipoprotein-receptor complex on human fibroblasts”. In: *The Journal of Cell Biology* 95.3, pp. 846–852.

Barroca, Thomas, Karla Balaa, Julie Delahaye, Sandrine Lévêque-Fort, and Emmanuel Fort (2011). “Full-field supercritical angle fluorescence microscopy for live cell imaging”. In: *Optics Letters*, pp. 1–3.

Barroca, Thomas, Karla Balaa, Sandrine Lévêque-Fort, and Emmanuel Fort (2012). “Full-Field Near-Field Optical Microscope for Cell Imaging”. In: *Physical Review Letters* 108.21, p. 218101.

Basché, T and W E Moerner (1991). “Optical modification of a single impurity molecule in a solid”. In: *Nature*.

Bates, Mark, Timothy R Blosser, and Xiaowei Zhuang (2005). “Short-range spectroscopic ruler based on a single-molecule optical switch.” In: *Physical Review Letters* 94.10, p. 108101.

Bates, Mark, Bo Huang, Graham T Dempsey, and Xiaowei Zhuang (2007). “Multicolor super-resolution imaging with photo-switchable fluorescent probes.” In: *Science* 317.5845, pp. 1749–1753.

Bates, Mark, Graham T Dempsey, Kok Hao Chen, and Xiaowei Zhuang (2012). “Multicolor Super-Resolution Fluorescence Imaging via Multi-Parameter Fluorophore Detection”. In: *ChemPhysChem* 13.1, pp. 99–107.

Baumgart, Florian, Andreas M Arnold, Konrad Leskovar, Kaj Staszek, Martin Fölser, Julian Weghuber, Hannes Stockinger, and Gerhard J Schütz (2016). “Varying label density allows artifact-free analysis of membrane-protein nanoclusters”. In: *Nature Methods* 13.8, pp. 661–664.

Beck, M, M Aschwanden, and A Stemmer (2008). “Sub-100-nanometre resolution in total internal reflection fluorescence microscopy”. In: *Journal of Microscopy* 232.1, pp. 99–105.

Bellve, Karl, Clive Standley, Lawrence Lifshitz, and Kevin Fogarty (2014). “Design and implementation of 3D focus stabilization for fluorescence microscopy”. In: *Biophysical Journal* 106.2, 606a.

Benda, Ale, Hayden Aitken, Danielle S Davies, Renee Whan, and Claire Goldsbury (2016). “STED imaging of tau filaments in Alzheimer’s disease cortical grey matter”. In: *Journal of Structural Biology* 195.3, pp. 345–352.

Betzig, E (1995). “Proposed method for molecular optical imaging.” In: *Optics Letters* 20.3, pp. 237–239.

Betzig, E and R J Chichester (1993). “Single molecules observed by near-field scanning optical microscopy.” In: *Science* 262.5138, pp. 1422–1425.

Betzig, E, J K Trautman, T D Harris, J S Weiner, and R L Kostelak (1991). “Breaking the diffraction barrier: optical microscopy on a nanometric scale.” In: *Science* 251.5000, pp. 1468–1470.

Betzig, Eric, George H Patterson, Rachid Sougrat, O Wolf Lindwasser, Scott Olenych, Juan S Bonifacino, Michael W Davidson, Jennifer Lippincott-Schwartz, and Harald F Hess (2006). “Imaging Intracellular Fluorescent Proteins at Nanometer Resolution”. In: *Science* 313.5793, pp. 1642–1645.

Bewersdorf, J, R SCHMIDT, and S W Hell (2006). “Comparison of I5M and 4Pi-microscopy”. In: *Journal of Microscopy* 222.2, pp. 105–117.

Bewersdorf, Joerg, Jordan R Myers, and Travis J Gould (2011). “Total internal reflection STED microscopy”. In: *Optics express* 19.14, pp. 13351–13357.

Biteen, Julie S, Michael A Thompson, Nicole K Tselentis, Grant R Bowman, Lucy Shapiro, and WE Moerner (2008). “Super-resolution imaging in live Caulobacter crescentus cells using photoswitchable EYFP”. In: *Nature Methods* 5.11, pp. 947–949.

Biteen, Julie S, Erin D Goley, Lucy Shapiro, and W E Moerner (2012). "Three-Dimensional Super-Resolution Imaging of the Midplane Protein FtsZ in Live Caulobacter crescentus-Cells Using Astigmatism". In: *ChemPhysChem* 13.4, pp. 1007–1012.

Blom, Hans and Jerker Widengren (2017). "Stimulated Emission Depletion Microscopy." In: *Chemical Reviews*.

Bock, H, C Geisler, C A Wurm, C von Middendorff, S Jakobs, A Schönle, A Egner, S W Hell, and C Eggeling (2007). "Two-color far-field fluorescence nanoscopy based on photoswitchable emitters". In: *Applied Physics B* 88.2, pp. 161–165.

Boettiger, Alistair N et al. (2016). "Super-resolution imaging reveals distinct chromatin folding for different epigenetic states". In: *Nature* 529.7586, pp. 418–422.

Böhm, Ulrike, Stefan W Hell, and Roman Schmidt (2016). "4Pi-RESOLFT nanoscopy". In: *Nature Communications* 7, pp. 1–8.

Booth, Martin J (2007). "Adaptive optics in microscopy". In: *Philosophical Transactions of the Royal Society of London A: Mathematical, Physical and Engineering Sciences* 365.1861, pp. 2829–2843.

Bossi, Mariano, Jonas Fo lling, Vladimir N Belov, Vadim P Boyarskiy, Rebecca Medda, Alexander Egner, Christian Eggeling, Andreas Scho nle, and Stefan W Hell (2008). "Multicolor Far-Field Fluorescence Nanoscopy through Isolated Detection of Distinct Molecular Species". In: *Nano letters* 8.8, pp. 2463–2468.

Botcherby, Edward J, Rimas Juskaitis, Martin J Booth, and Tony Wilson (2007). "Aberration-free optical refocusing in high numerical aperture microscopy". In: *Optics letters* 32.14.

Bouissou, Anais et al. (2017). "Podosome Force Generation Machinery: a Local Balance between Protrusion at the Core and Traction at the Ring". In: *ACS Nano*, acsnano.7b00622–46.

Bourg, N, C Mayet, G Dupuis, T Barroca, P Bon, S Lécart, E Fort, and S Lévêque-Fort (2015). "Direct optical nanoscopy with axially localized detection". In: *Nature Photonics*, pp. 1–8.

Bretschneider, Stefan, Christian Eggeling, and Stefan W Hell (2007). "Breaking the diffraction barrier in fluorescence microscopy by optical shelving." In: *Physical Review Letters* 98.21, p. 218103.

Broeken, Jordi, Bernd Rieger, and Sjoerd Stallinga (2014). "Simultaneous measurement of position and color of single fluorescent emitters using diffractive optics". In: *Optics Letters* 39.11, pp. 3352–4.

Brown, Timothy A, Ariana N Tkachuk, Gleb Shtengel, Benjamin G Kopek, Daniel F Bogenhagen, Harald F Hess, and David A Clayton (2011). "Superresolution fluorescence imaging of mitochondrial nucleoids reveals their spatial range, limits, and membrane interaction." In: *Molecular and cellular biology* 31.24, pp. 4994–5010.

Brunstein, Maia, Karine Hérault, and Martin Oheim (2014). "Eliminating Unwanted Far-Field Excitation in Objective-Type TIRF. Part II. Combined Evanescent-Wave Excitation and Supercritical-Angle Fluorescence Detection Improves Optical Sectioning". In: *Biophysical journal* 106.5, pp. 1044–1056.

Brunstein, Maia, Lopamudra Roy, and Martin Oheim (2017). "Near-Membrane Refractometry Using Supercritical Angle Fluorescence". In: *Biophysical journal* 112.9, pp. 1940–1948.

Burgert, Anne, Sebastian Letschert, Sören Doose, and Markus Sauer (2015). "Artifacts in single-molecule localization microscopy". In: *Histochemistry and Cell Biology*, pp. 1–9.

Burke, Daniel, Emil B Kromann, Joerg Bewersdorf, Martin J Booth, and Travis J Gould (2013). "Auto-aligning stimulated emission depletion microscope using adaptive optics". In: *Optics Letters* 38.11, pp. 1860–1862.

Burke, Daniel, Brian Patton, Fang Huang, Joerg Bewersdorf, and Martin J Booth (2015). "Adaptive optics correction of specimen-induced aberrations in single-molecule switching microscopy". In: *Optica* 2.2, pp. 177–185.

Carlini, Lina, Seamus J Holden, Kyle M Douglass, and Suliana Manley (2015). "Correction of a Depth-Dependent Lateral Distortion in 3D Super-Resolution Imaging". In: *PLOS ONE* 10.11, e0142949.

Case, Lindsay B, Michelle A Baird, Gleb Shtengel, Sharon L Campbell, Harald F Hess, Michael W Davidson, and Clare M Waterman (2015). "Molecular mechanism of vinculin activation and nanoscale spatial organization in focal adhesions." In: *Nature cell biology* 17.7, pp. 880–892.

Chao, Jerry, E Sally Ward, and Raimund J Ober (2016). "Fisher information theory for parameter estimation in single molecule microscopy: tutorial". In: *JOSA A* 33.7, B36–B57.

Chen, Bi-Chang et al. (2014). "Lattice light-sheet microscopy: Imaging molecules to embryos at high spatiotemporal resolution". In: *Science* 346.6208, pp. 1257998–1257998.

Chen, Kok Hao, Alistair N Boettiger, Jeffrey R Moffitt, Siyuan Wang, and Xiaowei Zhuang (2015). "Spatially resolved, highly multiplexed RNA profiling in single cells". In: *Science* 348.6233, aaa6090.

Chmyrov, Andriy, Jan Keller, Tim Grotjohann, Michael Ratz, Elisa d'Este, Stefan Jakobs, Christian Eggeling, and Stefan W Hell (2013). "Nanoscopy with more than 100,000 'doughnuts'". In: *Nature Methods* 10.8, pp. 737–740.

Chozinski, Tyler J, Lauren A Gagnon, and Joshua C Vaughan (2014). "Twinkle, twinkle little star: photoswitchable fluorophores for super-resolution imaging." In: *FEBS letters* 588.19, pp. 3603–3612.

Chung, Euiheon, Daekeun Kim, Yan Cui, Yang-Hyo Kim, and Peter T C So (2007). "Two-dimensional standing wave total internal reflection fluorescence microscopy: superresolution imaging of single molecular and biological specimens." In: *Biophysical journal* 93.5, pp. 1747–1757.

Churchman, L Stirling and James A Spudich (2012). "Colocalization of Fluorescent Probes: Accurate and Precise Registration with Nanometer Resolution". In: *Cold Spring Harbor Protocols* 2012.2, pdb.top067918.

Churchman, L Stirling, Zeynep Ökten, Ronald S Rock, John F Dawson, and James A Spudich (2005). "Single molecule high-resolution colocalization of Cy3 and Cy5 attached to macromolecules measures intramolecular distances through time". In: *Proceedings of the National Academy of Sciences of the United States of America* 102.5, pp. 1419–1423.

Cloin, Bas MC et al. (2017). "Efficient switching of mCherry fluorescence using chemical caging". In: *Proceedings of the National Academy of Sciences*, p. 201617280.

Coles, Benjamin C, Stephen E D Webb, Noah Schwartz, Daniel J Rolfe, Marisa Martin-Fernandez, and Valentina Lo Schiavo (2016). "Characterisation of the effects of optical aberrations in single molecule techniques". In: *Biomedical Optics Express* 7.5, pp. 1755–1767.

Collins, Tony J et al. (2007). "ImageJ for microscopy". In: *Biotechniques* 43.1 Suppl, pp. 25–30.

Coto Hernández, Iván, Marco Castello, Luca Lanzanò, Marta d'Amora, Paolo Bianchini, Alberto Diaspro, and Giuseppe Vicidomini (2016). "Two-Photon Excitation STED Microscopy with Time-Gated Detection." In: *Scientific reports* 6, p. 19419.

Cox, Guy and Colin J R Sheppard (2003). "Practical limits of resolution in confocal and non-linear microscopy". In: *Microscopy Research and Technique* 63.1, pp. 18–22.

Cox, Susan, Edward Rosten, James Monypenny, Tijana Jovanovic-Talisman, Dylan T Burnette, Jennifer Lippincott-Schwartz, Gareth E Jones, and Rainer Heintzmann (2012). "Bayesian localization microscopy reveals nanoscale podosome dynamics". In: *Nature Methods* 9.2, pp. 195–200.

Curdt, Franziska, Johann Engelhardt, Roman Schmidt, Simon J Herr, Stefan W Hell, Steffen J Sahl, and Tobias Lutz (2015). "isoSTED nanoscopy with intrinsic beam alignment". In: *Optics express* 23.24, pp. 30891–30903.

Dani, Adish, Bo Huang, Joseph Bergan, Catherine Dulac, and Xiaowei Zhuang (2010). "Superresolution Imaging of Chemical Synapses in the Brain". In: *Neuron* 68.5, pp. 843–856.

Danzl, Johann G, Sven C Sidenstein, Carola Gregor, Nicolai T Urban, Peter Ilgen, Stefan Jakobs, and Stefan W Hell (2016). "Coordinate-targeted fluorescence nanoscopy with multiple off states". In: *Nature Photonics*, pp. 1–8.

Davidovits, Paul and M David Egger (1969). “Scanning laser microscope”. In: *Nature* 223.5208, pp. 831–831.

Demmerle, Justin, Eva Wegel, Lothar Schermelleh, and Ian M Dobbie (2015). “Assessing resolution in super-resolution imaging”. In: *Methods* 88, pp. 3–10.

Dempsey, Graham T, Mark Bates, Walter E Kowtoniuk, David R Liu, Roger Y Tsien, and Xiaowei Zhuang (2009). “Photoswitching Mechanism of Cyanine Dyes”. In: *Journal of the American Chemical Society* 131.51, pp. 18192–18193.

Dempsey, Graham T, Joshua C Vaughan, Kok Hao Chen, Mark Bates, and Xiaowei Zhuang (2011). “Evaluation of fluorophores for optimal performance in localization-based super-resolution imaging”. In: *Nature Methods* 8.12, pp. 1027–1036.

Denk, Winfried, James H Strickler, Watt W Webb, et al. (1990). “Two-photon laser scanning fluorescence microscopy”. In: *Science* 248.4951, pp. 73–76.

Dertinger, T, R Colyer, G Iyer, S Weiss, and J Enderlein (2009). “Fast, background-free, 3D super-resolution optical fluctuation imaging (SOFI)”. In: *Proceedings of the National Academy of Sciences of the United States of America* 106.52, pp. 22287–22292.

Deschamps, Joran, Markus Mund, and Jonas Ries (2014). “3D superresolution microscopy by supercritical angle detection”. In: *Optics express* 22.23, pp. 29081–29091.

Deschamps, Joran, Andreas Rowald, and Joran Ries (2016). “Efficient homogeneous illumination and optical sectioning for quantitative single-molecule localization microscopy”. In: *Optics express* 24.24, pp. 28080–28090.

Deschout, Hendrik, Francesca Cella Zanacchi, Michael Mlodzianoski, Alberto Diaspro, Joerg Bewersdorf, Samuel T Hess, and Kevin Braeckmans (2014). “Precisely and accurately localizing single emitters in fluorescence microscopy”. In: *Nature Methods* 11.3, pp. 253–266.

Dickson, Robert M, Andrew B Cubitt, Roger Y Tsien, and WE Moerner (1997). “On/off blinking and switching behaviour of single molecules of green fluorescent protein”. In: *Nature* 388.6640, pp. 355–358.

Diekmann, Robin, Deanna Wolfson, Christoph Spahn, Mike Heilemann, Mark Schüttpelz, and Thomas Huser (2016). “Nanoscopy of bacterial cells immobilized by holographic optical tweezers”. In: *Nature Communications* 7.

Diezmann, Alex von, Maurice Y Lee, Matthew D Lew, and W E Moerner (2015). “Correcting field-dependent aberrations with nanoscale accuracy in three-dimensional single-molecule localization microscopy”. In: *Optica* 2.11, pp. 985–993.

Diezmann, Alex von, Yoav Shechtman, and W E Moerner (2017). “Three-Dimensional Localization of Single Molecules for Super-Resolution Imaging and Single-Particle Tracking”. In: *Chemical Reviews*, acs.chemrev.6b00629–32.

Ding, Jun B, Kevin T Takasaki, and Bernardo L Sabatini (2009). “Supraresolution Imaging in Brain Slices using Stimulated-Emission Depletion Two-Photon Laser Scanning Microscopy”. In: *Neuron* 63.4, pp. 429–437.

Dlasková, Andrea, Jitka Šantorová, Joerg Bewersdorf, John M Schreiner, Katarina Smolková, Michael J Mlodzianoski, Petr Ježek, and Steven P Callahan (2011). “Sample drift correction in 3D fluorescence photoactivation localization microscopy”. In: *Optics express* 19.16, pp. 15009–15019.

Dong, Biqin, Luay Almassalha, Ben E Urban, The-Quyen Nguyen, Satya Khuon, Teng-Leong Chew, Vadim Backman, Cheng Sun, and Hao F Zhang (2016). “Super-resolution spectroscopic microscopy via photon localization.” In: *Nature Communications* 7, p. 12290.

Donnert, Gerald et al. (2007). “Two-Color Far-Field Fluorescence Nanoscopy”. In: *Biophysical journal* 92.8, pp. L67–L69.

Douglass, Kyle M, Christian Sieben, Anna Archetti, Ambroise Lambert, and Suliana Manley (2016). “Super-resolution imaging of multiple cells by optimised flat-field epi-illumination.” In: *Nature Photonics* 10.11, pp. 705–708.

Drexhage, KH (1970). “Influence of a dielectric interface on fluorescence decay time”. In: *Journal of luminescence* 1, pp. 693–701.

Dries, K van den, S L Schwartz, J Byars, M B M Meddens, M Bolomini-Vittori, D S Lidke, C G Figdor, K A Lidke, and A Cambi (2013). “Dual-color superresolution microscopy reveals nanoscale organization of mechanosensory podosomes.” In: *Molecular Biology of the Cell* 24.13, pp. 2112–2123.

Durisic, Nela, Antoine G Godin, Claudia M Wever, Colin D Heyes, Melike Lakadamyali, and Joseph A Dent (2012). “Stoichiometry of the human glycine receptor revealed by direct subunit counting.” In: *The Journal of neuroscience : the official journal of the Society for Neuroscience* 32.37, pp. 12915–12920.

Durisic, Nela, Lara Laparra Cuervo, and Melike Lakadamyali (2014). “Quantitative super-resolution microscopy: pitfalls and strategies for image analysis.” In: *Current opinion in chemical biology* 20, pp. 22–28.

Dyba, Marcus and Stefan W Hell (2002). “Focal spots of size lambda/23 open up far-field fluorescence microscopy at 33 nm axial resolution.” In: *Physical Review Letters* 88.16, p. 163901.

Dyba, Marcus, Stefan Jakobs, and Stefan W Hell (2003). “Immunofluorescence stimulated emission depletion microscopy.” In: *Nature Biotechnology* 21.11, pp. 1303–1304.

Edelstein, Arthur, Nenad Amodaj, Karl Hoover, Ron Vale, and Nico Stuurman (2010). *Computer Control of Microscopes Using µManager*. Hoboken, NJ, USA: John Wiley & Sons, Inc.

Eggeling, Christian, Christian Ringemann, Marcel Leutenegger, Stefan W Hell, and Theo Lasser (2012). “Fluorescence correlation spectroscopy with a total internal reflection fluorescence STED microscope (TIRF-STED-FCS)”. In: *Optics express* 20.5, pp. 5243–5263.

Einstein, Albert (1917). “Zur Quantentheorie der Strahlung”. In: *Physikalische Zeitschrift* 18.

Elmokadem, Ahmed and Ji Yu (2015). “Optimal Drift Correction for Superresolution Localization Microscopy with Bayesian Inference.” In: *Biophysical journal* 109.9, pp. 1772–1780.

Enderlein, Jörg (1999). “Fluorescence detection of single molecules near a solution/glass interface–an electrodynamic analysis”. In: *Chemical physics letters* 308.3, pp. 263–266.

Enderlein, Jörg, Thomas Ruckstuhl, and Stefan Seeger (1999). “Highly efficient optical detection of surface-generated fluorescence”. In: *Applied optics* 38.4, pp. 724–732.

Endesfelder, Ulrike and Mike Heilemann (2014). “Art and artifacts in single-molecule localization microscopy: beyond attractive images”. In: *Nature Methods* 11.3, pp. 235–238.

Engelhardt, Johann, Jan Keller, Patrick Hoyer, Matthias Reuss, Thorsten Staudt, and Stefan W Hell (2011). “Molecular Orientation Affects Localization Accuracy in Superresolution Far-Field Fluorescence Microscopy”. In: *Nano letters* 11.1, pp. 209–213.

Erdélyi, M, J Sinkó, R Kákonyi, A Kelemen, E Rees, D Varga, and G Szabó (2015). “Origin and compensation of imaging artefacts in localization-based super-resolution microscopy”. In: *Methods* 88, pp. 122–132.

Errico, Claudia, Juliette Pierre, Sophie Pezet, Yann Desailly, Zsolt Lenkei, Olivier Couture, and Mickael Tanter (2015). “Ultrafast ultrasound localization microscopy for deep super-resolution vascular imaging”. In: *Nature* 527.7579, pp. 499–502.

Facomprez, Aurélie, Emmanuel Beaurepaire, and Delphine Débarre (2012). “Accuracy of correction in modal sensorless adaptive optics”. In: *Optics express* 20.3, pp. 2598–2612.

Finan, Kieran, Anika Raulf, and Mike Heilemann (2015). “A Set of Homo-Oligomeric Standards Allows Accurate Protein Counting”. In: *Angewandte Chemie International Edition* 54.41, pp. 12049–12052.

Fiolka, Reto, Lin Shao, E Hesper Rego, Michael W Davidson, and Mats G L Gustafsson (2012). “Time-lapse two-color 3D imaging of live cells with doubled resolution using structured illumination”. In: *Proceedings of the National Academy of Sciences of the United States of America* 109.14, pp. 5311–5315.

Fölling, J, V Belov, R Kunetsky, R Medda, A Schönle, A Egner, C Eggeling, M Bossi, and S W Hell (2007). “Photochromic Rhodamines Provide Nanoscopy with Optical Sectioning”. In: *Angewandte Chemie International Edition* 46.33, pp. 6266–6270.

Fölling, Jonas, Mariano Bossi, Hannes Bock, Rebecca Medda, Christian A Wurm, Birka Hein, Stefan Jakobs, Christian Eggeling, and Stefan W Hell (2008). "Fluorescence nanoscopy by ground-state depletion and single-molecule return". In: *Nature Methods* 5.11, pp. 943–945.

Fourier, J (1822). *Theorie analytique de la chaleur*.

Franke, Christian, Markus Sauer, and Sebastian van de Linde (2016). "Photometry unlocks 3D information from 2D localization microscopy data." In: *Nature Methods*.

Fricke, Franziska, Joel Beaudouin, Roland Eils, and Mike Heilemann (2015). "One, two or three? Probing the stoichiometry of membrane proteins by single-molecule localization microscopy." In: *Scientific reports* 5.1, p. 14072.

Frohn, Jan T, Helmut F Knapp, and Andreas Stemmer (2000). "True optical resolution beyond the Rayleigh limit achieved by standing wave illumination". In: *Proceedings of the National Academy of Sciences of the United States of America* 97.13, pp. 7232–7236.

Fu, Guo, Tao Huang, Jackson Buss, Carla Coltharp, Zach Hensel, and Jie Xiao (2010). "In vivo structure of the E. coli FtsZ-ring revealed by photoactivated localization microscopy (PALM)." In: *PLOS ONE* 5.9, e12682.

Fujimaki, Y and H Taniguchi (2014). "Reduction of speckle contrast in multimode fibers using piezoelectric vibrator". In: *SPIE LASE*, 89601S.

Funatsu, T, Y Harada, M Tokunaga, and K Saito (1995). "Imaging of single fluorescent molecules and individual ATP turnovers by single myosin molecules in aqueous solution". In: *Nature*.

Gallego, Raquel Salvador, Markus Mund, Katia Cosentino, Jale Schneider, Joseph Unsay, Ulrich Schraermeyer, Johann Engelhardt, Jonas Ries, and Ana J García Sáez (2016). "Bax assembly into rings and arcs in apoptotic mitochondria is linked to membrane pores". In: *The EMBO Journal*, e201593384.

Gao, Liang, Lin Shao, Christopher D Higgins, John S Poulton, Mark Peifer, Michael W Davidson, Xufeng Wu, Bob Goldstein, and Eric Betzig (2012). "Noninvasive Imaging beyond the Diffraction Limit of 3D Dynamics in Thickly Fluorescent Specimens". In: *Cell* 151.6, pp. 1370–1385.

Gao, Liang, Lin Shao, Bi-Chang Chen, and Eric Betzig (2014). "3D live fluorescence imaging of cellular dynamics using Bessel beam plane illumination microscopy". In: *Nature Protocols* 9.5, pp. 1083–1101.

Garcia-Parajo, Maria F, Alessandra Cambi, Juan A Torreno-Pina, Nancy Thompson, and Ken Jacobson (2014). "Nanoclustering as a dominant feature of plasma membrane organization". In: *Journal of Cell Science* 127.23, pp. 4995–5005.

Gautier, Arnaud, Alexandre Juillerat, Christian Heinis, Ivan Reis Corrêa, Maik Kindermann, Florent Beaufils, and Kai Johnsson (2008). "An engineered protein tag for multiprotein labeling in living cells." In: *Chem Biol* 15.2, pp. 128–136.

Geerts, H, M De Brabander, R Nuydens, S Geuens, M Moeremans, J De Mey, and P Hollenbeck (1987). "Nanovid tracking: a new automatic method for the study of mobility in living cells based on colloidal gold and video microscopy". In: *Biophysical journal* 52.5, pp. 775–782.

Geisler, C, A Sch nle, C von Middendorff, H Bock, C Eggeling, A Egner, and S W Hell (2007). "Resolution of $\lambda/10$ in fluorescence microscopy using fast single molecule photoswitching". In: *Applied Physics A* 88.2, pp. 223–226.

Gelles, Jeff, Bruce J Schnapp, and Michael P Sheetz (1988). "Tracking kinesin-driven movements with nanometre-scale precision". In: *Nature* 331.6155, pp. 450–453.

Georgiades, Pantelis, Viki J Allan, Mark Dickinson, and Thomas A Waigh (2016). "Reduction of coherent artefacts in super-resolution fluorescence localisation microscopy." In: *Journal of Microscopy*.

Gliko, Olga, Gaddum D Reddy, Bahman Anvari, William E Brownell, and Peter Saggau (2006). "Standing wave total internal reflection fluorescence microscopy to measure the size of nanostructures in living cells". In: *Journal of Biomedical Optics* 11.6, pp. 064013–064013–5.

Gliko, Olga, Duemani G Reddy, William E Brownell, and Peter Saggau (2008). “Development of fast two-dimensional standing wave microscopy using acousto-optic deflectors”. In: 68610B–68610B.

Goodman, J W (1968). *Introduction to Fourier Optics*.

Gordon, Matthew P, Taekjip Ha, and Paul R Selvin (2004). “Single-molecule high-resolution imaging with photobleaching”. In: *Proceedings of the National Academy of Sciences of the United States of America* 101.17, pp. 6462–6465.

Göttfert, Fabian, Christian A Wurm, Veronika Mueller, Sebastian Berning, Volker C Cordes, Alf Honigmann, and Stefan W Hell (2013). “Coaligned Dual-Channel STED Nanoscopy and Molecular Diffusion Analysis at 20 nm Resolution”. In: *Biophysical journal* 105.1, pp. L01–L03.

Gould, Travis J, Daniel Burke, Joerg Bewersdorf, and Martin J Booth (2012). “Adaptive optics enables 3D STED microscopy in aberrating specimens”. In: *Optics express* 20.19, pp. 20998–21009.

Graetzel, Chauncey, Marcel Suter, and Manuel Aschwanden (2015). “Reducing laser speckle with electroactive polymer actuators”. In: *SPIE*. Ed. by Yoseph Bar-Cohen. SPIE, p. 943004.

Griffié, Juliette et al. (2016). “A Bayesian cluster analysis method for single-molecule localization microscopy data”. In: *Nature Protocols* 11.12, pp. 2499–2514.

Griffié, Juliette et al. (2017). “3D Bayesian cluster analysis of super-resolution data reveals LAT recruitment to the T cell synapse.” In: *Scientific reports* 7.1, p. 4077.

Grover, Ginni, Rafael Piestun, and Wyatt Mohrman (2015). “Real-time adaptive drift correction for super-resolution localization microscopy”. In: *Optics express* 23.18, pp. 23887–23898.

Gu, M and C J R Sheppard (1995). “Comparison of three-dimensional imaging properties between two-photon and single-photon fluorescence microscopy”. In: *Journal of Microscopy* 177.2, pp. 128–137.

Gunewardene, Mudalige S, Fedor V Subach, Travis J Gould, Gregory P Penoncello, Manasa V Gudheti, Vladislav V Verkhusha, and Samuel T Hess (2011). “Superresolution imaging of multiple fluorescent proteins with highly overlapping emission spectra in living cells.” In: *Biophysical journal* 101.6, pp. 1522–1528.

Gunzenhauser, Julia, Nicolas Olivier, Thomas Pengo, and Suliana Manley (2012). “Quantitative super-resolution imaging reveals protein stoichiometry and nanoscale morphology of assembling HIV-Gag virions.” In: *Nano letters* 12.9, pp. 4705–4710.

Gur, Aviram, Zeev Zalevsky, Vicente Mic, Javier Garc a, and Dror Fixler (2010). “The Limitations of Nonlinear Fluorescence Effect in Super Resolution Saturated Structured Illumination Microscopy System”. In: *Journal of Fluorescence* 21.3, pp. 1075–1082.

Gustafsson, M G L (2000). “Surpassing the lateral resolution limit by a factor of two using structured illumination microscopy”. In: *Journal of Microscopy* 198.2, pp. 82–87.

Gustafsson, Mats G L (2005). “Nonlinear structured-illumination microscopy: Wide-field fluorescence imaging with theoretically unlimited resolution”. In: *Proceedings of the National Academy of Sciences of the United States of America* 102.37, pp. 13081–13086.

Gustafsson, Mats G L, David A Agard, and John W Sedat (1995). “Sevenfold improvement of axial resolution in 3D wide-field microscopy using two objective lenses”. In: *IS&T/SPIE's Symposium on Electronic Imaging: Science & Technology* 2412, pp. 147–156.

Gustafsson, Mats G L, Lin Shao, Peter M Carlton, C J Rachel Wang, Inna N Golubovskaya, W Zacheus Cande, David A Agard, and John W Sedat (2008). “Three-Dimensional Resolution Doubling in Wide-Field Fluorescence Microscopy by Structured Illumination”. In: *Biophysical journal* 94.12, pp. 4957–4970.

Gustafsson, Mats GL, David A Agard, and John W Sedat (1996). “3D widefield microscopy with two objective lenses: experimental verification of improved axial resolution”. In: pp. 62–67.

Gustavsson, Anna-Karin, Petar N Petrov, Maurice Y Lee, Yoav Shechtman, and WE Moerner (2017). "3D Single-Molecule Super-Resolution Microscopy With A Tilted Light Sheet". In: *bioRxiv*, p. 135699.

Ha, T, T Enderle, D F Ogletree, D S Chemla, P R Selvin, and S Weiss (1996). "Probing the interaction between two single molecules: fluorescence resonance energy transfer between a single donor and a single acceptor." In: *Proceedings of the National Academy of Sciences of the United States of America* 93.13, pp. 6264–6268.

Ha, Woosung, Sejin Lee, Yongmin Jung, Jun-Ki Kim, and Kyunghwan Oh (2009). "Acousto-optic control of speckle contrast in multimode fibers with a cylindrical piezoelectric transducer oscillating in the radial direction." In: *Optics express* 17.20, pp. 17536–17546.

Hajj, Bassam, Jan Wisniewski, Mohamed El Beheiry, Jiji Chen, Andrey Revyakin, Carl Wu, and Maxime Dahan (2014). "Whole-cell, multicolor superresolution imaging using volumetric multifocus microscopy." In: *Proceedings of the National Academy of Sciences of the United States of America* 111.49, pp. 17480–17485.

Hajj, Bassam, Mohamed El Beheiry, and Maxime Dahan (2016). "PSF engineering in multifocus microscopy for increased depth volumetric imaging". In: *Biomedical Optics Express* 7.3, pp. 726–731.

Hanne, Janina, Fabian Göttfert, Jiří Schimer, Maria Anders-Össwein, Jan Konvalinka, Johann Engelhardt, Barbara Müller, Stefan W Hell, and Hans-Georg Kräusslich (2016). "Stimulated Emission Depletion Nanoscopy Reveals Time-Course of Human Immunodeficiency Virus Proteolytic Maturation." In: *ACS Nano* 10.9, pp. 8215–8222.

Hecht, B, D W Pohl, H Heinzelmann, and L Novotny (1995). ""Tunnel" near-field optical microscopy: TNOM-2". In: *Ultramicroscopy* 61.1-4, pp. 99–104.

Heilemann, Mike, Dirk P Herten, Rainer Heintzmann, Christoph Cremer, Christian M ller, Philip Tinnefeld, Kenneth D Weston, J rgen Wolfrum, and Markus Sauer (2002). "High-Resolution Colocalization of Single Dye Molecules by Fluorescence Lifetime Imaging Microscopy". In: *Analytical Chemistry* 74.14, pp. 3511–3517.

Heilemann, Mike, Emmanuel Margeat, Robert Kasper, Markus Sauer, and Philip Tinnefeld (2005). "Carbocyanine Dyes as Efficient Reversible Single-Molecule Optical Switch". In: *Journal of the American Chemical Society* 127.11, pp. 3801–3806.

Heilemann, Mike, Sebastian van de Linde, Mark Schüttpelz, Robert Kasper, Britta Seefeldt, Anindita Mukherjee, Philip Tinnefeld, and Markus Sauer (2008). "Subdiffraction-resolution fluorescence imaging with conventional fluorescent probes." In: *Angewandte Chemie International Edition* 47.33, pp. 6172–6176.

Heilemann, Mike, Sebastian van de Linde, Anindita Mukherjee, and Markus Sauer (2009). "Super-Resolution Imaging with Small Organic Fluorophores". In: *Angewandte Chemie International Edition* 48.37, pp. 6903–6908.

Heintzmann, Rainer and Christoph G Cremer (1999). "Laterally modulated excitation microscopy: improvement of resolution by using a diffraction grating". In: *BiOS Europe '98* 3568, pp. 185–196.

Heintzmann, Rainer, Thomas M Jovin, and Christoph Cremer (2002). "Saturated patterned excitation microscopy–a concept for optical resolution improvement." In: *Journal of the Optical Society of America A* 19.8, pp. 1599–1609.

Hell, S, G Reiner, C Cremer, and E H K Stelzer (1993). "Aberrations in confocal fluorescence microscopy induced by mismatches in refractive index". In: *Journal of Microscopy* 169.3, pp. 391–405.

Hell, S W (2009). "Microscopy and its focal switch". In: *Nature Methods* 6.1, pp. 24–32.

Hell, S W and M Kroug (1995). "Ground-state-depletion fluorscence microscopy: A concept for breaking the diffraction resolution limit". In: *Applied Physics B: Lasers and Optics*.

Hell, S W and J Wichmann (1994a). *Breaking the Diffraction Resolution Limit by Stimulated Emission Depletion Fluorescence Microscopy Optics Letters vol. 19*. Washington.

Hell, Stefan and Ernst HK Stelzer (1992). "Properties of a 4Pi confocal fluorescence microscope". In: *JOSA A* 9.12, pp. 2159–2166.

Hell, Stefan W (2003). “Toward fluorescence nanoscopy”. In: *Nature Biotechnology* 21.11, pp. 1347–1355.

Hell, Stefan W and Jan Wichmann (1994b). “Breaking the diffraction resolution limit by stimulated emission: stimulated-emission-depletion fluorescence microscopy”. In: *Optics Letters* 19.11, pp. 780–782.

Hell, Stefan W, Marcus Dyba, and Stefan Jakobs (2004). “Concepts for nanoscale resolution in fluorescence microscopy”. In: *Current Opinion in Neurobiology* 14.5, pp. 599–609.

Hell, SW, S Jakobs, and L Kastrup (2003). “Imaging and writing at the nanoscale with focused visible light through saturable optical transitions”. In: *Applied Physics A: Materials Science & Processing* 77.7, pp. 859–860.

Hellen, Edward H and Daniel Axelrod (1987). “Fluorescence emission at dielectric and metal-film interfaces”. In: *JOSA B* 4.3, pp. 337–350.

Henriques, Ricardo, Mickaël Lelek, Eugenio F Fornasiero, Flavia Valtorta, Christophe Zimmer, and Musa M Mhlanga (2010). “QuickPALM: 3D real-time photoactivation nanoscopy image processing in ImageJ”. In: *Nature Methods* 7.5, pp. 339–340.

Hess, Samuel T, Thanu P K Girirajan, and Michael D Mason (2006). “Ultra-High Resolution Imaging by Fluorescence Photoactivation Localization Microscopy”. In: *Biophysical journal* 91.11, pp. 4258–4272.

Hess, Samuel T, Travis J Gould, Manasa V Gudheti, Sarah A Maas, Kevin D Mills, and Joshua Zimmerberg (2007). “Dynamic clustered distribution of hemagglutinin resolved at 40 nm in living cell membranes discriminates between raft theories.” In: *Proceedings of the National Academy of Sciences of the United States of America* 104.44, pp. 17370–17375.

Holden, Seamus J, Stephan Uphoff, and Achillefs N Kapanidis (2011). “DAOSTORM: an algorithm for high- density super-resolution microscopy”. In: *Nature Methods* 8.4, pp. 279–280.

Holden, Seamus J, Thomas Pengo, Karin L Meibom, Carmen Fernandez Fernandez, Justine Collier, and Suliana Manley (2014). “High throughput 3D super-resolution microscopy reveals Caulobacter crescentus in vivo Z-ring organization.” In: *Proceedings of the National Academy of Sciences of the United States of America* 111.12, pp. 4566–4571.

Hooke, Robert (1665). *Micrographia: or some physiological descriptions of minute bodies made by magnifying glasses, with observations and inquiries thereupon*. London: Martyn and Allestry.

Huang, B, W Wang, M Bates, and X Zhuang (2008a). “Three-Dimensional Super-Resolution Imaging by Stochastic Optical Reconstruction Microscopy”. In: *Science* 319.5864, pp. 810–813.

Huang, Bo, Sara A Jones, Boerries Brandenburg, and Xiaowei Zhuang (2008b). “Whole-cell 3D STORM reveals interactions between cellular structures with nanometer-scale resolution”. In: *Nature Methods* 5.12, pp. 1047–1052.

Huang, Fang, Samantha L Schwartz, Jason M Byars, and Keith A Lidke (2011). “Simultaneous multiple-emitter fitting for single molecule super-resolution imaging”. In: *Biomedical Optics Express* 2.5, pp. 1377–1393.

Huang, Fang et al. (2013). “Video-rate nanoscopy using sCMOS camera-specific single-molecule localization algorithms”. In: *Nature Methods* 10.7, pp. 653–658.

Huang, Fang et al. (2016). “Ultra-High Resolution 3D Imaging of Whole Cells”. In: *Cell*, pp. 1–37.

Hummer, Gerhard, Franziska Fricke, and Mike Heilemann (2016). “Model-independent counting of molecules in single-molecule localization microscopy.” In: *Molecular Biology of the Cell*, mbc.E16–07–0525.

Iinuma, Ryosuke, Yonggang Ke, Ralf Jungmann, Thomas Schlichthaerle, Johannes B Woehrstein, and Peng Yin (2014). “Polyhedra Self-Assembled from DNA Tripods and Characterized with 3D DNA-PAINT”. In: *Science* 344.6179, pp. 65–69.

Inoué, S et al. (2001). “Centrifuge polarizing microscope. I. Rationale, design and instrument performance”. In: *Journal of Microscopy* 201.3, pp. 341–356.

Izeddin, I et al. (2012a). "Wavelet analysis for single molecule localization microscopy". In: *Optics express* 20.3, pp. 2081–2095.

Izeddin, Ignacio, Mohamed El Beheiry, Jordi Andilla, Daniel Ciepielewski, Xavier Darzacq, and Maxime Dahan (2012b). "PSF shaping using adaptive optics for three-dimensional single-molecule super-resolution imaging and tracking". In: *Optics express* 20.5, pp. 4957–4967.

Jesacher, Alexander, Clemens Roider, Monika Ritsch-Marte, and Stefan Bernet (2014). "Axial super-localisation using rotating point spread functions shaped by polarisation-dependent phase modulation". In: *Optics express* 22.4, pp. 4029–4037.

Jia, Shu, Joshua C Vaughan, and Xiaowei Zhuang (2014). "Isotropic three-dimensional super-resolution imaging with a self-bending point spread function". In: *Nature Photonics*, pp. 1–5.

Jiang, Shenghang, Seongjin Park, Sai Divya Challapalli, Jingyi Fei, and Yong Wang (2017). "Robust nonparametric quantification of clustering density of molecules in single-molecule localization microscopy." In: *PLOS ONE* 12.6, e0179975.

Jones, Sara A, Sang-Hee Shim, Jiang He, and Xiaowei Zhuang (2011). "Fast, three-dimensional super-resolution imaging of live cells." In: *Nature Publishing Group* 8.6, pp. 499–508.

Juette, Manuel F, Travis J Gould, Mark D Lessard, Michael J Mlodzianoski, Bhupendra S Nagpure, Brian T Bennett, Samuel T Hess, and Joerg Bewersdorf (2008). "Three-dimensional sub–100 nm resolution fluorescence microscopy of thick samples". In: *Nature Methods* 5.6, pp. 527–529.

Jungmann, Ralf, Christian Steinhauer, Max Scheible, Anton Kuzyk, Philip Tinnefeld, and Friedrich C Simmel (2010). "Single-Molecule Kinetics and Super-Resolution Microscopy by Fluorescence Imaging of Transient Binding on DNA Origami". In: *Nano letters* 10.11, pp. 4756–4761.

Jungmann, Ralf, Maier S Avendaño, Johannes B Woehrstein, Mingjie Dai, William M Shih, and Peng Yin (2014). "Multiplexed 3D cellular super-resolution imaging with DNA-PAINT and Exchange-PAINT". In: *Nature Methods* 11.3, pp. 313–318.

Jungmann, Ralf, Maier S Avendaño, Mingjie Dai, Johannes B Woehrstein, Sarit S Agasti, Zachary Feiger, Avital Rodal, and Peng Yin (2016). "Quantitative super-resolution imaging with qPAINT." In: *Nature Methods* 13.5, pp. 439–442.

Kanchanawong, Pakorn, Gleb Shtengel, Ana M Pasapera, Ericka B Ramko, Michael W Davidson, Harald F Hess, and Clare M Waterman (2010). "Nanoscale architecture of integrin-based cell adhesions". In: *Nature* 468.7323, pp. 580–584.

Kao, H P and A S Verkman (1994). "Tracking of single fluorescent particles in three dimensions: use of cylindrical optics to encode particle position." In: *Biophysical journal* 67.3, pp. 1291–1300.

Karathanasis, Christos, Franziska Fricke, Gerhard Hummer, and Mike Heilemann (2017). "Molecule Counts in Localization Microscopy with Organic Fluorophores." In: *ChemPhysChem* 18.8, pp. 942–948.

Keller, Philipp J, Annette D Schmidt, Anthony Santella, Khaled Khairy, Zhirong Bao, Joachim Wittbrodt, and Ernst H K Stelzer (2010). "Fast, high-contrast imaging of animal development with scanned light sheet-based structured-illumination microscopy". In: *Nature Methods* 7.8, pp. 637–642.

Keppler, Antje, Horst Pick, Claudio Arrivoli, Horst Vogel, and Kai Johnsson (2004). "Labeling of fusion proteins with synthetic fluorophores in live cells." In: *Proceedings of the National Academy of Sciences of the United States of America* 101.27, pp. 9955–9959.

Kittel, Robert J et al. (2006). "Bruchpilot Promotes Active Zone Assembly, Ca²⁺ Channel Clustering, and Vesicle Release". In: *Science* 312.5776, pp. 1051–1054.

Klar, T A and S W Hell (1999). "Subdiffraction resolution in far-field fluorescence microscopy." In: *Optics Letters* 24.14, pp. 954–956.

Klar, T A, S Jakobs, M Dyba, A Egner, and S W Hell (2000). "Fluorescence microscopy with diffraction resolution barrier broken by stimulated emission." In: *Proceedings of the National Academy of Sciences of the United States of America* 97.15, pp. 8206–8210.

Kner, Peter, Bryant B Chhun, Eric R Griffis, Lukman Winoto, and Mats G L Gustafsson (2009). "Super-resolution video microscopy of live cells by structured illumination". In: *Nature Methods* 6.5, pp. 339–342.

Köhler, A (1893). *Köhler: Ein neues Beleuchtungsverfahren für mikrophotog... - Google Scholar*. Zeitschrift für wissenschaftliche Mikroskopie und für ...

Kopek, Benjamin G, Gleb Shtengel, C Shan Xu, David A Clayton, and Harald F Hess (2012). "Correlative 3D superresolution fluorescence and electron microscopy reveal the relationship of mitochondrial nucleoids to membranes". In: *Proceedings of the National Academy of Sciences of the United States of America* 109.16, pp. 6136–6141.

Kopfermann, H and R Ladenburg (1928). "Experimental Proof of 'Negative Dispersion.'" In: *Nature* 122, pp. 438–439.

Köthe, Ullrich, Frank Herrmannsdörfer, Ilia Kats, and Fred A Hamprecht (2014). "SimpleSTORM: a fast, self-calibrating reconstruction algorithm for localization microscopy". In: *Histochemistry and Cell Biology* 141.6, pp. 613–627.

Kubota, Shigeo and Joseph W Goodman (2010). "Very efficient speckle contrast reduction realized by moving diffuser device." In: *Applied Optics* 49.23, pp. 4385–4391.

Kuratomi, Yuhei, Kazuo Sekiya, Hiroaki Satoh, Tatsuhiro Tomiyama, Tohru Kawakami, Baku Katagiri, Yoshito Suzuki, and Tatsuo Uchida (2010). "Speckle reduction mechanism in laser rear projection displays using a small moving diffuser." In: *JOSA A* 27.8, pp. 1812–1817.

Kwakwa, Kwasi, Alexander Savell, Timothy Davies, Ian Munro, Simona Parrinello, Marco A Purbhoo, Chris Dunsby, Mark A A Neil, and Paul M W French (2016). "easySTORM: a robust, lower-cost approach to localisation and TIRF microscopy." In: *Journal of biophotonics* 9.9, pp. 948–957.

Lacoste, Thilo D, Xavier Michalet, Fabien Pinaud, Daniel S Chemla, A Paul Alivisatos, and Shimon Weiss (2000). "Ultrahigh-resolution multicolor colocalization of single fluorescent probes". In: *Proceedings of the National Academy of Sciences of the United States of America* 97.17, pp. 9461–9466.

Laine, Romain F, Anna Albecka, Sebastian van de Linde, Eric J Rees, Colin M Crump, and Clemens F Kaminski (2015). "Structural analysis of herpes simplex virus by optical super-resolution imaging." In: *Nature Communications* 6, p. 5980.

Laplante, Caroline, Fang Huang, Irene R Tebbs, Joerg Bewersdorf, and Thomas D Pollard (2016). "Molecular organization of cytokinesis nodes and contractile rings by super-resolution fluorescence microscopy of live fission yeast". In: *Proceedings of the National Academy of Sciences of the United States of America* 113.40, E5876–E5885.

Lee, Sang-Hyuk, Jae Yen Shin, Antony Lee, and Carlos Bustamante (2012). "Counting single photoactivatable fluorescent molecules by photoactivated localization microscopy (PALM)." In: *Proceedings of the National Academy of Sciences of the United States of America* 109.43, pp. 17436–17441.

Legant, Wesley R, Lin Shao, Jonathan B Grimm, Timothy A Brown, Daniel E Milkie, Brian B Avants, Luke D Lavis, and Eric Betzig (2016). "High-density three-dimensional localization microscopy across large volumes." In: *Nature Publishing Group*.

Lehmann, Martin, Gregor Lichtner, Haider Klenz, and Jan Schmoranzer (2015). "Novel organic dyes for multicolor localization-based super-resolution microscopy". In: *Journal of biophotonics* 9.1-2, pp. 161–170.

Levet, Florian, Eric Hosy, Adel Kechkar, Corey Butler, Anne Beghin, Daniel Choquet, and Jean-Baptiste Sibarita (2015). "SR-Tesseler: a method to segment and quantify localization-based super-resolution microscopy data". In: *Nature Methods*.

Lew, M D and W E Moerner (2014). "Azimuthal Polarization Filtering for Accurate, Precise, and Robust Single-Molecule Localization Microscopy". In: *Nano letters* 14.11, pp. 6407–6413.

Lew, Matthew D, Steven F Lee, Majid Badieirostami, and W E Moerner (2011a). "Corkscrew point spread function for far-field three-dimensional nanoscale localization of pointlike objects." In: *Optics Letters* 36.2, pp. 202–204.

Lew, Matthew D, Steven F Lee, Jerod L Ptacin, Marissa K Lee, Robert J Twieg, Lucy Shapiro, and W E Moerner (2011b). "Three-dimensional superresolution colocalization of intracellular protein superstructures and the cell surface in live Caulobacter crescentus". In: *Proceedings of the National Academy of Sciences of the United States of America* 108.46, E1102–E1110.

Lew, Matthew D, Mikael P Backlund, and W E Moerner (2013). "Rotational Mobility of Single Molecules Affects Localization Accuracy in Super-Resolution Fluorescence Microscopy". In: *Nano letters* 13.9, pp. 3967–3972.

Li, Dong et al. (2015). "Extended-resolution structured illumination imaging of endocytic and cytoskeletal dynamics". In: *Science* 349.6251, aab3500.

Li, Yiming, Markus Mund, Philipp Hoess, Ulf Matti, Bianca Nijmeijer, Vilma Jimenez Sabinina, Jan Ellenberg, Ingmar Schoen, and Jonas Ries (2017). "Fast, robust and precise 3D localization for arbitrary point spread functions". In: *bioRxiv*. DOI: `10.1101/172643`. eprint: `http://www.biorxiv.org/content/early/2017/08/08/172643.full.pdf`. URL: `http://www.biorxiv.org/content/early/2017/08/08/172643`.

Lidke, K A, B Rieger, T M Jovin, and R Heintzmann (2005). "Superresolution by localization of quantum dots using blinking statistics". In: *Optics express*.

Linde, Sebastian van de, Ulrike Endesfelder, Anindita Mukherjee, Mark Schüttpelz, Gerd Wiebusch, Steve Wolter, Mike Heilemann, and Markus Sauer (2009). "Multicolor photoswitching microscopy for subdiffraction-resolution fluorescence imaging." In: *Photochemical & photobiological sciences : Official journal of the European Photochemistry Association and the European Society for Photobiology* 8.4, pp. 465–469.

Linde, Sebastian van de, Ivan Krstić, Thomas Prisner, Sören Doose, Mike Heilemann, and Markus Sauer (2011). "Photoinduced formation of reversible dye radicals and their impact on super-resolution imaging". In: *Photochemical & Photobiological Sciences* 10.4, pp. 499–506.

Lippincott-Schwartz, Jennifer and George H Patterson (2009). "Photoactivatable fluorescent proteins for diffraction-limited and super-resolution imaging". In: *Trends in cell biology* 19.11, pp. 555–565.

Long, Fan et al. (2011). "Localization-based super-resolution microscopy with an sCMOS camera". In: *Optics express* 19.20, pp. 19156–19168.

Los, Georgyi V et al. (2008). "HaloTag: A Novel Protein Labeling Technology for Cell Imaging and Protein Analysis". In: *ACS Chemical Biology* 3.6, pp. 373–382.

Löschberger, Anna, Sebastian van de Linde, Marie-Christine Dabauvalle, Bernd Rieger, Mike Heilemann, Georg Krohne, and Markus Sauer (2012). "Super-resolution imaging visualizes the eightfold symmetry of gp210 proteins around the nuclear pore complex and resolves the central channel with nanometer resolution". In: *Journal of Cell Science* 125.3, pp. 570–575.

Löschberger, Anna, Christian Franke, Georg Krohne, Sebastian van de Linde, and Markus Sauer (2014). "Correlative super-resolution fluorescence and electron microscopy of the nuclear pore complex with molecular resolution". In: *J Cell Sci* 127.20, pp. 4351–4355.

Lukosz, W (1979). "Light emission by magnetic and electric dipoles close to a plane dielectric interface. III. Radiation patterns of dipoles with arbitrary orientation". In: *JOSA* 69.11, pp. 1495–1503.

Lukosz, W and RE Kunz (1977a). "Light emission by magnetic and electric dipoles close to a plane dielectric interface. II. Radiation patterns of perpendicular oriented dipoles". In: *JOSA* 67.12, pp. 1615–1619.

— (1977b). "Light emission by magnetic and electric dipoles close to a plane interface. I. Total radiated power". In: *JOSA* 67.12, pp. 1607–1615.

Ma, Hongqiang, Rao Fu, Jianquan Xu, and Yang Liu (2017a). "A simple and cost-effective setup for super-resolution localization microscopy". In: *Scientific reports* 7.1, p. 1542.

Ma, Hongqiang, Jianquan Xu, Jingyi Jin, Yi Huang, and Yang Liu (2017b). "A Simple Marker-Assisted 3D Nanometer Drift Correction Method for Superresolution Microscopy". In: *Biophysical journal* 112.10, pp. 2196–2208.

Macklin, J J, J K Trautman, T D Harris, and L E Brus (1996). "Imaging and time-resolved spectroscopy of single molecules at an interface". In: *Science*.

Maiman, T H, R H Hoskins, I J d'Haenens, C K Asawa, and V Evtuhov (1961). "Stimulated Optical Emission in Fluorescent Solids. II. Spectroscopy and Stimulated Emission in Ruby". In: *Physical Review* 123.4, pp. 1151–1157.

Manley, Suliana, Jennifer M Gillette, George H Patterson, Hari Shroff, Harald F Hess, Eric Betzig, and Jennifer Lippincott-Schwartz (2008). "High-density mapping of single-molecule trajectories with photoactivated localization microscopy." In: *Nature Publishing Group* 5.2, pp. 155–157.

Manzo, Carlo and Maria F Garcia-Parajo (2015). "A review of progress in single particle tracking: from methods to biophysical insights". In: *Reports on Progress in Physics*, pp. 1–29.

McGorty, Ryan, Daichi Kamiyama, and Bo Huang (2013). "Active microscope stabilization in three dimensions using image correlation". In: *Optical Nanoscopy* 2.1, p. 3.

McGorty, Ryan, Joerg Schnitzbauer, Wei Zhang, and Bo Huang (2014). "Correction of depth-dependent aberrations in 3D single-molecule localization and super-resolution microscopy". In: *Optics Letters* 39.2, pp. 275–4.

Merckle, F, P Kern, P Léna, F Rigaut, JC Fontanella, G Rousset, C Boyer, JP Gaffard, and P Jagourel (1989). "Successful tests of adaptive optics." In: *The Messenger* 58, pp. 1–4.

Mertz, Jerome (2000). "Radiative absorption, fluorescence, and scattering of a classical dipole near a lossless interface: a unified description". In: *JOSA B* 17.11, pp. 1906–1913.

Metha, D S, D N Naik, R K Singh, and M Takeda (2012). "Laser speckle reduction by multimode optical fiber bundle with combined temporal, spatial, and angular diversity". In: *Applied Optics*, pp. 1894–1904.

Meyer, Lars, Dominik Wildanger, Rebecca Medda, Annedore Punge, Silvio O Rizzoli, Gerald Donnert, and Stefan W Hell (2008). "Dual-Color STED Microscopy at 30-nm Focal-Plane Resolution". In: *Small* 4.8, pp. 1095–1100.

Middendorff, Claas von, Alexander Egner, Claudia Geisler, Stefan W Hell, and Andreas Schönle (2008). "Isotropic 3D Nanoscopy based on single emitter switching." In: *Optics express* 16.25, pp. 20774–20788.

Minoshima, Masafumi and Kazuya Kikuchi (2017). "Photostable and photoswitching fluorescent dyes for super-resolution imaging". In: *JBIC Journal of Biological Inorganic Chemistry* 90.418, pp. 1103–14.

Minsky, Marvin (1961). "Microscopy apparatus". In:

Mlodzianoski, Michael J, Manuel F Juette, Glen L Beane, and Joerg Bewersdorf (2009). "Experimental characterization of 3D localization techniques for particle-tracking and super-resolution microscopy". In: *Optics express* 17.10, pp. 8264–8277.

Moerner, W E (2002). "A Dozen Years of Single-Molecule Spectroscopy in Physics, Chemistry, and Biophysics". In: *The journal of physical chemistry. B* 106.5, pp. 910–927.

Moerner, W E and L Kador (1989). "Optical detection and spectroscopy of single molecules in a solid". In: *Physical Review Letters* 62.21, p. 2535.

Moffitt, Jeffrey R, Junjie Hao, Dhananjay Bambah-Mukku, Tian Lu, Catherine Dulac, and Xiaowei Zhuang (2016a). "High-performance multiplexed fluorescence in situ hybridization in culture and tissue with matrix imprinting and clearing". In: *Proceedings of the National Academy of Sciences of the United States of America* 113.50, pp. 14456–14461.

Moffitt, Jeffrey R, Junjie Hao, Guiping Wang, Kok Hao Chen, Hazen P Babcock, and Xiaowei Zhuang (2016b). "High-throughput single-cell gene-expression profiling with multiplexed error-robust fluorescence in situ hybridization." In: *Proceedings of the National Academy of Sciences of the United States of America* 113.39, pp. 11046–11051.

Moneron, Gael and Stefan W Hell (2009). "Two-photon excitation STED microscopy." In: *Optics express* 17.17, pp. 14567–14573.

Mortensen, Kim I, L Stirling Churchman, James A Spudich, and Henrik Flyvbjerg (2010). "Optimized localization analysis for single-molecule tracking and super-resolution microscopy". In: *Nature Methods* 7.5, pp. 377–381.

Mueller, V et al. (2011). "STED Nanoscopy Reveals Molecular Details of Cholesterol- and Cytoskeleton-Modulated Lipid Interactions in Living Cells". In: *Biophysical journal* 101.7, pp. 1651–1660.

Mund, Markus (2016). "Superresolution imaging of clathrin-mediated endocytosis in yeast." PhD thesis. Universität Heidelberg.

Mund, Markus, Charlotte Kaplan, and Jonas Ries (2014). "Localization microscopy in yeast." In: *Methods in cell biology* 123, pp. 253–271.

Muranyi, Walter, Sebastian Malkusch, Barbara Müller, Mike Heilemann, and Hans-Georg Kräusslich (2013). "Super-Resolution Microscopy Reveals Specific Recruitment of HIV-1 Envelope Proteins to Viral Assembly Sites Dependent on the Envelope C-Terminal Tail". In: *PLOS Pathogens* 9.2, e1003198.

Nahidiazar, Leila, Alexandra V Agronskaia, Jorrit Broertjes, Bram van den Broek, and Kees Jalink (2016). "Optimizing Imaging Conditions for Demanding Multi-Color Super Resolution Localization Microscopy." In: *PLOS ONE* 11.7, e0158884.

Nan, Xiaolin, Eric A Collisson, Sophia Lewis, Jing Huang, Tanja M Tamgüney, Jan T Liphardt, Frank McCormick, Joe W Gray, and Steven Chu (2013). "Single-molecule superresolution imaging allows quantitative analysis of RAF multimer formation and signaling". In: *Proceedings of the National Academy of Sciences of the United States of America* 110.46, pp. 18519–18524.

Neil, M A A, R Juškaitis, and T Wilson (1997). "Method of obtaining optical sectioning by using structured light in a conventional microscope". In: *Optics Letters* 22.24, pp. 1905–1907.

Neil, M A A, R Ju kaitis, and T Wilson (1998). "Real time 3D fluorescence microscopy by two beam interference illumination". In: *Optics communications* 153.1-3, pp. 1–4.

Neubeck, Alexander and Luc Van Gool (2006). "Efficient Non-Maximum Suppression". In: *Conference paper*, pp. 1–6.

Nieuwenhuizen, Robert P J, Keith A Lidke, Mark Bates, Daniela Leyton Puig, David Grünwald, Sjoerd Stallinga, and Bernd Rieger (2013). "Measuring image resolution in optical nanoscopy". In: *Nature Methods* 10.6, pp. 557–562.

Nixon-Abell, Jonathon et al. (2016). "Increased spatiotemporal resolution reveals highly dynamic dense tubular matrices in the peripheral ER". In: *Science* 354.6311, aaf3928.

Novotny, L (2007). "The history of near-field optics". In: *Progress in optics*.

Novotny, Lukas (1996). "Allowed and forbidden light in near-field optics. I. A single dipolar light source". In: *Optical Society of America*, pp. 1–14.

Novotny, Lukas and Bert Hecht (2010). *Principles of Nano-Optics*.

Olivier, Nicolas, Debora Keller, Pierre Gönczy, and Suliana Manley (2013a). "Resolution doubling in 3D-STORM imaging through improved buffers." In: *PLOS ONE* 8.7, e69004.

Olivier, Nicolas, Debora Keller, Vinoth Sundar Rajan, Pierre Gönczy, and Suliana Manley (2013b). "Simple buffers for 3D STORM microscopy". In: *Biomedical optics express* 4.6, pp. 885–899.

Ong, Wei Qiang, Y Rose Citron, Joerg Schnitzbauer, Daichi Kamiyama, and Bo Huang (2015). "Heavy water: a simple solution to increasing the brightness of fluorescent proteins in super-resolution imaging". In: *Chemical Communications* 51.70, pp. 13451–13453.

Orrit, M and J Bernard (1990). "Single pentacene molecules detected by fluorescence excitation in a p-terphenyl crystal." In: *Physical Review Letters* 65.21, pp. 2716–2719.

Ovesný, Martin, Pavel Křížek, Josef Borkovec, Zdeněk Švindrych, and Guy M Hagen (2014). "ThunderSTORM: a comprehensive ImageJ plug-in for PALM and STORM data analysis and super-resolution imaging". In: *Bioinformatics* 30.16, pp. 2389–2390.

Pageon, Sophie V, Philip R Nicovich, Mahdie Mollazade, Thibault Tabarin, and Katharina Gaus (2016). "Clus-DoC: a combined cluster detection and colocalization analysis for single-molecule localization microscopy data". In: *Molecular Biology of the Cell* 27.22, pp. 3627–3636.

Parthasarathy, Raghuveer (2012). "Rapid, accurate particle tracking by calculation of radial symmetry centers". In: *Nature Publishing Group*, pp. 1–5.

Patterson, George H and Jennifer Lippincott-Schwartz (2002). "A Photoactivatable GFP for Selective Photolabeling of Proteins and Cells". In: *Science* 297.5588, pp. 1873–1877.

Patton, Brian R, Daniel Burke, David Owald, Travis J Gould, Joerg Bewersdorf, and Martin J Booth (2016). "Three-dimensional STED microscopy of aberrating tissue using dual adaptive optics." In: *Optics express* 24.8, pp. 8862–8876.

Pavani, Sri Rama Prasanna, Michael A Thompson, Julie S Biteen, Samuel J Lord, Na Liu, Robert J Twieg, Rafael Piestun, and W E Moerner (2009). "Three-dimensional, single-molecule fluorescence imaging beyond the diffraction limit by using a double-helix point spread function". In: *Proceedings of the National Academy of Sciences of the United States of America* 106.9, pp. 2995–2999.

Pepperkok, Rainer and Jan Ellenberg (2006). "High-throughput fluorescence microscopy for systems biology." In: *Nature Reviews Molecular Cell Biology* 7.9, pp. 690–696.

Planchon, Thomas A, Liang Gao, Daniel E Milkie, Michael W Davidson, James A Galbraith, Catherine G Galbraith, and Eric Betzig (2011). "Rapid three-dimensional isotropic imaging of living cells using Bessel beam plane illumination." In: *Nature Publishing Group* 8.5, pp. 417–423.

Prabhat, P, S Ram, E S Ward, and R J Ober (2006). "Simultaneous imaging of several focal planes in fluorescence microscopy for the study of cellular dynamics in 3D". In: *Proceedings of the SPIE*.

Puchner, Elias M, Jessica M Walter, Robert Kasper, Bo Huang, and Wendell A Lim (2013). "Counting molecules in single organelles with superresolution microscopy allows tracking of the endosome maturation trajectory." In: *Proceedings of the National Academy of Sciences of the United States of America* 110.40, pp. 16015–16020.

Qu, Xiaohui, David Wu, Laurens Mets, and Norbert F Scherer (2004). "Nanometer-localized multiple single-molecule fluorescence microscopy". In: *Proceedings of the National Academy of Sciences of the United States of America* 101.31, pp. 11298–11303.

Ram, S, P Prabhat, E S Ward, and R J Ober (2009). "Improved single particle localization accuracy with dual objective multifocal plane microscopy". In: *Optics express*.

Ram, Sripad, Prashant Prabhat, Jerry Chao, E Sally Ward, and Raimund J Ober (2008). "High Accuracy 3D Quantum Dot Tracking with Multifocal Plane Microscopy for the Study of Fast Intracellular Dynamics in Live Cells". In: *Biophysical journal* 95.12, pp. 6025–6043.

Ram, Sripad, Dongyoung Kim, Raimund J Ober, and E Sally Ward (2012). "3D Single Molecule Tracking with Multifocal Plane Microscopy Reveals Rapid Intercellular Transferrin Transport at Epithelial Cell Barriers". In: *Biophysical journal* 103.7, pp. 1594–1603.

Rayleigh, J W (1896). "On the theory of optical images, with special reference to the microscope". In: *The London*.

Rees, Eric J, Miklós Erdélyi, Gabriele S Kaminski Schierle, Alex Knight, and Clemens F Kaminski (2013). "Elements of image processing in localization microscopy". In: *Journal of Optics* 15.9, p. 094012.

Rego, E Hesper, Lin Shao, John J Macklin, Lukman Winoto, Göran A Johansson, Nicholas Kamps-Hughes, Michael W Davidson, and Mats G L Gustafsson (2012). "Nonlinear structured-illumination microscopy with a photoswitchable protein reveals cellular structures at 50-nm resolution". In: *Proceedings of the National Academy of Sciences of the United States of America* 109.3, E135–E143.

Riedl, Julia et al. (2008). "Lifeact: a versatile marker to visualize F-actin". In: *Nature Methods* 5.7, pp. 605–607.

Rieger, Bernd and Sjoerd Stallinga (2013). "The Lateral and Axial Localization Uncertainty in Super-Resolution Light Microscopy". In: *ChemPhysChem* 15.4, pp. 664–670.

Rieger, Bernd, Robert Nieuwenhuizen, and Sjoerd Stallinga (2014). "Image Processing and Analysis for Single-Molecule Localization Microscopy imaging". In: *IEEE Signal Processing Magazine* 32.1, pp. 49–57.

Ries, Jonas, Thomas Ruckstuhl, Dorinel Verdes, and Petra Schwille (2008). "Supercritical Angle Fluorescence Correlation Spectroscopy". In: *Biophysical journal* 94.1, pp. 221–229.

Ries, Jonas, Charlotte Kaplan, Evgenia Platonova, Hadi Eghlidi, and Helge Ewers (2012). "A simple, versatile method for GFP-based super-resolution microscopy via nanobodies". In: *Nature Methods* 9.6, pp. 582–584.

Rivolta, Claudio (1986). "Airy disk diffraction pattern: comparison of some values of f/no. and obscuration ratio". In: *Applied optics* 25.14, pp. 2404–2408.

Rollins, Geoffrey C, Jae Yen Shin, Carlos Bustamante, and Steve Pressé (2015). "Stochastic approach to the molecular counting problem in superresolution microscopy". In: *Proceedings of the National Academy of Sciences of the United States of America* 112.2, E110–E118.

Rossy, Jérémie, Dylan M Owen, David J Williamson, Zhengmin Yang, and Katharina Gaus (2012). "Conformational states of the kinase Lck regulate clustering in early T cell signaling". In: *Nature Immunology* 14.1, pp. 82–89.

Rousset, G et al. (1990). "First diffraction-limited astronomical images with adaptive optics". In: *Astronomy and Astrophysics* 230, pp. L29–L32.

Rubin-Delanchy, Patrick, Garth L Burn, Juliette Griffi, David J Williamson, Nicholas A Heard, Andrew P Cope, and Dylan M Owen (2015). "Bayesian cluster identification in single-molecule localization microscopy data". In: *Nature Methods* 12.11, pp. 1072–1076.

Ruckstuhl, Thomas, Jörg Enderlein, Stefan Jung, and Stefan Seeger (2000). "Forbidden Light Detection from Single Molecules". In: *Analytical Chemistry* 72.9, pp. 2117–2123.

Ruckstuhl, Thomas, Dorinel Verdes, Christian M Winterflood, and Stefan Seeger (2011). "Simultaneous near-field and far-field fluorescence microscopy of single molecules". In: *Optics express*, pp. 1–9.

Rust, Michael J, Mark Bates, and Xiaowei Zhuang (2006). "Sub-diffraction-limit imaging by stochastic optical reconstruction microscopy (STORM)." In: *Nature Methods* 3.10, pp. 793–795.

Sako, Yasushi, Shigeru Minoghchi, and Toshio Yanagida (2000). "Single-molecule imaging of EGFR signalling on the surface of living cells". In: *Nature cell biology* 2.3, pp. 168–172.

Scarselli, Marco, Paolo Annibale, and Aleksandra Radenovic (2012). "Cell type-specific β2-adrenergic receptor clusters identified using photoactivated localization microscopy are not lipid raft related, but depend on actin cytoskeleton integrity." In: *Journal of Biological Chemistry* 287.20, pp. 16768–16780.

Schaefer, L H, D Schuster, and J Schaffer (2004). "Structured illumination microscopy: artefact analysis and reduction utilizing a parameter optimization approach." In: *Journal of Microscopy* 216.Pt 2, pp. 165–174.

Schawlow, A L and C H Townes (1958). "Infrared and Optical Masers". In: *Physical Review* 112.6, p. 1940.

Schermelleh, Lothar et al. (2008). "Subdiffraction Multicolor Imaging of the Nuclear Periphery with 3D Structured Illumination Microscopy". In: *Science* 320.5881, pp. 1332–1336.

Schmidt, T, G J Schütz, W Baumgartner, H J Gruber, and H Schindler (1996). "Imaging of single molecule diffusion." In: *Proceedings of the National Academy of Sciences of the United States of America* 93.7, pp. 2926–2929.

Schmied, Jörgen J, Carsten Forthmann, Enrico Pibiri, Birka Lalkens, Philipp Nickels, Tim Liedl, and Philip Tinnefeld (2013). "DNA origami nanopillars as standards for three-dimensional superresolution microscopy". In: *Nano letters* 13.2, pp. 781–785.

Schnitzbauer, J, R McGorty, and B Huang (2013). "4Pi fluorescence detection and 3D particle localization with a single objective". In: *Optics express* 21.17, pp. 19701–19708.

Schnitzbauer, Joerg, Maximilian T Strauss, Thomas Schlichthaerle, Florian Schueder, and Ralf Jungmann (2017). "Super-resolution microscopy with DNA-PAINT." In: *Nature Protocols* 12.6, pp. 1198–1228.

Schoen, Ingmar, Jonas Ries, Enrico Klotzsch, Helge Ewers, and Viola Vogel (2011). "Binding-Activated Localization Microscopy of DNA Structures". In: *Nano letters* 11.9, pp. 4008–4011.

Schütz, Gerhard J, Gerald Kada, Vassili Ph Pastushenko, and Hansgeorg Schindler (2000). "Properties of lipid microdomains in a muscle cell membrane visualized by single molecule microscopy". In: *The EMBO Journal* 19.5, pp. 892–901.

Sengupta, Prabuddha, Tijana Jovanovic-Talisman, Dunja Skoko, Malte Renz, Sarah L Veatch, and Jennifer Lippincott-Schwartz (2011). "Probing protein heterogeneity in the plasma membrane using PALM and pair correlation analysis". In: *Nature Methods* 8.11, pp. 969–975.

Sengupta, Prabuddha, Tijana Jovanovic-Talisman, and Jennifer Lippincott-Schwartz (2013). "Quantifying spatial organization in point-localization superresolution images using pair correlation analysis". In: *Nature Protocols* 8.2, pp. 345–354.

Seo, Denny, Henry Y Lu, Keng C Chou, Libin Abraham, Michael R Gold, and Reza Tafteh (2016). "Real-time 3D stabilization of a super-resolution microscope using an electrically tunable lens". In: *Optics express* 24.20, pp. 22959–22970.

Shannon, C E (1949). "Communication in the presence of noise". In: *Proceedings of the IRE*.

Shao, Lin, Berith Isaac, Satoru Uzawa, David A Agard, John W Sedat, and Mats G L Gustafsson (2008). "I5S: wide-field light microscopy with 100-nm-scale resolution in three dimensions." In: *Biophysical journal* 94.12, pp. 4971–4983.

Shao, Lin, Peter Kner, E Hesper Rego, and Mats G L Gustafsson (2011). "Super-resolution 3D microscopy of live whole cells using structured illumination". In: *Nature Methods* 8.12, pp. 1044–1046.

Sharonov, Alexey and Robin M Hochstrasser (2006). "Wide-field subdiffraction imaging by accumulated binding of diffusing probes." In: *Proceedings of the National Academy of Sciences of the United States of America* 103.50, pp. 18911–18916.

Shcherbakova, Daria M, Prabuddha Sengupta, Jennifer Lippincott-Schwartz, and Vladislav V Verkhusha (2014). "Photocontrollable Fluorescent Proteins for Superresolution Imaging". In: *Annual Review of Biophysics* 43.1, pp. 303–329.

Shechtman, Yoav, Steffen J Sahl, Adam S Backer, and W E Moerner (2014). "Optimal point spread function design for 3D imaging." In: *Physical Review Letters* 113.13, p. 133902.

Shechtman, Yoav, Lucien E Weiss, Adam S Backer, Steffen J Sahl, and W E Moerner (2015). "Precise Three-Dimensional Scan-Free Multiple-Particle Tracking over Large Axial Ranges with Tetrapod Point Spread Functions". In: *Nano letters* 15.6, pp. 4194–4199.

Shechtman, Yoav, Lucien E Weiss, Adam S Backer, Maurice Y Lee, and W E Moerner (2016). "Multicolour localization microscopy by point-spread-function engineering". In: *Nature Photonics*, pp. 1–6.

Sheppard, C J R and Min Gu (1992). "The significance of 3-D transfer functions in confocal scanning microscopy". In: *Journal of Microscopy* 165.3, pp. 377–390.

Shim, Sang-Hee et al. (2012). "Super-resolution fluorescence imaging of organelles in live cells with photoswitchable membrane probes." In: *Proceedings of the National Academy of Sciences of the United States of America* 109.35, pp. 13978–13983.

Shroff, Hari, Catherine G Galbraith, James A Galbraith, Helen White, Jennifer Gillette, Scott Olenych, Michael W Davidson, and Eric Betzig (2007). "Dual-color superresolution imaging of genetically expressed probes within individual adhesion complexes." In:

Proceedings of the National Academy of Sciences of the United States of America 104.51, pp. 20308–20313.

Shroff, Hari, Catherine G Galbraith, James A Galbraith, and Eric Betzig (2008). "Live-cell photoactivated localization microscopy of nanoscale adhesion dynamics". In: *Nature Methods* 5.5, pp. 417–423.

Shtengel, Gleb, Harald F Hess, Jennifer Lippincott-Schwartz, and Suliana Manley (2009). "Interferometric fluorescent super-resolution microscopy resolves 3D cellular ultrastructure". In: *Proceedings of the National Academy of Sciences of the United States of America*, pp. 1–6.

Sidenstein, Sven C, Elisa d'Este, Marvin J Böhm, Johann G Danzl, Vladimir N Belov, and Stefan W Hell (2016). "Multicolour Multilevel STED nanoscopy of Actin/Spectrin Organization at Synapses." In: *Scientific reports* 6, p. 26725.

Siskova, Zuzana et al. (2014). "Dendritic Structural Degeneration Is Functionally Linked to Cellular Hyperexcitability in a Mouse Model of Alzheimer?s Disease". In: *Neuron* 84.5, pp. 1023–1033.

Small, A R and R Parthasarathy (2014). "Superresolution localization methods". In: *Annual review of physical chemistry*.

Smith, Carlas S, Nikolai Joseph, Bernd Rieger, and Keith A Lidke (2010). "Fast, single-molecule localization that achieves theoretically minimum uncertainty". In: *Nature Methods* 7.5, pp. 373–375.

Sochacki, Kem A, Andrea M Dickey, Marie-Paule Strub, and Justin W Taraska (2017). "Endocytic proteins are partitioned at the edge of the clathrin lattice in mammalian cells". In: *Nature cell biology* 12, pp. 517–41.

Spahn, Christoph, Frank Herrmannsdörfer, Thomas Kuner, and Mike Heilemann (2016). "Temporal accumulation analysis provides simplified artifact-free analysis of membrane-protein nanoclusters". In: *Nature Methods* 13.12, pp. 963–964.

Stemmer, Andreas, Markus Beck, and Reto Fiolka (2008). "Structured illumination in total internal reflection fluorescence microscopy using a spatial light modulator". In: *Optics Letters* 33.14, pp. 1629–1631.

Stokes, G G (1852). "On the change of refrangibility of light". In: *Philosophical Transactions of the Royal Society of Science*.

Streibl, N (1985). "Three-dimensional imaging by a microscope". In: *JOSA A*.

Subach, Fedor V, George H Patterson, Suliana Manley, Jennifer M Gillette, Jennifer Lippincott-Schwartz, and Vladislav V Verkhusha (2009). "Photoactivatable mCherry for high-resolution two-color fluorescence microscopy". In: *Nature Methods* 6.2, pp. 153–159.

Synge, E H (1928). "A suggested method for extending microscopic resolution into the ultra-microscopic region". In: *The London*.

Szymborska, Anna, Alex de Marco, Nathalie Daigle, Volker C Cordes, John A G Briggs, and Jan Ellenberg (2013). "Nuclear Pore Scaffold Structure Analyzed by Super-Resolution Microscopy and Particle Averaging". In: *Science* 341.6146, pp. 655–658.

Tam, Johnny, Guillaume Alan Cordier, Joseph Steven Borbely, Ángel Sandoval Álvarez, and Melike Lakadamyali (2014). "Cross-Talk-Free Multi-Color STORM Imaging Using a Single Fluorophore". In: *PLOS ONE* 9.7, e101772.

Tehrani, Kayvan F, Jianquan Xu, Yiwen Zhang, Ping Shen, and Peter Kner (2015). "Adaptive optics stochastic optical reconstruction microscopy (AO-STORM) using a genetic algorithm." In: *Optics express* 23.10, pp. 13677–13692.

Testa, Ilaria et al. (2010). "Multicolor Fluorescence Nanoscopy in Fixed and Living Cells by Exciting Conventional Fluorophores with a Single Wavelength". In: *Biophysical journal* 99.8, pp. 2686–2694.

Thompson, Michael A, Jason M Casolari, Majid Badieirostami, Patrick O Brown, and W E Moerner (2010). "Three-dimensional tracking of single mRNA particles in Saccharomyces cerevisiae using a double-helix point spread function". In: *Proceedings of the National Academy of Sciences of the United States of America* 107.42, pp. 17864–17871.

Thompson, Russell E, Daniel R Larson, and Watt W Webb (2002). "Precise Nanometer Localization Analysis for Individual Fluorescent Probes". In: *Biophysical journal* 82.5, pp. 2775–2783.

Valley, Christopher C, Sheng Liu, Diane S Lidke, and Keith A Lidke (2015). "Sequential Superresolution Imaging of Multiple Targets Using a Single Fluorophore". In: *PLOS ONE* 10.4, e0123941.

Van Engelenburg, Schuyler B, Gleb Shtengel, Prabuddha Sengupta, Kayoko Waki, Michal Jarnik, Sherimay D Ablan, Eric O Freed, Harald F Hess, and Jennifer Lippincott-Schwartz (2014). "Distribution of ESCRT machinery at HIV assembly sites reveals virus scaffolding of ESCRT subunits". In: *Science* 343.6171, pp. 653–656.

Van Oijen, A M, G J Brakenhoff, J Köhler, J Schmidt, and M Muller (1999). "Far-field fluorescence microscopy beyond the diffraction limit". In: *JOSA A* 16.4, pp. 909–915.

Vancevska, Aleksandra, Kyle M Douglass, Verena Pfeiffer, Suliana Manley, and Joachim Lingner (2017). "The telomeric DNA damage response occurs in the absence of chromatin decompaction". In: *Genes & Development* 31.6, pp. 567–577.

Vaughan, Joshua C, Shu Jia, and Xiaowei Zhuang (2012). "Ultrabright photoactivatable fluorophores created by reductive caging". In: *Nature Methods* 9.12, pp. 1181–1184.

Veatch, Sarah L, Benjamin B Machta, Sarah A Shelby, Ethan N Chiang, David A Holowka, and Barbara A Baird (2012). "Correlation functions quantify super-resolution images and estimate apparent clustering due to over-counting." In: *PLOS ONE* 7.2, e31457.

Vogelsang, Jan, Thorben Cordes, Carsten Forthmann, Christian Steinhauer, and Philip Tinnefeld (2009). "Controlling the fluorescence of ordinary oxazine dyes for single-molecule switching and superresolution microscopy." In: *Proceedings of the National Academy of Sciences of the United States of America* 106.20, pp. 8107–8112.

Wäldchen, Sina, Julian Lehmann, Teresa Klein, Sebastian van de Linde, and Markus Sauer (2015). "Light-induced cell damage in live-cell super-resolution microscopy". In: *Scientific reports* 5, p. 15348.

Wang, Siyuan, Jeffrey R Moffitt, Graham T Dempsey, X Sunney Xie, and Xiaowei Zhuang (2014). "Characterization and development of photoactivatable fluorescent proteins for single-molecule–based superresolution imaging". In: *Proceedings of the National Academy of Sciences of the United States of America* 111.23, pp. 8452–8457.

Wang, Siyuan, Jun-Han Su, Brian J Beliveau, Bogdan Bintu, Jeffrey R Moffitt, Chao-ting Wu, and Xiaowei Zhuang (2016). "Spatial organization of chromatin domains and compartments in single chromosomes." In: *Science* 353.6299, pp. 598–602.

Wang, Wenqin, Gene-Wei Li, Chongyi Chen, X Sunney Xie, and Xiaowei Zhuang (2011). "Chromosome Organization by a Nucleoid-Associated Protein in Live Bacteria". In: *Science* 333.6048, pp. 1445–1449.

Watanabe, Tomonobu M, Takashi Sato, Kohsuke Gonda, and Hideo Higuchi (2007). "Three-dimensional nanometry of vesicle transport in living cells using dual-focus imaging optics." In: *Biochemical and biophysical research communications* 359.1, pp. 1–7.

Waters, Jennifer C (2009). "Accuracy and precision in quantitative fluorescence microscopy". In: *The Journal of Cell Biology* 185.7, pp. 1135–1148.

Westphal, Volker, Silvio O Rizzoli, Marcel A Lauterbach, Dirk Kamin, Reinhard Jahn, and Stefan W Hell (2008). "Video-Rate Far-Field Optical Nanoscopy Dissects Synaptic Vesicle Movement". In: *Science* 320.5873, pp. 246–249.

Wiedenmann, Jörg, Sergey Ivanchenko, Franz Oswald, Florian Schmitt, Carlheinz Röcker, Anya Salih, Klaus-Dieter Spindler, and G Ulrich Nienhaus (2004). "EosFP, a fluorescent marker protein with UV-inducible green-to-red fluorescence conversion." In: *Proceedings of the National Academy of Sciences of the United States of America* 101.45, pp. 15905–15910.

Wildanger, Dominik, Giuseppe Vicidomini, Johanna Bückers, Lars Kastrup, and Stefan W Hell (2011). "Simultaneous multi-lifetime multi-color STED imaging for colocalization analyses". In: *Optics express* 19.4, pp. 3130–3143.

Williams, C S and O A Becklund (1989). *Introduction to the Optical Transfer Function*. SPIE Press.

Williamson, David J, Dylan M Owen, Jérémie Rossy, Astrid Magenau, Matthias Wehrmann, J Justin Gooding, and Katharina Gaus (2011). "Pre-existing clusters of the adaptor Lat do not participate in early T cell signaling events". In: *Nature Immunology* 12.7, pp. 655–662.

Willig, Katrin I, Silvio O Rizzoli, Volker Westphal, Reinhard Jahn, and Stefan W Hell (2006). "STED microscopy reveals that synaptotagmin remains clustered after synaptic vesicle exocytosis". In: *Nature* 440.7086, pp. 935–939.

Wilson, T (1989). "Optical sectioning in confocal fluorescent microscopes". In: *Journal of Microscopy* 154.2, pp. 143–156.

— (2011). "Resolution and optical sectioning in the confocal microscope". In: *Journal of microscopy* 244.2, pp. 113–121.

Wilson, T and C Sheppard (1984). *Theory and practice of scanning optical microscopy*.

Winterflood, Christian M, Thomas Ruckstuhl, Dorinel Verdes, and Stefan Seeger (2010). "Nanometer Axial Resolution by Three-Dimensional Supercritical Angle Fluorescence Microscopy". In: *Physical Review Letters* 105.10, p. 108103.

Winterflood, Christian M, Evgenia Platonova, David Albrecht, and Helge Ewers (2015). "Dual-color 3D superresolution microscopy by combined spectral-demixing and biplane imaging." In: *Biophysical journal* 109.1, pp. 3–6.

Wollman, Roy and Nico Stuurman (2007). "High throughput microscopy: from raw images to discoveries". In: *Journal of cell science* 120.21, pp. 3715–3722.

Wolter, Steve, Mark Schüttpelz, Marko Tscherepanow, Sebastian Van de Linde, Mike Heilemann, and Markus Sauer (2010). "Real-time computation of subdiffraction-resolution fluorescence images". In: *Journal of microscopy* 237.1, pp. 12–22.

Xu, Ke, Guisheng Zhong, and Xiaowei Zhuang (2013). "Actin, Spectrin, and Associated Proteins Form a Periodic Cytoskeletal Structure in Axons". In: *Science* 339.6118, pp. 452–456.

York, Andrew G, Alireza Ghitani, Alipasha Vaziri, Michael W Davidson, and Hari Shroff (2011). "Confined activation and subdiffractive localization enables whole-cell PALM with genetically expressed probes". In: *Nature Methods* 8.4, pp. 327–333.

Young, Thomas (1802). "The Bakerian lecture: On the theory of light and colours". In: *Philosophical transactions of the Royal Society of London* 92, pp. 12–48.

Zanacchi, Francesca Cella, Carlo Manzo, Angel S Alvarez, Nathan D Derr, Maria F Garcia-Parajo, and Melike Lakadamyali (2017). "A DNA origami platform for quantifying protein copy number in super-resolution". In: *Nature Publishing Group*, pp. 1–7.

Zhang, Mingshu et al. (2012). "Rational design of true monomeric and bright photoactivatable fluorescent proteins". In: *Nature Methods* 9.7, pp. 727–729.

Zhang, Zhengyang, Samuel J Kenny, Margaret Hauser, Wan Li, and Ke Xu (2015). "Ultrahigh-throughput single-molecule spectroscopy and spectrally resolved super-resolution microscopy." In: *Nature Publishing Group* 12.10, pp. 935–938.

Zhao, Zeyu, Bo Xin, Luchang Li, and Zhen-Li Huang (2017). "High-power homogeneous illumination for super-resolution localization microscopy with large field-of-view". In: *Optics express* 25.12, pp. 13382–14.

Zheng, Qinsi, Manuel F Juette, Steffen Jockusch, Michael R Wasserman, Zhou Zhou, Roger B Altman, and Scott C Blanchard (2014). "Ultra-stable organic fluorophores for single-molecule research". In: *Chemical Society Reviews* 43.4, pp. 1044–1056.

Zhong, Guisheng, Jiang He, Ruobo Zhou, Damaris Lorenzo, Hazen P Babcock, Vann Bennett, Xiaowei Zhuang, and Robert H Singer (2015). "Developmental mechanism of the periodic membrane skeleton in axons". In: *eLife* 3, e04581.

Zhuang, X (2009). "Nano-imaging with STORM". In: *Nature Photonics* 3.7, pp. 365–367.

Zipfel, Warren R, Rebecca M Williams, and Watt W Webb (2003). "Nonlinear magic: multiphoton microscopy in the biosciences". In: *Nature Biotechnology* 21.11, pp. 1369–1377.

Zwier, J M, G J van Rooij, J W Hofstraat, and G J Brakenhoff (2004). "Image calibration in fluorescence microscopy". In: *Journal of Microscopy* 216.1, pp. 15–24.